The origin of polymetallic Ni-Co-As-Bi-Sb(-Ag-U) veins in the East Arm Basin and southern Slave Province, Northwest Territories

By
Jordan Scott Burke

A thesis submitted to Saint Mary's University, Halifax, Nova Scotia in partial fulfillment of the requirements for the Degree of Master of Science in Applied Science

April 2019, Halifax, Nova Scotia

Approved: Dr. Jacob Hanley
Supervisor
Department of Geology
Saint Mary's University

Approved: Luke Ootes
Supervisory Committee
Geological Survey of British Columbia

Approved: Dr. Dan Kontak
Supervisory Committee
Department of Geology
Laurentian University

Approved: Dr. Jason Clyburne
Supervisory Committee
Departments of Chemistry/ Environmental Science
Saint Mary's University

April 2019

Abstract

The origin of polymetallic Ni-Co-As-Bi-Sb(-Ag-U) veins in the East Arm Basin and southern Slave Province, Northwest Territories

By: Jordan Scott Burke

Polymetallic, "five-metals association (FMA)"-type Ni-Co-As-Bi-Sb (-Ag-U) hydrothermal vein deposits occur in the vicinity of the East Arm Basin, Great Slave Lake, at Blanchet Island and Copper Pass, Northwest Territories of Canada (Great Slave Lake East Arm basin), the locations of this study. Integration of bulk and microanalytical methods (e.g., cathodoluminescence (CL), scanning electron microscopy (SEM), fluid inclusion microthermometry, secondary ion mass spectrometry (SIMS), and laser ablation inductively coupled mass spectrometry (LA-ICPMS)) was focused on these systems with the goal of updating the current model for this deposit style.

The vein systems in the East Arm Basin occur over 55 km, and share similar microthermometric, isotopic, ore tenor and paragenetic characteristics. Fluid inclusion results indicates salinity (~18-23 wt% $CaCl_2$ equiv.) and minimum entrapment T (~170-250°C) varied little with time during vein formation. An entrapment window between ~145 and 225 ^{o}C and 0.5 to 0.95 kbar is estimated for coeval brine and carbonic inclusions. Fluid $\delta^{18}O$ values increased by as much as 10 ‰ at the onset of mineralization. Quartz-carbonate hosted fluid inclusions in mineralized veins are enriched in Ca-Sr-Ba-Mg-Mn-Pb-Zn but contain only low-ppm concentrations of ore metals. Primary coeval bitumen inclusions, in contrast, are *significantly* enriched in U-Ni-Co-Bi-Ag-Sb-As-Mo-Cu. Integration of all data types strongly suggests that the precipitation of metals and bitumen was triggered by isothermal mixing of ^{18}O-rich basinal brines and metal-rich bitumen particles or oil droplets; oxidation of this hydrocarbon phase resulted in metal precipitation. The basinal brines and associated metal-rich bitumen are thought to be derived from formly overlying outliers of the Athabasca -Hornby Bay -Thelon sedimentary basins that now outcrop ~300-1000 km away from the study areas. This work provides a direct confirmation for the involvement of basinal ore fluids, supporting recent models (i.e fluid mixing) and demonstrating hydrocarbons participated as metal transport agents.

April 2019

Acknowledgments

I thank first and foremost, Dr. Jacob Hanley for his willingness to take me on for this project and for providing his time, assistance, and guidance over the duration of my thesis to provide me with everything I needed to succeed. Dr. Hanley created an environment that allowed me to work independently and productively to make my own thoughts and models for the study area. I also thank my committee members Luke Ootes (British Columbia Geological Survey), Dr. Dan Kontak (Laurentian University), and Dr. Jason Clyburne (Saint Mary's University) for their continued support throughout this thesis. I specifically thank Luke Ootes for all the time and patience he has dedicated and shown throughout this project, and for the many lessons taught during our time in the field. I thank Dr. Mathias Burisch for acting as my external examiner for this work. I would like to acknowledge all the help, support, and funding by the Northwest Territories Geological Survey, without your support, this work would not have been possible. A special thanks to the Hanley Lab group members, especially Glen, Mitch, Kevin, Corwin and Dan, for constantly putting up with my complaining, my fantasy football chats, and obnoxiously loud music pounding through my ear buds. Last but not least, I thank my amazing parents, Karen and Ian, brothers Ryan and Taylor, and long-time partner Lisa for their immense patience and support throughout my graduate degree. I would not have had the opportunity to complete this project if it were not for your support.

Table of Contents

List of Figures

***In* Chapter 1**

***In* Chapter 2**

List of Tables

Chapter 1: Introduction

1.0 Structure of Thesis

This study is comprised of three chapters: Chapter 1 contains a brief outline of the thesis structure, research objectives, and a general description of polymetallic "five metals association" veins (characteristics and ore genesis models). Chapter 2 provides a detailed petrographic and mineralogical description of arsenide/sulfarsenide mineralization styles present at two sub-economic mineral deposit settings (Blanchet Island and Copper Pass, East Arm of Great Slave Lake, NWT, Canada), and presents comprehensive fluid inclusion, mineral chemistry and stable and radiogenic isotope data for the two deposits. These data are used to define a model for the formation of this style of mineralization in the study area and elsewhere. Chapter 3 reiterates the main conclusions of Chapter 2 and proposes future work to further elucidate the formation of the polymetallic "five-metals association" veins in the study area and elsewhere.

1.1 Objectives of thesis

Polymetallic, FMA deposits remain understudied when compared with other mineral deposit types (e.g Orogenic gold, Ni-Cu-PGE or Cu-Mo porphyry), despite being historically imporant as high grade sources of Ag±U in Canada (e.g., Cobalt-Gowganda, Ontario and Port Radium, NWT) and elsewhere globally in the early 20th c. FMA deposits have not received attention in research and mineral exploration in recent decades. While these deposits have high grades and multi-commodities, their low tonnage discontinuous vein-hosted nature has rendered them less attractive targets relative to bulk-mineable U, Ag and Co. The main objectives of the study are: (i) to constrain fluid PTX conditions, depth of ore emplacement, conditions of ore formation, metal source rock or magma; (ii) to compare deposits and evaluate the influence of local geology on ore-

grade and mineralization style (host rock composition, proximity to metal sources, proximity to intrusive rocks). (iii) to develop a model for the evolution of the "five-metals association" mineralizing systems in the study area by establishing the relationship between mineralization and metal/fluid source/s, and (iv) to illustrate the potential influence and importance of sedimentary basins as sources of sedimentary bitterns, hydrocarbons and metals required for this style of mineralization. This project uses mineralogical, geochemical and isotope methodologies to provide an updated model for polymetallic five-metal veins at Blanchet Island, which is hosted by Great Slave Supergroup rocks (Paleoproterozoic), and at Copper Pass, which is hosted by Yellowknife Supergroup rocks (Archean) in the East Arm region of Great Slave Lake. The results are compared to historical deposits, of similar classification, in the Great Bear Lake area, and to other deposits distributed globally. This comparison provides insights into the fundamental controls required for the generation of economic vs. subeconomic deposits. While the mineralization styles at Blanchet Island and Copper Pass are similar (*sensu lato* five-metals vein deposits), they have different metal associations (i.e., Co-dominated mineralization at Blanchet Island, Ni-dominated mineralization at Copper Pass), and they are hosted in two different geological settings with contrasting host rocks of different age. This study provides insight into the conditions of ore formation in these five-metal associated veins, including temperature, fluid salinity, paleodepth and mechanisms for metal precipitation, as well as fluid and metal sources.

1.2 List of abbreviations

Table 1: List of acronyms and abbreviations used throughout this thesis

Abbreviation	Meaning
anna	annabergite
BI	Blanchet Island occurrence
BSE	backscattered electrons
btm	bitumen
ca	calcite
carb	carbonate
carbonic	fluid composed of CO_2 and/or hydrocarbons
cbt	cobaltite
CIS	Compton intrusive suite
CL	cathodoluminescence
CLG	Caribou Lake Gabbro occurrence
clv	cleavage plane
CP	Copper Pass occurrence (alt: BM, NIX, GOGO, Sachowia Lake)
Fe-dol	ferroan dolomite
FIA	fluid inclusion assemblage
FMA	"five metal association"
GC	gas chromatography
gdf	gersdorffite
gn	galena
HC	hydrocarbon
LA-ICP-MS	laser ablation inductively coupled plasma mass spectrometry
L_{aq}	aqueous liquid phase
$L_{carbonic}$	carbonic liquid phase
LB	Labelle Penninsula (occurrence)
ME	metal
nk	nickeline
polymetallic	"five-metal vein association" main: Ni-Co-As-Ag-Bi; other: Sb, U, Cu, Pb, Zn, Mo
py	pyrite
qtz	quartz
ram	rammelsbergite
saf	safflorite
S_{brine}	secondary origin brine fluid inclusion trail
$S_{carbonic}$	secondary origin carbonic fluid inclusion trail
SIMS	secondary ion mass spectrometry

skut	skutterudite
TD-MS	total digestion mass spectrometer
T_h	temperature of homogenization
$T_h^{carbonic}$	temperature of homogenization for carbonic phase
T_m^{ice}	temperature of final ice melting
UI	Union Island shale occurrence
urn	uraninite
V	vapour phase
$V_{carbonic}$	carbonic vapour
wt.%	weight percentage
wt.% $CaCl_2$ eq. or equiv.	fluid inclusion bulk salinity in weight percentage $CaCl_2$ equivalent

1.3 Introduction to polymetallic "five-metal association" deposits

Polymetallic veins deposits enriched in *Ni, Co, As, Ag, Bi*, Sb, U, Mo, Cu, Zn, Pb and other metals, traditionally defined as "five-metal association" (FMA) veins (Badham, 1975; Kissin 1992), occur worldwide with major examples, in Canada, Czech Republic (Jachymov: Ondrus et al., 2003), Switzerland (Jaffe, 1986; Penninic Alps: Kreissl et al., 2018), Germany (Odenwald: Burisch et al., 2017; Schneeberg: Lipp and Flach 2003), Mexico (Batopilas: Wilkerson et al., 1988), Morocco (Bou Azzer: Ahmed et al., 2009), and Norway (Kongsberg: Lietz, 1939; Neumann, 1944; Staude et al., 2007). Canada hosts three of the largest FMA vein deposits in the world at Cobalt-Gowganda (Boyle, 1968; Andrews et al., 1986; Marshall et al., 1993), and Thunder Bay, Ontario (Franklin et al., 1986), and the Great Bear Lake region, Northwest Territories (Robinson and Ohmoto, 1973; Changkakoti et al., 1986; Changkakoti and Morton, 1986).

Mineral exploration and historic mining activity in the Northwest Territories identified many other FMA vein systems in the southern Slave Province and East Arm basin of Great Slave Lake. Compared to deposits in the Great Bear Lake region, these FMA systems have not been studied in

detail and their genetic kinship to the larger deposits in the Great Bear Lake region is unknown. Two FMA occurrences are found at Blanchet Island in the Great Slave Supergroup and Copper Pass in the Yellowknife Supergroup and are the topic of this study (Fig. 1). These mines produced minor amounts of cobalt and nickel (Table 2).

Table 2 Summary of polymetallic "five-metals association" (FMA) veins in the NWT (Silke, 2009)

Name	Commodity	Tonnage, grade details	Historical grade
Bear Portal	Ag	unknown	unknown
Blanchet Island	Co-Ni	330 tons	15% Ni + 11% Co
Bonanza	Ag	unknown	unknown
Contact Lake	U+Ag	16995 tons (678,000 oz Ag and 6933 lbs U_3O_8)	unknown
Contact Lake Portal	Ag-Cu	unknown	unknown
Copper Pass	Ni	>450 tons	33-35% Ni
Echo Bay	Ag-Cu	363,140 tons (23,544,461 oz Ag, 4505 tons Cu)	unknown
El Bonanza	Ag	2.95 tons (30,175 oz Ag)	unknown
Eldorado	U-Ra-Ag-Cu-Ni-Co-Pb	1,366,602 tons (6,079 tons U_3O_8, 450g Ra, 13,371,382 oz Ag, 2,389 tons Cu, 140 tons Ni, 250 tons Co, 8 tons Pb)	4,328 oz/ton Ag
Glacier Bay	Ag	unknown	4 oz/ton Ag, 0.02% U_3O_8
Mystery Island	U-Ra	unknown	unknown
Norex	Ag	53,697 tons (2,066,744 oz Ag)	unknown
Northrim	Ag	12,000 tons (30,000 oz Ag)	unknown
Smallwood Lake	Ag	18,204 tons (169,720 oz Ag)	unknown
Terra	Ag-Cu	507,629 tons (14,236,325 oz Ag, 2,248 tons Cu)	unknown

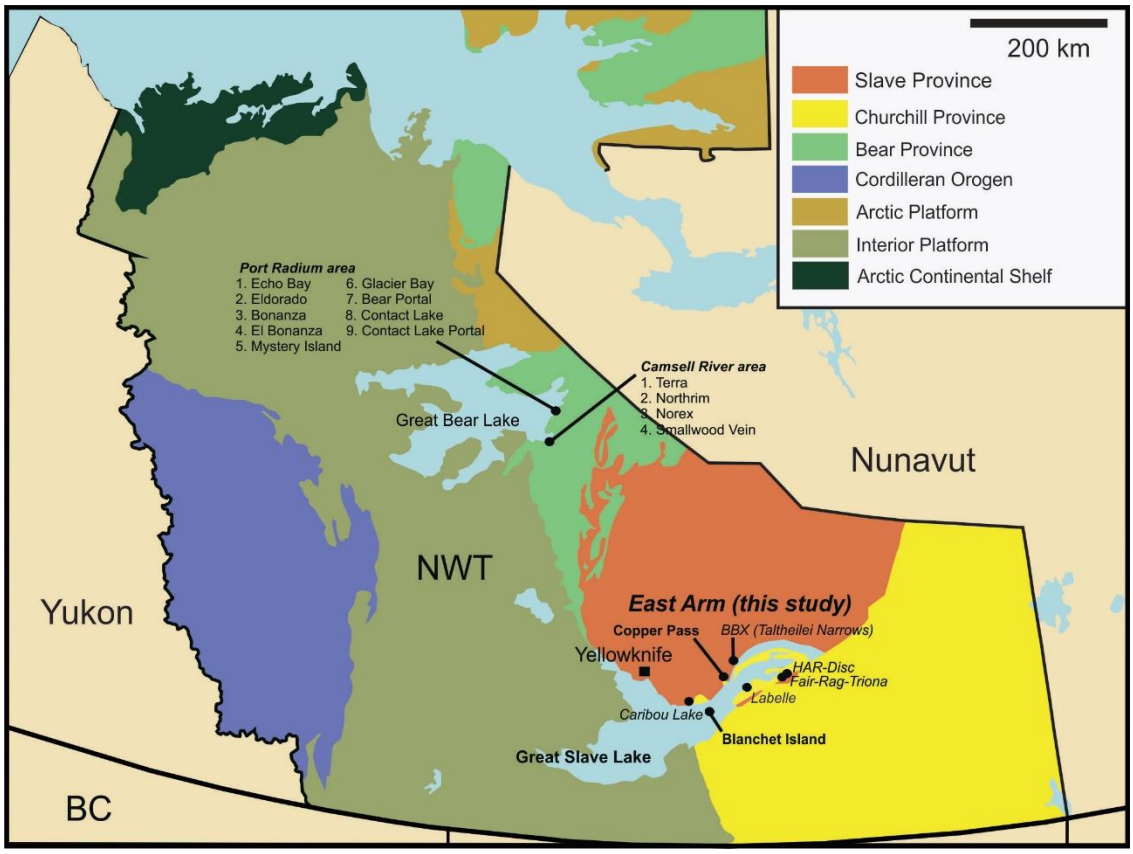

Figure 1 - Geological map of the Northwest Territories, Canada, showing major geological divisions and historical and existing polymetallic FMA-type vein deposits of the Port Radium, Camsell River and East Arm basin areas.

1.3.1 Paragenetic sequence of FMA vein systems

The mineralogy of FMA veins is their most distinctive feature, containing a combination of mineral species considered rare in other deposit settings (Kissin 1992). Kissin (1992) summarizes the typical sequence of mineral assemblages (i.e., stages of mineralization) present in FMA systems (cf. Bastin, 1939; Boyle, 1968; Boyle and Dass, 1971; Petruk, 1971; Badham, 1975; Andrews et al., 1986; Changkakoti and Morton, 1986; Marshall et al., 1993; Ondrus et al., 2003; Markl et al., 2016; Gandhi et al., 2018 and others therein):

- Stage 1- Early barren stage. Quartz precipitated, sometimes with base metal sulfides (pyrite, chalcopyrite, and sphalerite).
- Stage 2- U stage. Uraninite-quartz precipitation occurs. This stage is absent in many large deposit examples (e.g., Cobalt-Gowganda, Ontario), but economically important in others (e.g., Port Radium district, Great Bear Lake, NWT).
- Stage 3- Ni-Co arsenide-Ag stage. Ni-Co arsenide mineralization occurs with native Ag and Bi, occurring with carbonate gangue (calcite or dolomite).
- Stage 4- Sulfarsenide-sulfide stage. A gradational stage following Stage 3, comprised of Ni-Co-sulfarsenides and later base metal sulfide (pyrite, galena, chalcopyrite, sphalerite) mineralization occurring with native Ag, argentite in carbonate gangue with minor quartz, barite, fluorite. Native arsenic and antimony may occur in this stage, as well as Sb-As-Ag sulfosalts.
- Stage 5- Late barren stage. Dominated by low temperature carbonate precipitation (calcite) with minor barite, fluorite.

Kissin (1992) further noted the Ni-Co arsenide-Ag stage is most diagnostic of FMA systems and not all stages of mineralization are present within all FMA deposits. Badham (1975) described the complex mineralogical variance within polymetallic veins of Ni-Co-Ag with trace Bi, with observations from the Camsell River area (district) of the Great Bear Lake region, NWT. The chemistry and mineralogy of arsenides may be extremely variable, but generally they may consist of (i) Ni monoarsenides (nickeline), (ii) Ni diarsenides (rammelsbergite), (iii) Co-Fe diarsenides (safflorite, smaltite and loellingite) and (iv) Co-Fe rich, Ni-poor triarsenides (skutterudite) (Kissin 1992). Antimony analogues of the Ni monoarsenides may also be present (e.g., breithauptite). Typically, arsenides in FMA systems grow into dendrites and rosettes, and usually show remarkable compositional zonation from Ni-rich core zones to Co-rich margins and rims, and with sporadic concentrations in the outer parts of Fe. Silver concentrations occur within the core of the arsenide structure, typically with nickeline. Transitional sulfarsenides (e.g. Ni-cobaltite, Co-gersdorffite) and later base-metal sulfides (chalcopyrite, pyrite, sphalerite and galena) are often associated with FMA veins. Gangue minerals quartz and calcite dominate the early and late stage mineralization and often host microinclusions of hematite and magnetite (Leblanc, 1986). Alteration assemblages are spatially restricted to within ~10 cm of mineralized veins and comprise primarily propylitic assemblages (chlorite -albite nearest vein contact, epidote-carbonate away from the contact) as well as hematitization and minor sericitization peripherally (Andrews et al., 1986; Kissin, 1992).

1.3.2 The silver-arsenide association, mechanism of metal deposition, and metal sources

The FMA deposit style is a distinct vein style, with Ag found in association with Co-Ni-Fe sulfarsenides and arsenide mineral assemblages. Kissin (1992) highlights that host rocks can be of

varying composition and age, suggesting FMA deposition is not limited to one specific period or periods, or host rock types. Metal associations and ore mineralogy and textures are similar between deposits styles. However, studies of the alteration styles, fluid composition and physicochemical characteristics, stable isotope systematics and other features demonstrate significant variability between deposits, with several alternative ore genesis models proposed (cf. Kissin, 1992; Markl et al., 2016; Burisch et al., 2017; Gandhi et al., 2018; Kreissl et al., 2018 and authors therein). Generally, previous literature highlighted depositional environments for FMA systems are characterized by: (i) tectonic environments broadly characterized by basinal subsidence and rifting; (ii) spatial association between the deposits and regional-scale faults; and (iii) close spatial and temporal relationship between the deposits and mafic or felsic intrusions, with both mineralizing solutions and magmas potentially utilizing deep fault systems to access the upper levels of the crust (Andrews, 1986).

Marshall et al. (1993) and Marshall et al. (2000) discuss that Ag deposition (i.e., at Cobalt), occurred via three possible mechanisms: (i) the hydrothermal boiling of Ag-saturated saline solutions; (ii) cooling of Ag-saturated fluid; or (iii) mixing of a Ag-saturated fluid with a less saline fluid (of meteoric or magmatic origin). These mechanisms assume that Ag was transported as a chloride complex (rather than bisulfide complex) in the saline brines. Fluid inclusion studies confirm the presence of highly saline brines as the primary fluid phase responsible for vein deposition (Scott and O'Connor, 1971: Kerrich et al., 1986: Marshall et al., 1993); and the low sulfur fugacity associated with vein formation, indicated by lack of aqueous or gaseous sulfur species in fluid inclusions, and sulfur deficiency interpreted from the Ag-arsenide association (Marshall et al., 2000).

Fluid inclusion studies in the Cobalt deposits (Kerrich et al. 1986 and Andrews et al. 1986), and Great Bear Lake deposits (Robinson and Ohmoto 1973 and Changkakoti et al. 1986b), investigated fluid inclusions in the Cobalt and Great Bear Lake deposits, respectively. Deposits in the Cobalt-Gowganda district formed from highly saline brines (~30-54 wt% NaCl equiv.) in the temperature range of 150-250^{o}C at depth of ~2 km (Andrews et al., 1986), and in the Great Bear Lake region from highly saline brines (15-35 wt% NaCl equiv.) between 200-300^{o}C at a depth of 2-4 km (Robinson and Ohmoto, 1973; Changkakoti et al., 1986). Kerrich et al. (1986) and Changkakoti et al. (1986) provided textural and microthermometric evidence of boiling (homogenization of liquid-rich and vapor-rich simultaneously, at the same T) supporting a much shallower depth of formation (< 600 bar and < 200 bar, for Cobalt and Great Bear Lake deposits, respectively) and supporting a hydrothermal boiling model for silver deposition. However, it has been suggested (Marshall and Watkinson, 2000) that owing to an incomplete microthermometric data set, it is impossible to make a distinction between true boiling assemblages and assemblages that suffered post-entrapment volume changes and phase separation (due to leakage). This challenged the boiling theory.

Evidence from stable isotope data of gangue minerals, although limited, supports the fluid mixing ore depositional model (e.g., at Cobalt-Gowganda). While $\delta^{18}O$ and δD compositions for carbonates and quartz span broadly from the field for magmatic waters, through metamorphic fluids and seawater, towards the meteoric water line, a distinct binary mixing trend was identified between a high $\delta^{18}O$, high-salinity end-member and low $\delta^{18}O$, and low-salinity end-member (Kerrich et al., 1986). Marshall et al. (1993) confirmed a transient mixing event at the time of silver deposition; specifically, high salinity (halite-saturated) inclusions predate and postdate silver deposition, whereas less saline (halite-undersaturated) inclusions are a syn-silver deposition.

Kissin (1992) suggested that silver deposition may have been further promoted by fluid interaction with rock or mineralogical units of a reducing nature, such as pre-existing Ni-As-Co-S minerals, or graphite/sulfur-bearing shales.

Suspected metal sources for the FMA deposit style remain controversial. Kissin (1992) summarized FMA deposit in the Great Bear Lake, Cobalt-Gowganda and Thunder Bay districts. These include:

(i) A hydrothermal/magmatic model, where granitic intrusions are thought to be a source of silver.

(ii) A hydrothermal/metamorphic model, where thermal and chemical effects are thought to occur from mafic (diabase sills; metamorphic heating) intrusions in-situ or at depth.

(iii) Mixing of hydrothermal solutions of mafic and granitic affinities.

(iv) By hydrothermal/metamorphic processes concentrating components from organic-rich black shales, pre-existing massive sulphides, or metal-rich volcanoclastic rocks.

(v) A syngenetic model, where an exhalative process is responsible for a syngenetic stratiform deposits.

(vi) A non-magmatic model, where FMA solutions originate at depth, near the crust-mantle boundary.

(vii) By introduction, via deep fractures, of a juvenile five-element solution in a basalt-generating environment near the crust-mantle boundary.

(vii) Circulation of connate brines in a continental rift environment.

A considerable gap in the literature exists after 1992 until recently. Markl et al. (2016) considered textural evidence, stable isotope data, and mineral assemblage chemistry and proposed an elegant mass balance model for the formation of FMA deposits involving the sudden influx of hydrocarbons, liberated through "natural fracking" induced by cyclic seismic events, and subsequent mixing of CH_4 with metal-rich aqueous fluid causing rapid metal precipitation (and changes in fluid chemistry) through redox and pH changes. Burisch et al. (2016) tested the general model of Markl et al. (2016) in the Odenwald district, in SW Germany, combining mineralogical and textural observations with geochronological, stable isotope, and fluid inclusion (microthermometry, Raman spectroscopy) data to model the formation of the FMA ores as the products of mixing of three distinct fluids (a metal-rich crystalline basement brine, a sulfide-bearing basinal [sedimentary] brine, and methane-dominated fluid. They asserted that metals were derived from basement brines, and confirmed the present of (trace) CH_4 and HS^- in fluid inclusions in carbonate. They related the ore-forming process through lithotectonic considerations and geochronology to be linked to opening of the North Atlantic basin in the mid-Jurassic. In a study by Kreissl et al. (2018), the earlier work of Markl et al. (2016) and Burisch et al. (2016) was tested further through a comprehensive mineral chemical, textural, fluid inclusion, stable isotope and geochronological study of an FMA vein system in the Penninic Alps, Switzerland. They highlight the mineralogical and thermodynamic complexity of the earlier models along with identifying more complex hydrocarbons (e.g., kerogen) in fluid inclusions. That study conceptualized a model for the evolution of basinal fluids and reiterated the importance of basement lithologies (e.g., metal-enriched "fahlbands" in gneisses, or other mafic rocks and possibly granitoids) as likely metal sources for the FMA association.

1.4 Overview of study area

1.4.1 Regional geology

1.4.1.1 Slave Province

The Slave Province is one of 35 Archean cratons preserved worldwide. The Yellowknife Supergroup refers to a package of supracrustal rocks that includes volcanic and sedimenary units that were deposited in the Neoarchean, between ca. 2.74 and 2.62 Ga. The Yellowknife Supergroup overlays and older Meso to Paleoarchean core, and both were intruded by extensive plutons in the late Archean (ca. 2.63 to 2.58 Ga) (Bleeker and Hall 2007: Henderson 1970). Between 2595 and 2585 Ma (Bleeker and Hall 2007: Davis and Bleeker 1999) a craton-wide event known as the "granite bloom" transferred a significant fraction of heat-producing elements and lower crustal fluids into the upper crust, promoting slow cooling and stiffening of the crust. This allowed for the craton to be preserved long-term (Bleeker and Hall 2007). Located in the Yellowknife Supergroup are metasediments of amphibolite and greenschist facies, along with metavolcanics such as pillow basalts, breccia, tuff and amphibolite. The western portion of the Yellowknife Supergroup is dominated by mafic volcanic rocks, where the eastern limits are dominated by felsic rocks. These Late Archean granitic intrusions coincided with regional and contact metamorphic events. Stratigraphic subdivision of the supracrustal rocks of the supergroup are distinguished with three divisions: (a) the base, consisting of mainly mafic flows and intrusions (b) composed of conglomerates, quartzites, and intermediate to felsic volcanics (c) greywacke and slate (Healmstaedt and Padgham, 1986).

The East Arm refers to a geographic region of Great Slave Lake, NT. The north shore of the East Arm is underlain by Archean rocks of the Slave craton, in addition to the Blachford Intrusive complex (ca. 2.17 Ga; Figure 1). The south shore of the East Arm is underlain by mylonitic rocks

of the Great Slave Lake shear zone (ca. 2.6 to 1.92 Ga) (Hamner et al 1988). The East Arm basin refers to stratigraphic package of supracrustal and lesser intrusive rocks that were deposited between ca. 2.04 and 1.85 Ga (Bowring et al., 1984; Kjarsgaard et al. 2013; Sheen et al., 2019). These are preserved on a series of islands in the East Arm of Great Slave Lake, with lesser occurrences on the southern and northern mainland (Figure 1).

The East Arm basin is composed of four temporally and geologically distinct units (Hoffman, 1968, 1988), from base to top: the Union Island Group (ca. 2.04 Ga; Sheen et al., 2019); Wilson Island Group (ca. 1.93 Ga; Bowring et al., 1984); Great Slave Supergroup (<1.93 to 1.85 Ga; Kjarsgaard et al., 2013; Bowring et al., 1984), and; Et-Then Group (<1.85 Ga). Two assocaited ntrusive suites are known in the region, the Butte Island suite (ca. 1.89 Ga; Bowring et al., 1984) and the Compton Intrusive suite (ca. 1.87 Ga). Sedimentological studies of the EastArm basin led Hoffman (1968, 1969, 1970) to believe the basin was a preserved fold-belt, however was later interpreted to have developed as a failed rift (Athapuscow aulacogen) (Hoffman, 1973; Bowring et al., 1984; Sheen et al., 2018). Hoffman (1987) revisited the aulacogen model, rejecting it in favour of a model involving a syn-collisional transtensional basin during Slave-Rae provincial collision (Sheen et al., 2018).

The Great Slave Supergroup (1.93 Ga and 1.85 Ga; Bowring et al., 1984 and Kjarsgaard et al., 2013) is relavent to this study as it is host to the Blanchet Island deposit (Figure 1). It is composed of four lithostratigraphic formations (Hoffman, 1968, 1988), from base to top: the Sosan; Kahochella; Pethei, and; Christie Bay groups. The units of the Great Slave Supergroup consist of alternating fluviatile and marine sedimentary rocks (feldspathic sandstones, mudstones,

conglomerates, limestones and shales) with volcanic sequences of the Sosan (basalt, rhyolite), Kahochella (basalt, rhyolite, grabbro) and Christie Bay groups. The rock units of interest for this study are the Pethei Group and the Compton Intrusive Suite.

1.4.1.2 Pethei Group

The Pethei Group is composed of ten lithostratigraphic formations, representing a sequence consists of basinal and platformal lithologies, consisting of feldspathic wacke turbidites and greywackes and dolomitic limestones respectively. The FMA veins at the Blanchet Island deposit are hosted in the Blanchet Formation which consists of feldspathic wacke turbidites, marlstone, and limestone-argillite rhythmites that were deposited in deeper-water basins (Hoffman, 1968).

The Compton Intrusive Suite refers to a series of sills that extend the length of the East Arm basin (Bowring et al., 1984). These intrusions range from hornblende-biotite diorite to quartz monzonites and intruded at ca. 1.87 Ga (Bowring et al., 1984). The Compton Intrusive Suite are interpreted equivalents to the Great Bear Magmatic zone (1.85-1.87 Ga) of the Wopmay Orogen, preserved to the northwest (van Breeman et al., 2013). The Compton Intrusive Suite are geochemically classified as volcanic arc granites (Kjarsgaard et al., 2013).

1.4.2 Exploration History for Blanchet Island and Copper Pass

1.4.2.1 Blanchet Island

In 1968 Alfred V. Giauque discovereds and staked mineral claims for cobalt-nickel mineral occurrences at Blanchet Island. These claims were optioned to Jason Explorers Limited in 1969, who had staked additional claims near the original Blanchet showing. Blasting of open-cuts and

adits installation began in 1969, when 300 tons of Co-Ni-arsenide ore was bagged and shipped to France for processing. Ore was sold to Ugine-Kuhlmann SA of Paris, France, where the ore smelter reported assays of 11% cobalt and 12% nickel. Underground mining ceased in 1970, when the final shipment of 243 tons was shipped to France, yielding 5% cobalt and 15% nickel. Thirty tons of ore was left on the shores and was found by Dave Smith in 1980. In 1984 Highwood Resources Limited staked "HRL" claims on Blanchet Island, covering mineralized zones (Silke 2009).

1.4.2.2 Copper Pass

In 1940, the Cominco mining company staked initial claims; these lapsed and were re-staked by C. McAvoy in 1950. Venture Resourced Limited obtained the claims in 1957 and conducted surface mining from a primary trench. Venture Resources Limited blasted a deep trench in the Main Zone showing, consisting of ~260 cubic yards of rock in 1957. Claims were re-staked twice before being incorporated into the "Gogo" group claims in 1969 by J. McAvoy. Claims under the "Gogo" group were acquired by the Copper Pass Mines Limited Company in March, who shipped out 24 barrels of ore to Edmonton for grade estimation. These returned assays between 25% and 43% Ni, with trace cobalt, bismuth, and silver. By October 1969, 200 tons of ore had been mined from the open trench (Kelly, 1969; Silke, 2009).

1.5 References

Ahmed, H.A., Arai, S., Ikenne, M. 2009. Mineralogy and Paragenesis of the Co-Ni Arsenide Ores of Bou Azzer, Anti-Atlas, Morocco. Economic Geology. vol 104. pp 249-266

Andrews, A. 1986. Silver vein deposits: summary of recent research. Canadian Journal of Earth Sciences. vol 23. pp 1459-1462

Andrews, A., Owsiacki, L., Kerrich, R., Strong, D. 1986. The silver deposits at Cobalt and Gowganda, Ontario. I: Geology, petrography, and whole-rock geochemistry. Canadian Journal of Earth Science. vol 23. pp 1481-1506

Badham, J. 1975. Mineralogy, Paragenesis and Origin of the Ag-Ni, Co Arsenide Mineralisation, Camsell River, N.W.T Canada. Mineral Deposita. vol 10. pp 153-175

Bastin, E. 1939. The nickel-cobalt-native silver ore type. Economic Geology. vol 34. pp 1-40

Bleeker, W; Hall, B. 2007. The Slave Craton: Geological and Metallogenic Evolution. Mineral deposits of Canada: a synthesis of major deposit-types, district metallogeny, the evolution of geological provinces, and exploration methods. Goodfellow, W D (ed.). Geological Association of Canada, Mineral Deposits Division, Special Publication no. 5, pp 849-879

Bowring, S., Van Schmus, W., Hoffman, P. 1984. U-Pb zircon ages from Athapuscow aulacogen, East Arm of Great Slave Lake, N.W.T, Canada. Canadian Journal of Earth Sciences. vol 21. pp. 1315-1324

Boyle, R., and Dass, A. 1971. The origin of the native silver veins at Cobalt, Ontario. The Silver-Arsenide Deposits of the Cobalt-Gowganda Region, Ontario. The Canadian Mineralogist, vol 11. pp 414-417

Burisch, M., Gerdes, A., Walter, B., Neumann, U., Fettel, M., Markl, G. 2017 Methane and the origin of five-element veins: Mineralogy, age, fluid inclusion chemistry and ore forming processes in the Odenwald, SW Germany. Ore Geology Review. vol 81. pp 42-61.

Changkakoti, A., Morton, R. 1986. Electron microprobe analyses of native silver and associated arsenides from the Great Bear Lake silver deposits, Northwest Territories, Canada. Canadian Journal of Earth Science. vol 23. pp 1470-1479.

Davis, W.J. & Bleeker, Wouter. (2011). Timing of plutonism, deformation, and metamorphism in the Yellowknife Domain, Slave Province, Canada. Canadian Journal of Earth Sciences. 36. 1169-1187.

Franklin, J., Kissin, S., Smyk, M., and Scott, S. 1986. Silver deposits associated with the Proterozoic rocks of the Thunder Bay District, Ontario: Canadian Jounal of Earth Sciences. vol 23. pp 1963-1979

Ghandi, S., Potter, E., Fayek, M. 2018. New constraints on genesis of the polymetallic veins at Port Radium, Great Bear Lake, Northwest Canadian Shield. Ore Geology Reviews. vol 96. pp 28-47

Hamner, S. 1988. Great Slave Lake Shear Zone, Canadian Shield: reconstructed vertical profile of a crustal-scale fault zone. Tectonophysics. vol 149. pp 245-264

Helmstaedt, H. and Padgham, W. 1986. Evidence for spreading in the lower Kam Group of the Yellowknife greenstone belt: Implications for Archaean basin evolution in the Slave Province. Lunar and Planetary Institute. pp 116-119

Hoffman, P. 1968. Stratigraphy of the Lower Proterozoic (Aphebian), Great Slave Supergroup, East Arm of Great Slave Lake, District of Mackenzie. Geological Survey of Canada, Paper 68-42. pp 1-100

Leblanc, M. 1986. Co-Ni arsenide deposits with accessory gold, in ultramafic rocks from Morocco. Canadian Journal of Earth Sciences. vol 23. pp 1592-1602

Lietz J.1939. Mikroskopische und chemische Untersuchungen an Kongsberger Silbererzen. Z Angew Mineral vol 2. pp 65–113

Lipp, U., Flach, S., 2003. Wismut-, Kobalt-, Nickel-und Silbererze im Nordteil des Schneeberger Lagerstättenbezirkes. Sächsisches Landesamt für Umweltund Geologie, Dresden. pp 1–210.

Neumann, H. 1944. Silver deposits at Kongsberg: Norges Geologiske Undersokelse. vol 162. P 133.

Jaffe, F. 1986. Switzerland, in Dunning, F.W. and Evans, A., eds. Mineral Deposits of Europe, Central Europe: the Institution of Mining and Metallurgy and the Mineralogical Society, London. vol 3. pp 41-54

Kerrich, R., Strong, D., Andrews, A., Owsiacki, L. 1986. The silver deposits at Cobalt and Gowganda, Ontario. III: Hydrothermal regimes and source reservoirs- evidence for H, O, C, and Sr isotopes and fluid inclusions. Canadian Journal of Earth Sciences. vol 23. pp 1519-1550

Kissin, S. 1992. Five Element (Ni-Co-As-Ag-Bi) veins. Geoscience Canada. vol 19. n 3. pp 113-122

Kjarsgaard, B., Pearson, D., Dufrane, A., Heaman, L. 2013. Chapter 3. Proterozoic Geology of the East Arm Basin with emphasis on Paleoproterozoic magmatic rocks, East Arm MERA study area. Chapter 3 in Mineral and Energy Resource Assessment for the proposed Thaidene Nene National Park Reserve in the Area of the East Arm of Great Slave Lake, Northwest Territories (eds). Geological Survey of Canada. Open File 7196. pp. 51-92

Kreissl, S., Gerdes, A., Walter, B., Neumann, U., Wenzel, T., Markl, G. 2018. Reconstruction of a >200Ma multi-stage “five element” Bi-Co-Ni-Fe-As-S system in the Penninic Alps, Switzerland. Ore Geology Reviews. vol 95. pp 746-788

Lipp, U., Flach, S., 2003. Wismut-, Kobalt-, Nickel-und Silbererze im Nordteil des Schneeberger Lagerstättenbezirkes. Sächsisches Landesamt für Umweltund Geologie, Dresden. pp 1–210.

Marshall, D., Diamond, L., Skippen, G. 1993. Silver Transport and Deposition at Cobalt, Ontario, Canada: Fluid Inclusion Evidence. Economic Geology. vol 88. pp 837-854

Marshall, D., Watkinson, D. 2000. The Cobalt Mining District: Silver Sources, Transport and Deposition. Exploration Mining Geology. vol 9. pp 81-90.

Neumann, H. 1944. Silver deposits at Kongsberg: Norges Geologiske Undersokelse. vol 162. P 133.

Ondrus, P., Veselovsky, F., Gabasova, A., Hlousek, J., and Srein, V. 2003. Geology and hydrothermal vein system of the Jacbymov (Joachimsthal) ore district. Journal of the Czech Geological Society. vol 48. pp 3-18

Robinson, B. Ohmoto, H. 1973. Mineralogy, Fluid Inclusions, and Stable Isotopes of the Echo Bay U-Ni-Ag-Cu Deposits, Northwest Territories, Canada. Economic Geology. vol 68. pp 635-656

Staude S., Wagner T., Markl G.2007. Mineralogy, mineral compositions and fluid evolution at the Wenzel hydrothermal deposit, Southern Germany: implications for the formation of Kongsberg-type silver deposits. Canadian Mineralogist vol 45. pp 1147–1176

Wilkerson, G., Deng, Q., Llavona, R., Goodell, P. 1988. Batopilas mining district, Chihuahua. Economic Geology. vol 83. pp 1721-1736

Chapter 2: Geology, fluid characteristics, and paragenesis of polymetallic Ni-Co-As-Bi-Sb(-Ag-U) veins East Arm, Great Slave Lake, Northwest Territories, Canada

Jordan Burke*[1], Jacob Hanley[1], Corwin Trottier[1], Luke Ootes[23], Zoltán Zajacz[4], Ryan Sharpe[5], Mostafa Fayek[5]

[1]*Department of Geology, Saint Mary's University, Halifax, Nova Scotia, Canada*
[2]*Northwest Territories Geological Survey, Yellowknife, NWT, Canada*
[3]*British Columbia Geological Survey, Victoria, British Columbia, Canada*
[4]*Department of Earth Sciences, University of Toronto, Toronto, Ontario, Canada*
[5]*Department of Geological Sciences, University of Manitoba, Winnipeg, Manitoba, Canada*
*corresponding author email address: jordan_burke90@hotmail.com

Submitted to Precambrian Geology

Abstract

Polymetallic, "five-metals association (FMA)"-type Ni-Co-As-Bi-Sb(-Ag-U) hydrothermal vein deposits in the Northwest Territories of Canada show widely contrasting grade and tonnage characteristics from one deposit district to another, with historically world-class deposits in the Great Bear Lake region (e.g., Eldorado-Echo Bay, Terra) and smaller, sub-economic systems in the Great Slave Lake East Arm basin, and southern Slave Province, including Copper Pass and Blanchet Island, the locations of this study. Integration of a variety of bulk and microanalytical methods (e.g., CL, SEM, fluid inclusion microthermometry, SIMS, LA-ICPMS) was focused on these sub-economic systems with the goal of revising the current model for this deposit style, specifically with respect to fluid and metal sources, metal precipitation mechanisms, and reasons for variability in metal tenor at a regional scale.

Similarities in microthermometric, isotopic, ore tenor and paragenetic characteristics for vein systems in the East Arm basin indicates that a common mineralizing process operated over an area of 100 km^2. Fluid salinity (~18-23 wt% $CaCl_2$ equiv.) and minimum entrapment T (~170-250°C)

remained consistent during the evolution of vein formation. An entrapment window between ~145 and 225 ºC and 0.5 to 0.95 kbar is estimated for coeval brine and carbonic inclusions. Fluid $\delta^{18}O$ values increased by as much as 10 ‰ at the onset of mineralization. Fluid inclusions in mineralized quartz-carbonate veins are enriched in Ca-Sr-Ba-Mn-Pb-Zn but contain only low-ppm concentrations of ore metals. Coeval bitumen inclusions, in contrast, are *significantly* enriched in U-Ni-Co-Bi-Ag-Sb-As-Mo-Cu. Integration of all data types strongly indicates that the precipitation of metals and bitumen was triggered by isothermal mixing of ^{18}O-rich basinal brines and metal-rich bitumen particles, or oil droplets in structures within crystalline basement. Oxidative and thermal decomposition of the hydrocarbon phase resulted in metal and carbonate precipitation. The basinal brines and associated metal-rich bitumen are thought to be derived from former overlying outliers of the Athabasca-Hornby Bay-Thelon sedimentary basins that now only outcrop ~300-1000 km away from the study areas.

This study highlights the role of hydrocarbons in transporting metals in FMA hydrothermal systems. Importantly, high-grade polymetallic vein systems of this variety may be linked to the metal budgets of previously overlying sedimentary basins rather than the basement rocks in which the deposits are hosted. This work also supports independent models that indicate the involvement of basin-derived ore fluids, supported by the identification of Mg, Pb, and Zn in fluid inclusions. Vein systems at Copper Pass and Blanchet Island, East Arm of Great Slave Lake, may represent the deep expression of a much larger FMA hydrothermal system, where the evidence is eroded.

2.1 Introduction

Polymetallic “five-metals association” (FMA) hydrothermal veins are typically characterized by successions of open-space filling intergrowths of Ni-, Co-, and Fe-arsenides and sulfarsenides

with variable Ag and lesser amounts of Bi, Sb, As and rarely U (in a few global examples) enclosed by quartz and carbonate gangue minerals (*cf.* Bastin, 1939; Boyle, 1968; Boyle and Dass, 1971; Petruk, 1971; Badham, 1975; Andrews et al., 1986; Kissin, 1992; Marshall et al., 1993; Ondrus et al., 2003; Markl et al., 2016; Gandhi et al., 2018 and others therein). While this ore deposit style was historically a major source of Ag and U in the first half of the 20th century, they have not received attention in research and exploration endeavours in recent decades. However, with an increase in global demand for Co, and to a lesser extent, other strategic metals within this unique metal association (e.g. Bi), as well as new mining and exploration activity imminent regionally in the NWT (i.e., the polymetallic NICO Cu-Co-Au-Bi deposit; proven and probable reserves of 33 Mt containing 1.1 M oz Au, 82 M lbs Co, 102 M lbs Bi, 27 M lbs Cu), renewed interest for the FMA deposit style has arisen in the mineral resources community.

Five-metals association deposits occur worldwide in a diversity of igneous, metamorphic and sedimentary host rock settings of varied ages ranging from Archean to Oligocene (Kissin, 1992). Notable deposits under FMA classification or having many characteristics similar to such deposits are found in Canada (Cobalt-Gowganda: Boyle, 1968; Andrews et al., 1985; Marshall et al., 1993; Great Bear Lake: Robinson and Ohmoto, 1973; Changkakoti et al., 1986; Changkakoti and Morton, 1986; Thunder Bay district: Franklin et al., 1986), Czech Republic (Jachymov: Ondrus et al., 2003), Switzerland (Jaffe, 1986; Penninic Alps: Kreissl et al., 2018), Germany (Odenwald: Burisch et al., 2017; Schneeberg: Lipp and Flach 2003), Mexico (Batopilas: Wilkerson et al., 1988), Morocco (Bou Azzer: Ahmed et al., 2009), and Norway (Kongsberg: Lietz, 1939; Neumann, 1944; Staude et al., 2007). Metals, ore mineralogy, and textures are similar between deposits styles. However, studies of the alteration styles, fluid composition and physicochemical characteristics, and stable isotope systematics demonstrate significant variability between

deposits, with several alternative ore genesis models (*cf.* Kissin, 1992 and authors therein) proposed in the earlier literature: (i) by direct magmatic-hydrothermal fluid evolution from granitic intrusions (Badham, 1975); (ii) by direct magmatic-hydrothermal fluid evolution from mafic intrusions (locally and in-situ, or sourced at depth; Tanton, 1931; Jambor, 1971;) (iii) by mixing of hydrothermal solutions of mafic and granitic affinities (Badham, 1976) (iv) by hydrothermal/metamorphic processes concentrating components from organic-rich black shales (Kerrich et al., 1986); pre-existing massive sulfides (Goodz et al., 1986), or metal-rich volcanoclastic rocks (Boyle and Dass, 1971) (v) by syngenetic processes (Schneider, 1972) (vi) by introduction along deep fractures of a juvenile five-element solution in a basalt-generating environment near the crust-mantle boundary (Halls and Stumpll, 1972) (vii) by circulation of connate brines in an environment of continental rifting (Kissin, 1988).

None of these models are predictive in an exploration context, and there is ongoing ambiguity concerning the key factors (i.e., metal and fluid source, and precipitation mechanism) responsible for the development of deposits. Recent work (e.g., Markl et al., 2016; Burisch et al., 2017) has greatly modernized the model for such deposits within Europe, in particular through detailed geochemical modelling involving prediction of the conditions required for vein formation (and associated mineral precipitation). Studies implicate multiple fluid end-members (including hydrocarbons) as prerequisites for deposit formation and lend support to the earlier hypothesis (Robinson and Ohmoto, 1973; Morton and Changkakoti, 1987; Kissin, 1988) that sedimentary basinal fluids infiltrating basement rocks is a prerequisite for FMA vein systems.

This study characterizes polymetallic FMA systems in the southern Slave Craton (Archean) and East Arm basin (Paleoproterozoic) of Great Slave Lake, Northwest Territories, Canada. The study focuses on two occurrences, Blanchet Island, which occurs within the Hearne Channel, and

Copper Pass, which occurs on the mainland, north of Sachowia Point of the East Arm of Great Slave Lake. These localities were minor producers of Co, Ni and Ag (Badham, 1978) but unlike the much larger and higher grade FMA equivalents in the Great Bear Lake region (e.g., Eldorado and Echo Bay mines, and Port Radium), strongly mineralized surface outcrop are accessible at Blanchet Island and Copper Pass. Badham (1978) proposed that the leaching of ore metals from mafic minerals was essential for the genesis of required Co-Ni-As ore fluid. Using a range of complementary analytical techniques, we examine the paragenesis and radiogenic/stable isotope composition of ore and gangue assemblages, and the P-T evolution and chemical composition of fluid and hydrocarbon inclusions at these two localities.

New constraints on ore-forming processes, and the nature of metal and fluid sources in FMA vein systems. The results of this study implicate former intracratonic sedimentary basins overlying basement rocks as the source of metal-bearing hydrocarbons and metal-poor, but oxygenated brines necessary for ore formation. The study also provides unambiguous field evidence for some aspects of the ore-forming processes recently described by Markl et al. (2016), Burisch et al. (2017), and Kreissl et al. (2018) for European examples of FMA systems.

2.2 Geological Setting

The five-metal association (FMA) vein systems at Blanchet Island and Copper Pass (the study areas) occur in the East Arm area of Great Slave Lake, Northwest Territories. Relationships between these occurrences and host-rocks are depicted on Figure 1. The Blanchet Island deposit occurs on Blanchet Island in the Hearne Channel of Great Slave Lake. The Copper Pass deposit occurs on the Mainland, north of Sachowia Point on Great Slave Lake.

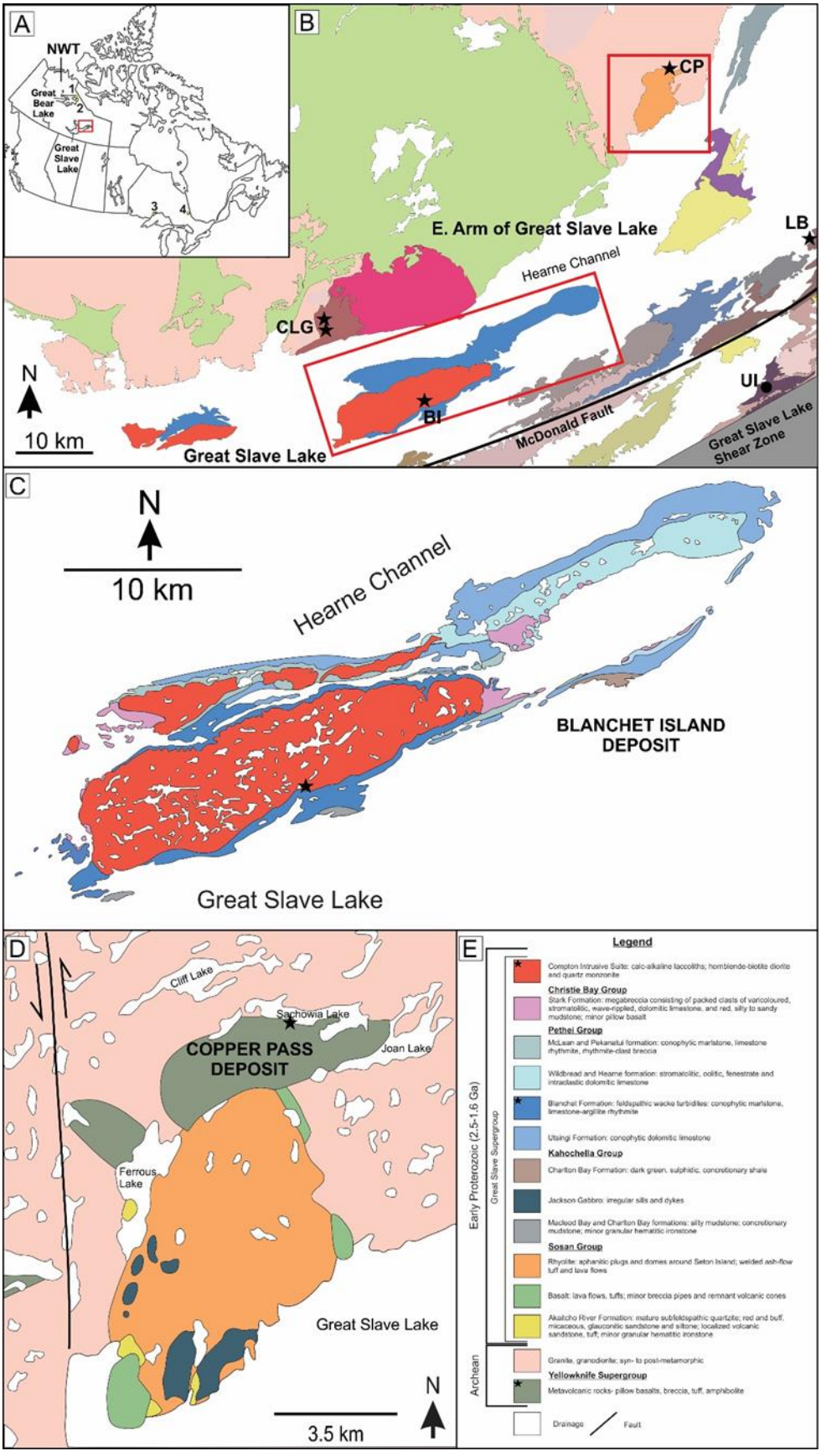
A
NWT
Great Bear Lake
Great Slave Lake
1
2
3
4
B
CP
E. Arm of Great Slave Lake
LB
Hearne Channel
CLG
BI
UI
McDonald Fault
Great Slave Lake Shear Zone
Great Slave Lake
N
10 km
C
N
10 km
Hearne Channel
BLANCHET ISLAND DEPOSIT
Great Slave Lake
D
Cliff Lake
Sachowia Lake
COPPER PASS DEPOSIT
Joan Lake
Ferrous Lake
Great Slave Lake
N
3.5 km
E
Legend
Compton Intrusive Suite: calc-alkaline laccoliths; hornblende-biotite diorite and quartz monzonite
Christie Bay Group
Stark Formation: megabreccia consisting of packed clasts of varicoloured, stromatolitic, wave-rippled, dolomitic limestone, and red, silty to sandy mudstone; minor pillow basalt
Pethei Group
McLean and Pekanatui formation: conophyric marlstone, limestone rhythmite, rhythmite-clast breccia
Wildbread and Hearne formation: stromatolitic, oolitic, fenestrate and intraclastic dolomitic limestone
Blanchet Formation: feldspathic wacke turbidites; conophytic marlstone, limestone-argillite rhythmite
Utsingi Formation: conophytic dolomitic limestone
Kahochella Group
Charlton Bay Formation: dark green, sulphidic, concretionary shale
Jackson Gabbro: irregular sills and dykes
Macleod Bay and Charlton Bay formations: silty mudstone; concretionary mudstone; minor granular hematitic ironstone
Sosan Group
Rhyolite: aphanitic plugs and domes around Seton Island; welded ash-flow tuff and lava flows
Basalt: lava flows, tuffs; minor breccia pipes and remnant volcanic cones
Akaitcho River Formation: mature subfeldspathic quartzite; red and buff, micaceous, glauconitic sandstone and siltone; localized volcanic sandstone, tuff; minor granular hematitic ironstone
Granite, granodiorite; syn- to post-metamorphic
Yellowknife Supergroup
Metavolcanic rocks- pillow basalts, breccia, tuff, amphibolite
Drainage
Fault
Early Proterozoic (2.5–1.6 Ga)
Great Slave Supergroup
Archean

Figure 1 (previous page). Geological maps showing the study. A) Map of Canada highlighting polymetallic "five metals ± U" vein deposits at Great Bear Lake, NWT (1,2), Cobalt-Gowganda, ON (3) and Lake Superior, ON (4) with the East Arm of Great Slave Lake highlighted with a box. **B**) Simplified geological map of the East Arm region of Great Slave Lake, NWT, highlighting vein occurrences at Blanchet Island (BI) and Copper Pass (CP) with other showings at the Labelle Peninsula (LB) and Caribou Lake (CLG), as well as the location of hydrothermal veins (for comparison) in the Union Island Group shales (UI) modified from Hoffman (1988). **C**) Geological map of Blanchet Island showing the vein location between the Blanchet Formation and Compton Intrusive Suite (black star). **D**) Geological map of Copper Pass demonstrating vein mineralization occurring within the Yellowknife Supergroup.

2.2.1 Slave Province

The Slave Province is one of 35 Archean cratons preserved worldwide. The Yellowknife Supergroup refers to a package of supracrustal rocks that includes volcanic and sedimenary units that were deposited in the Neoarchean, between ca. 2.74 and 2.62 Ga. The Yellowknife Supergroup overlays and older Meso to Paleoarchean core, and both were intruded by extensive plutons in the late Archean (ca. 2.63 to 2.58 Ga) (Bleeker and Hall 2007: Henderson 1970). Between 2595 and 2585 Ma (Bleeker and Hall 2007: Davis and Bleeker 1999) a craton-wide event known as the "granite bloom" transferred a significant fraction of heat-producing elements and lower crustal fluids into the upper crust, promoting slow cooling and stiffening of the crust. This allowed for the craton to be preserved long-term (Bleeker and Hall 2007). Located in the Yellowknife Supergroup are metasediments of amphibolite and greenschist facies, along with metavolcanics such as pillow basalts, breccia, tuff and amphibolite. The western portion of the Yellowknife Supergroup is dominated by mafic volcanic rocks, where the eastern limits are dominated by felsic rocks. These Late Archean granitic intrusions coincided with regional and contact metamorphic events. Stratigraphic subdivision of the supracrustal rocks of the supergroup are distinguished with three divisions: (a) the base, consisting of mainly mafic flows and intrusions (b) composed of conglomerates, quartzites, and intermediate to felsic volcanics (c) greywacke and slate (Healmstaedt and Padgham, 1986).

The East Arm refers to a geographic region of Great Slave Lake, NT. The north shore of the East Arm is underlain by Archean rocks of the Slave craton, in addition to the Blachford Intrusive complex (ca. 2.17 Ga; Figure 1). The south shore of the East Arm is underlain by mylonitic rocks of the Great Slave Lake shear zone (ca. 2.6 to 1.92 Ga) (Hamner et al 1988). The East Arm basin refers to stratigraphic package of supracrustal and lesser intrusive rocks that were deposited

between ca. 2.04 and 1.85 Ga (Bowring et al., 1984; Kjarsgaard et al. 2013; Sheen et al., 2019). These are preserved on a series of islands in the East Arm of Great Slave Lake, with lesser occurrences on the southern and northern mainland (Figure 1).

The East Arm basin is composed of four temporally and geologically distinct units (Hoffman, 1968, 1988), from base to top: the Union Island Group (ca. 2.04 Ga; Sheen et al., 2019); Wilson Island Group (ca. 1.93 Ga; Bowring et al., 1984); Great Slave Supergroup (<1.93 to 1.85 Ga; Kjarsgaard et al., 2013; Bowring et al., 1984), and; Et-Then Group (<1.85 Ga). Two assocaited ntrusive suites are known in the region, the Butte Island suite (ca. 1.89 Ga; Bowring et al., 1984) and the Compton Intrusive suite (ca. 1.87 Ga). Sedimentological studies of the EastArm basin led Hoffman (1968, 1969, 1970) to believe the basin was a preserved fold-belt, however was later interpreted to have developed as a failed rift (Athapuscow aulacogen) (Hoffman, 1973; Bowring et al., 1984; Sheen et al., 2018). Hoffman (1987) revisited the aulacogen model, rejecting it in favour of a model involving a syn-collisional transtensional basin during Slave-Rae provincial collision (Sheen et al., 2018).

The Great Slave Supergroup (1.93 Ga and 1.85 Ga; Bowring et al., 1984 and Kjarsgaard et al., 2013) is relavent to this study as it is host to the Blanchet Island deposit (Figure 1). It is composed of four lithostratigraphic formations (Hoffman, 1968, 1988), from base to top: the Sosan; Kahochella; Pethei, and; Christie Bay groups. The units of the Great Slave Supergroup consist of alternating fluviatile and marine sedimentary rocks (feldspathic sandstones, mudstones, conglomerates, limestones and shales) with volcanic sequences of the Sosan (basalt, rhyolite),

Kahochella (basalt, rhyolite, grabbro) and Christie Bay groups. The rock units of interest for this study are the Pethei Group and the Compton Intrusive Suite.

2.2.2 Pethei Group

The Pethei Group is composed of ten lithostratigraphic formations, representing a sequence consists of basinal and platformal lithologies, consisting of feldspathic wacke turbidites and greywackes and dolomitic limestones respectively. The FMA veins at the Blanchet Island deposit are hosted in the Blanchet Formation which consists of feldspathic wacke turbidites, marlstone, and limestone-argillite rhythmites that were deposited in deeper-water basins (Hoffman, 1968).

The Compton Intrusive Suite refers to a series of sills that extend the length of the East Arm basin (Bowring et al., 1984). These intrusions range from hornblende-biotite diorite to quartz monzonites and intruded at ca. 1.87 Ga (Bowring et al., 1984). The Compton Intrusive Suite are interpreted equivalents to the Great Bear Magmatic zone (1.85-1.87 Ga) of the Wopmay Orogen, preserved to the northwest (van Breeman et al., 2013). The Compton Intrusive Suite are geochemically classified as volcanic arc granites (Kjarsgaard et al., 2013).

2.3.3 Other polymetallic FMA occurrences in the East Arm

Several polymetallic type occurrences are also found within the East Arm Basin (Fig. 1B; *cf.* Badham, 1978). In the southern portion of the Slave Craton, located northwest of Blanchet Island, FMA veins occur (cross-cut) the Caribou Lake Gabbro, on the western extent of the Blatchford Intrusive Complex (2.184±2 Ma; Mumford, 2013). The veins consist of an early, barren (quartz±ankerite) stage, a main Ni-Co arsenide stage (nickeline) transitioning to sulfarsenides (cloanthite-rammelsburgite and safflorite-skutterudite solid solution ± ankerite ± quartz), a minor

base metal sulphide stage (pyrite ± galena ± chalcopyrite ± sphalerite ± ankerite ± quartz), and a late, barren (quartz ± ankerite) stage. East of Blanchet Island, FMA veins are found at the Labelle Peninsula hosted within Compton intrusive rocks. Veins at Labelle Peninsula consist of Fe-dolomite+ arsenides (nickeline) cored by quartz, calcite, tetrahedrite, Ag sulfides and sulfosalts, native Ag, uraninite and rare molybdenite (Badham, 1978). Located further northeast of Labelle Peninsula are two other suspected FMA-style showings called HAR-Disc and Fair-Rag-Triona; these are identified as Cu-Ag-Co and Co-Ni-Cu-As-Pb-Au-Ag-U veins, respectively. HAR-Disc is an outcrop of disseminated to fracture-filling "stratabound" sulfide mineralization. Finally, northeast of Copper Pass, along the Taltheilei Narrows, the BBX showing is an outcrop of possible FMA-related, sulfide-bearing polymetallic volcanic breccia enriched in Co-Ni-Cu-Fe-As-Ag-Au-Pb-Bi-U (J. Kerswill, communication, 2015).

2.3 Exploration History

2.3.1 Blanchet Island

At Blanchet Island, polymetallic vein-hosted Ni mineralization is hosted by carbonate sedimentary rocks of the Pethei Group (Great Slave Supergroup) and a monzonite sill of the Compton intrusive suite (Fig. 1C). In 1968 Alfred V. Giauque discovered cobalt-nickel mineral occurrences at Blanchet Island. These claims were optioned to Jason Explorers Limited in 1969, who had staked additional claims near the original Blanchet showing. Blasting of open-cuts and adits installation began in 1969 (Mason, 1969), when 300 tons of Co-Ni-arsenide ore was bagged and shipped to France for processing. Ore was sold to Ugine-Kuhlmann SA of Paris, France, where the smelter reported assays of 11% Co and 12% Ni. Underground mining ceased in 1970, when the final shipment of 243 tons was shipped to France, yielding 5% Co and 15% Ni. Thirty tons of

ore was left on the shores and was discovered by D. Smith in 1980. In 1984 Highwood Resources Limited staked “HRL” claims on Blanchet Island, inclusive of all known mineralized zones (Silke, 2009).

2.3.2 Copper Pass

The Yellowknife Supergroup and younger granitic rocks host cross-cutting hydrothermal veins and Ni-Co mineralization at Copper Pass, in the southwestern Slave craton (Fig. 1D). In 1940, Cominco staked initial claims at Copper Pass before it was re-staked by Chuck McAvoy in 1950. Venture Resourced Limited obtained the claims in 1957 and conducted surface mining from a primary trench. Venture Resources Limited blasted a deep trench in the Main Zone showing, consisting of ~260 cubic yards of rock in 1957. Claims were re-staked twice before being incorporated into the “Gogo” group claims in 1969 by Jim McAvoy. Claims under the “Gogo” group were acquired by the Copper Pass Mines Limited Company, who shipped 24 barrels of ore to Edmonton for grade estimation. These returned assays between 25 and 43 wt. % Ni, with trace Co, Bi, and Ag. By October 1969, 200 tons of ore had been mined from the open trench (Kelly, 1969; Silke, 2009).

2.4 Sampling and analytical methodology

2.4.1 Sample collection and processing

During the summer of 2015 samples were collected from five locations at Blanchet Island and Copper Pass. The samples consisted of fresh and altered host rocks and mineralized veins and breccias. Additionally, supplementary samples of mineralized veins and breccias from Copper Pass and the Labelle Penninsula were obtained from the Geological Survey of Canada (J. Kerswil,

communication, 2015). From the sample suite, 50 samples were cut and prepared into polished thin and fluid inclusion sections, highlighting representative ore and associated gangue mineralogy, and some host rock compositions (dolostone, metasediments and aplite). These sections formed the base collection for petrographic and mineral analysis, fluid inclusion microthermometry and petrography, Raman and LA-ICPMS analysis. A subset of these samples was selected, on the basis of petrographic and mineralogical characteristics for major and trace element analysis (assaying), and stable (O, C) and radiogenic (Sr) isotope analysis by bulk and in-situ methods (SIMS).

For the purposes of comparison with FMA data from the East Arm basin in order to assist with interpretation of sedimentary and basement fluid and metal sources, samples from two other geological environments were obtained. These were quartz-carbonate veins containing syn-mineralization brines from the Rabbit Lake U deposit (Athabasca intracratonic basin, northern Saskatchewan), syn-uraninite bitumens also from the Athabasca basin (Alexandre and Kyser, 2006), and quartz-carbonate-sulfide-pyrobitumen veins crosscutting the 2.043 Ga Union Island group shales, East Arm basin (S. Gandhi, communication, 2015; Sheen, 2017; Sheen et al., 2019).

2.4.2 Optical microscopy and SEM-EDS analysis of ore and gangue mineralization

All samples were characterized petrographically using conventional optical microscopy (transmitted and reflected light) and scanning electron microscopy (SEM) at Saint Mary's University to determine paragenetic (primary growth, overprinting) history of vein and gangue minerals. Optical microscopy was carried out using Olympus BX51 and BX41, and Nikon Eclipse 50i polarizing microscopes equipped with colour cameras. The SEM used for imaging as well as semiquantitative analysis of ore and gangue minerals, and bitumens, was a TESCAN MIRA 3

LMU Variable Pressure Schottky Field Emission SEM equipped with a back-scattered electron detector and a solid-state, 80 mm^2 X-max Oxford Instruments EDS detector. Analyses were obtained using an accelerating voltage between 20 and 30 kV, and a beam current of 40 uA, with a working distance of 20 mm.

2.4.3 Bulk rock geochemistry

Bulk rock analysis of host rock and vein mineralization styles was completed at Activation Laboratories, Ltd. (Ancaster, Ontario) by a combination of (i) closed-vessel, four acid digestion followed by ICP-MS (Method: TD-MS); (ii) sodium peroxide "total" fusion (Method: FUS-Na_2O_2) followed by ICP-OES or ICP-MS for over range determination of Ni, Co and As; (iii) fire assay followed by ICP-MS for Au determination (Method: FA-ICP); (iv) aqua regia digestion followed by ICP-OES for Ag determination (Method: AR-ICP); and (v) infrared following combustion for S determination (Method: CS-IR).

2.4.4 Fluid inclusion petrography and microthermometry

Optical microscopy of double-polished thick sections was done to characterize and classify fluid inclusion assemblages (FIA) in terms of their origin (i.e., relative to host phases, as primary, pseudosecondary, or secondary), contained phases at room temperature, and timing relationships relative to one another. Fluid inclusion microthermometry was performed using a Linkham FTIR600 heating-freezing stage attached to an Olympus BX51 microscope at Saint Mary's University. Stage calibration was done using synthetic fluid inclusion standards of pure CO_2 (melting at -56.6^oC) and pure H_2O (melting at 0^oC and homogenization at the critical point at 374.1 ^oC). Uncertainties for the microthermometric measurements are ±0.2°C for measurements around

0ºC, and ± 0.5 °C for measurements over 300 °C at a heating rate of 1°C/min. For two-phase L_{aq}-V inclusions, the programs BULK and ISOC (Bakker, 2003; empirical and theoretical equations of state from Oakes et al. 1990 and Zhang and Frantz, 1987, respectively) were used to calculate inclusion bulk salinity, molar volumes (cc/mol) and corresponding isochores utilizing the temperature of final ice melting (T_m^{ice}) and temperature of homogenization (by $L_{aq}+V \rightarrow L_{aq}$; T_h). Due to the low final ice melting temperatures commonly encountered ($T_m^{ice} < -21.3$ºC), the inclusions should be modelled in the system H_2O-NaCl-$CaCl_2$. However, in the absence of hydrohalite melting (not observed), the system H_2O-$CaCl_2$ system was used to model fluid inclusion compositions and all salinity determinations are reported in units of wt% $CaCl_2$ equivalent. Salinity values were averaged from samples (justified by consistency in microthermometric measurements; see below) and used for internal calibration of LA-ICP-MS data reduction for aqueous inclusions. For carbonic inclusions, BULK and ISOC (Bakker, 2003) were also used to calculate molar volumes (cc/mol) and corresponding isochores, but the equations of state of Bakker (1999) and Bowers and Helgeson (1983) were used to model end-member carbonic fluids in the CO_2-CH_4 system, with the X_{CH4} and X_{CO2} determined by confocal Raman spectroscopy (see below).

2.4.5 UV fluorescence microscopy

UV fluorescence microscopy was used for qualitative detection and imaging of hydrocarbons in fluid inclusions by combining a mercury burner (UV excitation source) and an Olympus filter cube U-MWUS3 (excitation: BP330–385 nm; emission: BA420 nm; dichroic beam splitter DM400, barrier filter BA420), and examining the resulting fluorescence using an UV-2A filter

block (Olympus) and RetigaEXi (QImaging) CCD camera mounted on an Olympus BX51 microscope.

2.4.6 Confocal Raman spectroscopy

Qualitative Raman spectroscopy analysis was performed on polished thin sections containing gangue mineralization hosting 2-phase LV fluid inclusions, as well as suspected hydrocarbon inclusions. Analyses were performed to identify the presence of certain dissolved ionic species volatile phases (CO_2, N_2, hydrocarbons, etc.) in individual inclusions trapped at different ore stages of FMA mineralization. Analyses were conducted at Saint Mary's University on a Jobin-Yvon Horiba LabRam HR confocal Raman microscope with an 800 mm spectrograph and Synapse 1024 x 256-pixel CCD detector. An 1800 groves/mm grating (spectral resolution of approximately ±0.5 cm^{-1}) and 100 μm confocal hole size were used during spectrum collection, with a 532 nm (green) Nd-YAG laser (~2.15 mW at sample surface) was used for excitation, directed through a 100x objective. Pure silicon was used as a frequency calibration standard. Spectrum collection over the range 100-4500 cm^{-1} was done at an acquisition of 30s per accumulation with 3 accumulations obtained per inclusion analysis. Semi-quantitative determination of the relative abundance of inclusion-hosted gas species (in mol%) was performed using the methodology and empirical quantification parameters described by Wopenka and Pasteris (1986, 1987), Dubessy et al. (1989), Burke (2001), and Beeskow et al. (2005). The instrument efficiency factors (z) for CO_2 and CH_4 were determined by comparing CO_2 and CH_4 contents determined by Raman spectroscopy to the results obtained via microthermometric analysis for quartz-hosted CO_2-CH_4 standard inclusions from the South Wales Coal Field (Beeskow et al., 2005). Instrument efficiencies for other gas species were assumed to be 1, in the absence of standards, and results in

a slight overestimation of the mole fraction (e.g., N_2). Uncertainties in the mole fractions of dissolved species in the carbonic phase of the inclusions are within 20% relative.

2.4.7 Laser ablation inductively-coupled plasma mass spectrometry (LA-ICPMS)

The major and trace element composition of quartz-hosted fluid and bitumen inclusions, and vein quartz and carbonates were determined by LA-ICPMS at the University of Toronto Magmatic and Ore Forming Processes Research Laboratory. The instrument used was a NWR 193UC ArF excimer laser ablation system attached to an Agilent 7900 quadrupole mass spectrometer. The typical analytical approach for fluid inclusions using a similar prototype system is described in Heinrich et al. (2003). The instrument was tuned to maximum sensitivity while maintaining robust plasma conditions (U≈Th on reference standard glass SRM610 from NIST) and low oxide and doubly charge ion production rates (ThO/Th < 0.3%; mass-21/mass-42 < 0.3%) at He and Ar carrier and make-up gas flow rates of 1.0 and ~0.85 l/min, respectively. The dwell time for all measured isotopes was 10 ms, except for 50 ms for ^{197}Au and ^{238}U. The NIST SRM610 silicate glass standard was used for calibration of analyte sensitivities during quantification. The analyses of no more than 16 unknowns were bracketed by 2 SRM610 standard analyses at the beginning and the end of each analysis block. For inclusions, a laser spot size was used that was ~10 μm larger than the diameter of each inclusion, typically ranging between 20 and 30 μm. For quartz and carbonate, a spot size of 25 μm was used. Laser pulse frequency was 10 Hz and fluence on the quartz surface was Aqueous fluid inclusion compositions were quantified using the software SILLS (Guillong et al., 2008 and approach described therein) applying a host correction for trace element contributions from quartz and utilizing microthermometric bulk salinities (in wt. % NaCl

equiv. converted from wt% $CaCl_2$ equiv.). Data for carbonates and quartz were quantified using Ca (wt%) and Si (wt%) for ideal ferroan dolomite and quartz, respectively.

Inclusions containing a solid or viscous liquid hydrocarbon phase, described below, were also analyzed semi-quantitatively by LA-ICPMS. Like aqueous fluid inclusions, background-corrected inclusion+quartz host transient signals were also quantified with SILLS but using knowledge of the bulk inclusion compositions estimated from SEM-EDS analysis of opened inclusions for internal standardization.

2.4.8 Bulk C-O and Sr isotope compositions and trace element analyses of vein carbonates

Approximately 30–60 μg of carbonate powder was excavated from each sample using a tungsten carbide microdrill bur (Komet Dental; 0.4 mm diameter) mounted on a dremel tool and weighed into glass vials (Saint Mary's University). Carbon and oxygen isotope ratios of carbonates were measured on a Nu Perspective dual-inlet isotope ratio mass spectrometer connected to a NuCarb carbonate preparation system at McGill University Stable Isotope Laboratory (Montréal, Canada). The powdered carbonates were then reacted individually with H_3PO_4 after heating to 90ºC for 1 hour (McGill University). The released CO_2 was collected cryogenically, and isotope ratios were measured against an in-house reference gas in dual inlet mode. Samples were calibrated to VPDB using house standards. For reporting data in this study, $\delta^{18}O$ values reported from the McGill facility relative to VPDB were converted to VSMOW. Uncertainties are ±0.05‰ (1σ) for both $\delta^{13}C$ and $\delta^{18}O$.

For Sr isotope analyses, approximately 15 mg of sample powder was collected for each sample using a tungsten carbide dental drill. Strontium isotope ratios were measured on a Thermo Scientific Triton™ thermal ionization mass spectrometer (TIMS) at the Université de Québec à Montréal/Geotop. Powders were first leached three times in 0.2M ammonium acetate, and then rinsed three times in MQH_2O. The calcite fraction of the samples was then dissolved in 0.5M acetic acid, which was then separated from the insoluble fraction by centrifugation, dried down, and taken up in 3N HNO_3. Sr was separated from the matrix following standard Sr chromatography procedures using EICHROM Sr Spec™ resin. Internal mass bias was corrected based on the ratio $^{86}Sr/^{88}Sr = 0.1194$. Analyses of NBS SRM 987 yielded a long-term average of 0.710245, compared to the accepted value of 0.710250. No correction was made to sample data.

2.4.9 Secondary ion mass spectrometry determination of $\delta^{18}O$ in vein quartz

Oxygen isotope ratios ($^{18}O/^{16}O$) of Copper Pass quartz in multiple crystals containing various growth zones classified using CL were collected using a CAMECA 7f SIMS at the University of Manitoba. Areas (spots) for analysis were chosen using cathodoluminescence images for texturally-early quartz along vein margins (see below). A cesium (Cs^+) primary beam with a 6.5 nA current for oxygen was accelerated (+10 kV) onto the sample surface with a sputtering diameter of ~25 µm. The instrument operated with a 200 V offset, –9 kV secondary accelerating voltage, and a mass resolving power of 350. Fayek et al. (2002) provides a detailed description of operating conditions and strategy for correction of instrumental mass fractionation and matrix effects. Grains of University of Wisconsin rose quartz (UWQ-1) with a $\delta^{18}O$ value of 12.3 ± 0.1‰ (Kelly et al., 2007) were used as the quartz standard for oxygen isotope analysis. Precision for individual analysis was 1.2 for $\delta^{18}O$ values. Therefore, the 1σ error for oxygen isotope analysis is 1.2. SIMS

results from the standards were compared to accepted isotopic compositions to calculate correction factors that were applied to the unknowns measured during the same analytical session (e.g., Holliger and Cathelineau, 1988) and results are reported as $\delta^{18}O_{VSMOW}$.

2.4.10 Cathodoluminescence imaging of quartz

Qualitative CL imaging of growth zoning in quartz was completed at Saint Mary's University for textural information for quartz. This was obtained using a Lumic HC4-LM hot-cathode CL microscope coupled to a Olympus BXFM focusing mount with images captured by a Kappa DX40C Peltier cooled camera operated using the DX40C-285FW software package. The hot CL was operated at an acceleration voltage between 12.4 and13.1 kV, a beam current of 0.35 mA, a filament current of 2.3 A, a deflection of 10 V and a focus of 5.5 V.

2.4.9 K-U-Th scintillometry

Radioactivity mapping (K-U-Th; concentrations equivalency derived from activity) mapping was carried out *in situ* in the field on mineralized veins of Copper Pass. This was completed using a handheld RS-125 Superspec – 6.3 cu ins sodium-iodide detector scintillometer. Spot analysis was carried out on each limb of the bifurcating vein in a 25cm by 25 cm grid on the trench surface. Scintillometer provided concentrations of K (%), U (ppm) and Th (ppm). Results demonstrated a strong relationship between uranium concentrations and vein-aplite margins.

2.5 Results

2.5.1 Field observations and macroscopic textures

Mineralized zones at Blanchet Island and Copper Pass can be easily identified at surface within former trenches and workings by the presence of weathering products annabergite [$Ni_3(AsO_4)_2$-$8H_2O$] (green-white colour) and erythrite [$Co_3(AsO_4)_2$-$8H_2O$] (pink) formed from Ni and Co arsenides/sulfarsenides, respectively. At Blanchet Island (Fig. 2A-C), vein-hosted styles of ”five metals” association mineralization occur within carbonate (dolostone) sedimentary rocks of the Paleoproterozoic Great Slave Supergroup, adjacent to (and within) monzonitic sills (Compton Intrusive Suite) and within skarns in host carbonates. Mineralization is confined to a 3-metre zone along the brecciated contact between dolostone and monzonite with multiple veins each having a maximum exposed length of ~0.6 m, and a maximum thickness of 4 cm. Cobalt-enriched mineralized veins strike approximately 184^o, and dip 20^o, and are oriented perpendicular to bedding in the host carbonate (striking 305^o) (Figure 2B). In addition to veins, irregular mineralized masses (Fig. 2C) are also observed. In addition to veins, irregular mineralized masses (Fig. 2C) are also observed.

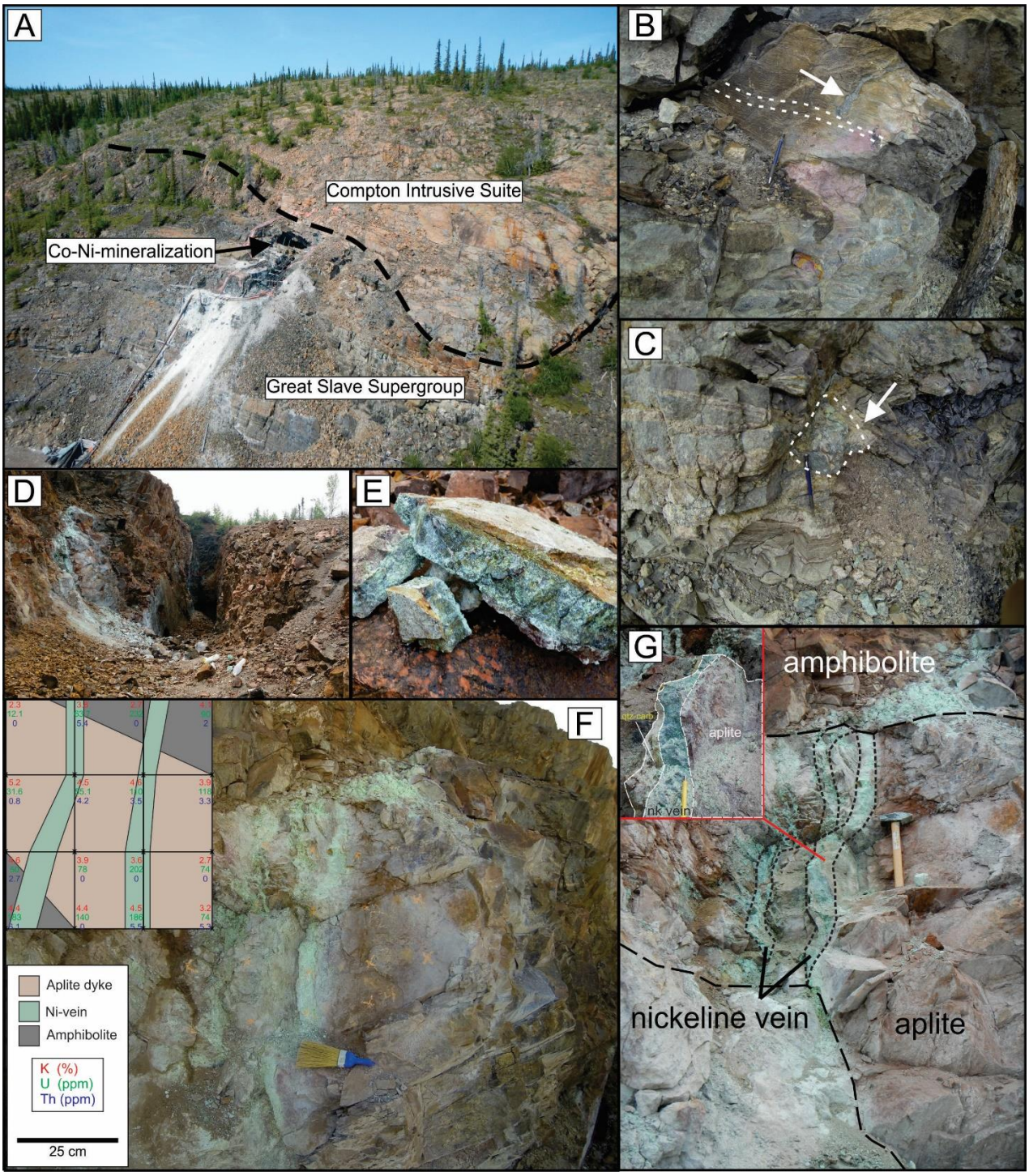
A
Compton Intrusive Suite
Co-Ni-mineralization
Great Slave Supergroup
B
C
D
E
F
Aplite dyke
Ni-vein
Amphibolite
K (%)
U (ppm)
Th (ppm)
25 cm
G
amphibolite
aplite
nickeline vein
aplite

Figure 2 (previous page). **Outcrop-scale images of East Arm deposits demonstrating spatial relations between host rocks and polymetallic veins. A**) Aerial field photo of Blanchet Island, demonstrating the spatial relationship of mineralization within host Great Slave Supergroup dolostone and Compton Intrusive Suite monzonite intruding the dolostone. Old mine workings (adits) visible at the top and bottom of slope where Co-Ni mineralization was extracted. **B)** Cobalt-rich polymetallic vein with secondary erythrite (pink) staining indicated by arrow, crosscutting primary bedding (dashed lines) of host dolostone of the Great Slave Supergroup at Blanchet Island. **C)** Massive aggregate of open-space filling Co(-Ni) mineralization highlighted by arrow at Blanchet Island. **D)** Field photo of an open (mined out) trench at the Copper Pass polymetallic vein showing. Secondary green staining (annabergite) highlights the mineralized zone rich in nickeline. **E**) Massive nickeline vein hand samples showing annabergite staining. **F)** Graphical representation (inset) of field-based radioactivity measurements (with estimated K, U, and Th contents at grid nodes) through the use of a scintillometer spot analysis of the mineralized nickeline vein and host rocks at Copper Pass. **G)** Anastomosing polymetallic veins cross-cutting associated Archean aplite dyke cross-cutting amphibolite of the Yellowknife Supergroup, occurring in a localized shear zone at the Copper Pass main showing. Inset demonstrates vein morphology, highlighting host aplite, massive nickeline vein and a synkinematic (late) carbonate vein. Mineral abbreviations: nk=nickeline; qtz=quartz; carb-carbonate.

At Copper Pass, two zones of mineralization occur (Main and West zones) and comprise massive nickeline-rich veins that cross-cut metasedimentary and metavolcanic (Yellowknife Supergroup) rocks and Archean aplite dyke (Figure 2D-G). At the Main zone, maximum vein thickness reaches 8 cm, with veins striking approximately 170^{o} and dipping sub-vertically (89^{o}) and lies parallel to a locally developed shear zone. Veins show anastomosing morphology (Fig. 2G). Synkinematic quartz-carbonate veining is visible along the contact between the massive nickeline-rich veins and aplite dyke (Fig. 2G inset). Near nickeline-rich veins, botryoidal masses of cobaltite-safflorite mineralization occur within the aplite dyke. At the West zone, west of the main zone, nickeline-rich veining occurs in outcrop over a ~20-30cm interval.

Polymetallic vein mineralization at Blanchet Island and Copper Pass is dominated by Ni-Co-arsenides and sulfarsenides with a variety of accessory Bi-Mo-Pb-U minerals and quartz-carbonate gangue. A range of ore textures occur at both locations (Fig. 3), consisting predominantly of arsenide-sulfarsenide mineral growth in open spaces (e.g., between brecciated fragments of wall rock) and structures (massive fracture infillings and partial replacements of wall rocks). Textures within veins and breccias range from massive to polycrystalline (subhedral to euhedral) to botryoidal, zoned arsenide-sulfarsenide aggregates with interstitial carbonate (Fig. 3A-G). Rims of sulfarsenide on arsenide, and concentric zoning within single crystals of arsenides are clearly visible in hand-sample (Fig. 3C, D). Textural evidence for multiple veining events in reactivated single structures (synkinematic veining and wall-rock delamination; Fig. 3E) and repeated brecciation (e.g., of earlier arsenide minerals; Fig. 3F) events is unambiguous.

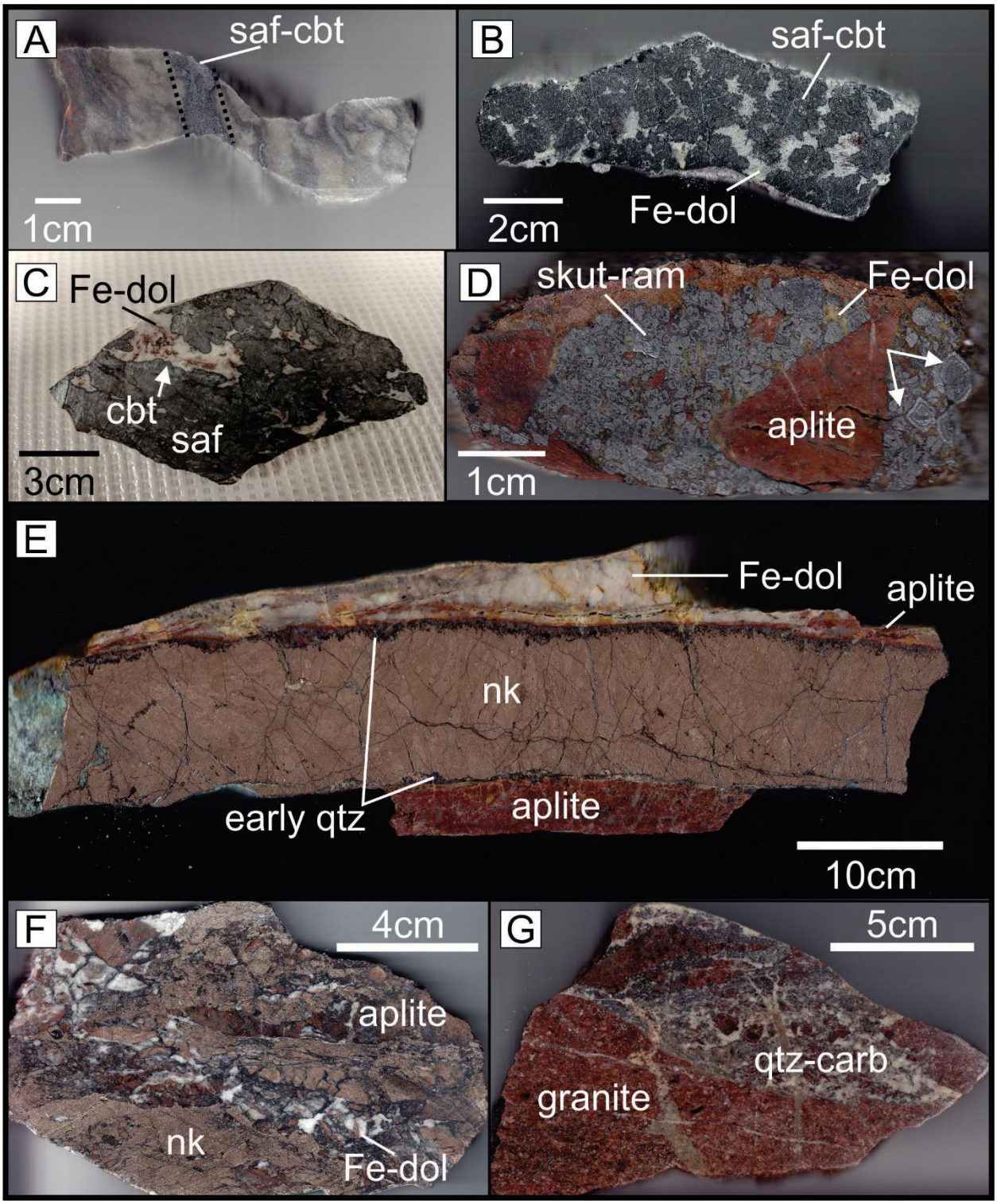
A
saf-cbt
1cm
B
saf-cbt
Fe-dol
2cm
C
Fe-dol
cbt
saf
3cm
D
skut-ram
Fe-dol
aplite
1cm
E
Fe-dol
aplite
nk
early qtz
aplite
10cm
F
4cm
aplite
nk
Fe-dol
G
5cm
qtz-carb
granite

Figure 3 (previous page). **Polymetallic vein styles in hand sample slabs from the East Arm deposits**. **A)** safflorite-cobaltite (saf-cbt) vein hosted in dolostone from Blanchet Island. **B)** Botryoidal safflorite-cobaltite ore slab showing infilling carbonate gangue (Fe-dol) from Blanchet Island. **C)** Botryoidal safflorite-cobaltite ore slab showing infilling carbonate gangue (Fe-dol) from Blanchet Island. Dark rims of cobaltite occur on massive safflorite. **D)** Hydrothermal breccia of skutterudite-rammelsbergite (skut-ram) and carbonate infilling between aplite fragments at Copper Pass. Concentric zoning in skut-ram is visible in large crystals on the right side of the image (white arrows). **E)** Massive nickeline vein hosted in aplite at Copper Pass. Nickeline is bordered by early comb-textured quartz, with later synkinematic carbonate (Fe-dol) vein. Thin, exfoliated aplite septae are visible at one contact. **F)** Hydrothermal breccia from Copper Pass showing nickeline-carbonate (Fe-dol) infilling around aplite fragments. Note fragmentation of the nickeline as well (see text for explanation). **G)** Brecciated Compton Suite granite showing weakly mineralized quartz-carbonate infilling and later carbonate veinlets from the Labelle Peninsula, a third location where polymetallic "five metals ± U" mineralization occurs.

2.5.2 Vein metal tenors

The results of the whole-rock geochemistry of mineralized veins at Blanchet Island (n=8) and Copper Pass (n=17) are summarized in Table 1. Non-normalized abundance patterns for metals are plotted in Figur 4A-B and show that Blanchet Island and Copper Pass have very similar ore and accessory metal tenors. Cobalt, Ni, As, and Fe are present in wt.% concentrations, but mineralization at Blanchet Island demonstrates greater enrichments in Co and lower Ni (up to 22.5 wt% Ni; up to 21.1 wt%; average Ni:Co ~1.1) compared to Copper Pass (Ni up to 36.6 wt%; Co up to 4.7 wt.%; average Ni:Co ~7.8). Iron concentrations in mineralized samples reach values up to 19.7 wt% and 7.1 wt% at Blanchet Island and Copper Pass, respectively. This reflects the higher abundances of ferroan dolomite present as vein gangue and within host rock dolostone. Arsenic reaches concentrations of 58.7 and 50.8 wt% for Blanchet Island and Copper Pass, respectively. This reflects assays of massive arsenides in some vein samples. Other metals sharing similar enrichment levels between deposits are Zn, Mo (higher at Copper Pass), Ag (higher at Copper Pass), Sb (higher at Blanchet Island), Te, Au, Pb, Bi and U (higher at Copper Pass). Of particular note are the Ag and U tenors, the main commodities in historically large FMA vein systems. At both study locations, Ag concentrations are less than ~ 20 ppm (range 4.8-19.1 ppm), and Uranium concentrations reach higher values at Copper Pass, as (up to 4030 ppm) compared to only 98 ppm at Blanchet Island. Partial assays for other FMA systems in the region (Caribou Lake Gabbro: LeBlanc et al., 2014; Labelle Penninsula: J. Kerswil, communication, 2015) are compared to Blanchet Island and Copper Pass in Figure 4C and show major similarities in metal tenors.

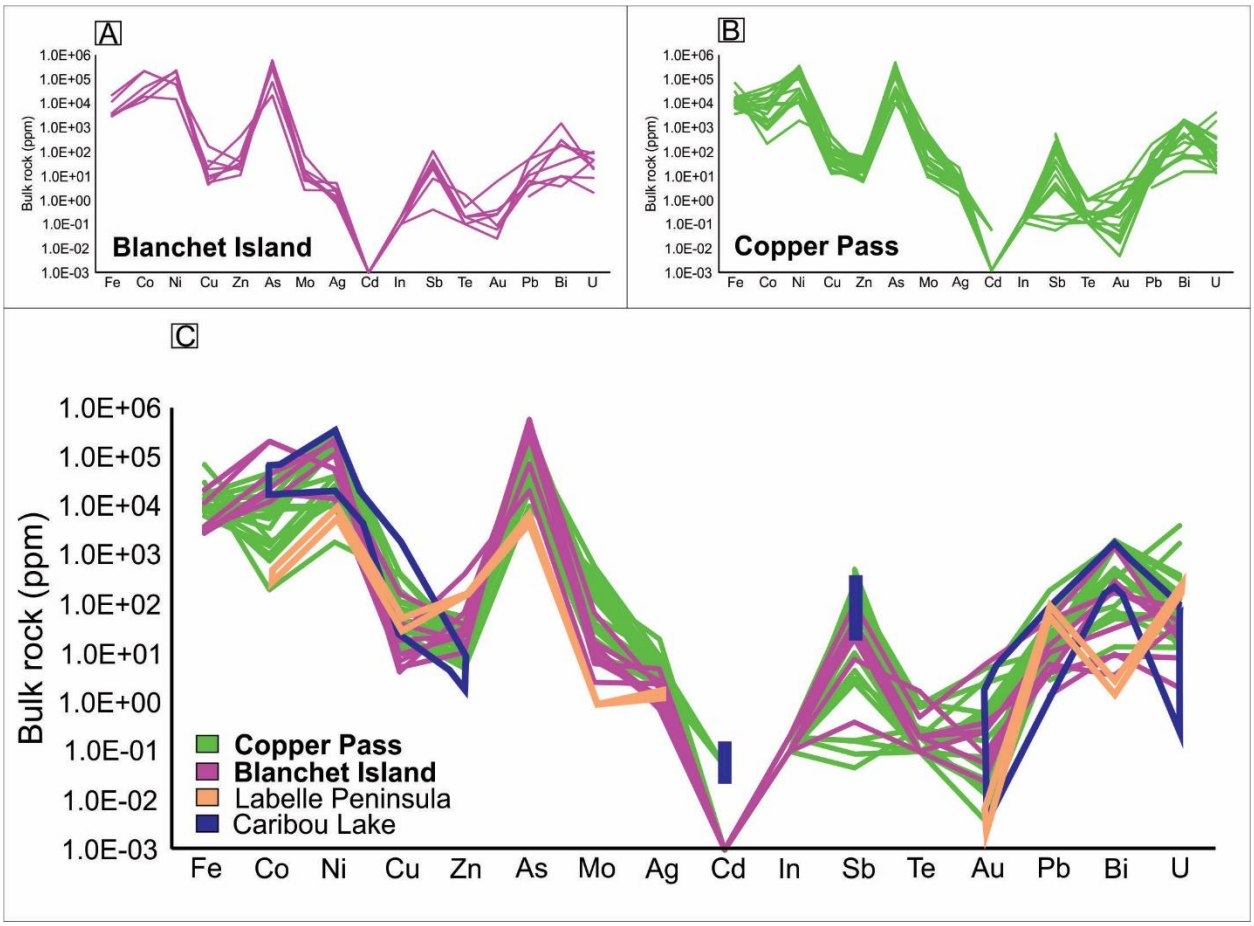

Figure 4. **Bulk rock ore metal abundances from mineralized samples in the East Arm of Great Slave Lake**. **A)** Comparison of main East Arm deposits studied (individual assays from Blanchet Island and Copper Pass) with other polymetallic vein showings in the Caribou Lake Gabbro (blue fields, partial data; Leblanc et al., 2014) and Labelle Peninsula (individual assays; Potter et al., 2013; Kerswil, communication, 2015). **B)** Individual analyses for Blanchet Island polymetallic veins. **C)** Individual analyses for Copper Pass polymetallic veins.

2.5.3 Vein ore petrography

2.5.3.1 Blanchet Island

Vein mineralization at Blanchet Island is dominated by Co-di/triarsenides and sulfarsenides. Arsenide phases consist of safflorite ($CoAs_2$) and skutterudite ($CoAs_3$) with minor nickeline (NiAs). Cobaltite (CoAsS) represents the only sulfarsenide phase. Gangue minerals consist of calcite and ferroan dolomite. Ore, gangue and accessory minerals textural relationships are shown in Figure 5.

2.5.3.1.1 Co-Ni-arsenides and sulfarsenides

Safflorite occurs as anhedral aggregate clumps, forming veinlets, and are often rimmed by cobaltite (Fig. 5A-B). In rare occurrences, safflorite contains minor Ni as seen in Figure 5G. Skutterudite occurs as massive, irregular to elongated crystals with cobaltite (rarely Ni-rich) rimming its grain boundaries or as fracture infilling. (Fig. 5B, E, F, J). The late paragenesis of cobaltite (exclusively found rimming, or as fracture infillings in, arsenides) is consistent with an increase in f_{S2} during mineralization. Althought mineralization is dominated by Co-rich species, minor Ni arsenides are also present as rammelsbergite ($NiAs_2$) demonstrating boxwork-type exsolution textures (Fig. 5H) and contemporaneous nickeline (NiAs), rarely Co-rich. Brecciation of arsenides and sulfarsenides (Fig. 5D) suggests reactivation of mineralized structures.

2.5.3.1.2 Base metal sulfides

Transitioning from arsenide-sulfarsenide mineralization, a base metal sulfide stage is represented by late pyrite veins that infill brecciation spaces in cobaltite (Fig. 5D). Small grains of chalcopyrite occur within the pyrite veins but is rare. Rarely, inclusions of galena occur along the boundaries between safflorite and cobaltite (Fig. 5B).

2.5.3.1.3 Uranium carriers

Uraninite occurs in fracture infillings with cobaltite in, along grain boundaries of, and as blebs in, skutterudite (Fig. 5I-J). Some uraninite grains showed elevated P and Al contents. An unidentified uranium carrier enriched in Ni, Co, As, V, Ti, Pb, Si, and Fe, occurs as zoned blebs with a U-rich rim and U-poor core, or colliform masses, both within calcite gangue. (Fig. 5K-L).

2.5.3.1.4 Gangue minerals

Calcite and ferroan dolomite comprise the main gangue minerals associated with mineralization. Calcite occurs as milky euhedral rhombohedral grains, where ferroan dolomite shows massive habit. Carbonates are unambiguously late, infilling spaces in the arsenide-sulfarsenide masses, and often showing strong compositional zonation and abundant, early fluid inclusions in crystal cores (Fig. 5C).

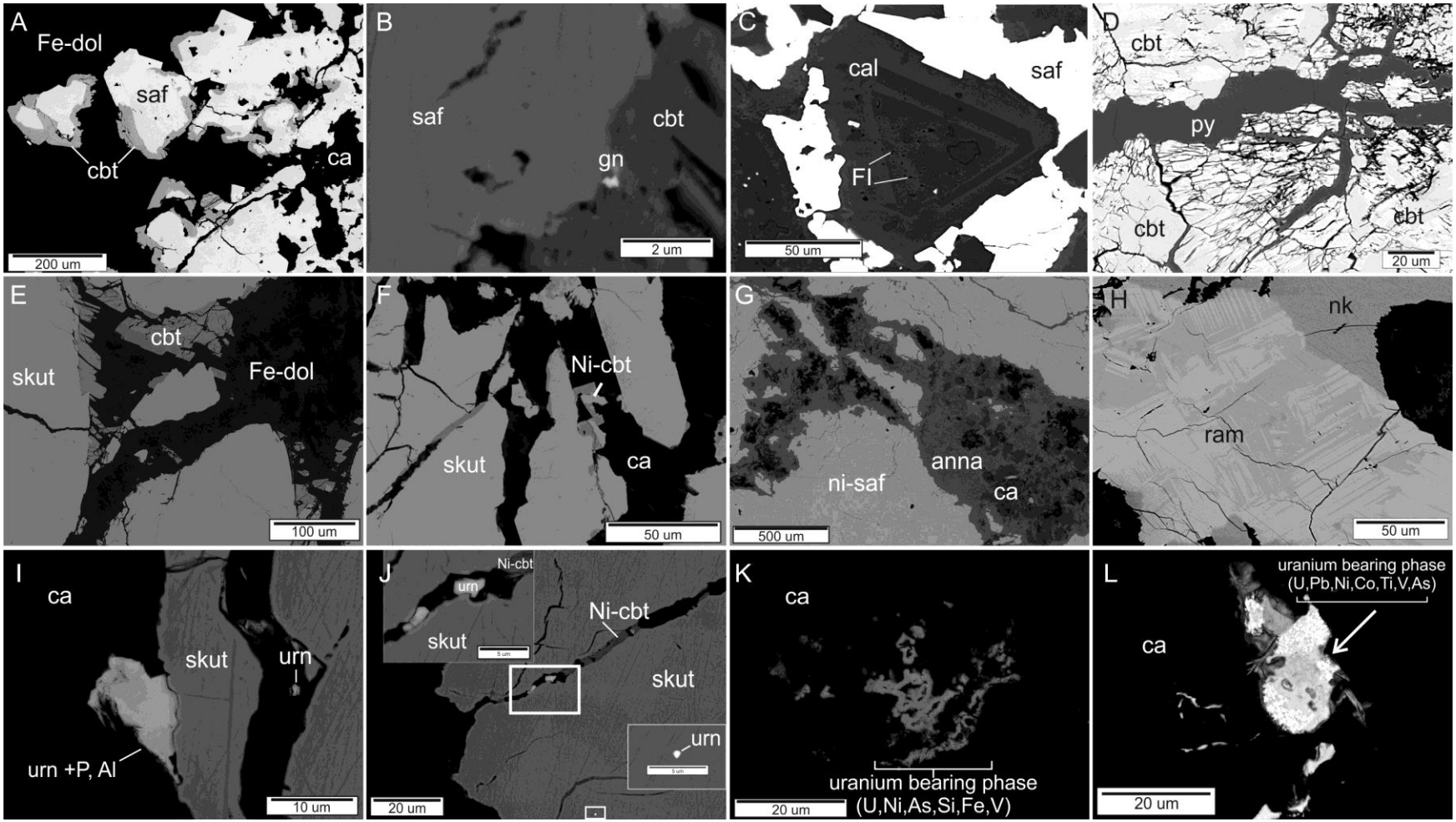
A
Fe-dol
saf
cbt
ca
200 um
B
saf
cbt
gn
2 um
C
cal
saf
Fl
50 um
D
cbt
py
cbt
cbt
20 um
E
cbt
skut
Fe-dol
100 um
F
Ni-cbt
skut
ca
50 um
G
anna
ni-saf
ca
500 um
H
nk
ram
50 um
I
ca
skut
urn
urn +P, Al
10 um
J
Ni-cbt
urn
skut
5 um
Ni-cbt
skut
urn
5 um
20 um
K
ca
uranium bearing phase
(U,Ni,As,Si,Fe,V)
20 um
L
uranium bearing phase
(U,Pb,Ni,Co,Ti,V,As)
ca
20 um

Figure 5 (previous page). **Scanning electron microscope (SEM-BSE) images showing textural relationships between (sulf)arsenides and trace/accessory phases at Blanchet Island, utilized for paragenetic interpretation**. **A**) Safflorite ($CoAs_2$) clumps rimmed by cobaltite (CoAsS) in a matrix of Fe-dolomite. **B)** Galena inclusion along grain boundary between safflorite and cobaltite. **C)** Safflorite (saf) masses with late calcite (cal) infilling. Calcite crystals show strong compositional zonation and crystal cores are rich in primary fluid inclusions. **D)** Massive cobaltite crosscut by a late pyrite (FeS_2) vein. **E)** Skutterudite ($CoAs_3$) clumps with partial cobaltite rims, and Fe-dolomite infilling. **F)** Skutterudite clumps with Ni-cobaltite and late calcite. **G)** Ni-safflorite with late calcite and secondary alteration product annabergite [$Ni(AsO_4)_2$-$8H_2O$]. **H)** Massive rammelsbergite ($NiAs_2$) showing exsolution lamellae with variable As content, and adjacent massive nickeline. **I)** Skutterudite in a matrix of calcite with uraninite (U_3O_8) included along skutterudite-calcite grain boundaries, or in calcite. **J)** Massive skutterudite with fracture infillings and inclusions of uraninite, and Ni-cobaltite. **K**) Unknown uranium-bearing phase lining late porosity infilling in calcite. **L)** Unknown uranium-bearing phase included in calcite. (Abbreviation: ca=calcite; Fe-dol=ferroan dolomite; skut=skutterudite; nk=nickeline; ram=rammelsbergite; saf=safflorite; cbt=cobaltite; gn=galena; urn=uraninite; anna=annabergite; py=pyrite; qz=quartz; Ni indicates nickel-rich).

2.5.3.2 Copper Pass

Vein mineralization at Copper Pass is dominated by Ni-di/triarsenides and sulfarsenides. Arsenide phases consist of nickeline (NiAs) and rammelsbergite ($NiAs_2$). Gersdorffite (NiAsS) represents the only sulfarsenide phase. Gangue minerals consist of early quartz and later ferroan dolomite. Ore, gangue and accessory minerals textural relationships are shown in Figure 6 and some representative SEM-EDS analyses of arsenides, sulfarsenides and accessory minerals are listed in Table 2.

2.5.3.2.1 Ni-arsenides and sulfarsenides

Nickeline is the dominant phase found at Copper Pass, forming massive vein and breccia matrix infillings. Nickeline also occurs as anhedral clumps in ferroan dolomite where this carbonate also occurs as late vein and breccia infill, mostly postdating or possibly synchronous to nickeline in a few cases (Fig. 6A-C). Nickeline demonstrates exsolution intergrowth or oscillatory zoning with (synchronous), and replacement (fracture controlled, or rimming) of, or by, rammelsbergite (Fig. 6A, D). Nickeline can also be found adjacent to (simple contacts) and between grain boundaries of early quartz, in association with later gersdorffite, uraninite, and ferroan dolomite (Fig. 6E-F). Nickeline in these early grain-boundary associations may be enriched in Sb. Gersdorffite is commonly found rimming grain boundaries, and within fractures of, nickeline, indicating increasing S:As as mineralization progressed (Fig. 6C, I, G, K). Although mineralization is dominated by Ni species, rarer Co species (safflorite, skutterudite and cobaltite) are present, usually found rimming nickeline (Fig. 6B, D) and occurring together as networks of interconnected veinlets in carbonate (Fig. 6L). Brecciation of Ni and Co carriers is evident, suggesting structural reactivation of mineralization-hosting faults after arsenide-sulfarsenide precipitation.

2.5.3.2.2 Base metal sulfides and native metals

FMA veins at Copper Pass contains a higher abundance of trace accessory phases in comparison to Blanchet Island. Native bismuth and moybdenite are the most abundant accessory phases, occurring as rims, crosscutting veins, fracture infills and isolated inclusions filling dissolution pits on, or in, ferroan dolomite, nickeline and gersdorffite (Fig. 6A-D, H, K). Molybdenite and bismuth are intergrown, suggesting simultaneous deposition (Fig. 6A, H). Galena occurs as inclusions in skutterudite-cobaltite (Fig. 6L).

2.5.3.2.3 Uranium carriers

Uraninite occurs as fracture infillings in nickeline and quartz after gersdorffite (Fig. 6I-J), and commonly intergrown ferroan dolomite in fracture infills and grain boundary junctions in quartz with nickeline and gersdorrfite (Fig. 6E-G). A single occurrence of Ag-enriched uraninite has been noted, occurring as fracture infill in nickeline (Fig. 6K).

2.5.3.2.4 Gangue Minerals

Trace ferroan dolomite appears to be intergrown with (rarely) Co and Ni phases at an early stage, but most commonly post-dates Co and Ni phases; therefore, its coprecipitation throughout vein formation is suggested but with the majority precipitated late in the paragenesis. Comb-textured quartz occurs as euhedral grains forming prior to, or possibly overlapping with the onset of, nickeline growth but is not present beyond nickeline growth. Ferroan dolomite appears to be in textural equilibrium with earlier quartz. Ferroan dolomite occurs as cloudy, massive clumps of subhedral-euhedral grains (Fig. 6A).

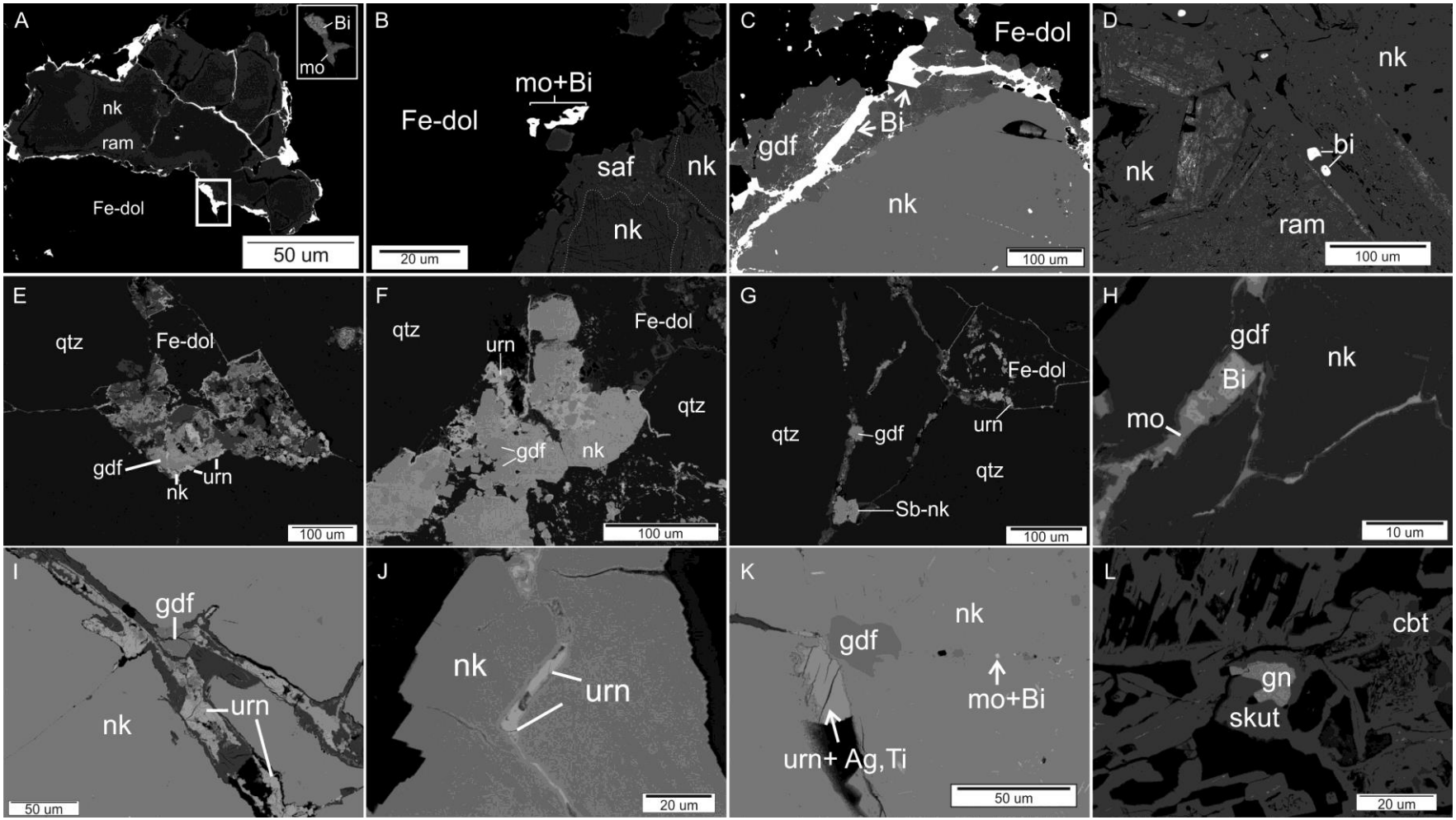
A
Bi
mo
nk
ram
Fe-dol
50 um
B
mo+Bi
Fe-dol
saf
nk
nk
20 um
C
Fe-dol
Bi
gdf
nk
100 um
D
nk
bi
nk
ram
100 um
E
qtz
Fe-dol
gdf
urn
nk
100 um
F
qtz
Fe-dol
urn
qtz
gdf
nk
100 um
G
Fe-dol
qtz
gdf
urn
qtz
Sb-nk
100 um
H
gdf
nk
Bi
mo
10 um
I
gdf
nk
urn
50 um
J
nk
urn
20 um
K
nk
gdf
mo+Bi
urn+ Ag,Ti
50 um
L
cbt
gn
skut
20 um

Figure 6 (previous page). **Scanning electron microscope (SEM-EDS) images of textural relationships between (sulf)arsenides and trace/accessory phases at Copper Pass, utilized for paragenetic interpretation**. **A**) Nickeline with rammelsbergite rimming hosted in a Fe-dolomite (Fe-dol) matrix. Fracture infillings and grain boundaries host native bismuth and molybdenite Inset shows lower brightness/contrast BSE image showing area in box, with Mo and Bi discriminated. **B)** Nickeline mineralization transitioning to safflorite rims, hosted in Fe-dol matrix. Blebs of native bismuth and molybdenite also visible. **C)** Nickeline bordered by gersdorffite (NiAsS) rim with native bismuth infilling fractures in gersdorffite and as inclusions (filling former porosity) in nickeline. **D)** Native bismuth inclusions (filling former porosity) in rammelsbergite-nickeline intergrowth. **E-F)** Nickeline-gersdorffite-Fe-dolomite intergrowth filling porosity at quartz grain junction. Uraninite infills fractures, grain boundaries and porosity in the earlier (sulf)arsenide-dolomite assemblage. **G)** Nickeline (Sb-rich)-gersdorffite-Fe-dolomite and later uraninite filling fractures and porosity in quartz. **H)** Massive nickeline with euhedral gersdorffite crystal in fracture. Massive native bismuth- molybdenite intergrowth fills fracture in nickeline, but surrounding gersdorffite. **I-K)** Late fracture and porosity infillings in nickeline composed of gersdorffite followed by uraninite. Trace molybenite and native bismuth also visible in K. **L)** Galena infilling porosity in skutterudite-cobaltite intergrowth. (Abbreviations: Bi=native bismuth; my=molybdenite; Fe-dol=ferroan dolomite; ram=rammelsbergite; nk=nickeline; saf=safflorite; gdf=gersdorffite; ga=galena; urn=uraninite; anna=annabergite; qtz=quartz; Sb indicates antimony-rich).

2.5.3.3 Alteration

At Blanchet Island and Copper Pass no alteration halos were observed at outcrop scale. In thin section, hydrothermal alteration of coherent and brecciated wall-rocks associated with the FMA vein systems in the East Arm basin was observed but is minimal, comprising low intensity and spatially restricted propylitic assemblages extending mm to cm distances into wall rock and breccia fragment margins. Weak propylitic alteration manifests as chloritization and hematitization of host dolostone at the margins of mineralized veins. Within the veins, chlorite and disseminated hematite forms rims and patches infilling grain boundaries and fractures in calcite and ferroan dolomite. White mica (sericitization) is present in trace amounts within calcite gangue in the veins. Albitization of plagioclase in wall-rock along vein margins, and wall-rock fragments within mineralized breccias is also noted. Carbonate microveinlets extend into wall rocks adjacent to veins.

2.5.4 Sulfarsenide chemistry and thermometry

SEM-EDS analyses of sulfarsenide phases from both localities are listed in Table 3 and the compositional ranges are portrayed on a ternary diagram of mole % abundances for Co, Fe, and Ni sulfarsenide end-members (Fig. 7; cobaltite, arsenopyrite, gersdorffite; Klemm, 1965). The majority of sulfarsenides at Copper Pass plot at or close to end-member gersdorffite, with some solid solution spread along the CoAsS-NiAsS join. In contrast, sulfarsenides from Blanchet Island show a wide range in composition along the CoAsS-NiAsS join, tending towards more Co-rich compositions approaching end-member cobaltite.

The ternary diagram also shows isotherms for a two-phase solvus. Plotting sulfarsenide compositions on this ternary diagram provides a constraint on sulfarsenide crystallization

temperature. Blanchet Island sulfarsenides intersect the limbs of the CoAsS-NiAsS solvus at a temperature of ~350^{o}C or less. Gersdorffite at Copper Pass, occurring at the edges of nickeline grains, intersects the solvus at significantly lower T than Blanchet Island, < 300^{o}C. These findings coincide with other constraints (e.g., microthermometry; see below), supporting a low temperature of mineralization

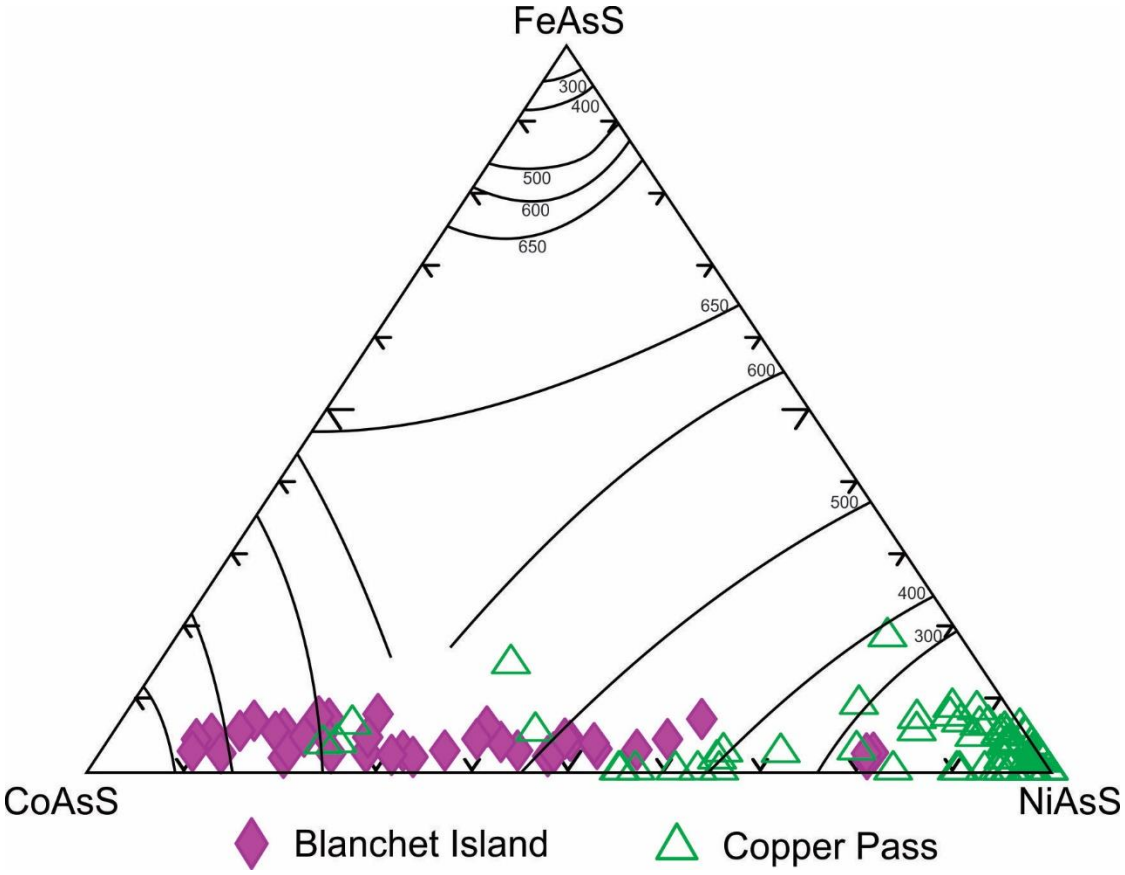

Figure 7. **Ternary diagram showing atomic weight % (relative) Ni-Co-Fe sulfarsenide solid solution end members (gersdorffite-cobaltite-arsenopyrite) and the composition of sulfarsenides from the East Arm deposits.** Isotherms (labelled with T in ^{o}C) are from Klemm (1965). Data show compositional ranges reflecting contrasting initial sulfarsenide compositions that crystallized prior to unmixing (Co-rich starting compositions at Blanchet Island; Ni-rich starting compositions at Copper Pass).

2.5.5 Fluid inclusion petrography, cathodoluminescence (CL) imaging and microthermometry

2.5.5.1 Petrography

Inclusions were grouped based on textural criteria using the fluid inclusion assemblage (FIA) method, whereby coevally trapped inclusions present in small clusters, growth zones, healed fracture trails, or along grain boundaries are grouped as an FIA. Accidentally trapped solid phases were recognized by variable proportion within an FIA as well as being included also in the host phase. Heterogeneous (coeval) fluid entrapment was recognized within an FIA by variable phase ratios. All inclusion types are very small, ranging typically from ~3 to 10 μm in diameter. Based on phases observed in inclusions at 20^{o}C in carbonate at Blanchet Island and carbonate/quartz at Copper Pass, five distinct fluid inclusion types are identified (Fig. 8, Fig. 9):

(i) Type 1 brine inclusions are 2-phase (L_{aq} + V) H_2O-NaCl-$CaCl_2$ inclusions. They are hosted in either carbonate (Fig. 8A-F) or quartz crystals (Fig. 8G, M, N, Fig. 9A) with V bubble proportions of ~10-15 vol%. *Type 1* inclusions occur (i) in the inclusion-rich cores of calcite and quartz crystals with relatively inclusion-poor rims characteristic of primary origin (Fig. 8A, B, M, N; cf. Roedder, 1984; Goldstein, 2003); (ii) in trails representing healed fractures (secondary origin) on their own (Fig. 9C) or heterogeneously trapped with *Type 3* (Fig. 9D) or *Type 4* (Fig. 9E-H) inclusions; (iii) in outer rim growth zones (primary origin) in quartz heterogeneously trapped with *Type 3* (Fig. 8Q-S) and *Type 5* inclusions (Fig. 8Q-S); (iv) as isolated, large inclusions (Fig. 8D-F) or in small clusters of unknown origin (Fig. 8C, Fig. 9A). Inclusion shapes may resemble host mineral habit (Fig. 8D, E) in carbonate inclusions and in rare occurrences, demonstrate some degree of necking down (Fig. 8F). Boiling is absent in *Type 1* FIA in quartz and carbonate from both localities.

(ii)Type 2 brine inclusions are rare, 2-3 phase (L_{aq} + V ± bitumen) H_2O-NaCl-$CaCl_2$ inclusions. They are hosted in early crystals of quartz at Copper Pass, occurring in clusters of unknown origin or in healed fractures (secondary origin) crosscutting the *Type 1* inclusion-rich cores and in the inclusion-poor rims. Commonly, they occur with heterogeneously trapped *Type 3* inclusions. *Type 2* inclusions may contain accidentally trapped, fluorescing particles of a solid HC phase ("bitumen") clinging to the vapour bubble (Fig. 8H-J). Vapour proportions are similar to or slightly larger than in *Type 1* brine inclusions. *Type 2* inclusions greatly resemble *Type 1* inclusions and can only be differentiated under UV light.

(iii)Type 3 carbonic inclusions are 1-4 phase ($L_{carbonic}$ ± $V_{carbonic}$ ± bitumen ± carbonate) CO_2±CH_4 inclusions. They occur in quartz at Copper Pass (i) in secondary trails and clusters of unknown origin on their own (Fig. 9B,C) or heterogeneously trapped with *Type 1* (Fig. 9D) or *Type 2* inclusions; and (ii) in outer rim growth zones (primary origin) in quartz heterogeneously trapped with *Type 1* (Fig. 8Q-S) and *Type 5* inclusions (Fig. 8Q-S). Similar to *Type 2* inclusions, *Type 3* inclusions accidentally trapped fluorescing particles of bitumen may be present (Fig. 8K-L) and in some inclusions, the entire inner wall of the inclusion fluoresces suggesting that a fluorescent liquid may also be present, or that particles of bitumen coat the inner wall of the inclusion. A second, rare, accidentally trapped phase is carbonate (Fe-dolomite; confirmed by Raman) recognized by its birefringence in cross-polarized transmitted light (Fig. 9B). Reflecting variable density, *Type 3* inclusions may or may not contain a $V_{carbonic}$ bubble at 20°C.

(iv)Type 4 liquid hydrocarbon (HC) inclusions are rare, 1-2 phase (L_{HC} ± $V_{carbonic}$) inclusions, resembling *Type 3* inclusions and show some post-entrapment modification (necking down) (Fig. 9E-H). They occur in quartz at Copper Pass, and are secondary in origin, occurring on their own or heterogeneously trapped with *Type 1* inclusions. *Type 4* inclusions exhibit strong bright yellow-

blue-green (when containing immiscible brine) to brown fluorescence (when coentrapped brine is not visible), indicating the presence of higher order hydrocarbons of variable maturity or composition.

(v) Type 5 "bitumen" inclusions contain a non-fluorescing, high density solid or viscous liquid hydrocarbon (thus, not low viscosity "fluid" inclusions *sensu-stricto*). They occur in outer rim primary growth zones in early quartz crystals at Copper Pass where they are heterogeneously trapped with *Type 1* and *Type 3* inclusions (Fig. 8O-S).

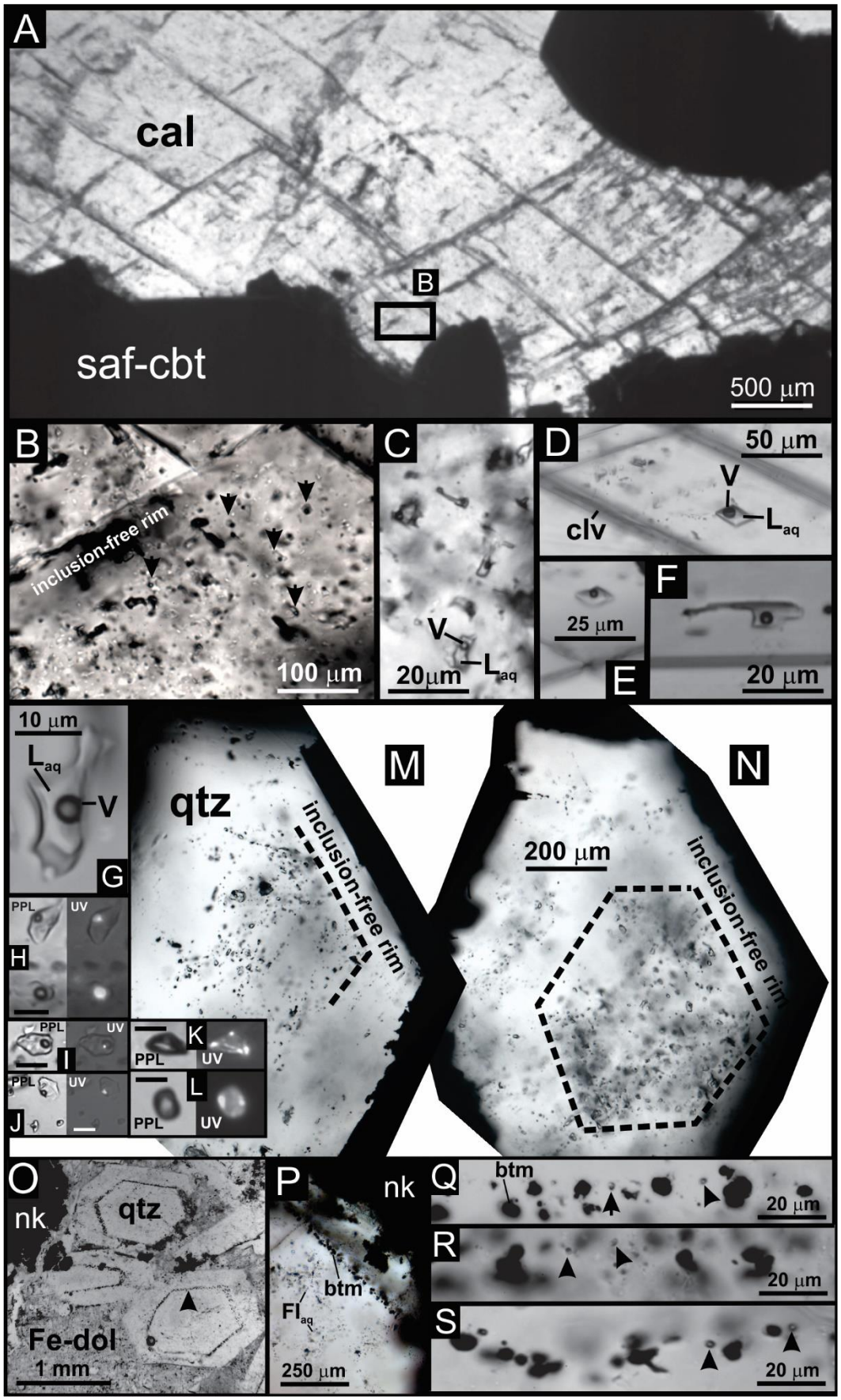
A
cal
B
saf-cbt
500 μm
B
inclusion-free rim
100 μm
C
V
L aq
20μm
D
50 μm
V
clv
L aq
25 μm
E
F
20 μm
10 μm
L aq
V
G
qtz
M
inclusion-free rim
N
200 μm
inclusion-free rim
PPL
UV
H
PPL
UV
I
K
PPL
UV
PPL
UV
J
L
PPL
UV
O
nk
qtz
Fe-dol
1 mm
P
nk
btm
Fl aq
250 μm
Q
btm
20 μm
R
20 μm
S
20 μm

Figure 8 (previous page). Photomicrographs of fluid inclusion types and relevant textural features in quartz and carbonate in mineralized veins. All images were obtained at 20ºC in transmitted, plane-polarized (PPL) light except for (**H**)-(**L**) that include images in combined transmitted PPL and reflected ultraviolet light (UV). (**A**) Massive safflorite-cobaltite (saf-cbt) with ferroan dolomite infill (calcite) showing typical host setting for *type 1* calcite-hosted inclusions at Blanchet Island. Inset box shows the location of inclusions shown in (**B**). **B**) Enlarged view of an area in (**A**) showing calcite crystal boundaries (not cleavage planes) with a relatively inclusion-free rim, and inclusion-rich core containing primary, *type 1* two phase (L_{aq}+V) brine inclusions marked with yellow arrows. **C**) Irregularly-shaped, secondary, two phase (L_{aq}+V) aqueous inclusions from Copper Pass. **D**)-**F**) Suspected primary *type 1*, two-phase (L_{aq}+V) inclusions in Fe-dol showing negative crystal shapes and adjacent cleavage planes (clv) from Copper Pass. **G**) Two-phase *type 1* (L_{aq}+V) brine inclusion in quartz from Copper Pass, hosted in the core of an euhedral quartz crystal. **H**)-**J**) Unclassified (unknown origin) *type 2* inclusions in quartz from Copper Pass containing fluorescing liquid or solid hydrocarbon (HC) phases in addition to an aqueous liquid. In frame (**H**) two adjacent inclusions contain a volumetrically-dominant L_{aq} but show variable bubble sizes, with bubbles containing a fluorescing HC phase (liquid or liquid film on vapour bubble). In frames (**I**) and (**J**), a strongly fluorescing phase appears to be a solid HC particle attached to the vapour or carbonic liquid bubbles. **K**)-**L**) Unclassified *type 3* inclusions in quartz from Copper Pass containing two fluorescing HC phases, as solid particles (brightly fluorescing) and a darker fluorescence throughout (liquid or liquid film on vapour bubble). **M**)-**N**) Quartz crystal (view down c-axis) shown at two different depths of focus. An inclusion-poor rim surrounds an inclusion-rich core containing abundant *type 1* (L_{aq}+V) aqueous inclusions of primary origin. **O**) Mineralized vein margin showing euhedral quartz crystals with interstitial Fe-dol and nickeline (nk). Black arrow marks a primary growth zone containing opaque, solid *type 5* bitumen inclusions. Growth zones containing these inclusions are seen in each quartz crystal. **P**) Enlarged view of the mineralized (nk) outer margin of a quartz crystal showing a growth zone containing solid HC (bitumen-btm) inclusions and two phase (L_{aq}+V) aqueous inclusions in the crystal core. **Q**)-**S**) Enlarged views of solid HC inclusion assemblages showing coeval *type 1* and *type 3* fluid inclusions containing aqueous and carbonic phases. Inclusions containing at least two phases (L_{aq}+V or L_{aq}+$L_{carbonic}$) are visible in frames **Q**) and **R**). Inclusions in frame **S**) appear to be carbonic liquid only (see text for description).

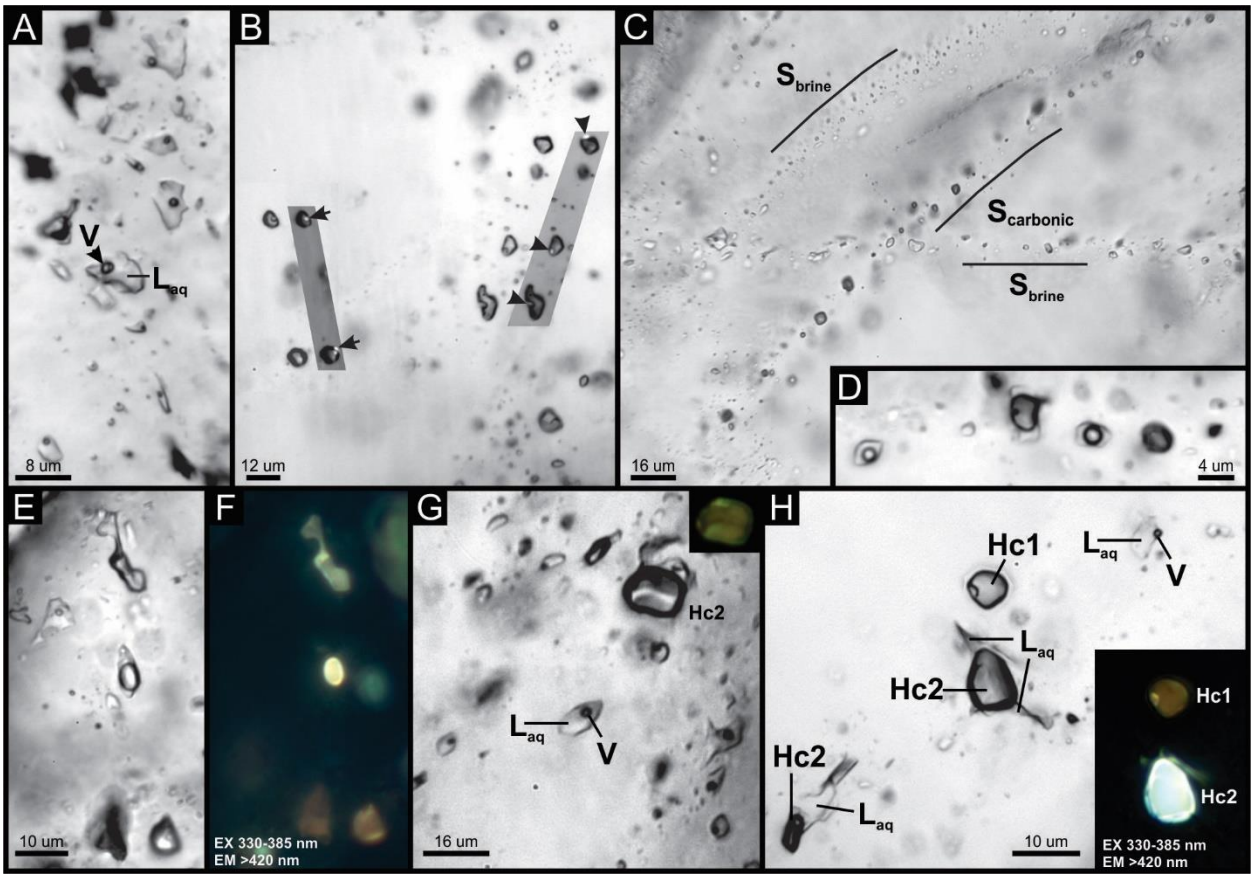

Figure 9. Quartz-hosted fluid inclusion assemblages in pre-mineralization quartz from Copper Pass showing interaction of hydrocarbon (HC) liquid and carbonic inclusions with brine. All images were obtained at 20ºC in transmitted, plane-polarized (PPL) light except insets that include images in combined transmitted PPL-XPL (B), and reflected ultraviolet light (UV; F, G, H). **A)** Unclassified, *type 1* two-phase brine (L_{aq}-V) inclusions. **B)** One to two phase *type 3* ($L_{carbonic}\pm V_{carbonic}\pm$carbonate) fluid inclusions demonstrating accidental calcite entrapment (birefringent phase highlighted by arrows) in XPL insets. **C)** Intersection of secondary (S) *type 1* brine and *type 3* carbonic (CO_2-CH_4) inclusion trails. **D)** Fluid inclusion assemblage demonstrating coentrapment of *type 1* brine and *type 3* carbonic phases (i.e., variable brine-carbonic phase ratios). **E-H)** UV-fluorescent *type 4* hydrocarbon (HC) liquid-rich inclusions associated with brine (L_{aq}-V) inclusions, showing coeval entrapment of immiscible brine and hydrocarbon liquid. Hydrocarbon (HC) liquid demonstrates UV fluorescence colour variance due to variations in hydrocarbon composition (Hc1=brown fluorescence; Hc2=yellow-blue-green florescence).

Spatial relationships amongst inclusions types based on petrographic observations from thin section at Copper Pass are sketched and represented in Figure 10. Pre-mineralization quartz (cross-cut by nickeline vein) contain inclusion types 1 (brine), 3 (carbonic), and 4 (HC liquid) in primary clusters and secondary intersecting trails (and heterogeneously trapped) (Fig. 9D and G). Although inclusion type 2 were not documented, it is reasonable to assume their presence due to the abundance of hydrocarbon-rich inclusions. As mineralization begins, early quartz hosts inclusion types 1-3 as aqueous brine, carbonic and bitumen phases are present as primary and secondary inclusions (Fig. 10 inset B). Bitumen colloids (type 5) are present in early quartz along aplite margins, occurring along growth zones with brine and carbonic inclusions (Fig. 8Q-S), showing evidence of homogeneous and heterogeneous entrapment. Ferroan dolomite along the aplite margin occurs as dirty massive carbonate and resulting in the lack of fluid inclusion identification. Along the other vein margin (Fig. 10 inset A), fluid inclusion types present is limited to type 1 brine inclusions in quartz and later stages of mineralization ferroan dolomite.

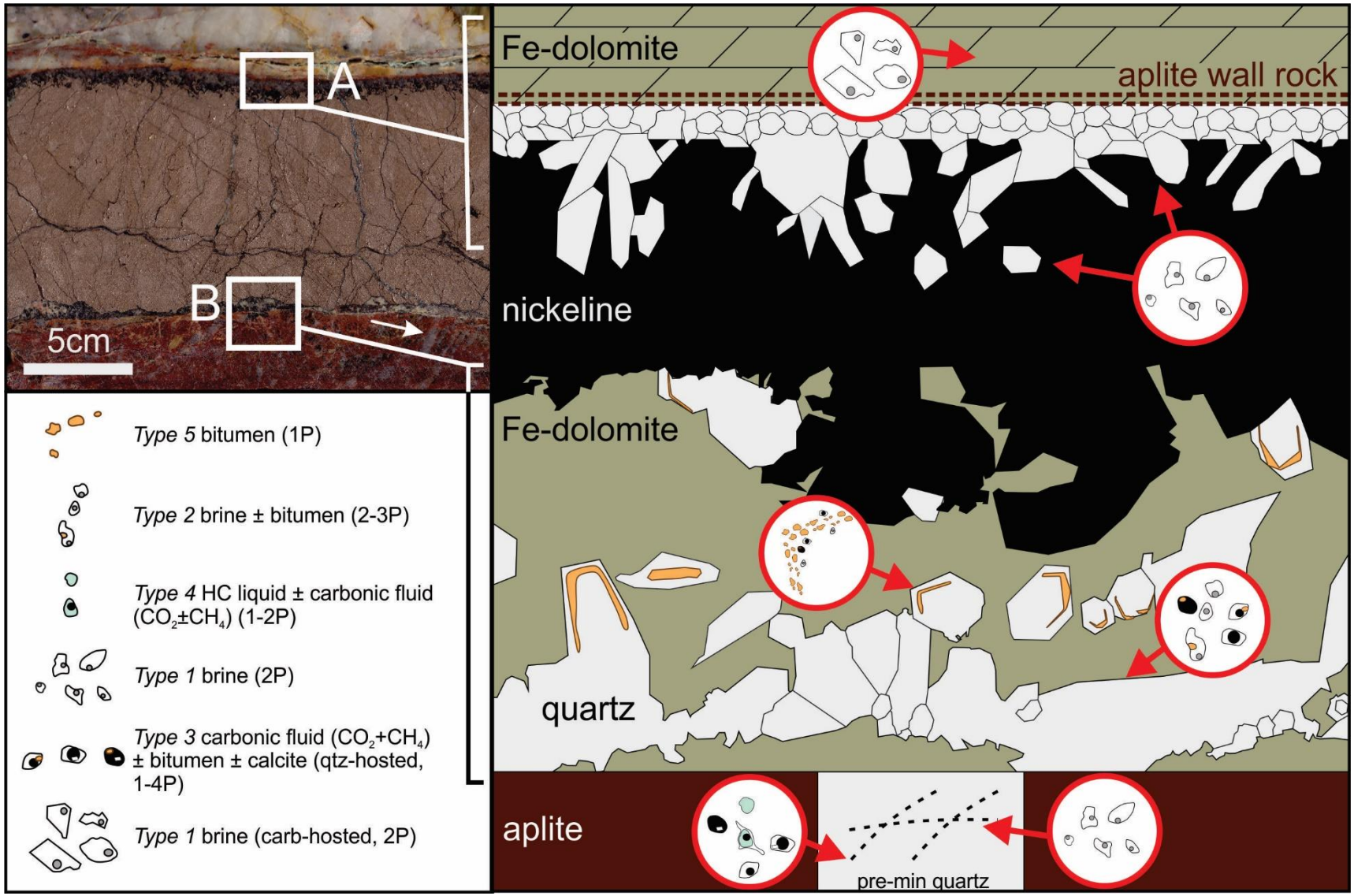
A
B
5cm
Type 5 bitumen (1P)
Type 2 brine ± bitumen (2-3P)
Type 4 HC liquid ± carbonic fluid (CO2±CH4) (1-2P)
Type 1 brine (2P)
Type 3 carbonic fluid (CO2+CH4) ± bitumen ± calcite (qtz-hosted, 1-4P)
Type 1 brine (carb-hosted, 2P)
Fe-dolomite
aplite wall rock
nickeline
Fe-dolomite
quartz
aplite
pre-min quartz

Figure 10 (previous page).- Schematic diagram, sketched based on petrographic observations from thin section, of the textural relationships between nickeline mineralization, early comb -textured quartz, Fe-dolomite gangue and fluid inclusion types at Copper Pass. 2-phase L_{aq}-V brine inclusions are commonly found in quartz and carbonate throughout all stages of mineralization. Pre-mineralization quartz (cross-cut by the nickeline-bearing vein) contains intersecting trails of (and heterogeneously trapped) brine, HC liquid, and carbonic (CO_2+CH_4) fluid inclusions. Early-stage quartz along one aplite vein margin (section B) contains bitumen, brine, and carbonic fluid inclusions showing evidence of homogeneous and heterogeneous entrapment. Textural variants range from early growth zones in quartz containing brine inclusions only, to later growth zones and cross-cutting secondary trails containing coentrapped bitumen, brine and carbonic fluid inclusions. Quartz along the other vein margin (section A) contains only brine inclusions. Crack-seal events have separated and trapped laminae of aplite wall rock that now lie between early quartz and later Fe-dolomite. Late Fe-dolomite, formed during the later stages of mineralization, contain only 2-phase L_{aq}-V brine inclusions.

2.5.5.2 Cathodoluminescence

A mineralized vein boundary with intergrown quartz, ferroan dolomite, and nickeline at Copper Pass (Fig. 11A) was imaged using hot cathodoluminescence (CL) colour microscopy. The resulting CL map reveals spectacular zonation in early vein quartz along the aplite dyke margin (Fig. 11B). Specifically, domains of early, comb-textured quartz demonstrate intense and variable styles of zonation showing blue-pink-yellow luminescence highlighting multiple growth zones (Fig.11B-D). Ferroan dolomite demonstrates speckled green-red-orange luminescence (Fig. 11B). Quartz demonstrates five growth zones, interpreted from enhanced and magnified CL images and shown as simple line diagrams in Figure 11C-D. Zones have been characterized as follows: A=core zone, dark with no distinct features and not observed in all quartz crystals (black-blue luminescence); B=core zone showing sectoral zoning and not observed in all quartz crystals, mid brightness (pink-orange luminescence); C=core zone showing irregular patches of luminescence and non-luminescence quartz, suggestive of dissolution-reprecipitation, bright (pink-orange luminescence); D1=transitional zone showing complete or partial, concentric euhedral crystal faces (very bright yellow-pink luminescence); D2=transitional zone showing complete or partial, concentric euhedral crystal faces (very bright pink luminescence); D3= transitional zone showing complete or partial, concentric diffuse luminescence (very bright blue); E=rim zone showing minimal features, dark (black-blue luminescence). It is important to note that along primary growth zones (highlighted by black arrows in Fig. 11A, and yellow arrows in Fig. 11C and D), coeval bitumen and fluid inclusions are hosted in zone D3, and specifically at or near the D2-D3 interface.

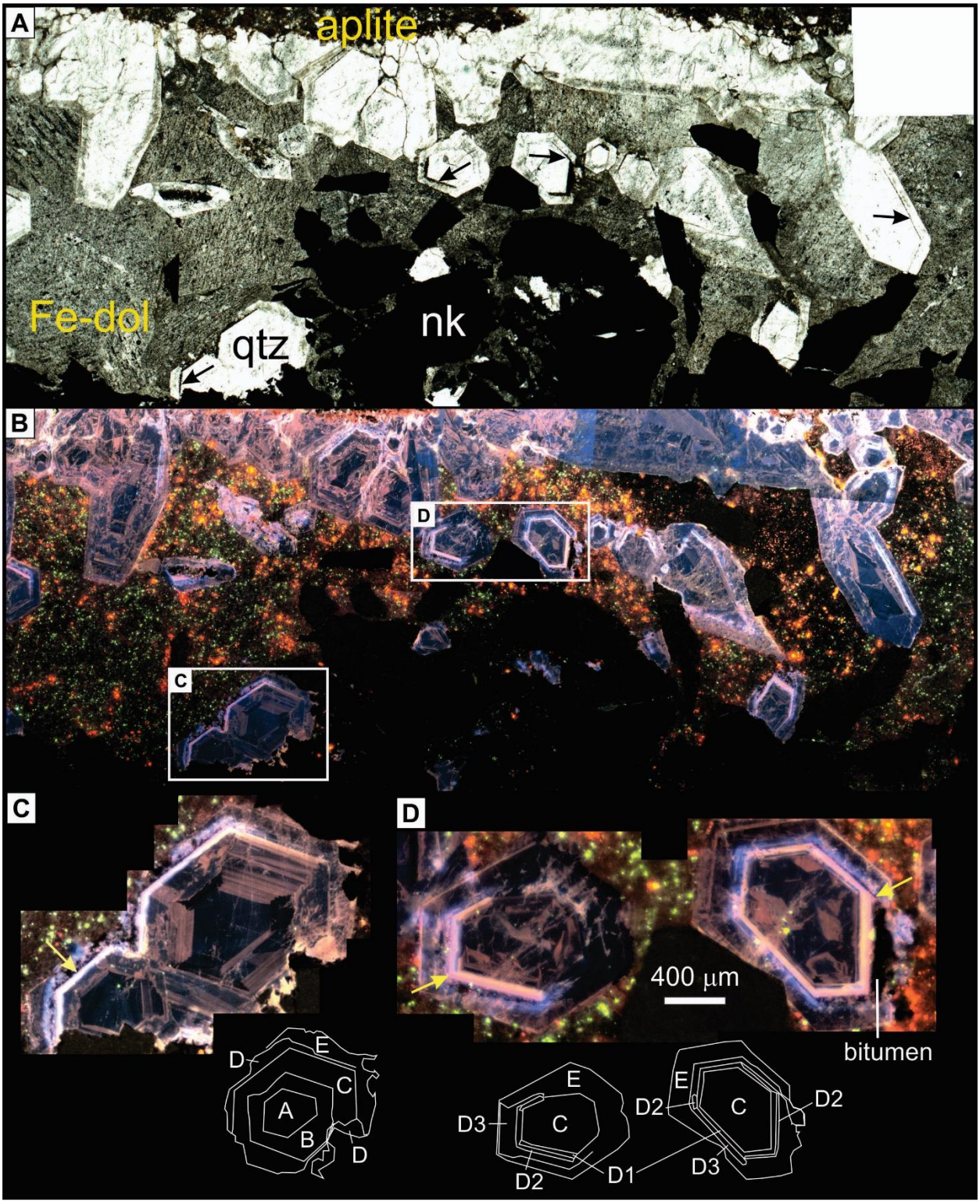
A
aplite
Fe-dol
qtz
nk
B
D
C
C
D
400 μm
bitumen
E
D
C
A
B
D
E
D3
C
D2
D1
E
D2
C
D2
D3

Figure 11 (previous page). Transmitted light and cathodoluminescence (hot CL) colour photomicrographs of early quartz along vein margins at Copper Pass. A) Transmitted light (plane-polarized) photomicrograph showing early quartz (qtz) crystals containing visible bitumen inclusions along primary growth zones (indicated with arrow), nickeline (nk) and Fe-dolomite (Fe-dol). B) Hot cathodoluminescence photomicrograph mosaic showing intense zonation in quartz (blue-pink-yellow zones) and speckled green-red-orange colours (Fe-dol). C-D) Enlarged quartz crystals from two inset areas (shown as boxes in A) showing systematic CL zonation, interpreted (classified) into distinct zones according to colour. Line drawings show growth zone classifications A through E.

2.5.5.3 Microthermometry

The results of fluid inclusion microthermometry on *Type 1* and *Type 3* inclusions are reported in Table 4 and summarized graphically in Figure 12 where data are grouped according to bulk sample measurements including multiple FIAs. (Single FIA data are reported in Table 4). Microthermometry was done on 187 (57 at Blanchet Island, 130 at Copper Pass) *Type 1* inclusions hosted in carbonate (calcite and ferroan dolomite) at Blanchet Island and *Type 1* and *Type 3* inclusions in quartz at Copper Pass.

For *Type 1* brine inclusions hosted in carbonate at Blanchet Island, final ice melting temperature (T_m^{ICE}) ranged between -12.4° and -23.5°C, corresponding to a bulk salinity of 16.0 to 23.5 wt.% $CaCl_2$ equiv. (avg.= 20.8±1.8 [1σ] wt% $CaCl_2$ equiv.) (Fig. 12A). No hydrohalite or clathrate was observed. Final homogenization of *Type 1* inclusions occurred by vapour bubble closure (L_{aq} + V → L_{aq}) at a T_h between 124.8° and 224.4°C (avg.= 176.1±25.3 [1σ] °C) (Fig. 12B). The narrow range in T_h values for individual samples and FIA within them, and consistency in T_h from sample to sample (Fig. 12, Table 4) suggests that inclusions at Blanchet Island experienced minimal post-entrapment modification (e.g., leakage, necking down) though a few outliers exist.

Type 1 inclusions hosted in quartz at Copper Pass show T_m^{ICE} between -17.4° and -24.8°C, corresponding to bulk salinities between 19.2 and 23.1 wt. % $CaCl_2$ equiv. (avg.= 21.46±0.61 [1σ] wt% $CaCl_2$ equiv.) (Fig. 12A). Homogenization of the vapour phase in *Type 1* inclusions occurred by vapour bubble closure between 122.4° and 252.7°C (1st to 3rd quartile; all data avg.= 187.7±61.6 [1σ] °C) (Fig. 12B), with maximum values reaching up to 359.5°C and minimum values reaching 70°C. Sample and FIA ranges in T_h are wider at Copper Pass (for quartz-hosted inclusions) and are attributed to post entrapment modification (leaking or necking down). Post entrapment modification contributes significant to the expansion of the isochore field for quartz-

hosted *Type 1* inclusions at Copper Pass, spuriously extending the possible range of entrapment conditions into the albite-epidote hornfels metamorphic fields (Fig. 13).

Type 1 inclusions hosted in ferroan dolomite at Copper Pass show T_m^{ICE} between -20.2° and -24.7°C, corresponding to bulk salinities of the aqueous phase ranging from 20.8 to 22.4 wt.% $CaCl_2$ equiv. (avg. = 22.2±0.5 [1σ] wt% $CaCl_2$ equiv.), (Fig. 12A). Homogenization temperatures of the vapour phase in type 1 carbonate hosted brine inclusions occurred by vapour bubble closure between 157.6° and 184.5°C (avg. = 168.51±32.18 [1σ]°C) (Fig. 12B). Isochores (Fig. 13) show the range in possible entrapment conditions for all analyzed *Type 1* inclusions. However, it is important to note that the range is much narrower for individual FIAs.

For one sample of quartz from Copper Pass showing homogeneously and heterogeneously trapped *Type 1* and *Type 3* inclusions (Fig. 9A-D; sample SL-M-1-2), microthermometric measurements (Table 4; Fig. 12) were obtained for each of the fluid types where they occurred along separate secondary trails for the purpose of P-T modeling using the method of intersecting isochores. *Type 1* inclusions showed T_m^{ICE} between -18.2° and -24.8°C for this sample, yielding bulk salinity values between 19.9 to 23.1 wt.% $CaCl_2$ equiv. (Fig. 12A). Homogenization of the vapour phase occurred by vapour bubble closure between 119.4° and 235.6°C (Fig. 12B). Thus, the data for this sample is representative of typical data for *Type 1* inclusions at Copper Pass. From this same sample, 14 *Type 3* inclusions were measured from multiple FIA (Table 4). Final melting of carbonic phase occurred at $T_m^{carbonic}$ between -58.1° and -56.3°C with the majority of inclusions showing carbonic phase melting within measurement uncertainty of -56.6°C indicating pure CO_2. A few inclusions contain minor CH_4 which lowers $T_m^{carbonic}$ (confirmed by Raman). Variation in temperature of homogenization for carbonic phase ($T_h^{carbonic}$) was observed, ranging from 8.9° to

28.4ºC (avg. 21.3±5.5 [1σ] ºC). Homogenization occurred by disappearance of the carbonic vapour bubble ($L_{carbonic} + V_{carbonic} \rightarrow L_{carbonic}$).

The overall consistency in homogenization and bulk salinity data at the FIA and sample scale is notable between Blanchet Island and Copper Pass. While at each locality subtle variations in salinity and T_h for samples with narrow data ranges likely reflect small but real fluctuations in trapping conditions and fluid salinity, Blanchet Island and Copper Pass share the same microthermometric characteristics with respect to the predominant fluid inclusion type present. Furthermore, there is relatively very little variation with time from early vein quartz to later carbonate at Copper Pass, indicating that fluid T-salinity remained more or less static throughout FMA vein formation.

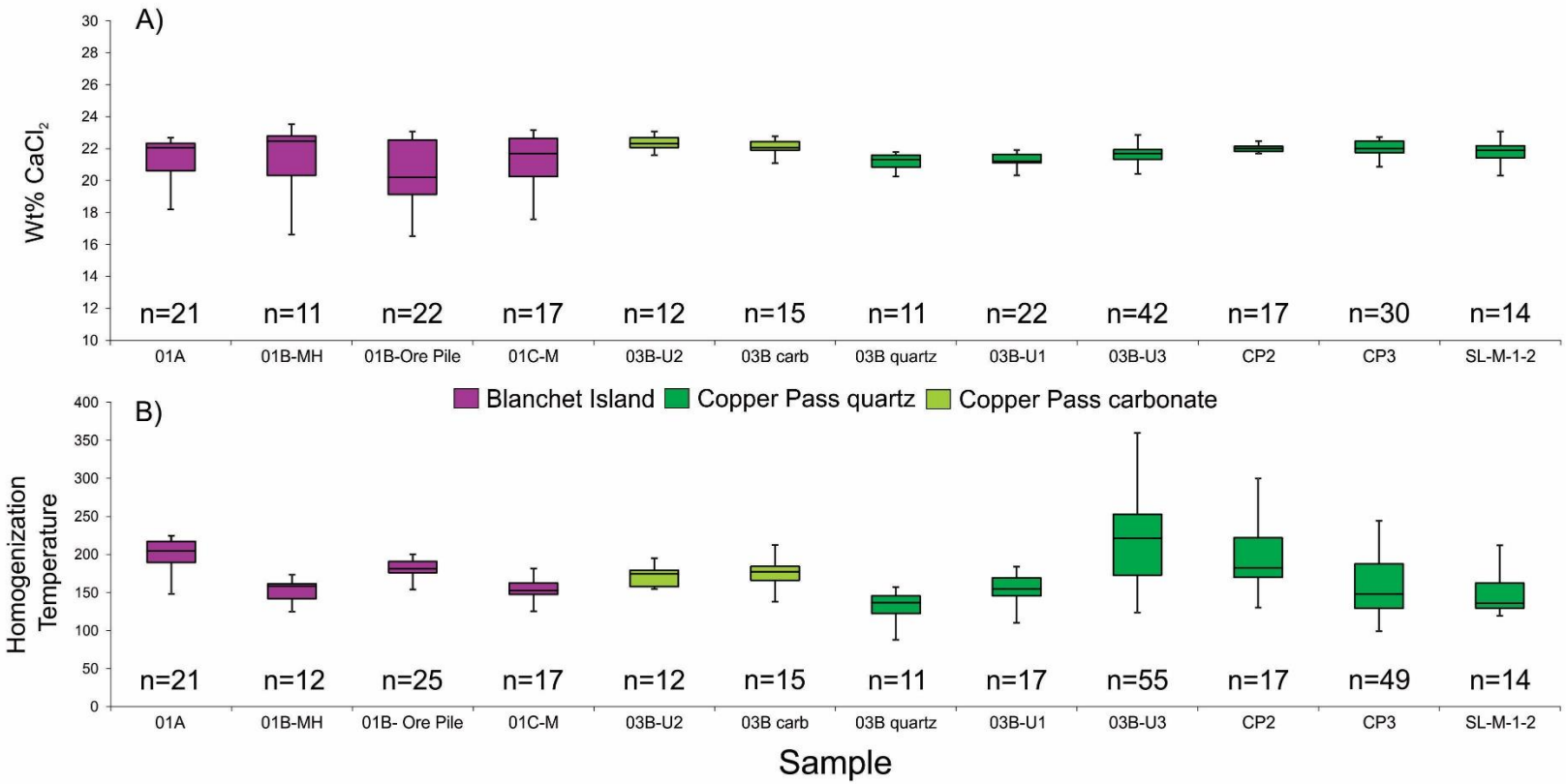

Figure 12 - Box and whisker plots summarizing microthermometric data for 2-phase (L_{aq}+V) brine inclusions at Blanchet Island and Copper Pass. The number `n` corresponds to the number of inclusions measured in each sample (Data for individual fluid inclusion assemblages are differentiated in Table 4). A) Ranges in salinity (wt% $CaCl_2$ equivalent) and B) Ranges in homogenization temperature (T_h). Microthermometry demonstrates that brines at Blanchet Island and Copper Pass had similarly high salinities, ranging from ~19-23 wt. % $CaCl_2$ equivalent (1^{st}-3^{rd} quartile range), and homogenization temperatures, ranging from 120–250 ^oC. At Copper Pass where inclusions in both carbonate and quartz were investigated, ranges in salinity and T_h within quartz- and carbonate-hosted inclusions are very similar.

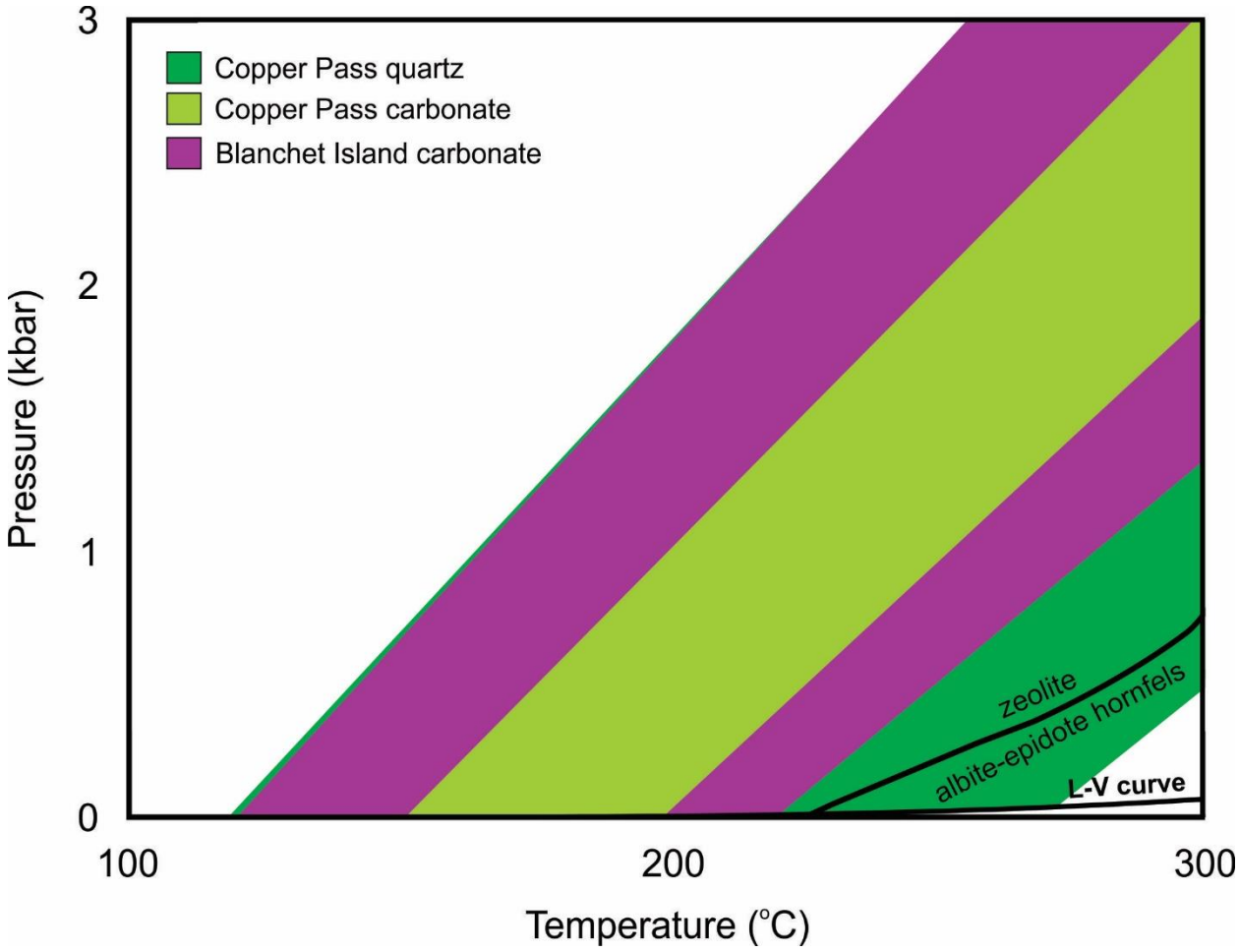

Figure 13 - P-T diagram of isochore fields showing range in possible trapping conditions for all 2-phase (at 20ºC) brine inclusions hosted in carbonate and quartz at Blanchet Island and Copper Pass. Note that the range in isochores is much narrower for individual fluid inclusion assemblages (Table 4). Black curve shows metamorphic facies boundary between zeolite and albite-epidote hornfels. The liquid-vapour curve shown is for a 20 wt% $CaCl_2$ fluid**.**

2.5.6 Raman Spectroscopy

The vapour and liquid phases of *Type 1* brine inclusions, carbonic phase in *Type 3* inclusions, fluorescing phases in *Type 4* HC liquid inclusions, and opaque material in *Type 5* bitumen inclusions were analyzed by confocal Raman microspectroscopy. Both CH_4 and H_2 were detected in the vapour phase of *Type 1* inclusions in vein quartz and carbonate from Blanchet Island and Copper Pass (Fig. 14, 15) while the coexisting liquid phase contained no detectable dissolved volatile phases. Additionally, CO_2 was detected in *Type 1* inclusions hosted in carbonate gangue. In all *Type 1* inclusions, a strong H_2O peak was observed with peak shape characteristics consistent with a high salinity (i.e., > ~20 wt. % NaCl equiv.) aqueous solution (Mernagh and Wilde, 1989; Frezzotti et al., 2012). Raman spectroscopy analysis coincides with microthermetric determination of brine salinity. It is important to note that some inclusions within individual FIA lacked any detectable volatile phases within the vapour bubble, whereas in other inclusions in the same FIA numerous volatile phases were detected. It is unlikely that this observation reflects analytical conditions (that are optimized for inclusion analysis). Heterogeneous entrapment of aqueous, carbonic, and liquid or solid hydrocarbon phases was observed at some stages of vein growth, and the detection of volatile species does not appear to be related to inclusion size (Fig. 14, 15).

Determination of the composition of the carbonic phase in simple *Type 3* inclusions showing only 1-2 phases ($L_{carbonic} \pm V_{carbonic}$) in one sample (SL-M-1-2) was performed on a inclusions homogenized to single phase ($L_{carbonic}$) using a simple heating stage held at 35ºC (OPTIKA M-666 stage and controller). Other than CO_2, CH_4 was the only volatile species detected in the inclusions. The calculated X_{CO2} and X_{CH4} range from ~1 to 0.95, and ~0 to 0.05, respectively, consistent with the results of microthermometry that show some inclusions showing carbonic melting below -

56.6ºC for pure CO_2. Other *Type 3* inclusions containing fluorescing bitumen inclusions were not analyzed.

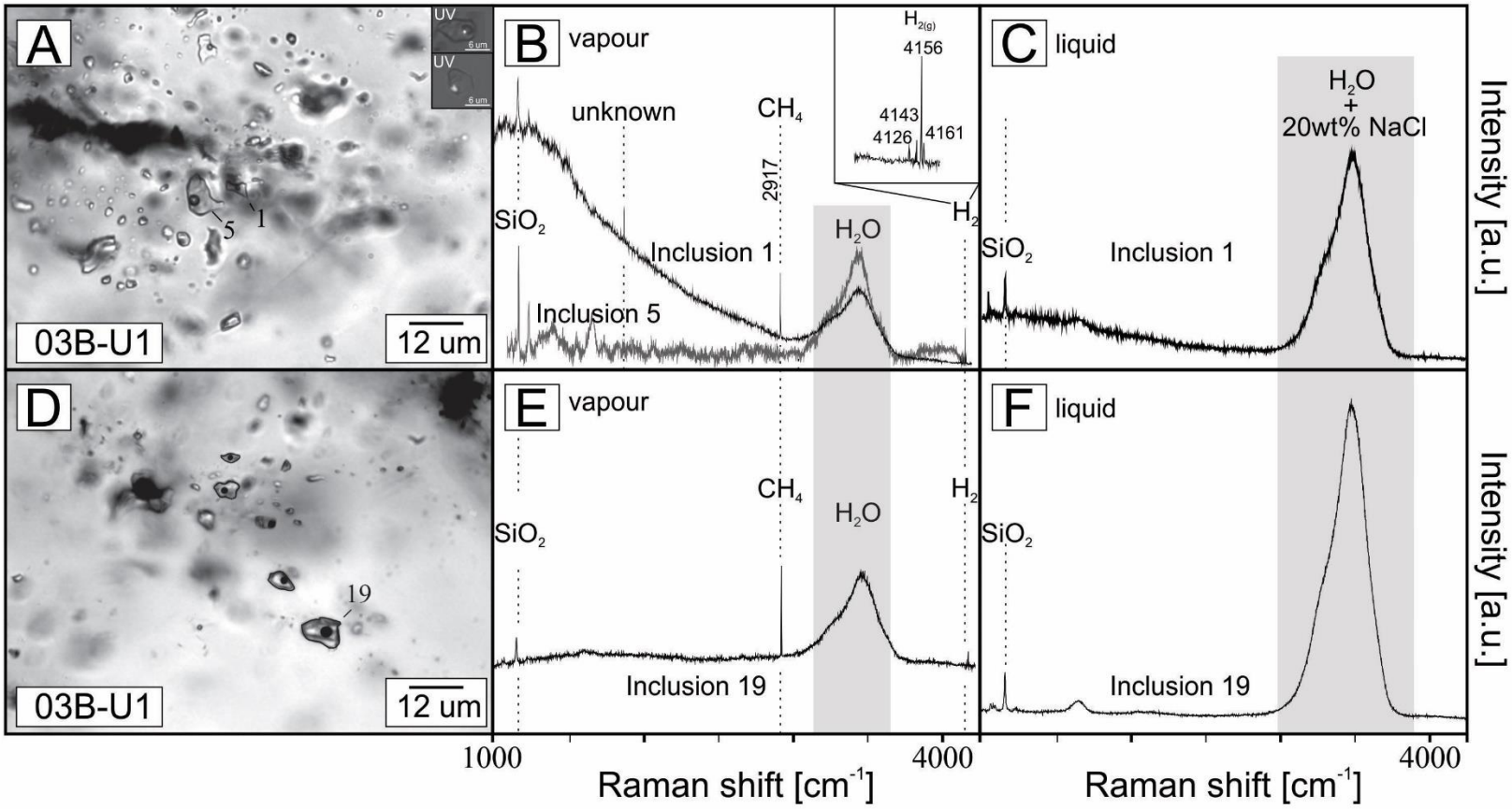

Figure 14- Raman spectra of 2-phase (L_{aq}-V) brine inclusions hosted in quartz. A) and **D)** Photomicrographs of quartz from sample 03B-U1 showing analyzed fluid inclusions within two FIAs. **B)** and **E)** Representative Raman spectra of vapour bubble (mixed with aqueous phase) for three inclusions in sample 03B-U1. Fluid inclusions 1 and 19 contains trace hydrocarbons (CH_4) and H_2 (black spectra) whereas 5 does not (grey spectrum). **C)** and **F)** Representative Raman spectrum of the aqueous phase of inclusion 1 showing peak characteristic of high salinity (>20wt% NaCl equiv.) aqueous fluid. Peaks for SiO_2 matrix are also show at lower wave numbers.

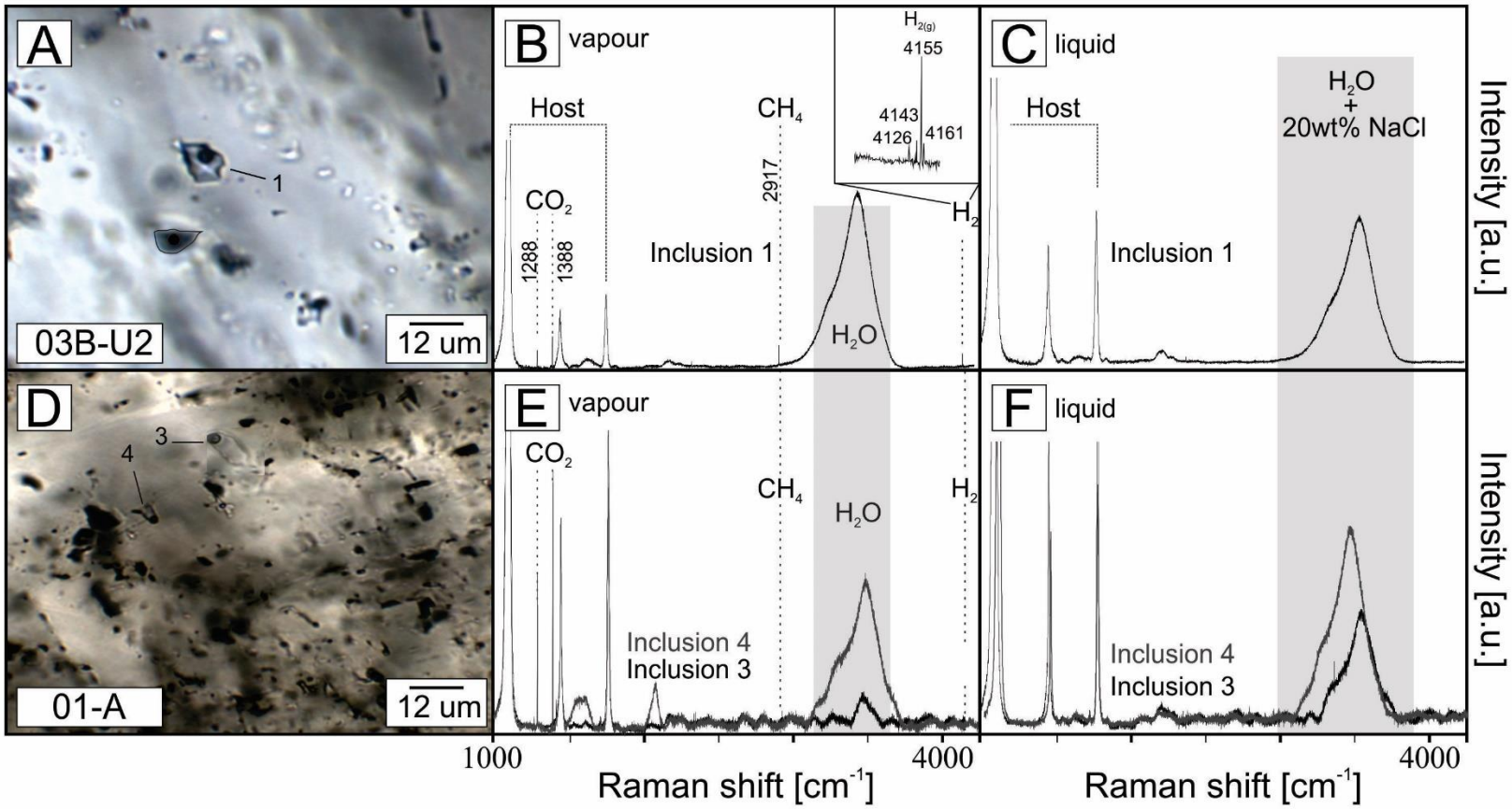

Figure 15 - Raman spectra of 2-phase (L_{aq}-V) brine inclusions hosted in carbonate A) and D) Photomicrographs of carbonate from sample 03B-U2 (Copper Pass) and 01-A (Blanchet Island) showing an analyzed fluid inclusion within two FIA. **B) and E)** Representative Raman spectra of vapour bubble (mixed with aqueous phase) for one inclusion from 03B-U2 and two inclusions from 01-A. Fluid inclusion 1 demonstrates peaks for a hydrocarbon (CH_4) phase , carbon dioxide (CO_2) and H_2 gas in the vapour bubble (black spectra). Fluid inclusions 3 and 4 contain the same gas species but at lower concentrations (peak intensity). Although peak intensities for gas species are not the same between Copper Pass and Blanchet Island, it is important to note that gas phases are the same between sites in the East Arm. **C) and F)** Representative Raman spectrum of the aqueous phase in inclusions 1,3, and 4 showing host carbonate peaks and broad peak for high salinity (>20wt% NaCl) H_2O liquid.

Type 4 quartz-hosted HC liquid inclusions at Copper Pass were analyzed by Raman spectroscopy to identify volatile and organic species in the vapour and liquid phases present (Fig. 16A). Peak identification was done through comparison with Raman spectral analyses of fluid inclusion volatile compounds summarized in Burke (2001) and Frezzoti et al. (2012). It was not possible to clearly differentiate between vapour and liquid phases, however, spectra showed weak Raman peaks for H_2, N_2 (2326 cm^{-1}), kerogen (1605 cm^{-1} "G" band), aqueous CO_3^{-2}, and strong peaks for CH_4 and various other aliphatic (olefin and paraffin) hydrocarbon species including C_2H_6 (2953 cm^{-1}), C_3H_8 (2897 cm^{-1}), aromatics (e.g., 3067 cm^{-1}), and unidentified alkanes (e.g., 3118 cm^{-1} peak) and alkenes (Fig. 16A). Inclusions with differing fluorescence colouration (Fig. 16A; inclusion 5 vs. 4) showed slightly differing peak intensities for hydrocarbon compounds, with darker fluorescing (brown) inclusions having lower intensity aliphatic and H_2 bands.

Primary bitumen (type 5) inclusions along growth zones in early quartz at Copper Pass were analyzed and contained no detectable volatiles with exception to a pronounced kerogen peak (1605 cm^{-1}) that had stronger peak intensity than in HC liquid inclusions (Fig. 16B).

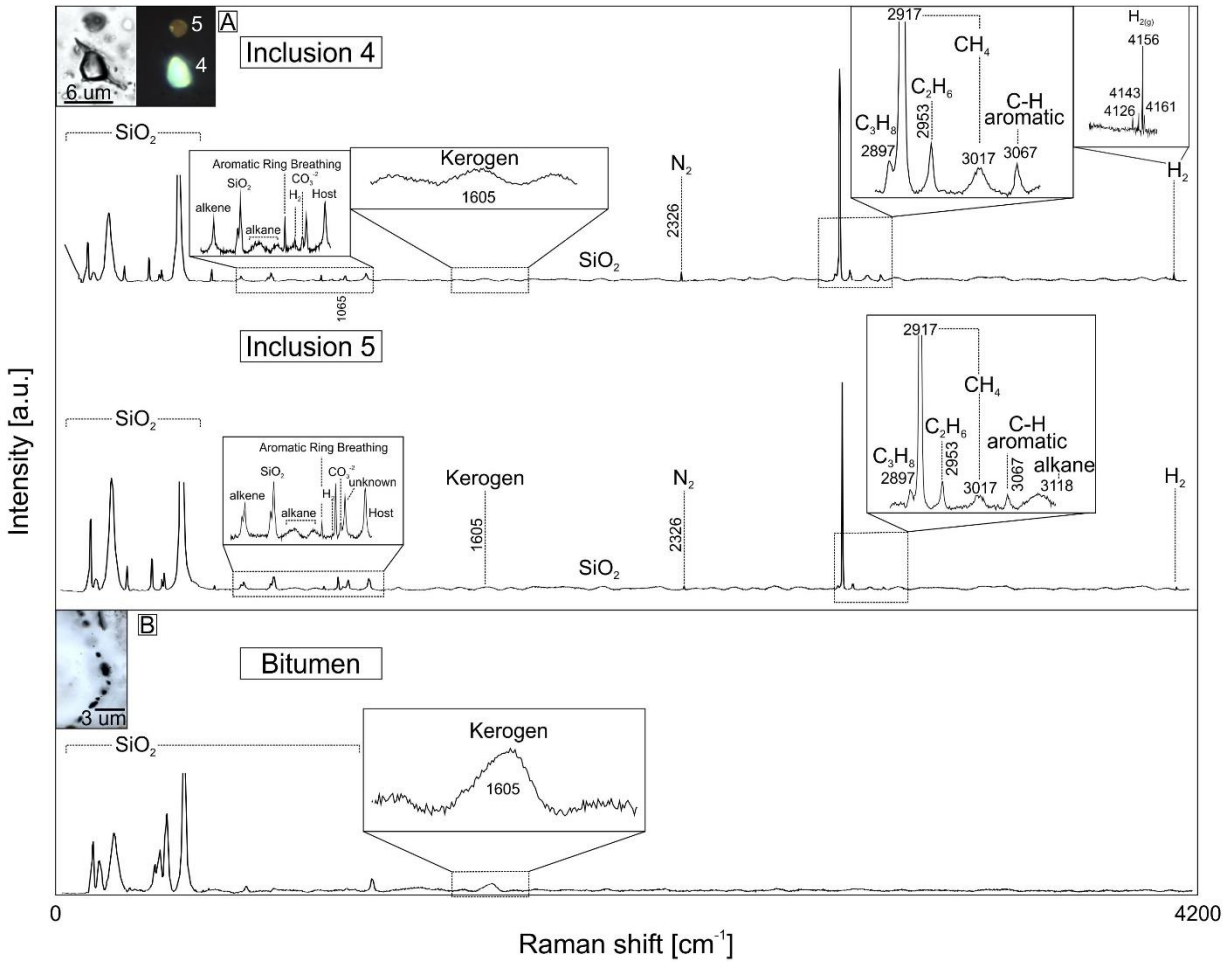

Figure 16 - Representative Raman spectra from fluorescence hydrocarbon (HC) liquid and bitumen inclusions found at Copper Pass. A) Hydrocarbon liquid inclusions 4 and 5 (inset, upper left corner) yielded Raman spectra with many characteristic peaks for alkanes, alkenes, aromatics, kerogen and methane, along with nitrogen (N_2) and hydrogen gas (H_2). Also present is a peak for CO_3^{-2}. **B)** Primary bitumen inclusions hosted in quartz growth zones showing demonstrating host silica peaks and a strong kerogen peak (1605 cm^{-1}). Peak identification was done through comparison with Raman spectral analyses obtained from Frezzoti et al. (2012) and Burke (2001).

2.5.7 SEM-EDS X-ray mapping of primary bitumen inclusions

Preliminary characterization of the metal content of *Type 5* primary bitumen inclusions exposed on polished thin section surfaces, hosted in growth zones of early quartz at Copper Pass was carried out by SEM-EDS (spot analyses and X-ray mapping). SEM-BSE and X-ray maps (Fig. 17) show that *Type 5* inclusions are zoned with lower density (dark; phase '2') cores and higher density (bright; phase '1') rims, with core zones having a radiating, fibrous morphology (Fig. 17A-C). Corresponding X-ray mapping (Fig. 17D) and corresponding SEM-EDS spectra of phase '1' and '2' (Fig. 17E and F, respectively) in the bitumen illustrates enrichments in many elements, notably C, U, Ni, As, and S with cores enriched in C, S, Ni and As, and rims enriched in U. This observation is important as it demonstrates that concentrations of FMA-style ore metals are present at high concentrations (i.e., wt.%) to be detected by SEM-EDS, having a routine detection limit of 0.1 wt% for heavy elements.

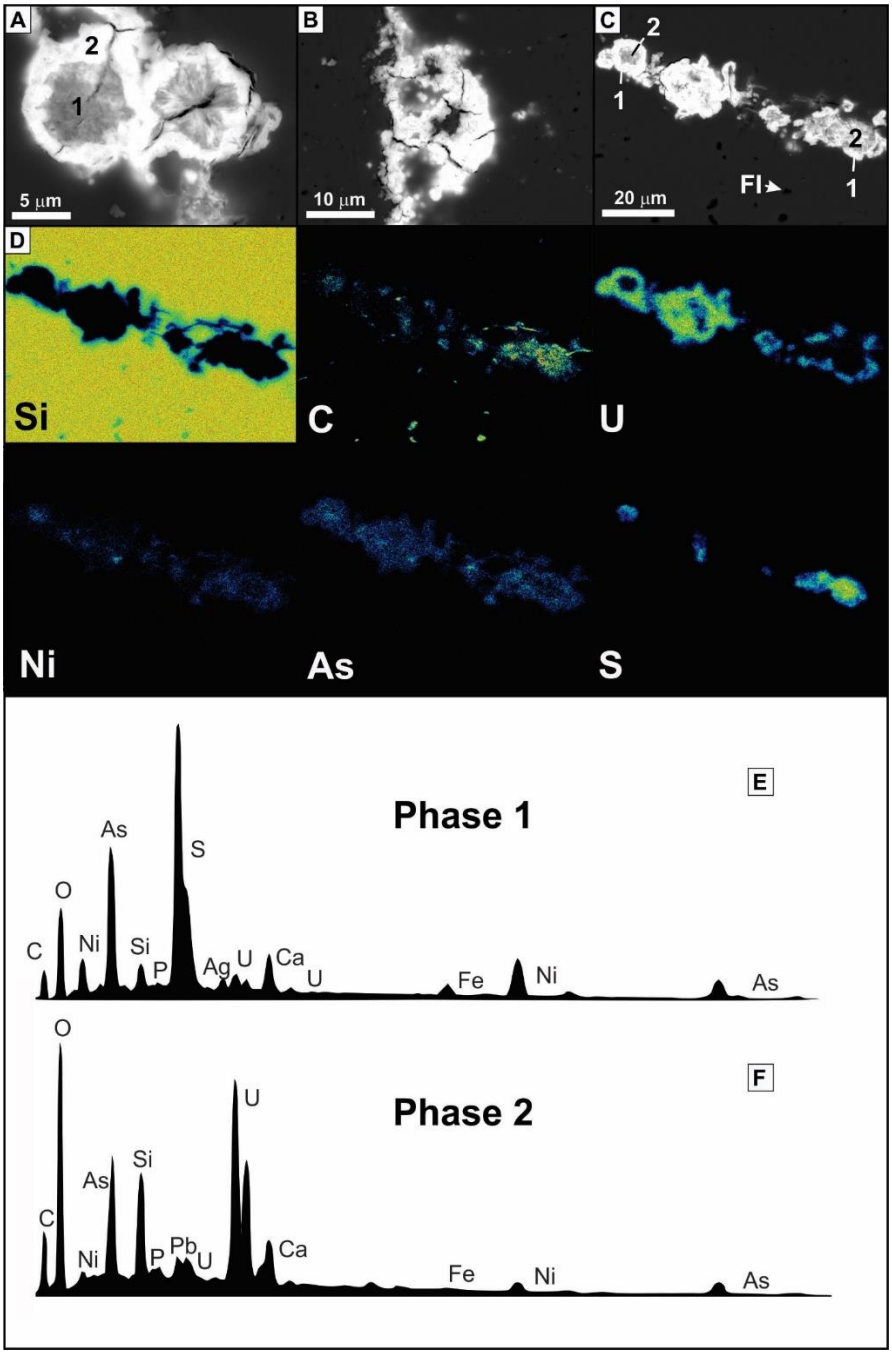

Figure 17 - SEM-BSE photomicrographs and SEM-EDS X-ray maps of bitumen inclusions in growth zones within early quartz at Copper Pass. A)-C) BSE photomicrographs of exposed bitumen inclusions on polished surface showing zoned nature of the inclusion with bright (higher density; phase '1') rims and dark (lower density; phase '2') cores with a radiating, fibrous morphology Opened fluid inclusions (FI) are visible in the quartz. Bitumen aggregates included along growth zone, corresponding to the area for which X-ray maps (D) were obtained. **D)** X-ray maps showing quantified element intensity for selected elements Si, C, U, Ni, As and S. Note the enrichment in C, S, Ni and As in phase 2 and U in phase 1. **E)** SEM-EDS spectra of phase '1' seen in **C)**. **F)** SEM-EDS spectra of phase '2' seen in **C).**

2.5.8 Laser ablation ICP-MS analyses of fluid inclusions, bitumen, and carbonates

2.5.8.1 Fluid inclusions

Representative primary *Type 1* brine inclusions from early quartz along margins (aplite margin, sample 03-A2; carbonate vein margin, 03B-U1) of nickeline (Ni-Co-As-Bi-Mo-Pb-Sb±Ag-U) veins at Copper Pass were analyzed by LA-ICP-MS. Data is summarized in Table 5 and plotted in Figure 18. Figure 19 shows a representative LA-ICP-MS transient signal for a *Type 1* inclusion. Elements in Figure 18 are grouped together whereby group I elements are major cations, group II are minor cations, and group III are ore and accessory metals. Group I elements are Na, Mg, K, Ca and Mn. Analysis shows that Na is the dominant cation in the fluid ranging from 60920 to 90782 ppm (avg 81990 ppm). In addition, brines are enriched in K (avg 7850 ppm), Ca (avg 15485 ppm), with lesser Mg (avg 945ppm) and Mn (avg 93.6 ppm). Group II elements consist of minor cations Rb, Sr, and Ba. Strontium values range from 91.2 to 1794.6 ppm (avg 866 ppm), with lesser Rb (avg 30.8 ppm) and Ba (avg 492.5 ppm). Group III elements comprise the ore metals Fe, Co, Ni, Cu, Zn, As, Mo, Ag, Sb, Pb, Bi, Th and U. Cobalt values are often below detection limits, however when, concentrations reach an average of 3 ppm when detected (n=4). Nickel contents were undetectable in all inclusions and routine detection limits are high owing to poor sensitivity of this method for Ni. Whereas average detection limits for Ni are in the 10^2 ppm range, the lowest detection limits, in the 20-40 ppm range for the largest inclusions analyzed are more representative of maximum concentrations for this element (Table 5). Likewise, while Ag was detected in two inclusion measurements (19.4 and 24.1 ppm), those concentrations are unusual and routine detection limits appear to be lower, in the low ppm-range. Copper content ranges from 8 to 331 ppm (avg 57 ppm). Zinc was detected in all inclusions, with ranges in concentration from 12 to 532 ppm (avg 145.2 ppm). Pb was detected in all inclusions ranging from 1 to 146 ppm (avg 40

ppm). As was detected in majority of inclusions ranging from 22 to 1167 ppm (avg 230 ppm) and is one of the few metals where enrichment in the brine is greater than bitumen.

2.5.8.2 Bitumen

LA-ICP-MS analyses of *Type 5* bitumen inclusions from Copper Pass, (pyro)bitumen from the Union Island shale, and bitumen from the Athabasca Basin are summarized in Table 6, and metal concentrations (Group III) for the *Type 5* inclusions from Copper Pass are plotted in Figure 18 in box-whisker format. Figure 19 shows a representative LA-ICP-MS transient signal for a *Type 5* inclusion.

Unlike *Type 1* inclusions for which independent salinity determination provides an internal standard, quantification of bitumen inclusions posed a challenge. The inclusions are composed of a dense hydrocarbon phase and the presence of elements other than C and H (not quantifiable by LA-ICPMS) could only be estimated independently (semi-quantitatively) through SEM-EDS analyses. SEM-EDS data (mapping and spectra) of *Type 5* inclusions shows that elements such as U, S, Ca, As, Fe and Ni are present in very high concentrations (wt% level), otherwise their main X-ray lines would not be detectable by EDS as the method has a widely recognized routine detection limit around the 0.1 wt% level. Quantification of LA-ICP-MS background-corrected count rates utilized the 'total oxides" routine in the program SILLS accounting for the sum of all analytes measured by LA-ICP-MS. Based on semi-quantitative SEM-EDS analyses, this constraint was set iteratively between 5 wt% and 50 wt% with the remaining mass assumed to be C+H. Using U, As, and Ni as examples, the 5 wt% total oxides constraint resulted in concentrations calculated using SILLS on the order of 10^2 ppm, 10^1 ppm, and 10^1 ppm, respectively. The 50 wt% total oxides constraint resulted in concentrations an order of magnitude higher for each element. The reported

data for the bitumens in Table 6 and Figure 19 is based on this 50 wt% total oxides constraint. Importantly, this is likely to be still an underestimate as the secondary X-ray peaks for these metals appear to be large and, for the purposes of comparing bitumens from Copper Pass to other bitumen compositions in other ore-forming systems, the relative concentrations of different trace elements are not impacted by changes in assumed quantification constraints.

Type 5 inclusions demonstrate a significant enrichment in Ca and the ore metals Co, Ni, Fe, As, Ag, Bi, Pb, Sb, and U, all (conservatively) in the 10^2 to 10^3 ppm range (U may reach up to 10^4 ppm in some inclusions). Sulfur, and the metals Cu and Mo are in the 10^4 range. Other elements reported include the REE, Zn and Au, all in the low ppm to 10^1 ppm range. Notably, and of significance to the interpretation of FMA vein formation, the FMA metals Co, Ni (detection limits in brines very high), Ag, Bi, and U are much higher in the bitumens than in early *Type 1* (brine) inclusions. The exceptions to this are As and Sb which appears to be present in the brine phase at comparable concentrations to the bitumen. The rare earth element (REE) concentrations of bitumen demonstrate a flat bell-shaped pattern where LREE << MREE > HREE and a small Eu anomaly is present (Fig. 26).

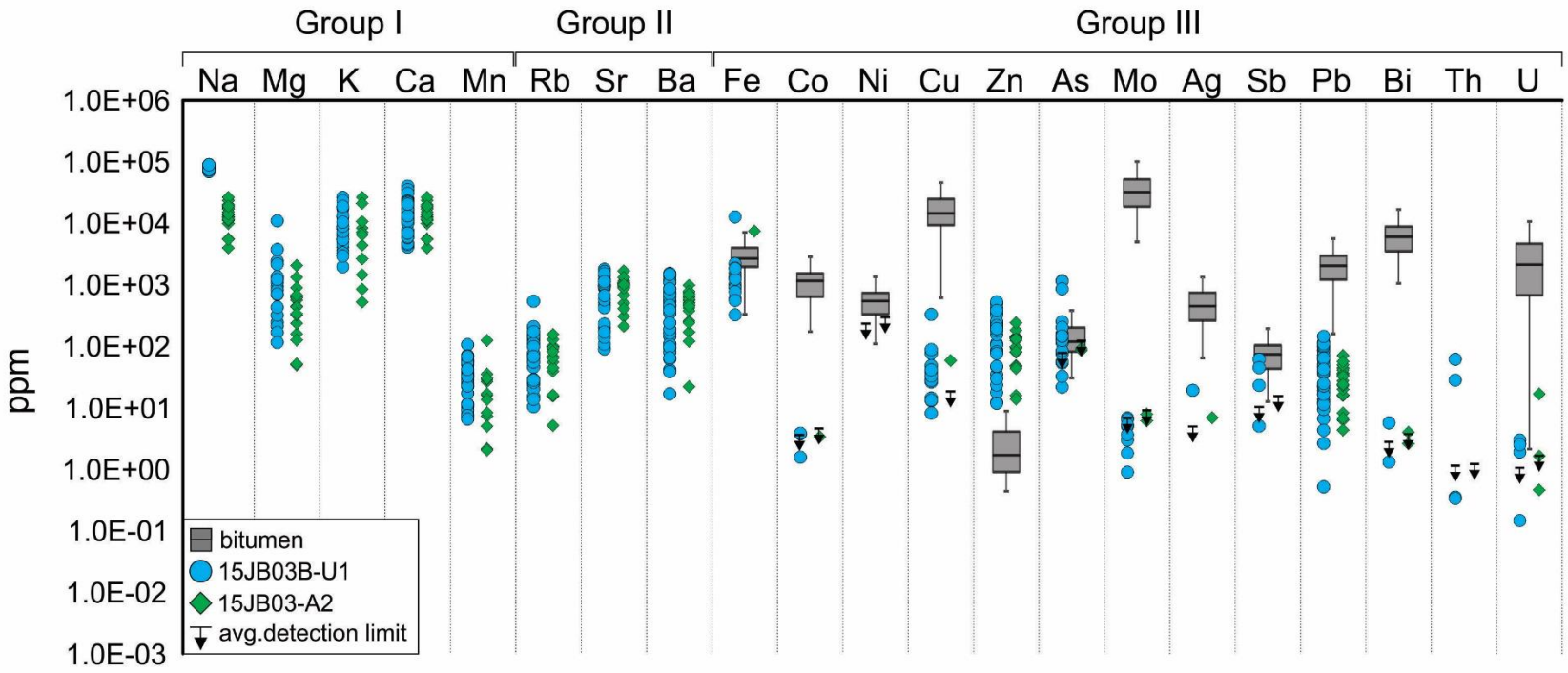

Figure 18 – **LA-ICPMS data summary showing measured concentrations (ppm) of major cations (Group I), minor cations (Group II), and and ore metals (Group III) in quartz-hosted brine (L_{aq}+V) and bitumen inclusions from early quartz in a mineralized (nickeline-rich) vein at Copper Pass.** Concentration data are shown for all inclusions analyzed in quartz crystals on both vein margins (sample 03-A2, in contact with aplite; and sample 03B-U1 with delaminated aplite and synkinematic carbonate vein). For metals in fluid inclusions, the average detection limit based on all fluid inclusions falling below detection limit is shown as a line and downward arrow. Metal concentrations in bitumen inclusions in growth zones in quartz are also shown as box-whisker plots (min, 1st quartile, median, 3rd quartile, max). Bitumens exhibit a metal-rich signature relative to brines.

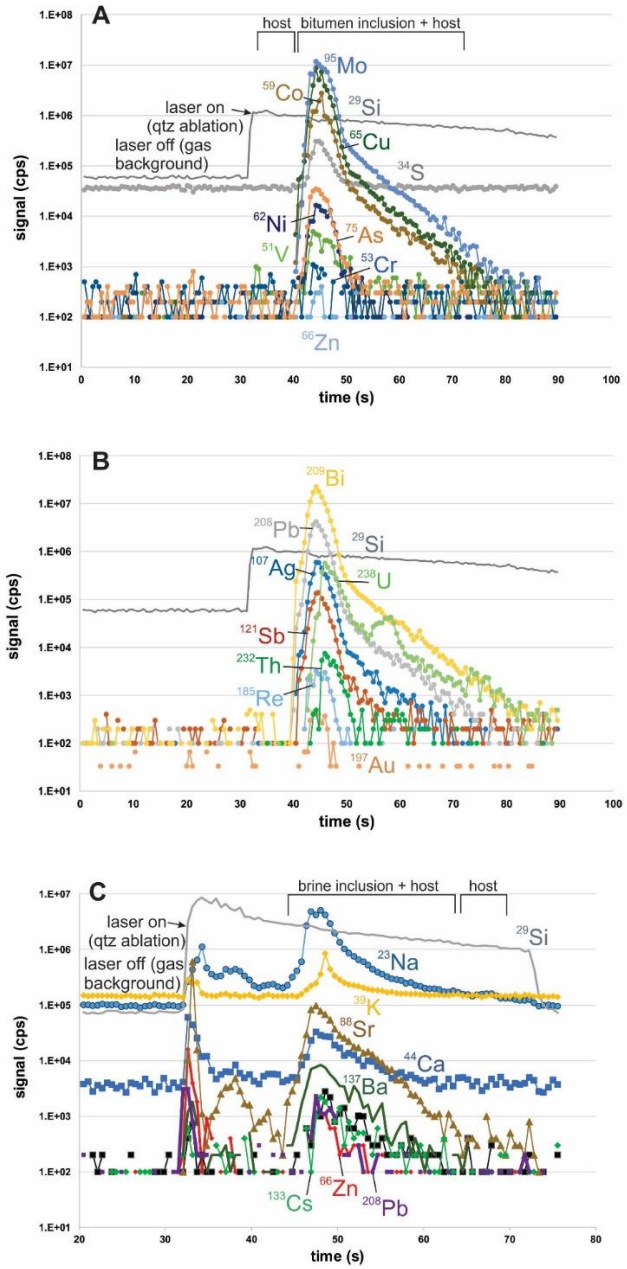

Figure 19 - LA-ICPMS transient signals (counts per second vs. time) for ablations of bitumen (A-B) and brine (C) inclusions. A-B) Transient signal for a 20 um diameter bitumen inclusion in quartz showing the same inclusion ablation in A and B, but different measured isotopes. A background interval is collected (laser off) for ~30s. The laser is turned on and the bitumen inclusion is intersected at ~40s at a depth of 10 um below the quartz wafer surface. The signals in A and B show all isotope count rates rising and falling synchronously, suggesting homogeneous distribution throughout the bitumen inclusion. **C)** A transient signal for a 20 um diameter brine (L+V) inclusion, showing a ~30s interval of background (laser off; only time interval between 20 and 30s shown) and some surface contamination when the laser is switched on. The brine inclusion is well resolved, intersected at ~43s, a depth of 15 um below the surface.

2.5.8.3 Carbonate

Complimenting analysis of the mineralizing fluids and bitumen chemistry, microanalysis of late carbonates (ferroan dolomite hosting *Type 1* inclusions) at Copper Pass were completed and summarized in Table 7. Carbonates (ferroan dolomite) demonstrate a bell shaped REE pattern, where LREE<< MREE > HREE, along with an Eu anomaly (Fig. 26A).

2.5.9 Stable O and C, and radiogenic Sr isotope composition of vein carbonates

2.5.9.1 Carbonate bulk oxygen and carbon isotopes

Oxygen and carbon isotope compositions were determined for 15 samples of microdrilled bulk vein carbonate (Fe-dolomite) from FMA mineralization at Blanchet Island and Copper Pass and are summarized in Table 8. Ferroan dolomite and calcite in cobaltite-safflorite veins at Blanchet Island has $\delta^{13}C_{VPDB}$ values between -2.73‰ to –2.02‰ (avg. -2.49‰, n=4) and $\delta^{18}O_{VSMOW}$ values between 12.06‰ to 13.46‰ (avg 12.99‰, n=4). Ferroan dolomite in nickeline-carbonate vein and breccias at Copper Pass has $\delta^{13}C_{VPDB}$ values between -4.06‰ to -1.13‰ (avg. -2.54‰, n=6) and $\delta^{18}O_{VSMOW}$ values between 10.85‰ to 16.24‰ (avg 13.28‰, n=6). A single analysis from FMA vein carbonate from the Labelle Peninsula veins has a $\delta^{13}C_{VPDB}$ value of 0.19‰ and a relatively high $\delta^{18}O_{VSMOW}$ value of 18.69‰. For comparison purposes, vein carbonates from the Rabbit Lake (Athabasca Basin) U deposit occurrence were analyzed, yielding $\delta^{13}C_{VPDB}$ values between -5.08‰ to -4.16‰ (avg. -4.50‰, n=4) and relatively high $\delta^{18}O_{VSMOW}$ values between 21.1‰ to 24.4‰ (avg. 22.7‰, n=4).

2.5.9.2 In-situ oxygen isotopes (SIMS) of early vein quartz

In-situ oxygen isotope compositions were obtained for 117 spots within the 7 different growth zone types in comb-textured quartz lining a nickeline-carbonate vein-aplite dyke contact at Copper Pass. Owing to textural complexity of the growth zoning, SIMS spot positioning was guided using detailed CL maps (ie. Fig. 11) combined with transmitted and reflected light petrography to ensure that single analyses could be tied to a specific growth zone. Data for growth zones in 6 quartz crystals are summarized in Table 9. Core zones A, B, and C have $\delta^{18}O_{VSMOW}$ values ranging from 3.9‰ to 7.4‰ (avg. 5.1‰, n=5), 4.0‰ to 10.4‰ (avg. 6.6‰, n=17), and 3.9‰ to 20.2‰ (avg 8.7‰, n=21) respectively. Transitional zones D1, D2, D3 exhibiting very bright CL luminescence have $\delta^{18}O_{VSMOW}$ values of 5.2‰ to 12.3‰ (avg. 9.9‰, n=20), 6.8‰ to 14.2‰ (avg 9.5‰, n=7), 5.2‰ to 22.6‰ (avg 15.5‰, n=14), respectively. The outermost rim (zone E) has $\delta^{18}O_{VSMOW}$ values of 6.7‰ to 22.6‰ (avg 16.4‰, n=33). Analyses highlight a systematic shift to higher $\delta^{18}O$ from core to rim. In particular, the transition from D2 to D3 shows an increase in the average $\delta^{18}O_{VSMOW}$ value of 6.5‰ coinciding to the textural position of primary, metalliferous bitumen inclusions.

2.5.9.3 Carbonate radiogenic Sr isotope data

Ratios of $^{87}Sr/^{86}Sr_{o,}$ representing values corrected for negligible radiogenic ingrowth using the Rb concentrations determined for the carbonates by solution ICP-MS, were determined for 15 samples of FMA vein carbonate from Blanchet Island, Copper Pass, Labelle Peninsula (East Arm) and vein carbonate from Rabbit Lake (Athabasca Basin) and are summarized in Table 8. Ferroan dolomite from Blanchet Island veins has $^{87}Sr/^{86}Sr_o$ ratios from 0.709655 to 0.710387 (avg. 0.7100±0.000064; 2σ, n=4). Ferroan dolomite of Copper Pass veins has $^{87}Sr/^{86}Sr_o$ ratios from 0.708093 to 0.719578 (avg. 0.7117±0.0011; 2σ, n=6). A single analysis of late carbonate at

Labelle Peninsula yields an $^{87}Sr/^{86}Sr_o$ value of 0.711159±0.000046 (2σ). For comparison, vein carbonate from Rabbit Lake has $^{87}Sr/^{86}Sr_o$ ratios from 0.708156 to 0.709081±000046 (avg 0.7084±0.000046; 2σ, n=4).

2.5.10 K-U-Th scintillometry

Radioactivity mapping (K-U-Th; concentrations equivalency derived from activity) mapping was carried out *in situ* in the field on mineralized veins at Copper Pass and are summarized in Table 10. Uranium values (scintillometer activity equivalent concentrations) for in situ veins at Copper pass reached levels up to 232 ppm U along vein-aplite margin, weakening into the country rock (Figure 2F). Assays yielded values up to 116.7 ppm U, with low levels ranging from 7.9 to 19.9 ppm U for Copper Pass. Samples collected from Blanchet Island were insignificant, with less than 10 ppm U, with the exception of a float sample, containing 86.4 ppm U.

2.6 Discussion

This study integrates field observations, petrography, microthermometry, Raman spectroscopy, LA-ICP-MS analysis of inclusions, and stable and radiogenic isotope composition of gangue minerals. These data provide new insight into the chemical composition and evolution of hydrothermal fluids as they relate to ore formation, and help constrain ore formation conditions, the origin of ore fluids, and source of ore metals.

2.6.1 Timing and paragenesis of FMA mineralization in the East Arm basin

2.6.1.1 Constraints on the relative and absolute age of mineralization

The age of FMA vein formation at Copper Pass and Blanchet Island relative to major rock types in the study area can be established at the outcrop scale by cross-cutting relationships. At Blanchet Island, mineralization is hosted in the Blanchet Formation of the Pethei Group (Great Slave Supergroup; 1.90-1.87 Ga; van Breeman et al., 2013) where veining is parallel and crosscuts bedding. The Compton Intrusive Suite monzonite occurs as a sill and topographically overlies the mineralization and intrudes the Pethei Group carbonates, providing a maximum FMA vein age, as mineralization does not crosscut the monzonite (due to competency). It is important to note that this relationship is limited by field exposure. It is reasonable to assume veins do not crosscut the monzonite as high fluid P would be required, inconsistent with low P conditions estimated for similar FMA veins at Copper Pass. At Copper Pass, mineralization is hosted within the Yellowknife Supergroup where veining crosscuts amphibolite and aplite dykes (Fig. 3G), providing a maximum vein age of 1.89 Ga. In the southern portion of the Slave Craton, FMA veins occur within the Caribou Lake gabbro and along the contact with the gabbro and the Hearne Channel granite, providing a maximum FMA vein age of ~2.18 Ga. Based on cross-cutting relationships at the three localities, a maximum age of 1.86 Ga is proposed for FMA veins in the East Arm basin.

Determining an absolute age of FMA vein formation is problematic due to absence of dateable minerals as noted in studies at Cobalt-Gowganda, Ontario (Marshall et al., 1985). Uraninite appears to be the only potentially dateable ore mineral for these mineralization styles. However, owing to its late remobilization (Fig. 7 I-K) and trace abundance, reliable age determination for

the primary FMA mineralizing event using U-Pb systematics analyses seems unlikely. It is most likely that U-Pb dating of uraninite would provide a minimum age as regional isotopic resetting of U-Pb isotopes has been reported in the region, related to orogenic or magmatic events at ~1.4 Ga (LeBlanc et al., 2014; Ghandi et al., 2018).

Occurring along growth zones in early stage quartz, U-rich bitumen in *Type 5* inclusions provides a potentially datable phase. Bitumen inclusions were isolated as droplets/particles along growth zones, possibly preventing Pb loss or gain during metamorphism. Alexandre and Kyser (2006) dated ancient bitumen successfully in the Athabasca basin. However, due to the insignificant quantities at Copper Pass an in-situ method (e.g., via SIMS) would need to be developed to provide an absolute age.

Looking at similar FMA systems (Ni-Co arsenides/sulfarsenides + U) in the NWT, veins from the Port Radium district provide a much higher grade-tonnage possible analog to deposits in the East Arm basin. The Port Radium FMA veins at the Eldorado deposit crosscut the Cleaver dyke swarm with a U-Pb baddeleyite age of 1.74 Ga and are crosscut by the 1.59 Ga Western channel diabase (Ghandi et al., 2018). The maximum age constraints for FMA veins in the East Arm basin, described above (between ~1.86 and ~1.4 Ga) agree broadly with the age bracket for the Eldorado deposit.

2.6.1.2 Paragenetic sequence of FMA veins

The complexity of textures seen at the study areas at multiple scales makes it difficult to establish the timing of individual ore minerals and so key groups of mineral species (and the textures they showed in association with other groups) were used to establish a paragenetic sequence involving multiple mineralization periods and stages. Petrographic observations (ore and

gangue minerals, inclusion timing) from mineralized veins at Blanchet Island and Copper Pass are summarized in a paragenetic sequence in Figure 20. The vein systems have been assigned early, main and, late development periods with the main development period further broken down into 4 stages. Ore minerals precipitated only within the 4 stages of the main vein development period, whereas gangue minerals may have formed throughout all development stages. Additionally, a barren stage (quartz-only with *Type 1* inclusions) is reported for Copper Pass, and a post-mineralization stage involving weathering (surficial) of Co and Ni phases to produce annabergite and erythrite is also documented in the paragenesis (but not discussed below).

2.6.1.1 Barren (pre-vein) stage and early vein period

These are characterized by early quartz and minor ferroan dolomite formation at Copper Pass but are not observed at Blanchet Island.

2.6.1.2 Main vein period, stages 1 and 2 - Arsenides

In these stages, mineralization begins with the formation of Ni-Co arsenides, as nickeline and safflorite-nickeline at Copper Pass and Blanchet Island, respectively. These minerals occur as massive clumps, botryoidal nodules or "blooms" within veins and vein breccias and are the primary ore minerals. As the system evolves, the As:Ni and As:Co ratios of the arsenides increases as seen by the precipitation of Ni and Co di/triarsenides (e.g., rammelsbergite, skutterudite). Rammelsbergite can be found sharing grain boundaries with nickeline (Fig. 5H) but also replacing, or (rarely) being replaced by nickeline (Fig. 6A, D). Skutterudite clumps are rimmed by of cobaltite and nickeline is rimmed by gersdorffite, reflecting an increase in S:As ratio. The increase in S marks a transition from the arsenide to sulfarsenide stage. In the ore assemblages, arsenides and sulfarsenides exhibit strongly zoned crystals, with dissolution-reprecipitation and compositional

zoning/rimming demonstrating disequilibria and significant changes in conditions or fluid composition with time. It is possible that some carbonate gangue is coprecipitated throughout these stages based on its occurrence both prior to and after these stages, as well as at the very end of Stage 2.

2.6.1.3 Main vein period, stage 3 - Sulfarsenides

In the sulfarsenide stage, an enrichment in S is recognized at the edges of arsenides where rims of Ni-Co sulfarsenides occur (Fig. 5A, 6C). Cobalt arsenides are rimmed by Co-sulfarsenides (cobaltite) exclusively, as Ni arsenides are rimmed by Ni sulfarsenides (gersdorffite). Independent of other controls, Ni-dominated sulfarsenides at Copper Pass may have crystallized at lower temperature than the Co-dominated sulfarsenides at Blanchett Island (Fig. 7). Carbonate gangue starts to precipitate at this stage, first coprecipitated with sulfarsenides (along quartz grain boundaries at Copper Pass) and mainly later, infilling and cementing spaces between arsenides and sulfarsenides (Fig. 5A, C, E, F, I).

2.6.1.4 Main vein period, stage 4 - Base metal sulfide and native Bi

Following the formation of sulfarsenides, base metal sulfides and trace native metal (Bi) grow in the veins in the final stage of mineralization. Brecciated arsenides and sulfarsenides from stages 1-3 are crosscut by pyrite veinlets and fracture infill (Fig. 5D). Native Bi precipitates along with trace sulfide minerals chalcopyrite, galena, and molybdenite and uraninite. These minerals occur as inclusions and fracture infillings in arsenides and sulfarsenides (Fig. 6 C,D,H). Bismuth and molybdenite is found associated with nickeline and gersdorffite, while uraninite and galena are

strictly associated with nickeline (Fig. 6I-K) and skutterudite (Fig. 5I-J, Fig. 6L). Carbonates continue to coprecipitate with base metal sulfides and native Bi.

2.6.1.5 Late vein period

The final stage of the mineralized vein stage consists of the precipitation of more hydrothermal carbonate (ferroan-dolomite and calcite at Blanchet Island, and ferroan dolomite at Copper Pass). Remaining porosity in the arsenide-sulfarsenide veins is filled in with carbonates, and secondary carbonate veins (i.e., at Copper Pass; Fig. 3) form along earlier vein margins delaminating older wall rock contacts.

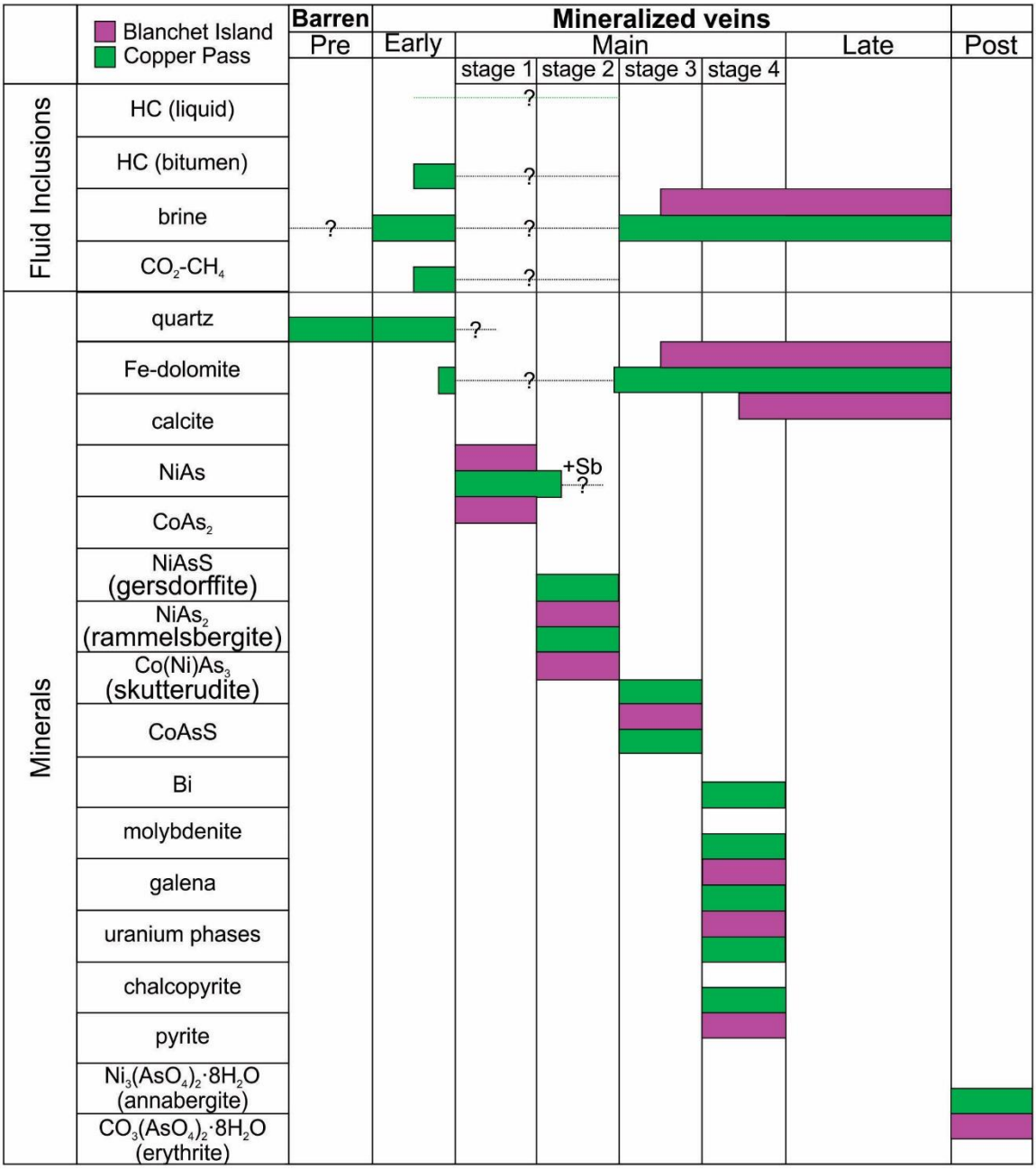

Figure 20 – Paragenetic sequence polymetallic Ni-Co-Bi-Ag-Sb-As-U veins including fluid inclusion and ore mineralogy of cobalt-dominated veins at Blanchet Island (pink) and nickel-dominated veins at Copper Pass (green) polymetallic veins. Dashed lines suggest implied phases (lacking physical record for specific vein stage) based on petrographic evidence. Solid bars indicated that phases were observed in various petrographic stages.

2.6.2 Comparison of FMA mineralization in the East Arm basin and Southern Slave province

As noted by Badham (1975) the chemistry and mineralogy of FMA veins can be extremely variable, and so the documentation of similarities between different deposits suggests kinship. Although separated by nearly 100 km, and hosted in very different host rocks, Blanchet Island, Copper Pass (and other showings in the East Arm basin) are remarkably similar with respect to ore and gangue mineralogy, paragenetic sequence, metal tenors enrichments and depletions (e.g., absence of significant U and Ag), fluid characteristics (bulk salinity/T_h), stable O-C, and radiogenic Sr isotope characteristics. The similarities in paragenesis and metal enrichments have already been described above in some detail. In particular, mineralizing fluids in each deposit were very similar with respect to their T_h and salinity characteristics. Figure 21A summarizes fluid inclusion salinity-T_h for all *Type 1* inclusions at Copper Pass and Blanchet Island showing close overlap. The majority of data for both deposits ranges from ~20-23 wt% $CaCl_2$ equiv. and ~100-220^{o}C. This range does not include anomalously high T_h excursion at Copper Pass resulting from post-entrapment modifications of few inclusions, and an excursion to lower salinity by some inclusion FIA at Blanchett Island (unexplained).

Volatile species including CH_4-CO_2 and H_2 are present in fluid inclusions from both localities (Figs. 14, 15) and while more complex hydrocarbons (e.g., oil, bitumen) were not observed in inclusions from Blanchet Island, an unusual trace, zoned uranium phase within carbonate containing enrichments in Ni, Co, and As was observed (Fig. 5K, L) and are remarkably similar to the metalliferous *Type 5* bitumen inclusions in growth zones within early quartz at Copper Pass. Figure 22 summarizes stable O and C, and radiogenic Sr isotope data for carbonates at Blanchet Island, Copper Pass, and FMA veins in the Caribou Lake Gabbro, illustrating consistency in these parameters between the two occurrences.

Differences in the mineralogy of FMA veins at Copper Pass and Blanchet Island include: (i) some variations in paragenesis (i.e., absence of some minerals, or differences in the timeline of occurrence for specific minerals); (ii) the domination of Ni phases at Copper Pass (mainly nickeline) vs. Co phases at Blanchet Island (mainly safflorite); (iii) the presence of early quartz at Copper Pass, and calcite at Blanchet Island; (iv) the absence of a base metal stage at Copper Pass (e.g., no pyrite); (v) accessory minerals: a greater abundance of late stage uraninite, and the presence of native bismuth and molybdenite, at Copper Pass, and the presence of an unidentified, late stage uranium phase with a polymetallic composition (U-Ni-As-Si-Fe-V-Ti) (similar to *Type 5* inclusions) at Blanchet Island. The Blanchet Island and Copper Pass deposits also differ in their host rock compositions. At Blanchet Island, veins are hosted in sedimentary carbonate rocks of the Pethei group (Utising Formation), where Copper Pass veins are hosted in metavolcanics and metasediments of the Yellowknife Supergroup, and older intrusive (aplite) rocks of Archean age.

Figure 21 summarizes fluid inclusion data for FMA veins in the Caribou Lake gabbro (LeBlanc et al., 2014) and carbonate-pyrobitumen veins cross-cutting the Union Island bituminous shale occurring east of Blanchett Island (Figure 1; fluid inclusion data from P. Ramlochund, communication, 2018). Brine inclusions from FMA veins in the Caribou Lake gabbro yielded a similar range in T_h as at Copper Pass and Blanchett Island, from 112^o to 185.5^{o}C, but with bulk salinities slightly higher, ranging from 23.4 to 25.7 wt% $CaCl_2$ equiv. Union Island brines (in carbonate) share similar T_h and salinities (though a wider range) with Blanchett Island and Copper Pass, ranging from 139.4 to 228.6 ^{o}C and from 14 - 25.1 wt. % $CaCl_2$ equiv. While only base metal sulfides are present in veins in the Union Island shale, it is proposed that based on fluid inclusion microthermometry and proximity to the other FMA veins that the fluids are related to the FMA veins.

The remarkable similarities between 3 (possibly 4) East Arm basin FMA localities suggests that these mineralized zones formed in small enclaves as parts of a much larger (FMA vein systems occur over a minimum of a ~20 x 50 km area), relatively thermally and compositionally homogeneous hydrothermal system. Furthermore, critical to any argument concerning the source of metals for FMA veins is the observation that despite different host rocks, local variability in host rocks appears to not have had a significant impact on vein characteristics at each locality, reinforcing the idea of a common and distal fluid and metal source.

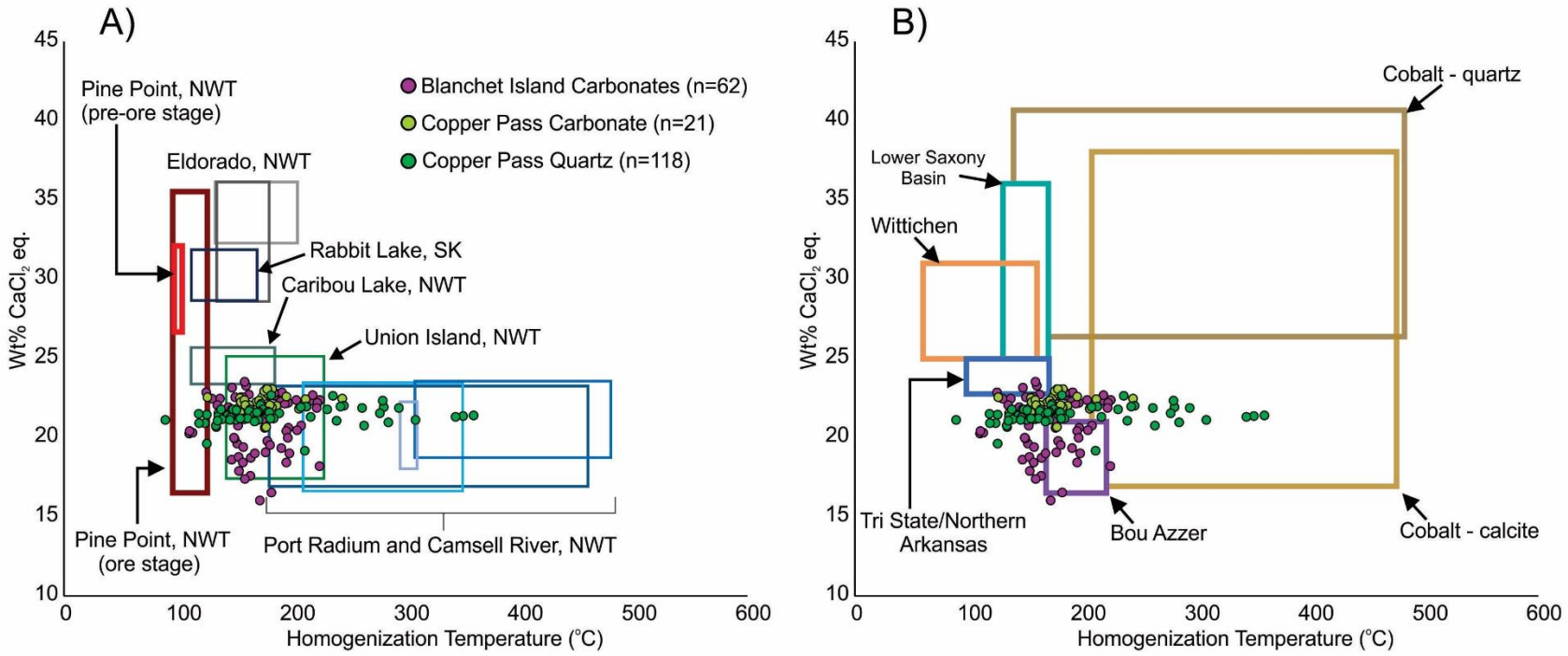

Figure 21 - Comparison of T_h-salinity data for brine inclusions at the Blanchet Island and Copper Pass vein systems with other relevant regional and global polymetallic FMA vein systems. **A)** Comparative fields from FMA vein deposits in the study area and those occurring regionally including the Port Radium and Camsell River districts (including the Eldorado Mine; Chankakoti et al., 1986b), Eldorado mine (C. Trottier, unpublished M.Sc. thesis, 2018), and within the Caribou Lake Gabbro in the Southern Slave Province, north of Blanchet Island (LeBlanc et al., 2014). Also shown are data for quartz-carbonate-pyrobitumen-sulfide veins hosted in the Union Island shale (P. Ramlochund, communication, 2018) and data for the Pine Point MVT deposit (Hannigan 2007). **B)** Comparative fields from FMA veins in the study area, and for FMA and relevant sediment-hosted deposits found globally including Bou Azzer (En Naciri et al., 1997), Cobalt (Kerrich et al., 1985), Lower Saxony Basin, Germany (Luders et al., 2012), Tristate/Northern Arkansas MVT deposits (Stoffell et al., 2008) amd Wittichen Ag-Bi-Co-Ni-U deposit (Staude et al., 2012) are plotted.

2.6.3 Comparison to other relevant regional and global deposit examples

2.6.3.1 Regionally

Located in the northwest region of the Northwest Territories at Great Bear Lake, high grade FMA vein deposits containing major Ag and U are found in the historic Camsell River and Port Echo Bay (including Port Radium) regions of the Great Bear Magmatic Zone. Importantly, unlike the East Arm basin FMA veins, the multitude of deposits in the Great Bear Lake region are consistently very enriched in Ag (and in one example, at the Eldorado deposit, very high U; Gandhi et al., 2018 and references therein) and showing a more extensive established vein paragenesis including productive U, Ag and base metal (Cu-Pb-Zn) stages. Fluid inclusion studies in these deposits are limited. Changkakoti et al. (1986b) provided the most extensive data set, constraining a wide range in T_h for early vein stages between ~180 to 480^{o}C, with a narrower range in salinities from ~17 to 24 wt. % $CaCl_2$ equiv. (Fig. 21A). Unpublished data (C. Trottier, communication, 2018) indicates that both the T_h and salinity data reported by Changkakoti is erroneous, owing to failure to recognize post-entrapment modification (leading to T_h values that are too high) and the presence of hydrohalite during microthermometric investigations (leading to salinity values that are too low). Figure 21A shows the revised ranges in data for the Eldorado deposit (C. Trottier, unpublished data), overlapping in T_h with the East Arm basin FMA deposits, but with much higher salinities between 28 and 36 wt% $CaCl_2$ equiv.

Other potentially relevant data for comparison to the East Arm basin FMA veins summarized in Figure 21A include data for the Pine Point Mississippi Valley-Type (MVT) deposit, NWT (T_h = ~100^o to 130^{o}C, salinity ~16 to 35 wt% $CaCl_2$ equiv.; Hannigan, 2007), and for brines within syn-U quartz-carbonate-hematite veins (T_h = ~100^o to 160^{o}C, salinity ~28 to 32 wt% $CaCl_2$ equiv

from the Rabbit Lake U deposit, Athabasca basin, Saskatchewan (G. Hodge, communication, 2018).

Stable O and C isotope data from the Echo Bay area deposits (Robinson and Ohmoto, 1973) for carbonates coeval with, and postdating, arsenide mineralization (Fig. 22) shows overlap between the postdating carbonate and similar late carbonate at Copper Pass and Blanchet Island.

2.6.3.2 Globally

Other world-class Canadian high-grade FMA vein deposits are located in the historic Cobalt-Gowganda district, Ontario. Unlike East Arm deposits, these are high-grade Ag deposits, associated with Ni-Co sulfarsenides. Fluid inclusions present in gangue minerals consist of 3-phase (liquid-vapour-halite) and 2-phase (liquid-vapour) inclusions with T_h values varying widely from 139.3 to 482.5 ^oC, and bulk salinities also varying widely from 16.9 to 42.1 wt. % $CaCl_2$ equiv. (Kerrich et al., 1985; Marshall and Watkinson, 2000 and authors therein; Fig. 21), extending to much high T and salinity than observed in the East Arm FMA veins. Raman spectroscopy (Marshall and Watkinson, 2000) did not identify volatile species (CO_2, H_2S, CH_4, N_2, and higher order hydrocarbons) associated with fluid inclusions in the East Arm FMA deposits. However, like the late carbonates in the deposits of the Great Bear Lake region, O and C isotope values for late carbonates in the Cobalt-Gowganda camp also overlap with those from the East Arm basin deposits.

Other relevant fluid inclusion T_h-salinity data sets for FMA-style deposits globally are summarized in Fig. 21, as well as MVT deposits (Bou Azzer: En Naciri et al., 1997; Lower Saxony

Basin, Germany: Luders et al., 2012; Tristate/Northern Arkansas MVT deposits: Stoffell et al., 2008; Wittichen Ag-Bi-Co-Ni-U deposit: Staude et al., 2012). Fluid inclusion microthermometry from the Odenwald FMA deposits, SW Germany (Burisch et al., 2016) yielded very similar ranges in T_h and salinity compared to the East Arm basin FMA veins. Furthermore, they reported similar volatile species in fluid inclusions.

2.6.4 Constraints on fluid and ore metal sources

2.6.4.1 Fluid sources

Fluid characteristics in the East Arm basin FMA veins were determined through microthermometry and LA-ICPMS analysis of *Type 1* inclusions and can be used to constrain the origin of the brines. The brines are highly saline (~18-24 wt% $CaCl_2$ equiv.), ore metal-poor, and contain minor abundances of multiple salt cations (K, Ba, Sr, Mg, Pb, Zn) in addition to the dominant Na and Ca (Table 5, Fig. 18). Fluid inclusion compositions analyzed by LA-ICP-MS were plotted on a range of devised ternary plots with the goal of comparing FMA fluids at Copper Pass with other relevant fluid reservoirs (Fig. 23) including crystalline basement brines (Munz et al., 1995; Hanley et al., 2005), sedimentary basin brines (including oil-field and MVT-type fluids: Carpenter et al., 1974; Stoffell et al., 2004), and brines from U deposits in the the Athabasca Basin (Richard et al., 2010; J. Hanley, communication, 2018), and geothermal fluids in the Salton Sea basin (Williams and McKibben 1989), produced by active metamorphism of sediments. The Ba*10-Sr-Mg ternary (Fig. 23A) demonstrates that Copper Pass brines share characteristics of Ba enrichment noted in crystalline basement brines from Norway and Sudbury, as well as geothermal brines from the Salton Sea. Barium (in addition to Sr and Ca) will be extracted from feldspars during fluid-rock interaction in basement rocks and or through the introduction of a basement-derived fluid formed by long-term water-rock interaction in crystalline rocks (Frape et al., 1984),

but is not typically enriched in basinal fluids (Richard et al., 2010). In Figure 23A, *Type 1* brine inclusion analyses lie near the Ba apex but appear to trend outward towards the Mg apex, with several analyzed inclusions showing significant Mg enrichment (up to 10^3 ppm; Table 5). Notably, fluids from the Athabasca Basin basement hydrothermal system at various U deposits lie near the Mg apex as do some MVT fluids, with Mg originating from evaporated seawater in those environments. The Ba*10-(Sr+Rb)-(Pb+Zn*10) ternary (Fig. 23B) demonstrates that Copper Pass brines lie close to, or overlap with, Athabasca Basin basement brines as well as Norway basement brines. The Ca/100-Sr/5-Ba and Ca*10-Na-Mg*100 ternary diagrams (Fig. 23C-D) show a similar result to the other diagrams: compositional range spanning between the fields for basinal brines and basement brines.

Stable O-C and radiogenic Sr isotope data for gangue minerals at Copper Pass are in support of a basinal fluid component present in the FMA hydrothermal system at the time of mineralization. For example, mineralizing fluids at Blanchet Island and Copper Pass (using the $^{87}Sr/^{86}Sr_o$ composition of hydrothermal carbonates as a proxy; Fig. 24) show a narrow range in Sr isotope composition and are only slightly more radiogenic that Paleoproterozoic seawater (est. at ~1.6 Ga; Veizier et al., 1989) and Athabasca sandstone (Pagel et al., 1993) but are much less radiogenic that would be expected if fluids derived Sr from interaction with metavolcanics in the study area (Fig. 24). Furthermore, while interaction of fluids with the Pethei carbonate host rock at Blanchet Island may be appealing to explain the isotope systematics observed, O, C, and Sr isotope data for the Pethei formation (Fig. 22) are distinct from the vein carbonates in the FMA deposits.

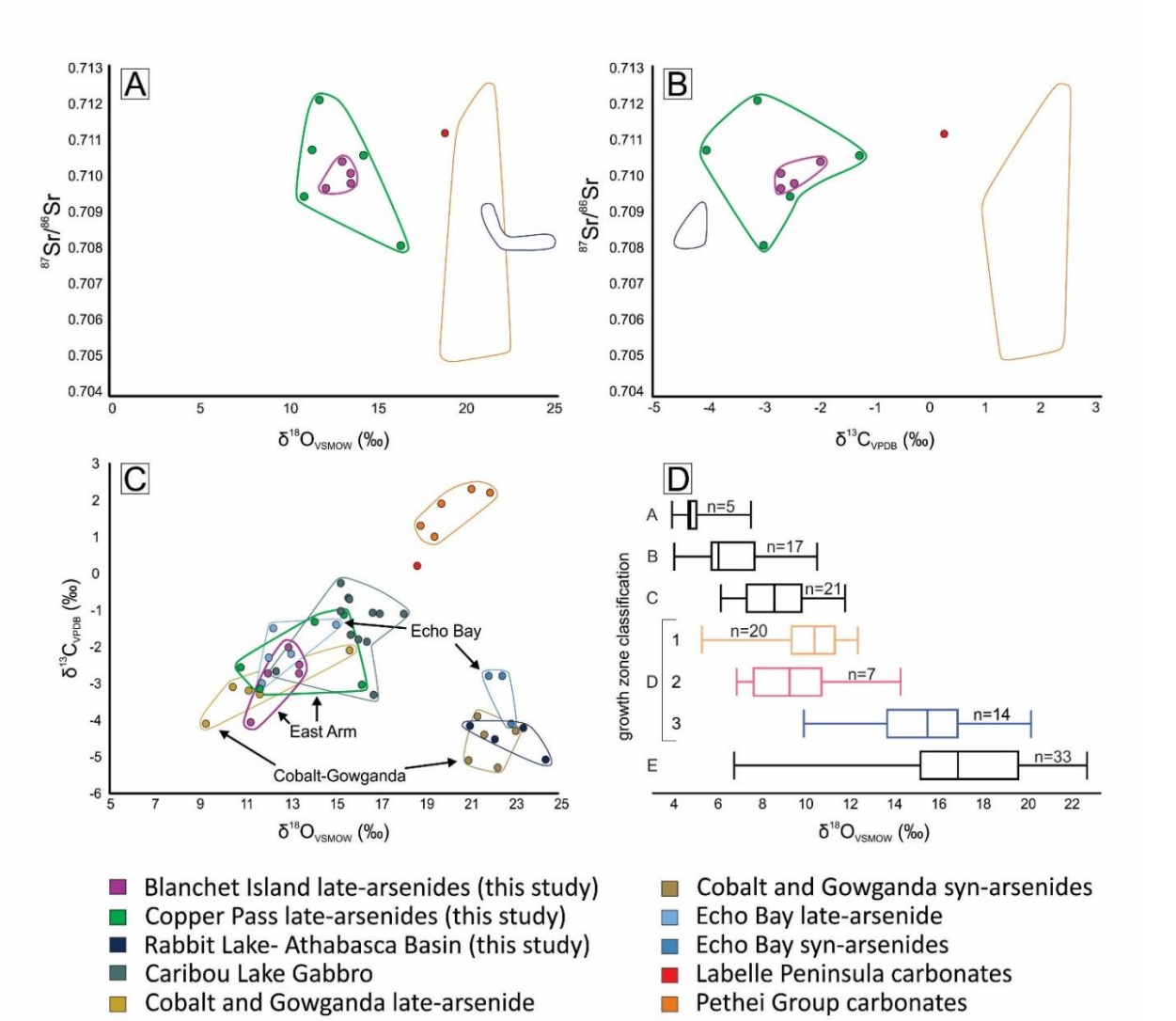

Figure 22 - Comparative isotope (Sr, O and C) diagram of East Arm deposits and Canadian polymetallic deposits from carbonate gangue. **A)** $^{87}Sr/^{86}Sr$ vs $\delta^{18}O_{VSMOW}$ (‰). **B)** $^{87}Sr/^{86}Sr$ vs $\delta^{13}C_{VPDB}$ (‰) **C)** $\delta^{13}C_{VPDB}$ (‰) vs $\delta^{18}O_{VSMOW}$ (‰). Polymetallic deposits and relative carbonate stages consist of Caribou Lake Gabbro (Leblanc 2014), Cobalt and Gowganda (Marshall et al., 1985) Deposits, Echo Bay (Robinson and Ohmoto 1973), Labelle Peninsula carbonates (this study), Pethei group carbonates (Whittaker et al., 1998). D) Box-whisker plot showing oxygen isotope compositional ranges (min, Q1, median, Q3, max) for growth zones in early euhedral quartz along margins of mineralized vein from Copper Pass, determined using secondary ion mass spectrometry (SIMS) targeted at zones identified through hot-cathode CL imaging. The number of analyses obtained for each zone classification is listed. Note the marked increase in $\delta^{18}O$ from core through to rim, in particular in the transition from zone D2 to D3. Colours of box-whisker symbols for zones D1-D3 correspond to colour of key transitional zones shown in Figure 10 and do not correspond to the caption colours in the legend below this figure.

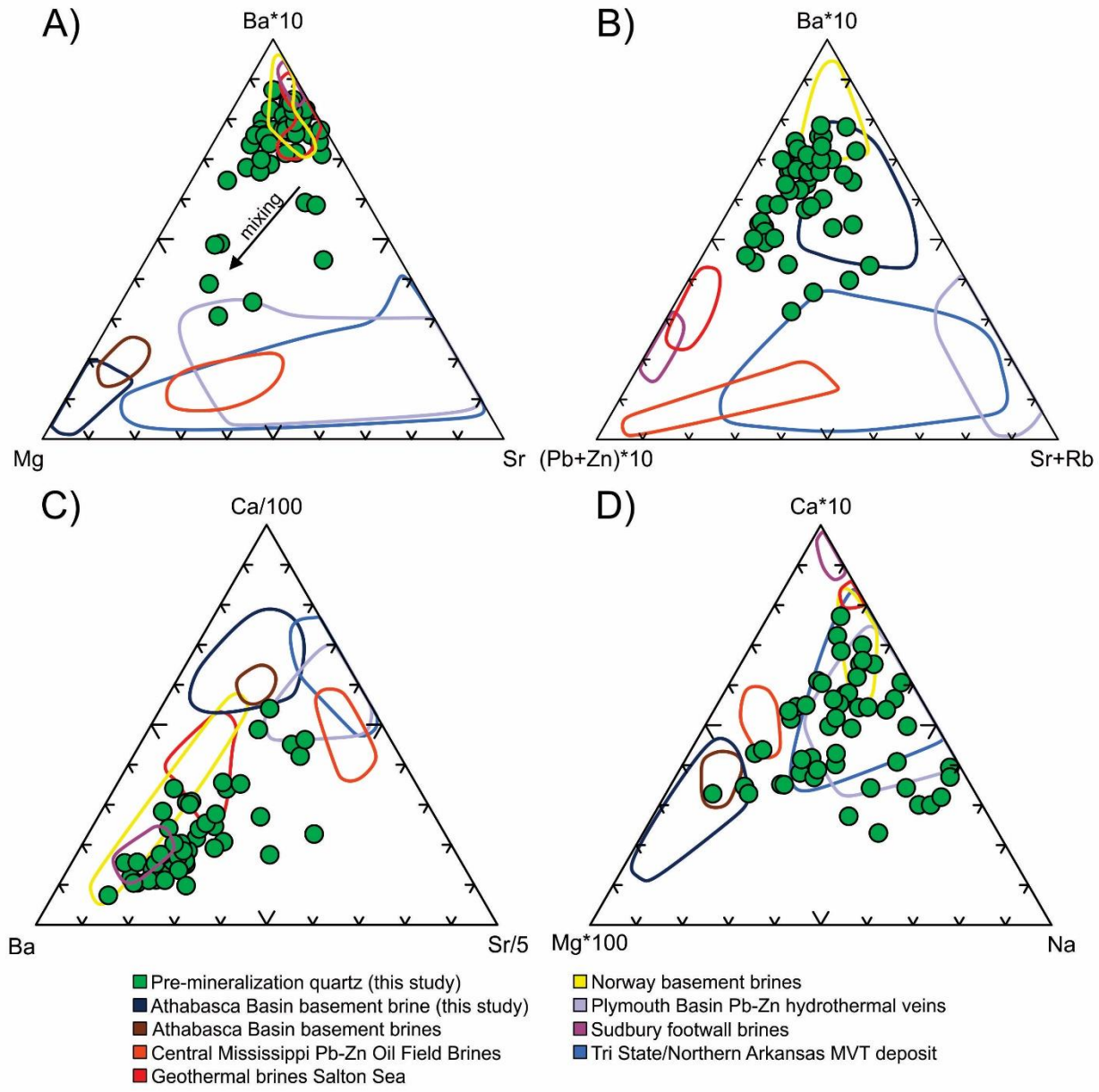

Figure 23 - Ternary plots of A) Ba*10-Mg-Sr; B) Ba*10-(Pb+Zn)*10-(Sr+Rb); C) Ba-Ca/100-Sr/5; and D) Mg*100-Ca*10-Na for *Type 1* fluid inclusion major and minor element compsitions comparing relevant fluid reservoirs to FMA vein fluids. Sedimentary deposits consist of the Plymouth Basin Pb-Zn hydrothermal veins (Stoffell et al 2004), Tri State/Northern Arkansas MVT deposit (Stoffell et al., 2008), Central Mississippi Pb-Zn oil field brines (Carpenter et al 1974), Salton Sea geothermal brines (Williams and McKibben, 1989), Norway basement brines (Munz et al., 1995), Athabasca Basin brines (Richard et al., 2010) and Sudbury footwall brines (Hanley et al., 2009).

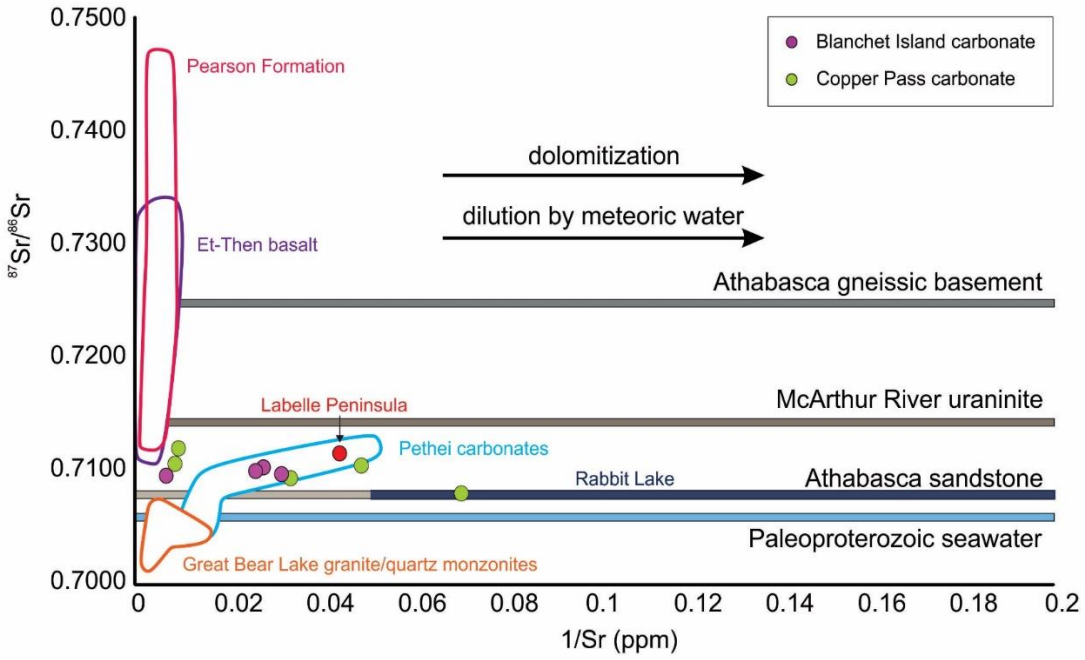

Figure 24 – **Plot of $^{87}Sr/^{86}Sr_{(o)}$ vs. 1/Sr comparing East Arm basin FMA vein carbonates to relevant rock units of the East Arm basin and Great Bear Magmatic zone, NWT** as well as basement, uraninite, carbonate and sandstone compositions from the Athabasca Basin. Rock units illustrated include Et-Then Formation basalts (Gandhi and Loveridge 1982), Great Bear Lake granite/quartz monzonites (Ootes et al., 2017), Labelle Peninsula carbonate (this study), Pearson Formation basalts (Goff et al., 1981), and Pethei group carbonates (Whittaker et al., 1998). Sedimentary basin analogues include Athabasca gneissic basement and Athabasca sandstones (Pagel et al., 1993), McArthur River uraninite (Fayek and Kyser 1997), and Paleoproterozoic seawater (Veizer et al., 1989). Data for carbonates from Rabbit Lake (Athabasca Basin) are reported in Table 8.

2.6.4.2 Metal sources

The results of LA-ICPMS analyses show that *Type 1* inclusions have low ppm-range concentrations of metals present in FMA veins at Copper Pass (e.g., Co, Ni, Ag, Bi, Mo, U) and ~10^2 ppm As. Bitumen grains are the proposed metal carrier for polymetallic veins owing to their high concentrations of metals relative to brines. Studies of bitumen composition (Parnell, 1988; Hurlbert, 1996; Alexandre and Kyser 2006; Johnson et al., 2017 and others therein) have demonstrated that bitumens are known to metal loads, including Co, Ni, Ag, Pb, Fe, Zn, and U. Parnell (1988) highlights that such metals occur as an intrinsic component of bitumens that are either (i) inherited from the hydrocarbon source rock as organometallic complexes (Poplavko et al., 1978; organophilic elements include elements such as V, Ni, Mo, and Se); (ii) scavenged by migrating hydrocarbon-bearing fluids, or (iii) deposited in the bitumens at the site of mixing of a metal-bearing and hydrocarbon-bearing fluids (Roberts, 1980). Additionally, as highlighted by Saxby (1976), there are five potential modes of interactions between dissolved metals and organic bitumens (bitumen and source rocks) that would result in the mobilization, or immobilization of ore metals including: (i) chemisorption of metals into organic materials, (ii) physical adsorption of metals onto organic materials, (iii) precipitation of organometallic compounds by reaction of metals with organic ligands, (iv) the change in oxidation state, resulting in reduction of metals by organic materials and consequent mineral precipitation, and (v) mobilization of metals by the formation of organometallic complexes and subsequent deposition of ore minerals after destabilization. Changkakoti and Morton (1987) proposed that Precambrian biota could play an important role in silver-bearing FMA vein associations, stating that potential source rocks include carbonaceous sedimentary rocks such as black shales, coals, and crude oil-bearing strata. Their "black shale metal association" (V, Cr, Mn, Co, Ni, Cu, Fe, Mo, Ag, Pb, U, Se, S, and As) is very

similar to enrichments seen in the *Type 5* inclusions and unidentified uranium carriers at Blanchet Island. Changkakoti and Morton (1987) further illustrate that organic fractions in sediments are responsible for the generation of polymetallic associations and could be the source for metals concentrated in FMA veins in the Great Bear Lake region. However, no direct comparison has been made thus far between the metal tenors of black shales and the actual ores. Hahn et al. (2013) illustrates the correlation of Late Paleoproterozoic basins of northern Canada, including the Thelon, Athabasca, and Hornby Bay basins. These basins contain organic mudstones (some of which are oil-bearing) which provide a possible source rock analogue for organic shale-associated FMA metals and hydrocarbons (oil, bitumen).

Metal enrichments in bitumen inclusions at Copper Pass provide insight into the relationship between East Arm FMA deposits and the possible source of hydrocarbons in the overlying units of basinal sediments (Athabasca, Hornby Bay and Thelon basins analogous). Due to the lack of bitumen geochemical analyses for analogues from Hornby Bay and Thelon basins, bitumen from the Athabasca Basin was used for comparison (Table 6, Fig. 25). Bulk rock geochemistry of Copper Pass shares many similarities with bitumen from Copper Pass, with comparable concentrations in Fe, Co, Sb, Au, and Bi. Elements enriched in bitumen are Cu, Mo, U, Ag, and Pb. Note that Pb values found in bitumen may be elevated partly as a product of radioactive decay of U. Metals Cu and Mo are enriched in bitumen compared to bulk rock chemistry. The reasons for this are unknown, but it may be related to the S-deficient nature of the ore forming system, preventing precipitation of these metals as sulfide as bitumens became oxidized, except for in trace quantities, as observed. Athabasca Basin bitumen share enrichments in Ni, As, Sb, Pb, and U with Copper Pass and highlighting the potential genetic relationship between the two. Shales of the Union Island group, another possible source unit for metals can be ruled out as remobilized

bitumen from those rocks are enriched in Ni, but contain very low concentrations of other FMA metals (Co, As, Sb, Bi, U; Table 6, Fig 25) due to their insufficient concentrations of FMA metals Co, As, Sb, Bi, and U.

The rare-earth element (REE) patterns for carbonates and bitumen from Copper Pass, Union Island and the Athabasca Basin are summarized in Tables 6 and 7 and plotted in Figure 26. Analysis of REE patterns are key for a definition of meaningful genetic model (Mercadier et al., 2011). Bitumens and carbonates of Copper Pass share REE patterns with Athabasca Basin bitumen characterized by a bell-shaped LREE<< MREE > HREE pattern, similar to uraninites of the Athabasca unconformity-related U deposits noted by Mercardier et al. (2011) and Ghandi et al. (2018). Comparing carbonate of Union Island shales with Copper Pass carbonate demonstrates similar characteristics with less inflection and vertical extent in LREE and contains a positive Eu anomaly. As a potential source rock, carbonate REE and bitumen metal chemistry demonstrates that the Union Island group shales are not a potential source rock for FMA deposits in the East Arm. Copper Pass carbonates also share REE patterns similar to bitumen, suggesting carbonate precipitation occurred following the breakdown of bitumens.

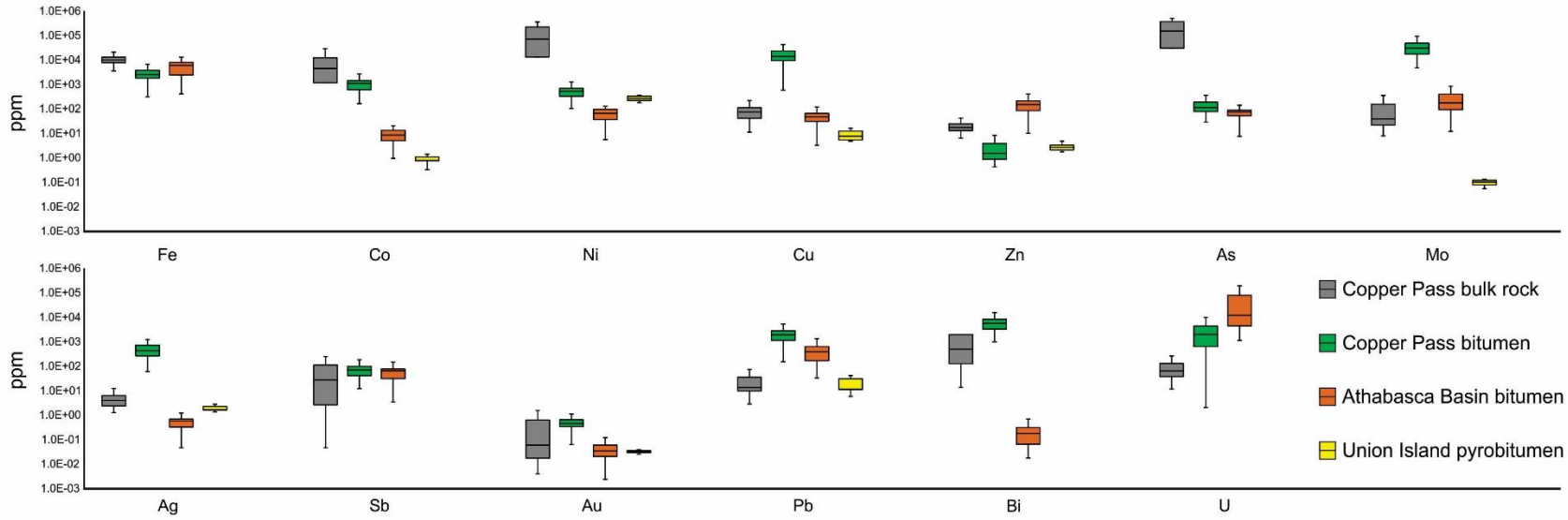

Figure 25 – **Box-whisker plot summarizing FMA ore metal contents bitumens and bulk mineralization.** Data for bulk mineralized veins at Copper Pass are from Table 1 (this study). Data for *Type 5* (bitumen) inclusions from Copper Pass (analyzed in this study), bitumen from the Athabasca Basin (analyzed in this study; samples from P. Alexandre, communication, 2016) and pyrobitumen from hydrothermal veins in the Union Island shale (analyzed in this study; samples from H. Falck, communication, 2016) are listed in Table 6. Elements not reported for Union Island locality (Fe, As, Sb, Bi, U) were below detection limits (see Table 6 for detection limits).

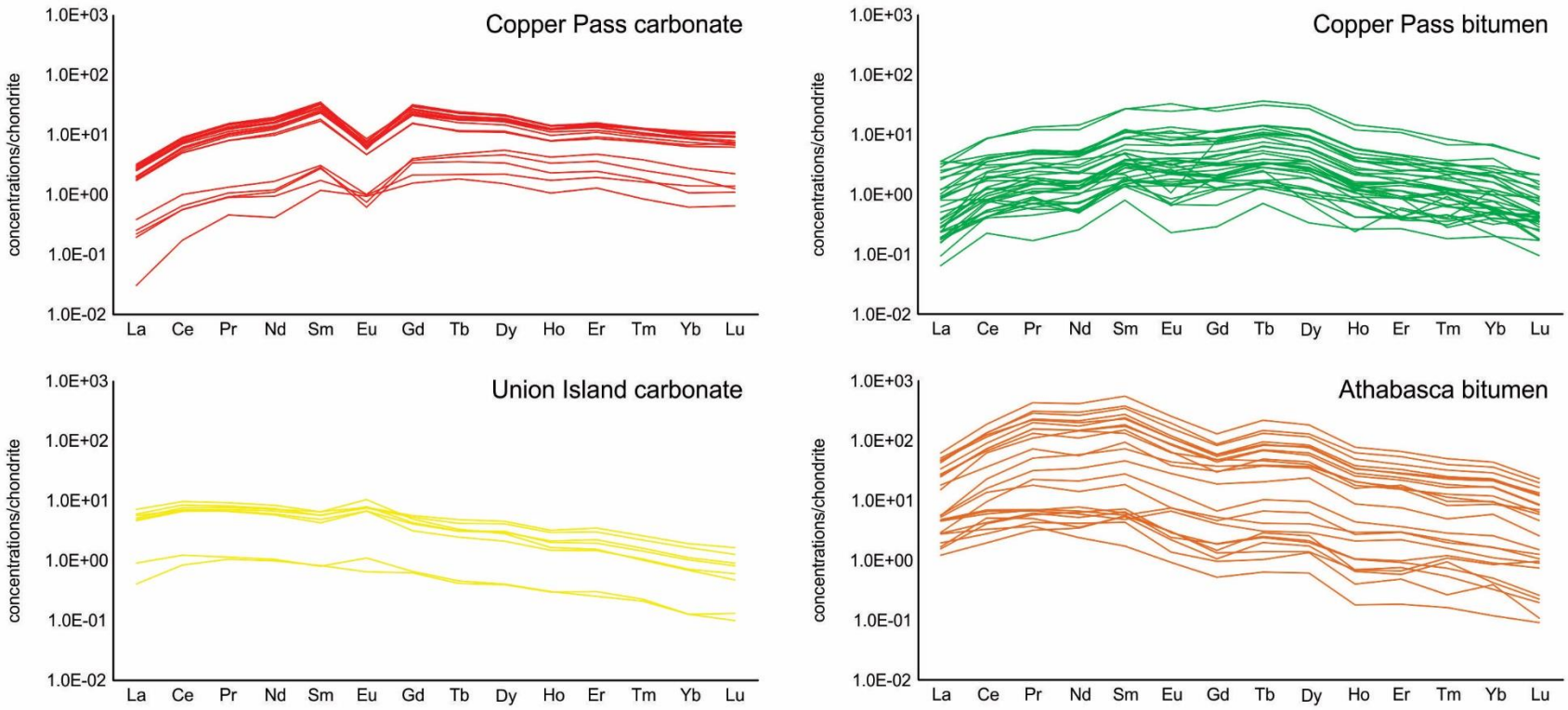

Figure 26– Normative abundance diagrams (unnormalized) comparing rare earth elements (REEs) of bitumen and carbonate gangue of Copper Pass with Union Island carbonate (this study) and Athabasca Basin bitumen (Alexandre and Kyser 2006).

2.6.5 Estimates of P-T conditions for FMA vein formation

There are numerous lines of evidence providing qualitative and semi-quantitive constraints on the P and T conditions of vein formation at Blanchet Island and Copper Pass. First, classic open-space filling mineral growth textures (comb-textured quartz with carbonate infilling; colliform and crustiform, botryoidal, and radiating masses of zoned arsenide-sulfarsenide minerals with carbonate infilling) within veins and breccias are characteristic of FMA veins globally as well as other deposit styles (e.g., MVT) and are associated with very shallow crustal conditions, confirmed independently for FMA vein systems by fluid inclusion studies (e.g., < 700 m paleodepth at Cobalt-Gowganda; Marshall et al., 1993).

Second, the presence of coeval bitumen and liquid hydrocarbons in some primary and secondary FIA in the veins at Copper Pass restricts vein deposition to low T. *Type 1* inclusion FIA showed T_h values between ~120-250^{o}C with few outliers above and below this range (Fig. 13; Table 4). This would imply not only that brine FIA heterogeneously trapped coevally with hydrocarbons were trapped not far above their homogenization temperatures (and therefore not far above P_h) but that any interaction between brine and hydrocarbons that took place in the East Arm basin at the time of FMA vein formation took place very close to the maximum thermal stability of oils/bitumens and methane (~180^{o}C and ~230^{o}C; Price, 1993; Dieckmann et al. 2002). Furthermore, in the absence of any significant P fluctuations during vein formation, the relatively consistent T_h values during different stages of vein formation (early quartz → vein infilling carbonate) indicates invariant fluid T. This is an important observation as it is inconsistent with the findings of Changkakoti et al. (1986b) who interpreted very high temperatures (up to ~450-500^{o}C) from microthermometric results for early stages of FMA vein formation I the Great Bear

Lake deposits (cf. Kissin, 1992), but consistent with modelling assumptions of Robinson and Ohmoto (1973).

Coeval carbonic (*Type 3*) and aqueous (*Type 1*) fluid inclusions in sample SL-M-1-2 from Copper Pass provides an opportunity to more accurately constrain the P-T conditions of vein formation using the method of intersecting isochores (Roedder and Bodnar, 1980; Mullis, 1987) as these inclusions satisfy several criteria: (i) FIA of each end-member most commonly occur in separate secondary inclusion trails that transect one another (Fig. 9A-C) but with unambiguous evidence of periodic heterogeneous entrapment (Fig. 9D); (ii) each end-member (carbonic and aqueous) did not arise from unmixing of a previously homogeneous single fluid phase, rather they correspond to the mixing of fluids from differing external sources; (iii) the inclusion types have measureable properties allow determination of their respective end-member isochores.

Consistent with microthermometric determination of $T_m^{carbonic}$, Raman spectroscopy analysis showed that *Type 3* inclusions in the measured assemblages (Table 4) contain a maximum X_{CH4}=0.05 with the majority of the carbonic phase as CO_2 ($X_{CO2} >$ 0.95) content in carbonic inclusions, with the majority of inclusions containing ~pure CO_2. The absolute range of resulting isochores for *Type 1* and *Type 2* inclusion FIA are shown in Figure 25 (red field 'F') constraints an entrapment window between ~145 and 225 ^oC and 0.5 to 0.95 kbar, representing the most accurate P-T constraint for vein formation that can be provided with available data in this study. This P-T range lies in the lower T portion of the isochore field for quartz-hosted fluid inclusions at Copper Pass (field 'E' in Fig. 27; 1st to 3rd quartile range from Table 4), in agreement with the statement that brine and hydrocarbon interaction would have taken place below but close to T condition sof maximum hydrocarbon stability. For comparison, also shown in Figure 27 is the maximum T_h value for fluid inclusions containing basinal brine in uraniferous sandstones of the

Athabasca basin (line 'D'; Richard et al., 2010), the maximum stability boundary for the assemblage rutile-carbonate-quartz at low X_{CO2}, an alteration assemblage observed in the margins of FMA veins in the Caribou Lake Gabbro by LeBlanc et al. (2014), and the fluid inclusion entrapment conditions for the main FMA vein stages at Eldorado deposit (Port Radium, Great Bear Lake; Changkakoti et al., 1986b).

The PT constraints described above have important implications for FMA vein formation in the East Arm basin. First, it confirms existing literature that the systems form at relatively shallow depths (in this case < 1 kbar). Second, the systems formed at low temperature (around the HC stability window). Third, a comparison of the P estimate for Copper Pass (0.5-0.95 kbar) with estimated lithostatic and hydrostatic pressures at different times in the development of the large, early-mid Proterozoic intracratonic sedimentary basins (Fig. 27; Athabasca, Thelon, Hornby Bay) provides insight into the possible timing of FMA vein formation relative to basin development, as critical sources of brine, hydrocarbons, and ore metals.

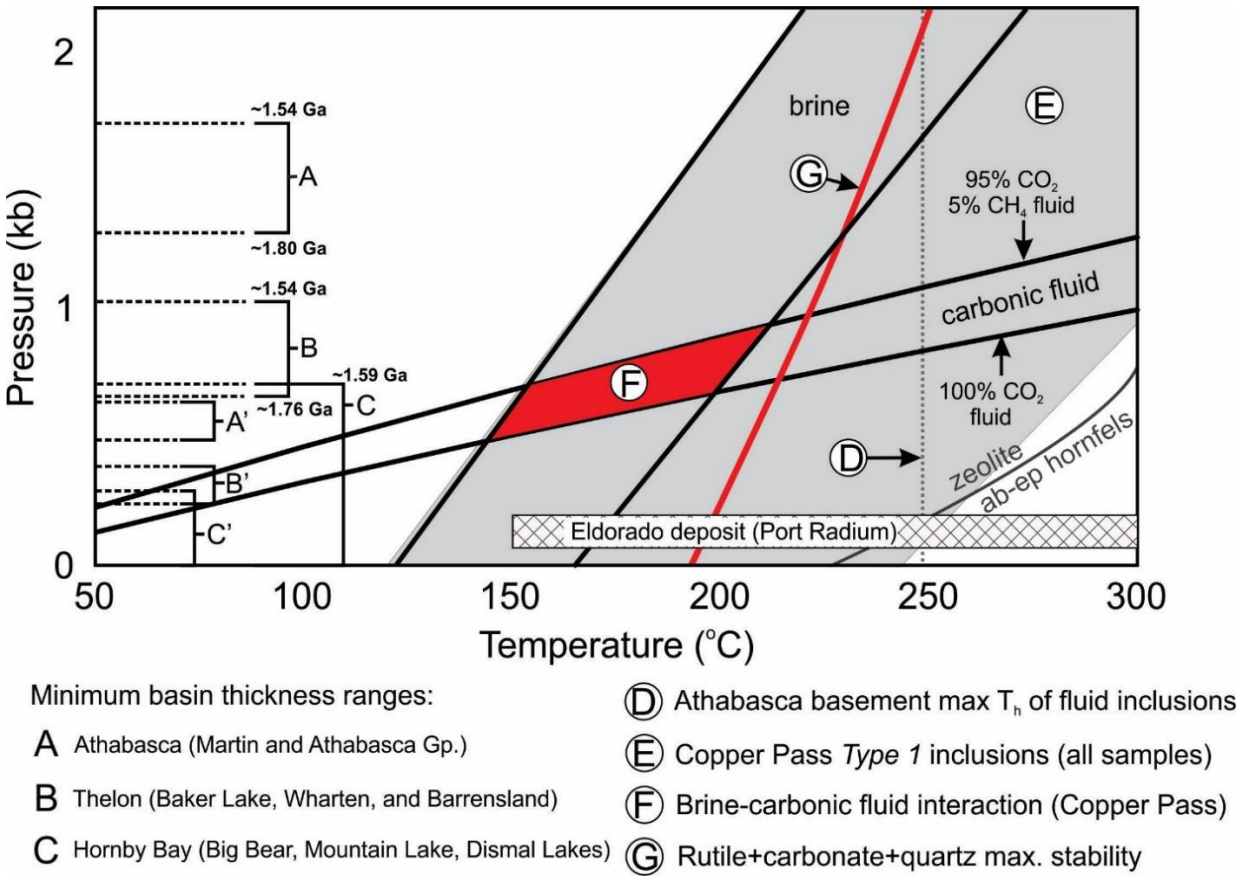

Figure 27 – Graphical estimation of trapping conditions for quartz-hosted, bitumen-free *Type 1* and *Type 3* inclusion assemblages at Copper Pass (sample SL-M-2-1). Fields and ranges identified by letters as follows: Ranges A-C are lithostatic pressure windows for minimum ranges in thickness of intracratonic basins, as analogues for those covering the study area. Pressures calculated based on stratigraphic thicknesses of the accumulating Martin and Athabasca Groups between ~1.80 and 1.54 Ga (Athabasca basin), the Baker Lake, Wharten and Barrensland Groups between ~1.76 and ~1.54 Ga (Thelon basin), and the Big Bear, Mountain Lake and Dismal Lakes Groups before ~1.59 Ga (Hornby Bay basin). Basin thickness data from R. Rainbird (communication, 2017) and Hahn et al. (2013). Ranges A'-C' are hydrostatic pressure windows for the same minimum basin thicknesses as for A-C. Line D is the maximum T_h reported for broadly syn-U brine inclusions in mineralized sandstones at the McArthur River U deposit (Athabasca basin; Richard et al., 2010). Field E is the total range in calculated isochores for *Type 1* brine inclusions at Copper Pass for all FIA. Field F is the range in *absolute* trapping conditions estimated for *Type 1* and *Type 3* secondary inclusion assemblages in quartz in sample SL-M-2-1, determined using the method of intersecting isochores. The field is defined as the intersection of maximum and minimum isochores for end-member brine FIA and carbonic FIA, ranging between ~145 and 225 ^{o}C and 0.5 to 0.95 kbar. Line 'G' the phase boundary between the assemblages rutile-quartz-carbonate and titanite (Castelli et al., 2007) for aqueous fluids with low dissolved CO_2 content (*Type 1 brines*), drawn from LeBlanc et al. (2014) who recognized rutile+carbonate rather than titanite in the alteration margins of FMA veins in the Caribou Lake gabbro, providing a maximum T constraint for the alteration assemblage.

Lithostatic and hydrostatic ranges in overburden P for the basins at different stages in their development were estimated using stratigraphic sections (Hahn et al., 2013; R. Rainbird, communication, 2017; lines A to C-lithostatic; lines A'-C'-hydrostatic in Fig. 27). As FMA veins at Copper Pass formed below the unconformity level (i.e., below sedimentary basin-crystalline basement interface), the P for inclusion entrapment (field 'F') reflects either the overlying mass of crystalline basement + sediment (lithostatic), or equivalent depth of fluid (hydrostatic) if the mineralizing fractures were behaving as open systems, or some intermediate scenario (i.e., lithostatic basement load + hydrostatic depth through the sediment column, or transient lithostatic-hydrostatic load coinciding to fault movement). Both P extremes of this situation can be considered. At purely lithostatic conditions (A-C; Fig. 27.), the estimated range of fluid entrapment P would only be achieved if the overlying load resulting from an unknown thickness of crystalline basement had a thin sediment column overtop, consistent with the Hornby Bay basin at an early stage in its evolution. At this time, thicker basin sequences like the Athabasca and Thelon basins would have imposed overlying lithstatic P loads that were too high to be consistent with the fluid inclusion entrapment window estimated. Alternately, if conditions were hydrostatic, or transitioning between hydrostatic and lithostatic conditions, vein formation under such conditions could have taken place at the conditions estimated at Copper Pass with a wide range in overlying basin thicknesses (A'-C'; Fig. 27.).

An accurate estimation of the thickness of sediment directly over the study areas is impossible but this exercise simply illustrates a concept that through comparison of hypothetic sediment loads in relation to estimated P of entrapment, it can be concluded that either overlying sedimentary columns were relatively thin and/or hydrostatic conditions prevailed at the time of vein formation. This lends considerable support to similar models (eg., Changkakoti et al., 1986b; Kissin, 1992;

Kreissl et al., 2018; Gandhi et al., 2018) that implicated meteoric water or seawater as an important fluid end-member during vein formation, and possibility of cyclic faulting events that would encourage a transiently open and interconnected shallow fracture network for deposit development (Markl et al., 2016; Burisch et al., 2016). The data for P conditions at Copper Pass also illustrates that deposits in the East Arm basin formed at considerably greater P than in the Great Bear Lake region (Fig. 27.), regardless of lithostatic or hydrostatic load.

2.6.6 A revised model for FMA vein formation in the East Arm basin and elsewhere

Existing models for FMA veins at Great Bear Lake are varied, with some authors favouring Aphebian magmatic intrusive and volcanic rocks as sites for ore vein localization as well as heat and metalliferous fluid sources (Badham, 1975) arguing that the FMA veins are the low temperature products of a continuum of mineralization styles deposited over a temperature gradient away from cooling intrusions, over multiple/repeated stages of structural preparation at the close of an orogenic cycle, beginning with high temperature sulfide skarns and IOCG-type deposits that are spatially related to FMA veins. Gandhi et al., (2018) have revisited the U-Pb geochronology, O isotope and REE composition of uraninite at the Eldorado deposit (Port Radium) demonstrating temporal and compositional kinship of the early uranium mineralization stage at Port Radium to basement-hosted unconformity-related U deposits in the Athabasca and Thelon intracratonic sedimentary basins, implicating the analogous Hornby Bay Basin.

Models for the formation of FMA vein deposits of the East Arm basin are limited to a single study (Badham, 1978) and their temporal and genetic relationship to larger FMA deposits in the Great Bear Lake region is unknown. On the basis of cross-cutting relations and structural relationship of this style mineralization to intrusive margins, Badham (1978) associated the veins

in the East Arm basin with the release of metals during alteration of mafic minerals in intrusive rocks of the Great Slave supergroup, and that the FMA veins may have some genetic association with later magnetite-apatite-amphibole deposits. Fluid circulation responsible for this alteration may have been related to regional heating by dioritic intrusions emplaced between 1845 and 1630 Ma (Hoffman, 1968) on the basis of cross-cutting relationships (xenoliths of Sosan group sandstone). FMA deposits located outside of the East Arm share similar deposit characteristics, however despite similarities among deposits, elements such as formation temperatures, fluid salinity, host rock and alteration styles, paragenesis, isotope compositions and bulk rock geochemistry can strongly vary between deposits (Kissin 1992; Changkakoti et al., 1986a,b,c; Staude et al., 2012; Markl et al., 2016; Burisch et al., 2016; Kreissl et al., 2018; Ghandi et al., 2018). Many authors have tried to explain the formation of these complex systems based on fluid inclusion or electrochemical agruments. Such arguments summarized by Markl et al. (2016) include iron oxidation (Ondrus et al., 2003), fluid mixing (Marshall et al., 1993), or boiling, and cooling, or a combination of factors (Kissin 1992). Many recent genetic models have been proposed regarding FMA deposits; Kissin (1998) suggests five-element veins form in environments of continuous continental rifting, where connate brines can circulate; Marshall et al. (1993) suggests a decrease of chlorine activity due to the mixture of a highly saline silver-rich fluid with meteoric water, resulting in the deposition of silver and associate arsenide/sulfarsenides. A more recent model proposed by Markl et al. (2016) supports claims of mixing by Marshall et al. (1993), sugging that five-element veins form due to the influx of a methane and/or hydrocarbon rich fluid with a pre-existing hydrothermal system, oxidizing CH_4 to CO_2, resulting in the precipitation of native metals with arsenides in a reducing environment. Bursich et al. (2017) concludes that ascending metal-rich deep-seated basement fluids were mixed closely below the

basement-cover unconformity with basinal/sedimentary fluids. These fluids contained sufficient amounts of methane, where subsequent oxidation of methane results in the precipitation of arsenides at very reducing conditions.

The criteria for the genetic model of FMA formation is based on crosscutting relationships, ore textures, alteration styles, fluid chemistry and isotopic data. Combining these comprehensive methods allows us to propose a model for FMA deposits, in which sedimentary style basement brines mix with metal-rich bitumen and oils, resulting in the abrupt reduction of the oxidized brine resulting in rapid precipitation of Ni-Co-rich arsenides. Oxidization of oils (heating), results in the breakdown into lower hydrocarbons (methane, ethane and propane), creating the necessary reducing agent to disrupt equilibrium, resulting in ore metal precipitation. As noted by Kerrich et al. (1986; Cobalt, Canada) and Burisch et al. (2016; Odenwald, SW Germany), methane and other hydrocarbons are present in fluid inclusions, and are presumed to be the reducing phase to drive metal precipitation (Markl et al., 2016).

Ore forming processes occur at far-from-equilibrium conditions, as highlighted by Markl et al. (2016), due to open space filling ore textures and weak wall rock alteration. Ore precipitation occurs when a hybrid sedimentary-basement brines (metal poor; fluid 1) mixes with a hydrocarbon (oil or bitumen) (metal rich; fluid 2) (Eq. 1).

$$\mathbf{Me_{poor}\ brine + Me(HC)} \quad (1)$$

Hydrocarbons are oxidized, resulting in the breakdown of oils into lower hydrocarbons (i.e methane). Arsenide precipitation can occur in multiple ways; (1) lower hydrocarbons and metal-chloride complexes react with As^{-2} ions to produce arsenides and CO_2 (Eq. 2), and/or through the reaction with metal-chlorides and AsO_3^{-3}, resulting in the production of arsenides and CO_2 (Eq. 3).

$$\mathbf{MeCl_4^{-2} + CH_4 + As^{-2} + 2H_2O = MeAs + 4Cl^- + CO_2 + 4H^+} \quad (2)$$

$$\mathbf{MeCl_4^{-2} + CH_4 + AsO_3^{-3} = MeAs + 4Cl^- + CO_2 + H_2O + 2H^+} \quad (3)$$

The breakdown of methane during mixing to produce CO_2 is evident as carbonate gangue is produced in the form of ferroan-dolomite precipitation (Eq. 4). Presented Raman data demonstrates that methane is present throughout the ore stage as carbonate inclusions contain amounts of methane.

$$\mathbf{Ca(Fe,Mg)Cl_2 + CO_2 + H_2O = Ca(Fe,Mg)CO_3 + 2H^+ + 2Cl^-} \quad (4)$$

Figure 28 shows a proposed model for polymetallic vein formation in the East Arm, NWT. The interpretations of fluid inclusion petrography, microthermometric and LA-ICP-MS data demonstrate that multiple fluids were mixed together to form these FMA ores. As previously highlighted, a highly saline sedimentary bittern (fluid 1) mixes with a hydrocarbon rich fluid (fluid 2) in existing fault-fracture intersections. These fluids use enhanced rock permeability, fractures and joints in an actively forming sedimentary basin, to migrate into the basement and precipitate. The potential of a basement component is highlighted by fluid 3, where heating convection may drive basement fluids into structures, mixing with fluids 1 and 2. Paleoproterozoic seawater infiltrates (step A) through a proposed evaporite sequence, extracting salt cations such as NaCl±K±(Mg,Ca)±Cl (step B) and migrates through the sedimentary basin and into basement rock (step E). As the sedimentary fluid migrates through the basin, added to the fluid is a combination of Ca-Mg-Pb-Zn through extraction from an interstitial bittern. Our sedimentary fluid has evolved into a sedimentary bittern (fluid 1) and infiltrates into the basement

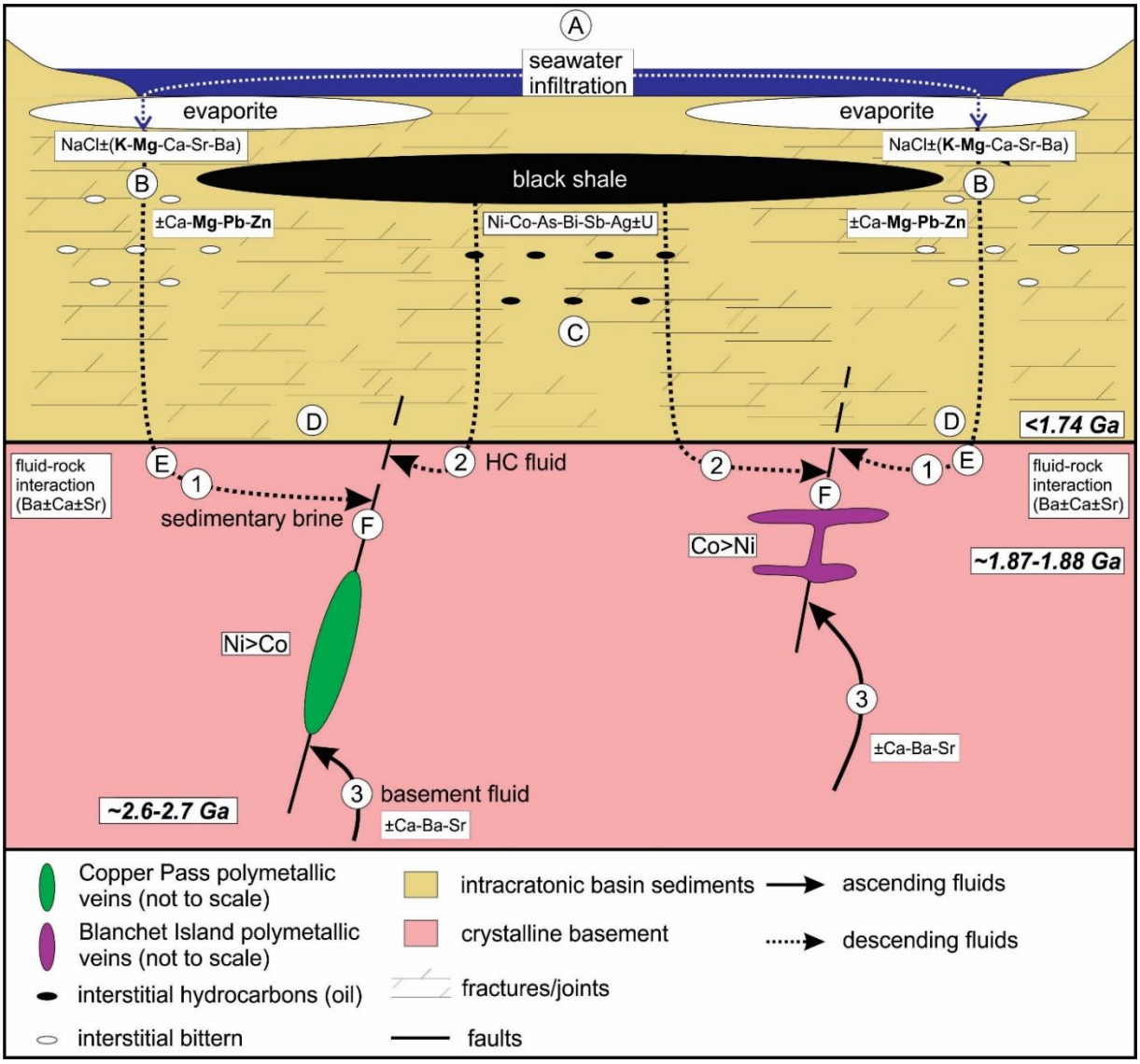
A
seawater infiltration
evaporite
evaporite
NaCl±(K-Mg-Ca-Sr-Ba)
NaCl±(K-Mg-Ca-Sr-Ba)
B
B
black shale
±Ca-Mg-Pb-Zn
Ni-Co-As-Bi-Sb-Ag±U
±Ca-Mg-Pb-Zn
C
D
D
<1.74 Ga
fluid-rock interaction (Ba±Ca±Sr)
E
1
sedimentary brine
2
HC fluid
F
2
1
E
F
Co>Ni
fluid-rock interaction (Ba±Ca±Sr)
~1.87-1.88 Ga
Ni>Co
3
±Ca-Ba-Sr
3
basement fluid
±Ca-Ba-Sr
~2.6-2.7 Ga
Copper Pass polymetallic veins (not to scale)
Blanchet Island polymetallic veins (not to scale)
interstitial hydrocarbons (oil)
interstitial bittern
intracratonic basin sediments
crystalline basement
fractures/joints
faults
ascending fluids
descending fluids

Figure 28 (previous page) - Schematic crustal section consisting of metamorphic and igneous crystalline basement rocks covered by overlying intracratonic sedimentary basin and the role of sedimentary fluids in the proposed genetic model of polymetallic vein precipitation. (A) Seawater infiltration into the sedimentary units (evaporites) through rock permeability and/or fractures/joints. (B) Infiltrated seawater picks up salt cations (Na±K-Mg-Ca-Sr-Ba) from evaporites before extracting interstitial bittern where Ca-Mg-Pb-Zn are added to the fluid, producing a sedimentary bittern (fluid 1). (C) Anoxic black shale units yield a hydrocarbon-rich fluid (fluid 2) that contains metals Ni-Co-As-Bi-Sb-Ag±U and interstitial hydrocarbons (oils) that migrate into the crystalline basement. (D) Basement infiltration through fault/fracture networks. (E) Descending sedimentary fluids penetrate into basement rocks where fluid rock interaction occurs, extracting Ba, Ca and Sr from plagioclase and feldspar minerals. (F) Mixing of fluids 1 and 2 occurs, resulting in precipitation of polymetallic veins. It is important to note that basement fluids (fluid 3) are a potential source of Ca, Ba and Sr as convection (driven by magmatic sources) upwells basement fluids into fault networks.

The hydrocarbon rich fluid (fluid 2) is believed to be sourced from anoxic (black) shale. As highlighted by Morton and Changkakoti (1986), the "black shale association" of metals: Ni, Co, Cu, Fe, Mo Ag, Pb, U, S, and As, along with organic hydrocarbons (oils), are added to the fluid through extraction from a seawater infiltration (step C). This organic-rich fluid migrates deep into the crystalline basement, before interacting with both sedimentary bittern and/or basement fluids.

As both fluids penetrate the crystalline basement, the potential for fluid-rock interaction, introducing Ba±Ca±Sr from feldspars and plagioclase dissociation, is possible (step E). Fluids 1 and 2 infiltrate fault structures where the system rapidly moves to far from equilibrium conditions as fault systems act as extremely efficient geochemical traps, resulting in the precipitation of Ni, Co, Ag, Bi and As (step F) as polymetallic veins (Markl et al., 2016). It is important to note that a potential 3rd fluid from the basement (fluid 3) could migrate through these fault networks, through convection, acting as a potential source of Ca-Ba-Sr.

Highlighted by Markl et al. (2016), Bursch et al. (2017) and Kissin (1992), ore precipitation happens geologically extremely rapid, on the order of hours to days, as conditions rapidly move from equilibrium, becoming more acidic. The glaring difference between Copper Pass and Blanchet Island ores is that the former is nickel dominated, where the latter is cobalt dominated. This highlights the change from a more alkaline to an increasingly acidic system. It is important to note that the difference in host rocks between the two localities (i.e metasediments and metavolcanics vs carbonates) could potentially act as buffers to the fluid system, explaining why the veins at Blanchet Island are Co-dominated.

2.7 Conclusions

Polymetallic veins enriched in Ni-Co-As and other metals within the East Arm basin and Southern Slave province, NWT, represent atypical "five-metals association (FMA)" mineralization as they are lacking productive U, Ag and base metal stages, but in terms of mineral textures, fluid chemistry and microthermometry, and stable/radiogenic isotopes, they share characteristics with other deposits of this type. The East Arm basin deposits were mineralized in 4 distinct stages (arsenides → di/triarsenides → sulfarsenides → base metals and native Bi). Blanchet Island and Copper Pass different significantly in their respective Ni and Co contents whereby Blanchet Island is Co-dominated with minor Ni, and Copper Pass is Ni-dominated, suggesting that at Blanchet Island, the main metal association (Co-Ni vs. Ni) was influenced by the fluid buffering capacity of the host carbonates deposits, buffering pH to higher values.

Early quartz, and later (capping, cementing) carbonate host a diversity of fluid inclusion types that record part of the evolution of the FMA veins. Fluid inclusion evidence constrain relatively constant fluid salinities (18.5 to 23.7 wt% $CaCl_2$ equiv.) and temperatures throughout vein formation, bracketing the oil stability window, and at relatively low pressure, between 0.5 and 0.95 kbar. Importantly, the unambiguous presence of coeval brines, carbonic fluids, liquid hydrocarbons and metalliferous bitumens in the fluid inclusion record, timed closely with metal and carbonate precipitation highlights the role of hydrocarbons as metal carriers but also identifies the mechanism (brine-HC interaction, and HC oxidation/thermal decomposition) critical for FMA vein formation.

The remarkable similarities between 3 (possibly 4) East Arm basin FMA localities suggests that these mineralized zones formed in small enclaves as parts of a much larger (FMA vein systems occur over a minimum of a ~20 x 50 km area), relatively thermally and compositionally

homogeneous hydrothermal system. Furthermore, critical to any argument concerning the source of metals for FMA veins is the observation that despite different host rocks, local variability in host rocks appears to not have had a significant impact on vein characteristics at each locality, reinforcing the idea of a common and distal fluid and metal source.

A conceptual model for the formation of the FMA veins favours mineralizing fluids descending as Ca-dominated, Mg-enriched sedimentary basin-derived bitterns derived from evaporite precipitation (fluid 1) and a metalliferous hydrocarbon-rich fluid (fluid 2) sourced from black shales. As these fluids migrate deep into the sedimentary basin and into crystalline basement rock through fault fracture networks (cf. Markl et al., 2016; Burisch et al., 2016; Kreissl et al., 2018), both fluids are heated by magmatic activity in the basement and the brine gets further enriched in Ca, Sr but also K and Ba through fluid-rock interaction (e.g., albitization of plagioclase and alkali feldspar) or through mixing with heated crystalline basement brines. The mixing of bittern and hydrocarbon liquid or bitumen results in a rapid thermal and oxidative decomposition of the metal-rich hydrocarbon, resulting in the precipitation of Ni-Co arsenide/sulfarsenides and other minerals. Metals are sourced from organic bitumen colloids as bitumen carry concentrations orders of magnitude higher in Co, Ni, Cu, Mo, Ag, Pb, Bi and U than the coeval brines.

The results of this study highlight key themes relevant to mineral exploration for this unusual metal association in the East Arm basin and elsewhere. The involvement of a sedimentary basin sequence as both a source of fluid and metals is implicated as a prerequisite in the formation of the FMA veins in the East Arm basin. This is based on the following observations: (i) hydrocarbon-brine interaction at the onset of FMA vein formation; (ii) the metalliferous nature of bitumens relative to brines; (iii) specific compositional characteristics of the brines (i.e., elevated Ca-Mg-Pb-Zn-Ba-Sr) straddling compositional fields for basinal (i.e. evaporitic bitterns, oil field brines)

and crystalline basement fluids; and (iv) isotopic evidence for involvement of a fluid of suspected sedimentary marine origin (i.e., from the marked positive shift in O isotopes at the onset of bitumen incursion and mineralization; and Sr isotopes). Furthermore, differences in the depth of formation of the FMA veins in the East Arm basin (fluid trapping pressure = 0.5-0.95 kbar; this study) and larger deposits at Great Bear Lake (0.07-0.2 kbar) suggest that these systems formed at different depths below the level of the basin-basement unconformity. Therefore, metalliferous fluids and hydrocarbons would have had to migrate further into the underlying basement and were possibly depleted of metals at shallower depths prior to reaching the level at which the East Arm basin veins formed. Sub-economic vein systems at Copper Pass and Blanchet Island may represent the deep expression of a much larger FMA hydrothermal system, now eroded away.

2.8 References

Ahmed, H.A., Arai, S., Ikenne, M. 2009. Mineralogy and Paragenesis of the Co-Ni Arsenide Ores of Bou Azzer, Anti-Atlas, Morocco. Economic Geology. vol 104. pp 249-266

Ahmed, H.A., Arai, S., Ikenne, M. 2009. Mineralogy and Paragenesis of the Co-Ni Arsenide Ores of Bou Azzer, Anti-Atlas, Morocco. Economic Geology. vol 104. pp 249-266

Alexandre, P., and Kyser, K. 2006. Geochemistry of uraniferous bitumen in the southwest Athabasca Basin, Saskatchewan, Canada. Economic geology. Vol 101. pp 1605-1612

Alexandre, P., Kyser, K., Polito, P. 2006. Alteration Mineralogy and Stable isotope Geochemistry of Paleoproterozoic Basement-Hosted Unconformity-Type Uranium Deposits in the Athabasca Basin, Canada. Economic Geology. Vol 100. pp 1547-1563

Andrews, A. 1986. Silver vein deposits: summary of recent research. Canadian Journal of Earth Sciences. vol 23. pp 1459-1462

Andrews, A., Owsiacki, L., Kerrich, R., Strong, D. 1986. The silver deposits at Cobalt and Gowganda, Ontario. I: Geology, petrography, and whole-rock geochemistry. Canadian Journal of Earth Science. vol 23. pp 1481-1506

Badham, J. 1975. Mineralogy, Paragenesis and Origin of the Ag-Ni, Co Arsenide Mineralisation, Camsell River, N.W.T Canada. Mineral Deposita. vol 10. pp 153-175

Badham, J. 1976. Orogenesis and metal-logenesis with reference to the silver-nickel, cobalt arsenide ore association. Geological Association of Canada, special paper 14. pp 559-571

Bakker, R. 1999. Adaption of Bowers and Helgeson (1983) equation of state to isochore and fugacity coefficient calculation in the H2O-CO2-CH4-N2-aCl fluid system: Chemical Geology, vol 154. pp 225–236.

Bastin, E. 1939. The nickel-cobalt-native silver ore type. Economic Geology. vol 34. pp 1-40

Beeskow, B., Rankin, A. H., Murphy, P. J., and Treloar, P. J. (2005) Mixed CH_4-CO_2 fluid inclusions in quartz from the South Wales Coalfield as suitable natural calibration standards for microthermometry and Raman spectroscopy. Chem. Geol. 223, 3-15.

Bleeker, W; and Hall, B. 2007. The Slave Craton: Geological and Metallogenic Evolution. Mineral deposits of Canada: a synthesis of major deposit-types, district metallogeny, the evolution of geological provinces, and exploration methods. Goodfellow, W D (ed.). Geological Association of Canada, Mineral Deposits Division, Special Publication no. 5, pp 849-879

Bowers, T., and Helgeson, H. 1983, Calculation of the thermodynamic and geochemical consequences of nonideal mixing in the system H2O-CO2-NaCl on phase relations in geologic systems: Metamorphic equilibria at high pressures and temperatures: American Mineralogist, vol 68. pp 1059–1075.

Bowring, S., Van Schmus, W., Hoffman, P. 1984. U-Pb zircon ages from Athapuscow aulacogen, East Arm of Great Slave Lake, N.W.T, Canada. Canadian Journal of Earth Sciences. vol 21. pp. 1315-1324

Boyle, R. 1968. The geochemistry of silver and its deposits. Geological Survey of Canada, Bulletin 160. pp 264

Boyle, R., and Dass, A. 1971. The origin of the native silver veins at Cobalt, Ontario. The Silver-Arsenide Deposits of the Cobalt-Gowganda Region, Ontario. The Canadian Mineralogist, vol 11. pp 414-417

Burisch, M., Gerdes, A., Walter, B., Neumann, U., Fettel, M., Markl, G. 2016 Methane and the origin of five-element veins: Mineralogy, age, fluid inclusion chemistry and ore forming processes in the Odenwald, SW Germany. Ore Geology Review. vol 81. pp 42-61.

Burke, E. 2001. Raman microspectrometry of fluid inclusions. Lithos. vol 55. pp 139-158

Castelli, D., Rolfo, F., Groppo, C., Compagnoni, R. 2007. Impure marbles from the UHP Brossasco-Isasca Unit (Dora-Maira Massif, western Alps): evidence for alpine equilibration in the diamond stability field and evaluation of the X(CO_2) fluid evolution. Journal of Metamorphic Geology. vol 25. pp. 587-603

Changkakoti, A., and Morton, R. 1986a. Electron microprobe analyses of native silver and associated arsenides from the Great Bear Lake silver deposits, Northwest Territories, Canada. Canadian Journal of Earth Science. vol 23. pp 1470-1479.

Changkakoti, A., Morton, R., Gray, J. 1986b. Hydrothermal environments during the genesis of silver deposits in the Northwest Territories of Canada: Evidence from fluid inclusions. Mineral Deposita. vol 21. pp 63-69

Changkakoti, A., Morton, R., Gray, J., Yonge, C. 1986c. Oxygen, hydron, and carbon isotopic studies of the Great Bear Lake silver deposits, Northwest Territories. Canadian Journal of Earth Sciences. vol 23 pp 1463-1469

Changkakoti, A., and Morton, R. 1987. The possible roles of Precambrian biota in the origin of magmatogene and hydrothermal silver-bearing vein deposits. Canadian Journal of Earth Science. vol 24. p 291-295

Connolly, J., Trommsdorff, V. 1991. Petrogenetic grids for metacarbonate rocks: pressure-temperature phase-diagram projection for mixed-volatile systems. Contribution to Mineralogy and Petrology. vol 108. pp 93-105.

Dieckmann, V., Caccialanza, P.G., and Galimberti, R. (2002) Evaluating the timing of oil expulsion: About the inverse behavior of light hydrocarbons and oil asphaltene kinetics. Organic Geochemistry, vol. 33,pp 1501-1513.

Dubessy, J., Poty, B., and Ramboz, C. 1989. Advances in C-O-H-N-S fluid geochemistry based on micro-Raman spectrometric analysis of fluid inclusions. *Eur. J. Mineral.vol* 1, p 517 - 534.

En-Naciri A, Barbanson L, Touray J (1997) Brine inclusions from the Co-As (Au) Bou Azzer district, Anti-Atlas Mountains, Morocco. Econ Geol 92:360–367
Etiope, G., and B. Sherwood Lollar. 2013. Abiotic methane on Earth. Reviews of Geophysics. Vol 51. Pp 276-299.

Fanlo, I., Subias, I., Manuel, J., Paniagua, A. 2008. Simple deposition versus replacement and
Gandhi, S., Loveridge, W. 1982. A Rb-Sr study of a differentiated quartz monzonite intrusion at Rainy Lake, Camsell River area, District of Mackenzie. Rb-Sr and U-Pb Isotpoic Age Studies, Geological Survey of Canada. vol 82-1C. pp 147-153.

Fayek, M.,, and Kyser, T. 1997. Chracterization of multiple fluid-flow events and Rare-earth-element mobility associated with formation of unconformity-type uranium deposits in the athabasca basin, saskatchewan. The Canadian Mineralogist. vol 35. pp 627-658.

Frape, S.K., Fritz, P., and McNutt, R.H. 1984. Water-rock interaction and the chemistry of groundwaters from the Canadian Shield. Geochimica et Cosmochimica Acta. vol 48. pp 1617-1627.

Feely, M., Costanzo, A., Lindner, F., George, J., Parnell, J., Bowden, S., Baba, M., Owens, P. 2017. Quartz-amethyst hosted hydrocarbon-bearing fluid inclusions from the Green Ridge Breccia in the Snoqualmie Granite, North Cascades, WA, USA. Minerals. vol 7. pp 1-16

Franklin, J., Kissin, S., Smyk, M., and Scott, S. 1986. Silver deposits associated with the Proterozoic rocks of the Thunder Bay District, Ontario: Canadian Jounal of Earth Sciences. vol 23. pp 1963-1979

Frezzoti, M., Tecca, F., Casagli, A. 2012. Raman spectroscopy for fluid inclusion analysis. Journal of Geochemical Exploration. vol 112. pp 1-20

Gandhi, S.S. and Loveridge. W.D., A Rb-Sr study of the Et-Then Group basalts, Great Slave Lake, District of Mackenzie; Rb-Sr and U-Pb Isotopic Age Studies, Report 5, Current Research. Part C, Geological Survey of Canada, Paper 82-1C. p. 155-160. 1982

Ghandi, S., Potter, E., Fayek, M. 2018. New constraints on genesis of the polymetallic veins at Port Radium, Great Bear Lake, Northwest Canadian Shield. Ore Geology Reviews. Vol 96. pp 28-47

Goldstein, R. 1986. Reequilibration of fluid inclusions in low-temperature calcium-carbonate cement. Geology. vol 14. pp 792-795

Goldstein, R. 2001. Fluid inclusions in sedimentary and diagenetic systems. Lithos. vol 55. Issue 1-4. pp 159-193

Goldstein, R. 2003. Petrographic analysis of fluid inclusions. Fluid Inclusions: analysis and interpretation. Mineralogical Association of Canada, Short Course 32. 9-53

Goodz, M., Watkinson, D., Smejkal, V., Pertold, Z. 1986. Sulfur-isotope geochemistry of silver-sulfarsenide vein mineralization, Cobalt, Ontario. Canadian Journal of Earth Sciences. vol 23. pp 1551-1567

Goff, S., Baadsgaard, H., Meuhlenbachs, K., Scarfe, C. 1981. Rb-Sr isochron ages, magmatic 87Sr*86Sr initial ratios, and oxygen isotope geochemistry of the Proterozoic lava flows and intrusions of the East Arm of Great Slave Lake, Northwest Territories, Canada. Canadian Journal of Earth Science. Vol 19. pp 343-356

Götze, J., Plötze, M., Habermann, D. 2001. Origin, spectral characteristics and practical applications of the cathodoluminescence (CL) of quartz – a review. Mineralogy and Petrology. vol 71. pp 225-250

Hall, C., Stumpll, E. 1972. The five-element (Ag-Bi-Co-Ni-As) vein deposit – a critical appraisal of the geological environments in which it occurs and of the theories affecting its origin: Proceedings, 24th international Geological Congress, Montreal, Sec. 4. pp 540.

Hamner, S. 1988. Great Slave Lake Shear Zone, Canadian Shield: reconstructed vertical profile of a crustal-scale fault zone. Tectonophysics. vol 149. pp 245-264

Helmstaedt, H. and Padgham, W. (1985) A new look at the stratigraphy of the Yellowknife supergroup at Yellowknife, NWT – implications for the age of gold-bearing shear zones and Archean basin evolution. Canadian Journal of Earth Sciences, v. 23, 454-475.

Hem, S., Makovicky, E. 2004. The system Fe-Co-Ni-As-S. II. Phase relations in the (Fe,Co,Ni)$As_{1.5}S_{0.5}$ section at 650 ºC and 500ºC. The Canadian Mineralogist. vol 42. Pp 63-86

Hoffman, P. 1968. Stratigraphy of the Lower Proterozoic (Aphebian), Great Slave Supergroup, East Arm of Great Slave Lake, District of Mackenzie. Geological Survey of Canada, Paper 68-42. pp 1-100

Holland, T., Powell, R. 1998. An internally consistent thermodynamic data set for phases of petrological interest. Journal of Metamorphic Geology. vol 16. pp 309-343

Hunt, J., Kerrick, D. 1977. The stability of sphere; experimental redetermination and geologic implications. Geochimical et Cosmochimica Asca. vol 41 pp 279 to 288

Hurlbert, L. 1996. Sedimentary nickel sulfides. Geology of Canadian Mineral Deposit Types (ed.). Geological Survey of Canada, Geology of Canada. vol 8. pp 152-158

Jaffe, F. 1986. Switzerland, in Dunning, F.W. and Evans, A., eds. Mineral Deposits of Europe, Central Europe: the Institution of Mining and Metallurgy and the Mineralogical Society, London. vol 3. pp 41-54

Jambor, J. 1971. Origin of the silver veins, in Berry, L.J., ed., The Silver-Arsenide Deposits of the Cobalt-Gowganda Region, Ontario: the Canadian Mineralogist. vol 11. Pp 402-413

Johnson, S., Large, R., Coveney, R., Kelley, K., Slack, J., Steadman, J., Gregory, D., Sack, P., Meffre, S. 2017. Secular distribution of highly metalliferous black shales corresponds with peaks in past atmosphere oxygenation. Mineral Deposita. vol 52. pp 791-798

Kerrich, R., Strong, D., Andrews, A., Owsiacki, L. 1986. The silver deposits at Cobalt and Gowganda, Ontario. III: Hydrothermal regimes and source reservoirs- evidence for H, O, C, and Sr isotopes and fluid inclusions. Canadian Journal of Earth Sciences. vol 23. pp 1519-1550

Kissin, S. 1988. Nickel-cobalt-native silver (five-element) veins: a rift-related ore type. North American ConL on Tectonic Control of Ore Deposits and the Vertical and Horizontal Extent of Ore Systems. Univ. Missouri Press, Rolla, pp 268-279.

Kissin, S. 1992. Five Element (Ni-Co-As-Ag-Bi) veins. Geoscience Canada. vol 19. n 3. pp 113-122

Kjarsgaard, B., Pearson, D., Dufrane, A., Heaman, L. 2013. Chapter 3. Proterozoic Geology of the East Arm Basin with emphasis on Paleoproterozoic magmatic rocks, East Arm MERA study area. Chapter 3 in Mineral and Energy Resource Assessment for the proposed Thaidene Nene National Park Reserve in the Area of the East Arm of Great Slave Lake, Northwest Territories (eds). Geological Survey of Canada. Open File 7196. pp. 51-92

Klemm, D.D. 1965. Synthesen und Analysen in den Dreiecksdiagrammen FeAsS-CoAsS-NiAsS und FeS2-CoS2-NiS2, N. Jb. Miner., Abh. vol. 103. pp 205-255.

Kreissl, S., Gerdes, A., Walter, B., Neumann, U., and Wenzel, T. 2018. Reconstruction of a > 200 Ma multi-stage “five element” Bi-Co-Ni-Fe-As-S system in the Penninic Alps, Switzerland. Ore Geology Reviews. vol 95. p 746-788

Leblanc, M. 1986. Co-Ni arsenide deposits with accessory gold, in ultramafic rocks from Morocco. Canadian Journal of Earth Sciences. vol 23. pp 1592-1602

Leblanc, H. 2014. Polymetallic Co-Ni-As-Bi-Sb-(Ag-U) Veins in the Southern Slave Province, Northwest Territories. NWT Geoscience Forum Abstracts.

Lietz J. 1939. Mikroskopische und chemische Untersuchungen an Kongsberger Silbererzen. Z Angew Mineral vol 2. pp 65–113

Lipp, U., Flach, S., 2003. Wismut-, Kobalt-, Nickel-und Silbererze im Nordteil des Schneeberger Lagerstättenbezirkes. Sächsisches Landesamt für Umweltund Geologie, Dresden. pp 1–210.

Lüders V, Plessen B, di Primio R (2012) Stable carbon isotopic ratios of CH4–CO2-bearing fluid inclusions in fracture-fill mineralization from the Lower Saxony Basin, Germany—a tool for tracing gas sources and maturity. Mar Pet Geol 30:174–183

Neumann, H. 1944. Silver deposits at Kongsberg: Norges Geologiske Undersokelse. vol 162. P 133.

MacDonald, A., Kreczmer, M., Kesler, S. 1986. Vein, manto, chimney mineralization at the Fresnillo silver-lead-zinc mine, Mexico. Canadian Journal of Earth Sciences. vol 23. pp 1603-1614

Markl, G., Burisch, M., Neumann, U. 2016. Natural fracking and the genesis of five-element veins. Mineral Deposita. vol 51. pp 703-712.

Marshall, D., Diamond, L., Skippen, G. 1993. Silver Transport and Deposition at Cobalt, Ontario, Canada: Fluid Inclusion Evidence. Economic Geology. vol 88. pp 837-854

Marshall, D., Watkinson, D. 2000. The Cobalt Mining District: Silver Sources, Transport and Deposition. Exploration Mining Geology. vol 9. pp 81-90.

Mernagh, T., Wilde, A. 1989. The use of the laser Raman microprobe for the determination of salinity in fluid inclusions. Geochimica et Cosmochimica Acta. vol 53. pp 765-771

Mercadier, J., Cuney, M., Lach, P., Boiron, M., Bonhoure, J., Richard, A., Leisen, M., and Kister, P. 2011. Origin of uranium deposits revealed by their rare earth element signature. Terra Nova. vol 23. p 264-269

Morton, R., Changkakoti, A. 1986. The possible roles of Precambrian biota in the origin of magmatogene and hydrothermal silver-bearing vein deposits. Canadian Journal of Earth Science. vol 24. pp 291-295

Mullis, J. 1987. Fluid inclusion studies during very low-grade metamorphism. *In*: Low temperature metamorphism (Frey, M., ed), Blackie, Glasgow. 162-199.

Mumford, T. 2013. Petrology of the Blatchford Lake Intrusive Suite, Northwest Territories, Canada. Unpublished Ph.D. thesis. Ottawa-Carleton Geoscience Centre and Department of Earth Sciences. pp 1-239

Nakai, S., Halliday, A., Kesler, S., Jones, H., Kyle, J., Lane, T. 1992. Rb-Sr dating of sphalerites from Mississippi Valley-type (MVT) ore deposits. Geochimica et Cosmochimica Acta. vol 57. pp 417-427

Ondrus, P., Veselovsky, F., Gabasova, A., Hlousek, J., and Srein, V. 2003. Geology and hydrothermal vein system of the Jacbymov (Joachimsthal) ore district. Journal of the Czech Geological Society. vol 48. pp 3-18

Ootes, L., Snyder, D., Davis, W.J., Acosta-Góngora, P., Corriveau, L., Mumin, A.H., Gleeson, S.A., Samson, I.M., Montreuil, J.-F., Potter, E., and Jackson, V.A., 2017. A Paleoproterozoic Andean-type iron oxide copper-gold environment, the Great Bear magmatic zone, NW Canada; Ore Geology Reviews, v. 81, p. 123-139.

Pagel, M., Michard, A., Juteau, M., Turpin. L. 1993. Sm-Nd, Pb-Pb- and Rb-Sr systematics of basement in the Cigar Lake area, Saskatchewan, Canada. Canadian journal of Earth Science. Vol 30. pp 731-742

Price, L.C. (1993) Thermal stability of hydrocarbons in nature: Limits, evidence, characteristics, and possible controls. Geochimica et Cosmochimica Acta, v. 57, 3261-3280.

Poplavko, E. M., Ivanov, V. V., Orekhov, V. S., Tarkhov, Yu A. 1978. Metal content of oil shales and some theories on their genesis. Geochem. Int. vol 15. p 90-97

Potter, J. and Konnerup-Madsen, J., 2003, A review of the occurrence and origin of abiogenic hydrocarbons in igneous rocks, in Petford, N. and McCaffrey, K.J.W. eds., Hydrocarbons in Crystalline Rocks: The Geological Society of London, Special Publications, v.214, p. 151-173.

Potter, E G; Corriveau, L; Kerswill, J A. 2013. Potential for iron oxide-copper-gold and affiliated deposits in the proposed national park region of the east arm of Great Slave Lake, Northwest

Territories: Insights from the Great Bear Magmatic Zone and global analogs; Mineral and Energy Resource Assessment of the proposed Thaidene Nene National Park Reserve in the area of the east arm of Great Slave Lake, Northwest Territories; Wright, D F (ed.); Ambrose, E J (ed.); Lemkow, D (ed.); Bonham-Carter, G (ed.). Geological Survey of Canada, Open File 7196, 2013 p. 477-493

Richard, A., Pettke, T., Cathelineau, M., Boiron, M., Mercadier, J., Cuney, M., Derome, D. 2010. Brine-rock interation in the Athabasca Basement (McArthur River U deposit, Canada): consequences for fluid chemistry and uranium uptake. Terra Nova. Vol 22. pp 303-308

Roberts, W. H. 1980. Design and function of oil and gas traps. AAPG Studies in Geology vol 10. p 317-340

Robinson, B., and Ohmoto, H. 1973. Mineralogy, Fluid Inclusions, and Stable Isotopes of the Echo Bay U-Ni-Ag-Cu Deposits, Northwest Territories, Canada. Economic Geology. vol 68. pp 635-656

Roedder, E., 1984, Fluid inclusions: Reviews in Mineralogy, vol 12. p 644

Roedder, E., and Bodnar, R.J. 1980. Geological pressure determination from fluid inclusion studies. Earth and Planetary Science Annual Reviews, v. 8, 263-301.

Roscoe, S., Gandhi, S., Charbonneau, B., Maurice, Y., Gibb, R. 1987. Mineral Resource Assessment of the Area in the East Arm (Great Slave Lake) and Artillery Lake Region, N.W.T., Proposed as a National Park. Geological Survey of Canada. Open File 1434.

Ruzicka, V. 1993. Vein uranium deposits. Ore Geology Reviews. vol 8. Issue 3-4. pp 247-276

Saintilan, N.J., Creaser, R.A., Bookstrom, A.A. 2017. Re-Os systematics and geochemistry of cobaltite (CoAsS) in the Idaho cobalt belt, Belt-Purcell Basin, USA: Evidence for middle Mesoproterozoic sediment0host Co-Cu sulfide mineralization with Grenvillian and Cretaceous remobilization. Ore Geology Reviews. vol 86. pp 509-525

Saxby, J. D. 1976. The significance of organic matter in ore genesis. In: Handbook of stratabound and stratiform ore deposits volume 2: geochemical studies, K. H. Wolf, Ed., p 111-133

Schneider, H. 192. Schichtgebundene Schichtgebundene, NE-metallund F-Ba-Lagerstatten im Sarrabus-Gerrei, SE Sardinien, Neues Jahrb. Mineral. Monatshefte. pp 529-541

Schubert, F., Diamond, L., Toth, T. 2007. Fluid-inclusion evidence of petroleum migration through a buried metamorphic dome in the Pannonian Basin, Hungary. Chemical Geology. vol 244. pp 357-381

Sheen, A. Geochronological and geochemical constraints on the origin of the Paleoproterozoic Union Island Group mafic magmatism, East Arm Basin, N.W.T. Department of Earth and Atmospheric Sciences, University of Alberta. pp 1-170

Sheen, A., Heaman, L., Kjarsgaard, B., Ootes, L., Pearson, D.G., Creaser, R. 2019. Athapuscow aulacogen revisited: Geochronology and geochemistry of the 2046 Ma Union Island Group mafic magmatism, East Arm of Great Slave Lake, Northwest Territories, Canada. Precambrian Research. vol 321. pp 85-102

Staude, S., Werner, W., Mordhorst, T., Wemmer, K., Jacob, D., Markl, G. 2012. Multi-stage Ag-Bi-Co-Ni-U and Cu-Bi vein mineralization at Wittichen, Schwarzwalk, Sw Germany: geological setting, ore mineralogy, and fluid evolution. Mineral Deposita. vol 47. pp 251-276

Staude S., Wagner T., Markl G.2007. Mineralogy, mineral compositions and fluid evolution at the Wenzel hydrothermal deposit, Southern Germany: implications for the formation of Kongsberg-type silver deposits. Canadian Mineralogist vol 45. pp 1147–1176

Tanton, T. 1931. For William and Port Arthur and Thunder Cape map areas, Thunder Bay District, Ontario: Geological Survey of Canada. pp 222.

Thorpe, R., Goodz, M., Jonasson, I., Blenkinsop, J. 1986. Lead-isotope study of mineralization in the Cobalt district, Ontario. Canadian Journal of Earth Sciences. vol 23. pp 1568-1575

van Breemen, O., Kjarsgaard, B., Tella, S., Lemkow, D., Aspler, L. 2013. U-Pb detrital zircon geochronology of clastic sedimentary rocks of the Paleoproterozoic Nonacho and East Arm basins, East Arm MERA study area. Chapter 4 in Mineral and Energy Resource Assessment for the Proposed Thaidene Nene National Park Reserve in the area of the East Arm of Great Slave Lake, Northwest Territories (eds). Geological Survey of Canada. Open File 7196. pp. 95-118

Vanko, D., Bodnar, R., Sterner, S. 1988. Synthetic fluid inclusions: VIII. Vapor-saturated halite solubility in part of the system Nacl-Cacl2-H2O, with application to fluid inclusions from oceanic hydrothermal systems. Geochimica et Cosmochimica Acta. Vol 52. pp 2451-2456

Veizier, J. 1989. Strontium isotopes in seawater through time. Annual Reviews of Earth Planetary Science. vol 17. pp 141-167

Wagner, T., and Lorenz, J. 2002. Mineralogy of complex Co-Ni-Bi vein mineralization, Bieber deposit, Spessart, Germany. Mineralogical Magazine. vol 66. pp 385-407

Walter, B., Burisch, M., Marks, M., Markl, G. 2017 Major element compositions of fluid inclusions from hydrothermal vein-type deposits record eroded sedimentary units in the Schwarzwald district, SW Germany. Mineral Deposita. vol 52. pp 1-14

Watkinson, D., Heslop, J., Ewert, W. 1975. Nickel Sulfide-Arsenide Assemblages Associated with Uranium Mineralization, Zimmer Lake Area, Northern Saskatchewan. Canadian Mineralogist. vol 13. pp. 198-204

Whittaker, S., Sami, T., Kyser, T., James, N. 1998. Petrogenesis of 1.9 Ga limestones and dolostones and their record of Paleoproterozoic environments. Precambrian Research. Vol 90. pp 187-202.

Wilkerson, G., Deng, Q., Llavona, R., Goodell, P. 1988. Batopilas mining district, Chihuahua. Economic Geology. vol 83. pp 1721-1736

Wopenka, B., and Pasteris, J. D. (1986) Limitations to quantitative analysis of fluid inclusions in geological samples by laser Raman microprobe spectroscopy. *Appl. Spectrosc.* **24**, 144–151.

Wopenka, B., and Pasteris, J. D. (1987) Raman intensities and detection limits of geochemically relevant gas mixtures for a laser Raman microprobe. *Anal. Chem.* **59**, 2165-2170.

Zajzon, N., Szentpeteri, K., Szakall, S., Kristaly, F. 2015. The origin of the Avram Iancu U-Ni-Co-Bi-As mineralization, Baita (Bihor) metallogenic district, Bihor Mrs., Romania. International Journal of Earth Science. vol 104. pp 1865-1887

Chapter 3: Key conclusions and future work

3.1 Key conclusions

The results of the study are described in Chapter 2 and summarize five-element vein associations with respect to ore mineralogy, ore texture, formation conditions and fluid chemistry. The main conclusions are summarized as:

(i) Bulk rock geochemistry demonstrates similar ore metal abundance between Blanchet Island and Copper Pass FMA deposits. Blanchet Island deposit is enrichment in Co relative to Copper Pass whereas the Copper Pass deposit is enriched in Ni and U relative to Blanchet Island. Blanchet Island is dominated by Co-arsenide/sulfarsenides (safflorite, skutterudite and cobaltite) while Copper Pass is dominated by Ni-arsenide/sulfarsenides (nickeline, rammelsbergite and gersdorffite). Paragenesis of ore vein mineralization at both Blanchet Island and Copper Pass deposits can be summarized in 4 stages of mineralization: 1) arsenides 2) di-tri-arsenides 3) sulfarsenides and 4) native metals and associated ore minerals with uraninite. Gangue mineralization marks the end of vein formation at Blanchet Island, while it marks the onset and end of mineralization at Copper Pass.

(ii) Fluid inclusion Microthermometry demonstrates the FMA veins formed from 124.8^{o} to 224.4 ^{o}C at Blanchet Island and 122.4^{o} to 252.7^{o}C at Copper Pass. Bulk salinities of fluids range from 16.0 to 23.5 wt% $CaCl_2$ and 19.2 and 23.1 wt% $CaCl_2$ at Blanchet Island and Copper Pass respectively. The fluid characteristics at both deposits overlap with respect to formation temperatures and bulk salinities support a genetic relationship. The East Arm deposits share fluid characteristics with sedimentary ore

deposits with respect to homogenization temperatures, bulk salinities, and brine chemistry.

(iii) The role of hydrocarbons as a reducing agent in metal precipitation mechanisms presented by Markl et al., (2016) and Burisch et al., (2017) is generally supported. Our supporting evidence is hydrocarbon liquid phases that are heterogeneously trapped with brines in fluid inclusion assemblages. Further analysis by Raman spectroscopy supports the notion that hydrocarbons are an abundant reducing agent in the metal precipitation mechanism, as hydrocarbon-bearing fluid inclusions hosted in both quartz and carbonate are abundant at both Blanchet Island and Copper Pass. Volatile species identified by Raman spectroscopy include CH4, H_2, N_2, kerogen, aqueous CO_3^{-2}, and various other aliphatic (olefin and paraffin) hydrocarbon species including C_2H_6, C_3H_8, aromatics, and other unidentified alkanes and alkenes.

(iv) Bitumen is the proposed metal sources for FMA deposits due to the lack of abundant metal concentrations in brines (through fluid inclusion analysis). Bitumen grains contain high concentrations (ranging 10^1 to 10^5 ppm) of metals, including Co-Ni-Ag-Pb-Fe-Mo-Bi-Zn-S-U, while brine-rich fluid inclusions lack these metals.

(v) Stable and Radiogenic isotopes demonstrate that Blanchet Island and Copper Pass deposits have similar $\delta^{13}C_{VPDB}$, $\delta^{18}O_{VSMOW}$, and $^{87}Sr/^{86}Sr$. Blanchet Island carbonates

contain $\delta^{13}C_{VPDB}$ between -2.73‰ to –2.02‰, $\delta^{18}O_{VSMOW}$ between 12.06‰ to 13.46‰, and $^{87}Sr/^{86}Sr_o$ from 0.709655 to 0.710387. Ferroan dolomite in the nickeline-carbonate veins and breccias at Copper Pass has $\delta^{13}C_{VPDB}$ between -4.06‰ to –1.13‰ and $\delta^{18}O_{VSMOW}$ between 10.85‰ to 16.24‰. Zoned quartz at Copper at Copper Pass contain $\delta^{18}O_{VSMOW}$ ranging from 3.9‰ to 20.2‰ between core to rim growth zones A-C. Transitional rim zones D1, D2, D3 contain $\delta^{18}O_{VSMOW}$ of 5.2‰ to 22.6‰. The outermost rim (zone E) has $\delta^{18}O_{VSMOW}$ values of 6.7‰ to 22.6‰. The $\delta^{18}O$ results indicate a systematic shift to higher $\delta^{18}O$ from core to rim. In particular, the transition from D2 to D3 shows an increase in the average $\delta^{18}O_{VSMOW}$ value of 6.5‰ coinciding with the textural position of primary, metalliferous bitumen inclusions. Ferroan dolomite from Blanchet Island veins has $^{87}Sr/^{86}Sr_o$ ratios from 0.709655 to 0.710387, while ferroan dolomite of Copper Pass veins has $^{87}Sr/^{86}Sr_o$ ratios from 0.708093 to 0.719578. Isotopic signatures of late carbonate are shared with late carbonates from major polymetallic vein deposits at Echo Bay, NWT, and Cobalt and Gowganda, ON deposits.

(vi) The preferred model for FMA deposits is the mixing of basinal-derived HC and brines, derived from separate areas in a sedimentary basin, but heated in the basement rocks compared to magmatic and/or basement-derived models. This is based on evidence provided through fluid inclusion petrography, laser ablation-ICPMS of brine and bitumen inclusions, Raman spectroscopy,

3.2 Future work

Additional work needs to be performed in order to improve the classification and understanding of formation conditions for all five-element vein types. Constraints on fluid provenance, metal sources, chemical processes affecting ore deposition (i.e reducing agents) and overall paragenetic model can be improved upon. To better constrain fluid and metal sources, further investigation into fluid chemistry and bitumen metal contents through fluid inclusion microthermometry and laser ablation-ICPMS of bitumens from other polymetallic systems is needed. This will allow for further insight into the effective roles that bitumen play in the formation of these unique deposit styles. Further petrographic analysis and data accumulation of fluid inclusion types in other FMA deposits is needed as the identification of bitumen and HC liquid inclusions in other polymetallic systems would provide analogous information between low grade East Arm FMA deposits and high grade FMA deposits found globally (i.e. Canada, Czech Republic, and Germany). Further classification of the role of HC liquid will need to be done through Raman spectroscopy and LA-ICPMS to provide a better understanding of speciation and metal concentrations affiliated with the fluid. An investigation into the radiogenic isotope analysis of other FMA deposits is needed to provide information on potential fluid source reservoirs as the role of sedimentary basin continues to gain steam compared to magmatic basement derived models. Additionally, robust thermodynamic modelling of the precipitation order and solubility model for FMA systems requires far more experimentally determined parameters, which at the present time are limited.

Table 1.1: List of acronyms and abbreviations used throughout this thesis

Abbreviation	Meaning
anna	annabergite
BI	Blanchet Island occurrence
BSE	backscattered electrons
btm	bitumen
ca	calcite
carb	carbonate
carbonic	fluid composed of CO_2 and/or hydrocarbons
cbt	cobaltite
CIS	Compton intrusive suite
CL	cathodoluminescence
CLG	Caribou Lake Gabbro occurrence
clv	cleavage plane
CP	Copper Pass occurrence (alt: BM, NIX, GOGO, Sachowia Lake)
Fe-dol	ferroan dolomite
FIA	fluid inclusion assemblage
FMA	"five metal association"
GC	gas chromatography
gdf	gersdorffite
gn	galena
HC	hydrocarbon
LA-ICP-MS	laser ablation inductively coupled plasma mass spectrometry
L_{aq}	aqueous liquid phase
$L_{carbonic}$	carbonic liquid phase
LB	Labelle Penninsula (occurrence)
ME	metal
nk	nickeline
polymetallic	“five-metal vein association” main: Ni-Co-As-Ag-Bi; other: Sb, U, Cu, Pb, Zn, Mo
py	pyrite
qtz	quartz
ram	rammelsbergite
saf	safflorite
S_{brine}	secondary origin brine fluid inclusion trail
$S_{carbonic}$	secondary origin carbonic fluid inclusion trail
SIMS	secondary ion mass spectrometry
skut	skutterudite
TD-MS	total digestion mass spectrometer
T_h	temperature of homogenization
$T_h^{carbonic}$	temperature of homogenization for carbonic phase
T_m^{ice}	temperature of final ice melting
UI	Union Island shale occurrence
urn	uraninite
V	vapour phase
$V_{carbonic}$	carbonic vapour
wt.%	weight percentage
wt.% $CaCl_2$ eq. or equiv.	fluid inclusion bulk salinity in weight percentage $CaCl_2$ equivalent

Table 1.2 Summary of polymetallic "five-metals association" (FMA) veins in the NWT (Silke, 2009)

Name	Commodity	Tonnage, grade details	Historical grade
Bear Portal	Ag	unknown	unknown
Blanchet Island	Co-Ni	330 tons	15% Ni + 11% Co
Bonanza	Ag	unknown	unknown
Contact Lake	U+Ag	16995 tons (678,000 oz Ag and 6933 lbs U_3O_8)	unknown
Contact Lake Portal	Ag-Cu	unknown	unknown
Copper Pass	Ni	>450 tons	33-35% Ni
Echo Bay	Ag-Cu	363,140 tons (23,544,461 oz Ag, 4505 tons Cu)	unknown
El Bonanza	Ag	2.95 tons (30,175 oz Ag)	unknown
Eldorado	U-Ra-Ag-Cu-Ni-Co-Pb	1,366,602 tons (6,079 tons U_3O_8, 450g Ra, 13,371,382 oz Ag, 2,389 tons Cu, 140 tons Ni, 250 tons Co, 8 tons Pb)	4,328 oz/ton Ag
Glacier Bay	Ag	unknown	4 oz/ton Ag, 0.02% U_3O_8
Mystery Island	U-Ra	unknown	unknown
Norex	Ag	53,697 tons (2,066,744 oz Ag)	unknown
Northrim	Ag	12,000 tons (30,000 oz Ag)	unknown
Smallwood Lake	Ag	18,204 tons (169,720 oz Ag)	unknown
Terra	Ag-Cu	507,629 tons (14,236,325 oz Ag, 2,248 tons Cu)	unknown

Table 1- Bulk Rock Geochemistry of East Arm polymetallic vein samples (Blanchet and Copper Pass localities)

		D.L.	Method	Sample no.	01A	01B-M	01C	01C-M	01-Diopide	01-Scarn	02C-M	02C-Carb	03-A1	03-A2	03B-Carb	03C	03-K1	03-K2	03-K3	03B-U	03B-Uaplite	03-R	04B-Aq	04A-(RG)	04B-Host	05A	05A-1/2	05B	05C
				Site Location	BI	BI	BI	BI	BI	BI	BI	BI	CP	CP	CP	CP	CP	CP	CP	CP	CP	CP	CP	CP	CP	CP	CP	CP	CP
				Sample type	1	1	1	1	2	3	1	5	1	1	1+5	3	1+3	1+3	1+3	1	3	4	2	4	3	1	1	1	1
C	%	0.01	CS		7.54	0.06	5.62	1.58	1.49	0.91	0.57	12.5	3.5	1.32	11.2	1.11	1.37	1.37	0.36	0.88	0.42	1.36	8.7	1.96	3.99	0.65	0.63	4.36	10.8
S	%	0.01	CS		0.4	0.68	0.21	0.32	1.35	0.08	17	< 0.01	1.12	0.16	0.3	8.75	2.32	3.01	0.06	1.12	0.36	1.52	0.56	0.64	3.77	1.66	1.06	0.39	0.06
Co	ppm	0.01	FUS-Na_2O_2		18500	210000	12100	23000	44300	> 500	211000	179	3520	770	1060	2130	30500	47100	340	7120	111	5940	1550	8790	200	29300	13700	16100	1820
Ni	ppm	0.5	FUS-Na_2O_2		14400	57300	115000	225000	197000	0	57100	0	305000	18500	26400	0	106000	155000	0	366000	0	172000	40500	245000	1860	311000	355000	40600	11800
B	ppm	1	TD-MS		< 1	< 1	< 1	2	< 1	10	< 1	7	10	69	8	237	19	3	7	< 1	115	34	16	20	80	< 1	5	34	< 1
Li	ppm	0.5	TD-MS		0.9	0.7	< 0.5	3.9	< 0.5	25.4	1.7	< 0.5	6.1	1.6	< 0.5	1.4	5.7	3.4	< 0.5	6.3	10.8	1.2	< 0.5	7.3	1.5	8.3	13.8	34	< 0.5
Cd	ppm	0.1	TD-MS		0.001	0.001	0.001	0.001	0.001	0.001	0.001	0.001	0.001	0.001	0.001	0.001	0.001	0.001	0.001	0.001	0.001	0.001	0.001	0.001	0.001	0.001	0.001	0.001	0.001
V	ppm	1	TD-MS		88	3	149	38	23	76	32	26	7	27	51	120	24	9	2	5	27	34	424	69	120	6	15	53	27
Cr	ppm	0.5	TD-MS		5.6	2.5	3.2	4.3	2.1	16.9	3.2	< 0.5	5.5	17.1	1.5	84.2	9.2	4.4	8.3	3.5	10.4	32.5	11	24	64.5	2.7	5.9	49.2	1.8
Mn	ppm	1	TD-MS		1950	110	1390	406	391	1190	1060	2350	1070	456	3470	250	1050	1560	263	530	183	509	3280	739	890	542	571	3100	3610
Fe	ppm	0.01	TD-MS		2800	11600	3500	3000	3900	197000	21200	100	9200	12600	8800	70600	14700	17500	6900	3600	10900	9700	6300	8200	30500	7700	7700	13500	10600
Hf	ppm	0.1	TD-MS		< 0.1	< 0.1	< 0.1	< 0.1	< 0.1	1.3	< 0.1	< 0.1	< 0.1	2	< 0.1	1	0.8	0.1	1.3	< 0.1	2.2	0.9	< 0.1	0.2	1.5	< 0.1	< 0.1	< 0.1	0.1
Er	ppm	0.1	TD-MS		< 0.1	< 0.1	< 0.1	< 0.1	< 0.1	< 0.1	< 0.1	< 0.1	< 0.1	< 0.1	< 0.1	< 0.1	< 0.1	< 0.1	< 0.1	< 0.1	0.2	< 0.1	< 0.1	< 0.1	< 0.1	< 0.1	< 0.1	< 0.1	< 0.1
Be	ppm	0.1	TD-MS		< 0.1	< 0.1	< 0.1	< 0.1	< 0.1	3.5	< 0.1	< 0.1	0.2	3	< 0.1	3.9	0.8	0.3	4.8	0.3	5.8	0.7	< 0.1	0.7	1.2	0.4	0.8	1	< 0.1
Ho	ppm	0.1	TD-MS		< 0.1	< 0.1	< 0.1	< 0.1	< 0.1	< 0.1	< 0.1	< 0.1	< 0.1	< 0.1	< 0.1	< 0.1	< 0.1	< 0.1	< 0.1	< 0.1	0.1	< 0.1	< 0.1	< 0.1	< 0.1	< 0.1	< 0.1	< 0.1	< 0.1
Ag	ppm	0.05	TD-MS		1.15	0.9	0.73	1.97	2.73	2.43	4.91	1.38	2.31	2.27	3.31	4.29	19.3	9.14	2.2	7.42	4.5	4.17	7.07	4.06	2.32	3.99	2.77	2.86	1.28
Cs	ppm	0.05	TD-MS		< 0.05	< 0.05	< 0.05	0.1	< 0.05	< 0.05	< 0.05	< 0.05	0.06	0.31	0.15	0.4	0.15	0.08	0.06	0.07	0.73	0.16	0.06	0.09	0.05	< 0.05	< 0.05	0.05	< 0.05
Eu	ppm	0.05	TD-MS		< 0.05	< 0.05	< 0.05	< 0.05	< 0.05	< 0.05	< 0.05	< 0.05	< 0.05	0.07	< 0.05	< 0.05	< 0.05	< 0.05	< 0.05	< 0.05	0.31	< 0.05	< 0.05	< 0.05	< 0.05	< 0.05	< 0.05	< 0.05	< 0.05
Bi	ppm	0.02	TD-MS		9.18	298	3.6	32.8	188	173	1450	9.71	> 2000	92.3	65.6	74.4	1670	> 2000	51.2	> 2000	340	468	61500	231	1830	> 2000	> 2000	441	13.8
Se	ppm	0.1	TD-MS		< 0.1	43.9	10.9	25.7	48.5	< 0.1	71.4	< 0.1	1	< 0.1	0.4	< 0.1	< 0.1	< 0.1	< 0.1	< 0.1	< 0.1	< 0.1	< 0.1	8.5	< 0.1	< 0.1	0.4	< 0.1	< 0.1	< 0.1
Zn	ppm	0.2	TD-MS		33	23.5	69.1	10.5	23.5	411	37.8	17.6	17.5	21	17.3	15.6	41.1	39.1	13	17.6	25.6	13.4	22.8	7.2	12.8	33.7	20.5	55.7	12.6
Ga	ppm	0.1	TD-MS		0.6	< 0.1	0.3	0.2	0.2	8.7	0.4	0.2	0.3	4.8	0.3	13.1	2.5	0.7	14.4	0.2	7.3	2.5	0.4	< 0.1	6	0.4	0.8	2.2	0.3
As	ppm	0.1	TD-MS		73300	587000	262000	521000	503000	20700	362000	361	385000	30600	42200	4740	356000	466000	4090	411000	30500	202000	47400	281000	1570	509000	414000	127000	20400
Rb	ppm	0.2	TD-MS		1.6	0.6	1.4	1.9	0.7	0.6	0.2	0.6	2.9	11	3.6	25.9	6.8	3.1	1.4	1.2	20.8	9.1	4.1	6.9	10.1	0.6	1.2	5.9	1.8
Y	ppm	0.1	TD-MS		< 0.1	0.3	< 0.1	0.1	< 0.1	0.3	< 0.1	< 0.1	< 0.1	0.2	< 0.1	< 0.1	< 0.1	< 0.1	< 0.1	< 0.1	1.3	< 0.1	< 0.1	0.3	0.1	< 0.1	< 0.1	< 0.1	< 0.1
Zr	ppm	1	TD-MS		< 1	< 1	8	< 1	< 1	33	< 1	< 1	< 1	52	< 1	26	< 1	< 1	18	< 1	61	< 1	< 1	26	38	< 1	< 1	< 1	4
Nb	ppm	0.1	TD-MS		13.9	12.1	16.2	2.4	1.7	11.1	11.7	11.2	13.1	23.3	15.9	14.2	14.9	13.7	11.9	17.1	32.4	13.7	12.6	9.5	9.8	16.1	15.1	15.4	19.1
Mo	ppm	0.05	TD-MS		13	9.47	14.8	66.8	17	2.58	6.2	7.1	29.9	40	15.7	7.95	171	56.4	10.7	172	41	222	216	125	19.4	38.7	33	33.6	9.13
In	ppm	0.1	TD-MS		< 0.1	0.2	0.1	0.2	0.2	0.2	0.2	< 0.1	0.1	< 0.1	< 0.1	< 0.1	0.1	0.2	< 0.1	0.2	< 0.1	< 0.1	< 0.1	0.1	< 0.1	0.2	0.2	0.1	< 0.1
Sn	ppm	1	TD-MS		1	1	4	1	< 1	3	< 1	< 1	1	3	1	5	2	1	2	< 1	3	1	1	1	3	1	1	2	1
Sb	ppm	0.1	TD-MS		31.2	44	7.6	23.7	37.5	19.7	104	0.4	0.047	21.3	86.5	4.5	160	178	2.5	0.09	41.7	253	34.2	121	3.1	0.167	0.166	83.2	10.3
Te	ppm	0.1	TD-MS		0.2	0.2	1.7	0.2	< 0.1	< 0.1	0.5	< 0.1	0.3	< 0.1	0.8	0.1	0.2	< 0.1	0.1	0.1	0.2	0.2	0.9	< 0.1	0.3	0.3	< 0.1	0.2	< 0.1
Ba	ppm	1	TD-MS		4	13	3	8	6	33	5	< 1	5	49	1	12	21	26	10	10	63	10	2	64	18	16	12	13	2
La	ppm	0.1	TD-MS		< 0.1	0.5	< 0.1	0.2	0.2	7.8	0.2	< 0.1	< 0.1	0.5	< 0.1	< 0.1	0.2	< 0.1	< 0.1	< 0.1	0.3	0.4	< 0.1	0.2	0.5	0.2	0.2	< 0.1	< 0.1
Ce	ppm	0.1	TD-MS		0.2	1.8	< 0.1	0.4	0.3	26.5	0.3	< 0.1	< 0.1	7.2	< 0.1	0.3	1.9	0.1	0.6	< 0.1	9.5	3.6	< 0.1	1	4.3	0.2	0.3	< 0.1	< 0.1
Pr	ppm	0.1	TD-MS		< 0.1	0.2	< 0.1	< 0.1	< 0.1	0.8	< 0.1	< 0.1	< 0.1	0.5	< 0.1	< 0.1	< 0.1	< 0.1	< 0.1	< 0.1	0.9	< 0.1	< 0.1	0.1	0.2	< 0.1	< 0.1	< 0.1	< 0.1
Nd	ppm	0.1	TD-MS		< 0.1	0.7	< 0.1	0.4	0.3	2.4	< 0.1	< 0.1	< 0.1	2.3	< 0.1	< 0.1	0.2	< 0.1	0.2	< 0.1	5.3	0.4	< 0.1	0.6	0.8	< 0.1	0.2	< 0.1	< 0.1
Sm	ppm	0.1	TD-MS		< 0.1	0.2	< 0.1	< 0.1	< 0.1	0.2	< 0.1	< 0.1	< 0.1	0.5	< 0.1	< 0.1	< 0.1	< 0.1	< 0.1	< 0.1	1.4	< 0.1	< 0.1	0.2	0.1	< 0.1	< 0.1	< 0.1	< 0.1
Gd	ppm	0.1	TD-MS		< 0.1	0.2	< 0.1	0.1	< 0.1	< 0.1	< 0.1	< 0.1	< 0.1	0.2	< 0.1	< 0.1	< 0.1	< 0.1	< 0.1	< 0.1	1.1	< 0.1	< 0.1	0.2	< 0.1	< 0.1	< 0.1	< 0.1	< 0.1
Tb	ppm	0.1	TD-MS		< 0.1	< 0.1	< 0.1	< 0.1	< 0.1	< 0.1	< 0.1	< 0.1	< 0.1	< 0.1	< 0.1	< 0.1	< 0.1	< 0.1	< 0.1	< 0.1	0.1	< 0.1	< 0.1	< 0.1	< 0.1	< 0.1	< 0.1	< 0.1	< 0.1
Dy	ppm	0.1	TD-MS		< 0.1	0.1	< 0.1	< 0.1	< 0.1	0.1	< 0.1	< 0.1	< 0.1	0.1	< 0.1	< 0.1	< 0.1	< 0.1	< 0.1	< 0.1	0.7	< 0.1	< 0.1	0.2	< 0.1	< 0.1	< 0.1	< 0.1	< 0.1
Cu	ppm	0.2	TD-MS		7	18.5	4.2	5.2	9.5	23.4	166	40.6	439	29.4	39.5	191	111	83	29.9	198	80.6	50.8	77.3	14.3	405	73.1	52.2	115	11.2
Ge	ppm	0.1	TD-MS		1.2	0.6	1.3	2.4	2.5	2.9	< 0.1	0.3	3.9	1.8	1.4	0.3	1.7	1.4	1.4	4.1	2.7	3.3	1	2.2	0.6	3.7	4.5	1.9	0.2
Tm	ppm	0.1	TD-MS		< 0.1	< 0.1	< 0.1	< 0.1	< 0.1	< 0.1	< 0.1	< 0.1	< 0.1	< 0.1	< 0.1	< 0.1	< 0.1	< 0.1	< 0.1	< 0.1	< 0.1	< 0.1	< 0.1	< 0.1	< 0.1	< 0.1	< 0.1	< 0.1	< 0.1
Yb	ppm	0.1	TD-MS		< 0.1	< 0.1	< 0.1	< 0.1	< 0.1	< 0.1	< 0.1	< 0.1	< 0.1	< 0.1	< 0.1	< 0.1	< 0.1	< 0.1	< 0.1	< 0.1	0.1	< 0.1	< 0.1	< 0.1	< 0.1	< 0.1	< 0.1	< 0.1	< 0.1
Lu	ppm	0.1	TD-MS		< 0.1	< 0.1	< 0.1	< 0.1	< 0.1	< 0.1	< 0.1	< 0.1	< 0.1	< 0.1	< 0.1	< 0.1	< 0.1	< 0.1	< 0.1	< 0.1	< 0.1	< 0.1	< 0.1	< 0.1	< 0.1	< 0.1	< 0.1	< 0.1	< 0.1
Ta	ppm	0.1	TD-MS		6.4	6.1	8	0.6	0.4	4.8	5.1	5.7	5.5	6	7.6	4.2	5.7	6.6	5.1	6.1	4.3	6.2	6.1	1.8	3.7	7.7	7.2	6.2	9.3
Sr	ppm	0.2	TD-MS		3.2	3.7	2.8	7.8	7	14.8	1.5	0.9	2.3	8	3.5	0.4	11.4	6.5	1.6	1.9	2.4	4.4	1.7	19.1	4.1	2.7	2.7	4.6	2.9
W	ppm	0.1	TD-MS		2.2	2	3.3	0.6	0.4	1.6	1.4	1.3	1.9	7.9	2.6	7.4	2.9	2.4	2.5	2.3	7.4	1.8	2.2	2.2	2.2	2.3	1.8	1.9	3.9
Re	ppm	0.001	TD-MS		0.016	0.01	0.024	0.035	0.099	0.006	0.026	0.007	0.013	0.016	0.013	0.008	0.043	0.012	0.007	0.061	0.019	0.042	0.012	0.013	0.011	0.009	0.008	0.015	0.007
Tl	ppm	0.05	TD-MS		< 0.05	< 0.05	0.05	0.1	< 0.05	< 0.05	0.21	< 0.05	0.06	0.15	< 0.05	0.28	0.41	0.13	< 0.05	0.28	0.23	0.48	0.16	0.36	0.1	< 0.05	< 0.05	0.11	0.07
Pb	ppm	0.5	TD-MS		4	3.8	6.1	10.4	14.7	47.4	47.8	1.4	5.1	38.8	7	8.8	192	77.5	11.1	47.2	81.8	11.1	11.2	27.1	13.1	14.3	9.5	15.2	2.9
Th	ppm	0.1	TD-MS		< 0.1	< 0.1	< 0.1	< 0.1	< 0.1	< 0.1	< 0.1	< 0.1	< 0.1	0.2	< 0.1	< 0.1	0.1	< 0.1	0.2	< 0.1	0.8	< 0.1	< 0.1	< 0.1	0.1	< 0.1	< 0.1	< 0.1	< 0.1
U	ppm	0.1	TD-MS		8.1	22.1	42	96.7	45.8	83.2	18.7	2	79.2	1750	56.9	17	87.6	11.9	51.2	397	4030	37.7	174	129	23.6	132	72.6	55.6	13.3
Au	ppb	2	FA-ICP		59	381	86	257	246	25	5820	< 2	165	28	2460	4	2720	22	4	723	14	361	4870	77	44	< 2	19	9.5	14	< 2
Hg	ppb	10	TD-MS		< 10	< 10	< 10	10	< 10	< 10	280	< 10	160	< 10	40	< 10	1710	1780	30	360	60	2030	30	320	< 10	150	190	50	< 10
Pd	ppb	5	FA-ICP		< 5	< 5	< 5	8	< 5	< 5	< 5	< 5	< 5	< 5	< 5	< 5	< 5	< 5	< 5	< 5	< 5	< 5	7	< 5	< 5	< 5	< 5	< 5	< 5
Pt	ppb	5	FA-ICP		< 5	< 5	< 5	< 5	< 5	< 5	< 5	< 5	19	< 5	< 5	< 5	< 5	< 5	< 5	9	< 5	7	< 5	< 5	< 5	< 5	< 5	< 5	< 5

Notes: Methods: combustion for sulfur (CS), sodium peroxide "total" fusion (FUS-Na2O2), four acid digestion followed by ICP-MS (TD-MS), fire assay followed by ICP-MS (FA-ICP). Sample type: 1) Vein 2) Ore 3) Host 4)Breccia 5) Gangue. Vein consists of Co/Ni-mineralized veins, Ore represents large grab samples of Co/Ni-mineralization, Host represents carbonate, metasediments, aplite host rocks, Breccia represents ore minerals with quartz and carbonate gangue.

Table 2. Representative SEM-EDS analysis (elemental weight %) of arsenide ores and accessory minerals at Blanchet Island and Copper Pass.

Sample	Location	Mineral	Ni	Co	Fe	As	S	Bi	Mo	Pb	Ag	U	Total
01B-M	Blanchet Island	skutterudite	-	25.4	1.8	71.3	1.5	-	-	-	-	-	100.0
01B-M	Blanchet Island	Ni-cobaltite	7.24	24.14	1.64	46.68	20.3	-	-	-	-	-	100.0
01B-M	Blanchet Island	safflorite	-	38.04	-	60.48	0.68	-	-	-	-	-	99.2
01B-M	Blanchet Island	Co-nickeline	27.7	12.2	-	60.05	-	-	-	-	-	-	100.0
01C-M	Blanchet Island	rammelsbergite	27.7	1.02	-	70.15	-	-	-	-	-	-	98.9
03-A2	Copper Pass	galena	-	-	-	-	10.08	-	-	85.22	-	-	95.3
03-A2	Copper Pass	uraninite[a]	2.19	-	-	0.68	-	-	-	6.51	-	61.1	70.5
03-A2	Copper Pass	Native bismuth+ antimony	26.76	-	-	0.44	7.36	63.08	-	-	-	-	97.6
03-A2	Copper Pass	[1]uraninite with native Ag inclusion	14.3	-	1.04	14.46	0.42	-	-	-	3.04	15.5	48.8
04B-V	Copper Pass	nickeline	50.56	-	-	49.31	-	-	-	-	-	-	99.9
04B-V	Copper Pass	[2]Native bismuth	-	-	-	-	-	94.41	-	-	-	-	94.4
04B-V	Copper Pass	gersdorffite	15.75	24.76	1.12	42.21	16.15	-	-	-	-	-	100.0
05A	Copper Pass	[3] molybdenite + native bismuth	1.02	-	0.62	0.37	-	54.47	38.56	-	-	-	95.0

Notes: [1] uranium phase with Ag found as an inclusion in nickeline (46.85 wt% O). [2] Inclusion hosted in nickeline. [3] Inclusion hosted in nickeline. [4] O not reported, thus low total.

Table 3. Representative SEM-EDS analyses (elemental weight %) of sulfarsenides at Blanchet Island and Copper Pass, NWT

Sample	Location	Mineral	Ni	Co	Fe	As	S	Total
01A	Blanchet Island	cobaltite	4.38	35.73	2.01	40.08	17.8	100
01A	Blanchet Island	cobaltite	3.89	36.77	1.72	39.87	17.75	100
01B-M	Blanchet Island	cobaltite	4.36	27.14	1.72	46.09	20.70	100
01B-M	Blanchet Island	cobaltite	4.17	28.01	0.73	47.37	19.72	100
01C-M	Blanchet Island	Ni-cobaltite	18.56	13.83	0.89	50.55	15.72	99.5
01C-M	Blanchet Island	Ni-cobaltite	12.11	20.86	0.87	49.41	16.75	100
01C-M	Blanchet Island	gersdorffite	25.31	5.35	0.72	51.74	15.39	98.5
01C-M	Blanchet Island	gersdorffite	26.11	5.91	0.46	51.51	15.22	99.2
03-Carb	Copper Pass	gersdorffite	39.55	-	0.6	42.07	16.47	98.7
03-Carb	Copper Pass	gersdorffite	38.31	-	0.82	44.47	15.05	98.7
03-Carb	Copper Pass	gersdorffite	39.46	-	-	40.56	18.29	98.3
03-A2	Copper Pass	gersdorffite	34.84	6.73	-	40.71	17.72	100
03-A2	Copper Pass	gersdorffite	39.87	-	-	39.48	18.47	97.8
03-A2	Copper Pass	gersdorffite	17.69	20.49	2.05	41.19	18.58	100
03-K1	Copper Pass	gersdorffite	37.94	1.57	0.59	40.03	17.37	98
03-K1	Copper Pass	gersdorffite	38.29	1.51	0.58	39.17	17.28	96.8
05A	Copper Pass	cobaltite	9.63	27.46	2.38	47.54	12.99	100
05A	Copper Pass	cobaltite	8.83	28.77	1.34	49.27	11.79	100
05A	Copper Pass	gersdorffite	40.35	0.69	-	40.02	17.55	99
05A	Copper Pass	gersdorffite	33.99	4.48	2.1	44.95	14.47	100
05C	Copper Pass	gersdorffite	34.29	1.56	2.25	45.11	16.78	100
05C	Copper Pass	gersdorffite	32.89	2.18	3.17	45.07	16.7	100
05C	Copper Pass	gersdorffite-S poor	22.55	11.78	0.51	56.79	7.21	99
05C	Copper Pass	gersdorffite-S poor	23.08	12.07	-	56.95	7.9	100
03-A2	Copper Pass	nickeline	50.41	-	-	49.59	-	100
03-A2	Copper Pass	nickeline	50.49	-	-	49.51	-	100

Table 4-Microthermometry of representative fluid inclusions from polymetallic vein deposits at Blanchet Island and Copper Pass, East Arm, Great Slave Lake

Location	Sample no.	Assemblage	Host	inclusion	T_m^{ICE} (°C)	T_h (°C)	wt% $CaCl_2$ eq.	$T_m^{carbonic}$ (°C)	$T_h^{carbonic}$ (°C)	Location	Sample no.	Assemblage	Host	inclusion	T_m^{ICE} (°C)	T_h (°C)	wt% $CaCl_2$ eq.	$T_m^{carbonic}$ (°C)	$T_h^{carbonic}$ (°C)
Blanchet Island	01-Ore Pile		carb	1	-26.1	-		-	-	Copper Pass		4	qtz	1	-21.9	118.3	21.50	-	-
			carb	2	-20.1	176.1	20.61	-	-			4	otz	2	-22.5	174.7	21.78	-	-
			carb	3	-21.2	174.7	21.16	-	-			4	otz	3	-24.5	181.9	22.68	-	-
			carb	6	-18.9	149.2	19.99	-	-			4	qtz	4	-21.8	178.6	21.45	-	-
			carb	7	-16.1	156.9	18.43	-	-			4	qtz	5	-22.2	179.2	21.64	-	-
			carb	9	-19.7	110.2	20.41	-	-			4	otz	6	-21.7	169.7	21.40	-	-
			carb	10	-17.1	167.4	19.01	-	-			4	otz	7	-	183.5	-	-	-
			carb	11	-	141.7	-	-	-			5	qtz	8	-22	277.3	21.55	-	-
			carb	12	-17.7	190.8	19.34	-	-			5	qtz	9	-22	189	21.55	-	-
			carb	13	-	200.2	-	-	-			5	otz	10	-22.1	180.2	21.59	-	-
			carb	14	-16.1	195.2	18.43	-	-		03B	1	qtz	82	-21.7	143.7	21.40	-	-
			carb	15	-18.5	178.4	19.78	-	-			1	qtz	83	-22.5	147.2	21.78	-	-
			carb	16	-24.7	187.8	22.77	-	-			1	qtz	84	-22.5	148.5	21.78	-	-
			carb	17	-17.2	176.9	19.06	-	-			1	otz	85	-22.5	137.7	21.78	-	-
			carb	18	-17.1	197.8	19.01	-	-			2	otz	86	-20.4	133.3	20.76	-	-
			carb	19	-19.7	195.1	20.41	-	-			2	qtz	87	-20.7	118.5	20.91	-	-
			carb	20	-24.9	191.3	22.85	-	-			2	qtz	88	-21.3	157.2	21.21	-	-
			carb	21	-18.9	196.4	19.99	-	-			2	otz	90	-21.5	100.2	21.31	-	-
			carb	22	-24.4	184.6	22.64	-	-			2	otz	91	-21.7	136.5	21.40	-	-
			carb	23	-18.1	180.7	19.53	-	-			2	qtz	92	-19.5	126.2	20.31	-	-
		6	carb	24	-13.1	182.1	16.53	-	-			2	qtz	93	-19.4	69.9	20.25	-	-
		6	carb	25	-	181.1	-	-	-		03B-U1	1	qtz	94	-21.1	170.7	21.11	-	-
		7	carb	26	-25.4	177.5	23.07	-	-			1	otz	95	-21.1	150.9	21.11	-	-
		8	carb	27	-24.8	184.5	22.81	-	-			1	otz	96	-21.4	146.2	21.26	-	-
		10	carb	29	-23.5	180.1	22.24	-	-			1	qtz	97	-21.4	-	21.26	-	-
	01B-MH	1	carb	30	-18.1	<80	19.53	-	-			1	qtz	98	-21.3	183.9	21.21	-	-
		2	carb	31	-23.1	134.6	22.06	-	-			1	otz	99	-21.3	181.2	21.21	-	-
		3	carb	32	-25.9	159.8	23.27	-	-			1	otz	100	-21		21.06	-	-
		3	carb	33	-26.5	158.5	23.52	-	-			1	qtz	101	-21.2	138.7	21.16	-	-
		4	carb	34	-16.6	163.9	18.72	-	-			1	qtz	102	-21.1	88.9	21.11	-	-
		4	carb	35	-24	129.8	22.46	-	-			1	otz	103	-18.2	125.3	19.62	-	-
		4	carb	36	-14.4	158.7	17.39	-	-			1	otz	104	-21.5	-	21.31	-	-
		4	carb	37	-17.3	-	19.10	-	-			1	qtz	105	-21	134.7	21.06	-	-
		5	carb	38	-12.4	171.8	16.04	-	-			1	qtz	106	-21.2	158	21.16	-	-
		6	carb	39	-22.8	144.4	21.92	-	-			1	otz	107	-21.1	145.6	21.11	-	-
		6	carb	40	-24.9	124.8	22.85	-	-			1	otz	108	-21.3	161.2	21.21	-	-
		6	carb	41	-22.6	-	21.83	-	-			1	qtz	109	-21.3	154.7	21.21	-	-
		6	carb	42	-24.3	173.3	22.59	-	-			1	qtz	110	-22.4	151.3	21.73	-	-
		7	carb	43	-	160.8	-	-	-			1	qtz	111	-22.2	170.7	21.64	-	-
		7	carb	44	-24.6	155.4	22.72	-	-			1	qtz	112	-22.1	169.4	21.59	-	-
	01A	1	carb	45	-23.5	211.2	22.24	-	-			1	qtz	113	-20.9	167.2	21.01	-	-
		1	carb	46	-18.8	149.6	19.94	-	-			2	otz	114	-22.7	-	21.87	-	-
		1	carb	47	-24.5	218.3	22.68	-	-			2	qtz	115	-22.5	-	21.78	-	-
		2	carb	48	-23.8	203.9	22.37	-	-			2	qtz	116	-22.4	-	21.73	-	-
		2	carb	49	-24	136.9	22.46	-	-			2	otz	117	-22.8	-	21.92	-	-
		3	carb	50	-23.4	196.5	22.19	-	-		03B	1	Fe-dol	118	-23.5	168.8	22.24	-	-
		3	carb	51	-23.1	212.2	22.06	-	-			1	Fe-dol	119	-24.2	173.8	22.55	-	-
		3	carb	52	-20.4	208.2	20.76	-	-			1	Fe-dol	120	-22.9	178.1	21.97	-	-
		4	carb	53	-16.7	153.3	18.78	-	-			1	Fe-dol	121	-24.7	178.4	22.77	-	-
		5	carb	54	-22.9	213	21.97	-	-			1	Fe-dol	122	-20.2	177.4	20.66	-	-
		6	carb	55	-21.4	171.7	21.26	-	-			1	Fe-dol	123	-22	135.4	21.55	-	-
		7	carb	56	-15.7	224.4	18.19	-	-			1	Fe-dol	124	-22.6	206.1	21.83	-	-
		8	carb	57	-23.3	193.8	22.15	-	-			1	Fe-dol	125	-24.2	125.9	22.55	-	-
		8	carb	58	-20.1	196.9	20.61	-	-			1	Fe-dol	126	-23	186.6	22.01	-	-
		8	carb	59	-24.1	189.4	22.51	-	-			1	Fe-dol	127	-23.7	171.1	22.33	-	-
		9	carb	60	-19.8	204.5	20.46	-	-			2	Fe-dol	128	-23.1	162.7	22.06	-	-
		10	carb	61	-17.8	157.3	19.40	-	-			2	Fe-dol	129	-24	244.3	22.46	-	-
			carb	62	-23.8	224.7	22.37	-	-			2	Fe-dol	130	-22.7	153.2	21.87	-	-
			carb	63	-23.7	217	22.33	-	-			2	Fe-dol	131	-22.8	182.3	21.92	-	-
			carb	64	-23.4	222.4	22.19	-	-			2	Fe-dol	132	-23.9	212.1	22.42	-	-
			carb	65	-22.7	221.9	21.87	-	-		03B-U2	1	Fe-dol	133	-24.1	154.4	22.51	-	-
Copper Pass	03B-U3	1	Fe-dol	1	-23.1	76.4	22.05	-	-			2	Fe-dol	134	-22.7	178.7	21.87	-	-
		1	Fe-dol	2	-25.1	135	22.94	-	-			2	Fe-dol	135	-23.3	173.2	22.15	-	-
		1	Fe-dol	3	-	139.5	-	-	-			2	Fe-dol	136	-23.5	155.1	22.24	-	-
		2	qtz	1	-20.8	284.8	20.96	-	-			3	Fe-dol	137	-23.1	180.6	22.06	-	-
		2	otz	2	-21.8	148.6	21.45	-	-			4	Fe-dol	138	-24.3	195.1	22.59	-	-
		2	otz	3	-20.7	123.5	20.91	-	-		SL-M-1-2	1	qtz	139	-23.23	152.3	22.37	-	-
		2	qtz	4	-20.2	133.7	20.66	-	-			1	qtz	140	-22.84	165.7	22.19	-	-
		3	qtz	5	-22.5	163.3	21.78	-	-			1	qtz	141	-24.80	172.1	23.07	-	-
		3	qtz	6	-21.8	125.4	21.45	-	-			1	qtz	142	-22.64	147.4	22.10	-	-
		3	qtz	7	-22.3	162.4	21.69	-	-			1	qtz	143	-23.52	128.9	22.51	-	-
		4	qtz	8	-21.6	135.4	21.35	-	-			2	qtz	144	-22.25	135.2	21.92	-	-
		4	qtz	9	-21.8	142.9	21.45	-	-			2	qtz	145	-21.65	133.7	21.64	-	-
		4	qtz	10	-	216.1	-	-	-			2	qtz	146	-20.87	126.4	21.26	-	-
		4	qtz	11	-23.1	172.4	22.06	-	-			2	qtz	147	-18.21	130.6	19.89	-	-
		5	qtz	12	-22.9	212.8	21.97	-	-			2	qtz	148	-21.06	119.4	21.35	-	-
		5	qtz	13	-23	245.6	22.01	-	-			2	qtz	149	-21.75	197.1	21.69	-	-
		5	qtz	14	-21.5	216.5	21.31	-	-			2	qtz	150	-20.87	235.6	21.26	-	-
		5	qtz	15	-17.4	211.3	19.18	-	-			2	qtz	151	-22.15	121.2	21.87	-	-
		5	qtz	16	-	191.7	-	-	-			2	qtz	152	-22.34	136.8	21.97	-	-
		5	qtz	17	-	226.3	-	-	-			3	qtz	153	-	-	-	-56.70	22.5
		5	qtz	18	-22.9	242.6	21.97	-	-			3	qtz	154	-	-	-	-56.30	24.9
		5	qtz	19	-	315.4	-	-	-			3	qtz	155	-	-	-	-56.30	25.1
		5	qtz	20	-	253	-	-	-			3	qtz	156	-	-	-	-56.50	26
		5	qtz	21	-	252.1	-	-	-			3	qtz	157	-	-	-	-56.60	21.9
		5	qtz	22	-22.8	207.7	21.92	-	-			4	qtz	158	-	-	-	-58.07	10.9
		5	qtz	23	-22.8	280.6	21.92	-	-			4	qtz	159	-	-	-	-56.50	8.9
		5	qtz	25	-	267.2	-	-	-			5	qtz	160	-	-	-	-57.09	17.2
		5	qtz	26	-	242.9	-	-	-			5	qtz	161	-	-	-	-56.60	27.3
		5	qtz	27	-	249.2	-	-	-			5	qtz	162	-	-	-	-56.40	22.3
		5	qtz	28	-	186.3	-	-	-			5	qtz	163	-	-	-	-56.40	23.4
		5	qtz	29	-	256.5	-	-	-			6	qtz	164	-	-	-	-56.40	19.9
		6	qtz	1	-24.4	236	22.64	-	-			6	qtz	165	-	-	-	-56.40	19.1
		6	qtz	2	-22.7	261.6	21.87	-	-				qtz	166	-	-	-	-56.40	28.4
		6	otz	3	-23.7	-	22.33	-	-										
		6	otz	4	-22.5	231.1	21.78	-	-										
		6	qtz	5	-23.7	279.7	22.33	-	-										
		6	qtz	6	-21.7	359.5	21.40	-	-										
		6	otz	7	-21.8	167.5	21.45	-	-										
		7	otz	8	-21.6	350.4	21.35	-	-										
		1	qtz	9	-22.4	173.9	21.73	-	-										
		2	qtz	10	-	>350	-	-	-										
		2	qtz	11	-	>350	-	-	-										
		2	qtz	12	-	209.9	-	-	-										
		2	qtz	13	-20.2	158.4	20.66	-	-										
		1	qtz	14	-	321.8	-	-	-										
		1	otz	15	-22.7	294	21.87	-	-										
		1	otz	16	-21.5	343.8	21.31	-	-										
		3	otz	17	-20.4	263.5	20.76	-	-										
		3	qtz	18	-21	239.2	21.06	-	-										
		3	qtz	19	-21.1	308.5	21.11	-	-										

Notes: dashes= no values recorded, T_m^{ICE} = final ice melting temperature, T_h= temperature of homogenization, $T_m^{carbonic}$ = final ice melting of carbonic inclusions, $T_h^{carbonic}$ = temperature of homogenization of carbonic phase, cal= calcite, qtz= quartz, Fe-dol= ferroan-dolomite, and blanks in the column "assemblage" indicate single inclusions. Homogenization of aqueous inclusions is from L_{aq} +V to L_{aq}. Homogenization of carbonic inclusions is from $L_{carbonic}$ + $V_{carbonic}$ to $L_{carbonic}$

Table 5. Laser ablation ICP-MS analyses[1,2,3] of major, minor and trace elements in brine inclusions (quartz-hosted) from Copper Pass (samples 153B03-A2-C, 153B03-A2-A and 153B03B-U1)

Sample no.	[4]Assemblage	^{23}Na	^{25}Mn	^{39}K	^{44}Ca	^{55}Mn	^{56}Fe	^{63}Cu	^{66}Zn	^{85}Rb	^{88}Sr	^{107}Ag	^{111}Cd	^{133}Cs	^{137}Ba	^{208}Pb	^{209}Bi	^{232}Th	^{238}U	NaiCa	Na/Rb	Fe/Pb	Rb/Cs	Pb/-Zn
2803-U1	1	60600	10980	8170	40265	543.0	12753	1.6	33.9	28.2	12.4	53.9	31.8	91.7	6.9	2.4	4.4	1.4	42.1	6.7	0.9	28.4	1.9	1.51	2.89	1.85	22.378	19.1
2803-U1	1	76297	1296	12936	23725	76.3	1807	1.4	98.2	87.9	125.9	57.7	1221	3.6	1.8	4.0	16.4	546.0	21.4	1.1	0.2	0.3	3.51	21.14	4.10	3.5175	109.3
2803-U1	1	83222	944.8	8761	12672	4.7	537.0	4.4	321.2	77.4	46.7	22.5	468.0	11.0	7.3	15.2	4.5	62.2	12.1	4.1	0.6	1.2	8.59	20.83	-	5.0031	58.7
2803-U1	1	87795	2471.0	5476	7692	46.6	4231.1	3.3	178.8	33.2	29.0	161.8	7.1	558.3	3.1	4.3	12.1	6.5	198.5	16.8	2.7	1.3	1.4	11.41	71.92	-	1.0978	45.9
2803-U1	1	82248	1091.0	12534	11876	46.3	801.1	4.0	275.3	331.2	17.2	114.5	35.5	425.2	3.8	5.7	13.7	3.6	143.9	22.7	2.9	1.3	0.8	7.05	11.98	-	9.7415	50.0
2803-U1	1	84188	1239	18945	4110	10.5	1098	0.8	59.2	48.8	17.9	83.3	50.2	91.2	1.5	2.8	2.9	17.0	4.4	0.7	0.3	0.3	20.48	1.82	4.10	17.49	22.3
2803-U1	2	81418	2446	3005	17158	69.1	379.1	2.1	147.5	9.1	490.8	1167.3	11.6	1197	1.0	2.2	5.8	11.2	763.8	46.0	1.3	0.4	0.6	4.75	102.9	10.68	1.0352	536.7
2803-U1	2	80118	1387	17299	11685	71.3	2206	0.6	35.8	2.4	111.9	133.3	57.3	991.9	1.0	0.7	1.7	7.2	471.4	13.7	0.4	0.1	0.1	6.87	17.31	8.20	8.0105	125.6
2803-U1	2	72500	2172	17930	21707	72.0	1035.4	3.3	206.4	14.4	427.2	61.7	71.6	1412	5.0	4.6	9.0	19.4	1388.8	64.0	2.3	1.0	2.6	3.39	19.73	6.68	3.6805	491.2
2803-U1	2	88876	215.1	6919	4701	15.5	326.5	0.6	41.6	26.4	23.7	56.6	22.5	573.4	0.9	0.6	1.9	6.2	110.1	12.4	0.4	0.1	0.1	18.91	25.50	1.92	3.6225	36.1
2803-U1	3	89762	168.9	5321	4533	29.4	175.03	1.5	110.9	39.0	35.2	75.8	11.6	109.3	2.4	2.7	5.1	2.0	94.0	19.2	1.6	0.6	0.7	19.80	9.40	1.83	5.7997	54.4
2803-U1	3	89792	116.5	5919	4734	24.5	248.8	2.8	168.4	88.9	46.7	44.1	16.5	141.1	3.6	2.9	7.6	3.5	80.5	9.5	1.9	0.8	0.8	18.97	13.38	4.93	2.9921	56.1
2803-U1	3	78363	822.9	3590	24691	75.8	288.6	2.5	146.4	10.2	228.2	136.0	7.9	964.4	2.5	2.6	8.2	9.0	1193.5	86.3	1.8	0.3	0.6	3.14	122.83	2.64	0.8731	314.5
2803-U1	3	68631	3774	26427	21662	205.3	1456	11.2	916.9	45.1	531.8	277.0	106.7	1795	15.1	17.1	46.0	40.3	1527.6	36.0	9.3	5.0	3.1	3.18	16.82	14.76	2.6457	567.8
2803-U1	3	72930	321.8	4035	35209	126.8	447.5	4.8	265.1	18.2	204.7	76.0	25.3	1249	10.5	6.2	13.5	27.6	869.9	71.7	3.2	1.4	1.1	2.07	49.37	2.86	0.9179	276.4
2803-U1	4	77514	1226	6292	23848	65.0	892.5	2.4	197.9	11.0	213.4	252.2	11.1	1114	3.1	4.5	9.4	8.9	1085.0	86.7	2.5	1.1	0.8	3.25	100.12	2.46	1.2501	300.1
2803-U1	4	75201	434.5	4599	30714	139.3	439.7	3.7	277.5	16.3	233.1	91.2	38.1	893.3	4.7	4.8	23.3	16.1	526.3	47.3	3.3	1.6	3.0	2.45	23.46	4.93	2.3634	280.5
2803-U1	4	87351	697.4	1970	10452	20.4	1556	3.8	38.4	28.2	47.0	84.8	9.2	262.6	1.8	19.4	61.9	4.5	163.4	11.5	1.3	61.9	2.6	8.36	22.03	4.11	2.0581	58.5
2803-U1	5	82856	709.2	5734	15102	13.9	42	0.3	30.0	1.6	104.7	21.9	35.0	1654	6.5	0.6	1.3	5.8	190.3	16.6	5.7	0.1	0.1	5.49	47.25	6.31	6.0682	121.3
2803-U1	5	80774	476.8	8870	17384	154.0	1687	13.2	958.5	59.7	155.5	1147.7	60.9	1137	37.6	24.9	49.4	28.4	547.3	38.7	14.9	4.9	4.7	4.65	16.68	4.01	2.1408	184.3
2803-U1	5	83738	389.0	5530	14509	26.2	169	1.5	108.2	7.9	82.0	26.6	17.4	992.3	3.7	1.8	5.4	7.3	722.9	51.1	0.9	0.2	0.5	5.77	57.17	1.61	2.364	133.1
2803-U1	5	80269	271.9	6541	26039	150.9	307	3.2	220.2	12.0	253.4	151.0	28.6	1001	4.2	4.5	9.6	15.6	444.2	72.7	2.4	1.2	0.9	4.01	35.05	3.48	1.8355	326.1
2803-U1	5	81191	444.2	8096	17235	150.7	599.6	1.4	104.0	6.4	225.0	32.7	33.6	941.4	1.6	2.9	5.1	18.4	345.7	116.1	1.3	0.7	0.5	4.71	28.00	1.94	1.8229	341.1
2803-U1	5	81958	473.0	12858	12424	147.8	1003	9.6	695.4	33.1	350.1	860.6	32.1	940.4	23.9	15.9	45.3	18.9	459.4	97.6	17.3	2.9	2.7	6.60	29.28	3.59	1.6951	447.7
2803-U1	6	82745	898.0	13414	16015	77.1	1345	0.7	77.9	5.0	320.6	204.2	54.4	939.3	5.3	1.7	2.9	18.2	620.7	102.7	1.0	0.2	0.3	8.26	17.28	3.12	2.9679	423.4
2803-U1	6	88895	245.9	5441	5877	55.9	774.2	2.5	235.9	41.6	47.8	124.9	22.9	178.6	4.4	6.0	11.3	4.6	97.6	22.9	2.9	1.1	1.3	15.13	7.79	2.09	4.9945	70.6
2803-U1	6	78262	1273	23229	11027	111.0	1240	3.4	253.8	15.2	179.0	147.0	70.5	969.7	2.8	4.2	9.5	14.2	707.2	60.0	2.6	0.9	1.1	7.10	13.75	2.98	4.9544	239.0
2803-U1	7	77661	743.1	8287	23081	269.4	1874	6.9	627.5	12.5	255.3	147.6	33.2	1321	10.3	9.3	20.6	14.5	482.4	110.1	6.2	2.6	2.2	3.36	33.72	2.32	2.2909	365.5
2803-U1	8	78684	192.8	7374	22652	99.4	521.8	5.2	386.1	21.2	216.8	98.9	11.4	1049	5.4	7.6	14.4	12.3	389.1	64.6	4.2	1.4	1.5	3.47	91.64	3.36	0.9302	281.4
2803-U1	9	77762	1030	8991	21781	172.6	558.8	5.0	401.3	25.2	194.5	193.7	32.6	1520	14.0	7.4	15.4	8.2	864.3	42.5	3.6	1.8	1.6	3.57	46.66	4.58	3.9609	297.0
2803-U1	9	81851	1076	10430	13264	28.4	1243	1.6	93.2	6.2	384.6	25.8	42.5	1133	1.1	1.9	4.1	10.5	1489.5	145.7	1.2	0.4	0.5	6.17	26.67	2.64	4.0354	530.4
2803-U1	9	74396	1916	18826	20575	68.5	1837	2.2	124.9	14.6	76.4	30.3	68.7	667.9	4.2	2.2	4.1	11.4	242.2	25.0	2.4	0.3	0.7	3.62	9.72	3.06	6.0469	101.4
2803-U1	9	89779	35.0	3317	6018	4.4	44.8	0.5	35.3	8.2	11.9	48.7	7.6	231.8	3.0	0.8	1.4	2.3	65.3	0.5	0.3	0.1	0.2	14.92	30.65	22.79	3.2914	12.5
2803-U1	9	89119	446.8	2953	6923	11.3	189.8	3.9	80.6	13.4	30.0	23.7	6.6	171.0	3.7	2.0	3.1	5.0	38.9	2.7	1.6	0.3	0.6	12.87	25.95	11.27	1.3204	32.7
2803-A2	10	79758	160.2	2642	17787	98.9	7508	1.2	84.7	5.2	48.9	35.5	7.4	1322	6.2	1.8	9.7	8.3	423.4	36.8	2.6	0.4	16.9	4.48	178.4	1.33	0.8936	85.7
2803-A2	10	88589	126.9	527	9946	39.6	632.7	3.8	288.7	14.2	95.0	113.7	7.8	308.1	7.2	7.3	17.9	6.5	171.3	44.9	3.9	1.6	1.7	8.91	-	2.11	1.2034	139.9
2803-A2	10	86302	128.6	1465	12816	59.3	897.0	9.2	477.8	34.7	95.8	174.7	11.9	1045	18.8	12.1	23.8	10.5	511.6	71.3	6.4	3.4	3.4	6.73	-	1.34	1.131	167.1
2803-A2	10	87075	204.8	1002	12451	105.8	1841.8	12.1	638.4	36.0	145.3	285.8	18.3	975.3	34.5	14.3	62.9	14.6	470.9	41.3	8.7	3.8	2.6	6.99	-	3.52	1.252	186.6
2803-A2	10	82862	565.0	4413	17138	100.4	336.1	1.6	146.9	7.7	93.0	60.4	26.9	936.4	2.1	3.2	7.3	13.3	631.1	15.9	2.3	0.8	0.6	4.83	34.83	5.85	2.0152	108.9
2803-A2	10	76215	2066	26588	13749	69.2	447.0	3.1	200.7	13.3	124.9	91.8	125.2	1089	3.5	4.1	10.3	28.0	987.5	27.6	2.5	1.1	1.0	5.54	8.69	4.53	4.4772	152.5
2803-A2	10	83423	638.1	176.7	18940	102.1	265.7	3.4	116.9	5.7	140.3	49.2	8.4	1166	1.2	2.1	22.9	15.9	652.3	34.7	1.2	0.7	0.6	4.40	139.3	4.04	0.5252	175.0
2803-A2	10	86304	50.0	112.8	13956	11.5	169.2	1.2	75.7	5.2	14.0	32.7	2.2	1077	1.6	1.7	6.4	4.2	379.7	24.3	1.0	0.4	0.3	6.18	463.9	0.66	0.5133	40.3
2803-A2	10	82286	617.7	8434	15355	55.7	433.9	2.4	170.4	10.3	140.3	86.5	16.1	1040	7.6	3.5	9.4	23.4	557.4	32.8	2.7	0.8	1.0	5.36	64.50	4.28	0.6895	173.1
2803-A2	10	80118	237.9	7199	20154	45.0	170.5	1.1	88.9	6.2	135.4	92.3	5.1	1085	7.9	1.5	71.2	11.0	585.0	16.4	4.0	0.5	0.5	3.98	214.6	8.27	0.4597	151.8
2803-A2	10	90782	52.0	855.1	5595	5.2	72.2	0.5	25.9	1.6	14.0	14.0	2.1	506.0	1.1	0.8	1.5	2.5	258.4	8.3	0.3	0.1	1.7	16.23	244.1	1.69	0.8137	22.4
2803-A2	10	73269	1327	21097	23528	64.4	642.6	2.9	326.1	17.0	46.9	124.6	35.6	1022	4.5	4.8	14.4	8.5	121.3	6.3	3.5	0.6	1.3	3.11	28.73	-	4.2085	53.2
2803-A2	10	86909	901.4	2654	11151	92.4	879.6	6.5	463.8	19.9	80.3	172.9	29.4	686.8	14.9	24.1	18.9	11.6	492.6	50.1	4.0	0.9	2.2	7.79	23.40	1.60	2.5342	130.4
2803-A2	10	89522	453.4	6552	3992	15.5	211.2	1.5	116.1	8.5	98.7	43.5	17.6	412.8	5.3	2.5	4.7	10.4	242.4	6.8	1.1	0.3	7.1	22.43	24.24	14.45	1.6441	105.5
2803-A2	10	87292	618.9	10707	5519	16.3	219.7	1.4	126.1	59.2	43.9	40.2	13.7	212.4	2.1	2.3	5.1	9.5	22.2	4.4	1.0	0.6	0.5	15.82	15.50	9.98	1.4486	48.3
2803-A2	10	87193	683.5	939.6	11595	95.4	1277.7	5.7	594.5	41.2	184.2	246.2	30.4	1887	20.0	11.8	32.6	20.2	754.9	20.1	6.7	1.1	2.6	7.52	55.46	9.14	1.5071	264.3
2803-A2	10	86247	323.8	717.2	14095	82.5	1113.4	5.8	634.9	37.0	82.8	216.4	16.0	896	9.7	11.2	25.0	15.2	453.3	23.0	5.7	1.3	2.3	6.12	-	3.59	1.0547	105.8
2803-A2	10	79173	438.2	533.5	26508	129.7	833.6	7.7	430.8	26.6	132.1	161.2	14.0	1326	8.9	8.5	19.3	16.9	790.8	24.3	5.4	1.2	2.2	2.99	94.99	5.43	0.8243	156.4
2803-A2	10	82089	340.7	91.7	19025	156.4	1014.8	9.5	645.3	49.4	242.4	235.9	17.5	1914	19.6	14.5	31.7	14.6	709.3	58.9	8.4	2.5	2.8	4.38	-	4.26	1.1988	299.3

Note: [1] Concentration listed in units listed. [2] Grey italicized values are bdl = below detection limit (varies based on inclusion size and other parameters). dash = not quantifiable. [3] Assemblages correspond to groups of inclusions that appear to be trapped simultaneously (do not correspond to assemblages in Table 4). Grey italicized ecoevents below detection limits. Superscript indicates the isotope measured for each analyte but quantified concentrations are for total analyte not isotope

Table 6 - Selected major, minor and trace element composition of bitumen and pyrobitumen from Copper Pass, Union Island and Athabasca Basin (LA-ICPMS)

Bitumen sample	Location	^{56}Fe	^{59}Co	^{61}Ni	^{65}Cu	^{66}Zn	^{75}As	^{95}Mo	^{107}Ag	^{121}Sb	^{197}Au	^{208}Pb	^{209}Bi	^{139}La	^{140}Ce	^{141}Pr	^{146}Nd	^{147}Sm	^{153}Eu	^{157}Gd	^{159}Tb	^{163}Dy	^{165}Ho	^{166}Er	^{169}Tm	^{172}Yb	^{175}Lu
19d03	Copper Pass	1922	541	1453	7870	5.40	361	15292	270	31.6	0.24	1618	3356	1057	2.31	0.42	0.86	0.51	1.71	1.39	1.28	1.68	0.89	0.72	0.40	0.92	0.36	*0.26*
19d04	Copper Pass	318	174	106	2543	4.04	29.6	4756	62.0	14.6	*0.16*	155	1009	19.83	*0.67*	0.02	*0.14*	*0.07*	*0.55*	*0.38*	*0.48*	*0.16*	*0.21*	*0.20*	0.12	*0.25*	*0.53*	*0.26*
19d05	Copper Pass	2666	1120	685	14200	4.12	256	25458	439	76.1	0.95	1161	6587	1358	1.87	0.43	0.60	0.74	1.35	0.67	0.65	1.31	1.25	0.41	0.43	0.31	0.52	*0.17*
19d06	Copper Pass	2065	1779	710	13917	*2.60*	194	23597	544	81.1	0.56	2927	7092	2.08	*0.96*	*0.04*	*0.20*	*0.22*	*0.79*	*0.54*	*0.92*	*0.76*	0.57	*0.28*	*0.35*	*0.72*	*0.76*	*1.21*
19d07	Copper Pass	3172	2018	846	21505	*1.01*	185	46825	729	123	0.63	1899	7645	197	0.27	0.08	*0.12*	*0.13*	0.22	*0.14*	0.16	0.22	0.26	0.19	0.20	*0.18*	*0.28*	*0.44*
19d08	Copper Pass	3156	1116	703	12739	4.02	301	38946	921	99.3	*0.29*	2838	7152	1761	2.78	1.27	1.01	1.40	1.92	0.70	1.96	3.14	3.60	1.29	1.40	1.16	0.99	*0.88*
19d10	Copper Pass	1866	232	621	4703	8.88	50.4	15628	170	12.3	3.10	1634	2969	2049	6.18	1.20	1.48	1.54	3.37	2.42	3.14	3.17	3.56	1.60	1.56	1.28	0.55	0.41
19d11	Copper Pass	5530	167	265	591	5.25	56.5	9704	136	12.9	3.43	448	1648	548	35.5	3.08	3.31	2.28	2.13	0.65	1.18	1.22	0.82	0.42	0.39	0.45	0.31	*0.40*
19d13	Copper Pass	6007	951	1060	30904	6.18	110	65340	1119	53.9	0.35	6426	10535	1042	1.59	0.53	0.90	0.48	1.76	1.47	1.70	2.49	0.70	0.24	0.59	0.41	1.18	*0.76*
19d15	Copper Pass	1768	982	386	12442	1.76	93.3	25587	360	83.8	66.5	1341	4952	647	0.64	0.22	0.17	0.26	0.80	0.23	0.29	0.70	0.33	0.26	0.27	0.18	0.20	*0.17*
19d18	Copper Pass	6662	1216	1230	25204	1.57	138.0	62950	942	97.3	0.83	3194	9999	2055	12.1	1.97	1.86	1.26	3.65	3.95	2.98	3.36	3.17	1.25	0.92	1.07	0.53	0.42
19d19	Copper Pass	426	323	158	3428	*2.82*	69.2	8839	99	34.0	*0.44*	611	1814	6564	2.32	2.30	2.68	3.79	4.72	1.05	7.92	10.9	9.24	3.63	3.28	2.14	2.31	2.14
19d23	Copper Pass	3571	1995	718	24379	6.30	185	39744	751	160	0.65	2293	8378	550	*0.43*	0.15	0.19	0.33	0.53	*0.54*	0.63	0.54	0.46	0.36	*0.16*	0.36	*0.39*	*0.83*
19d24	Copper Pass	2429	1461	538	18435	218	112	41643	497	94.9	0.44	2167	6341	2712	3.27	1.04	1.61	1.21	2.75	3.23	1.79	3.40	2.53	1.18	0.85	1.01	0.61	0.50
19d25	Copper Pass	9347	1333	501	34462	4.78	212	64721	829	122	0.53	5108	10213	4116	24.9	3.49	4.64	4.75	8.97	6.66	7.76	9.72	7.64	3.56	3.10	3.37	2.38	1.19
19d26	Copper Pass	1373	643	287	7530	*0.61*	327	16542	175	30.3	0.18	977	2443	34950	125	37.4	56.7	56.7	148	148	109	141	101	40.5	33.8	27.9	21.3	10.0
19d27	Copper Pass	2047	924	399	12025	1.34	169	30616	311	32.2	0.39	1428	3968	3836	19.0	2.77	3.37	3.06	6.73	6.51	6.88	9.06	5.75	2.56	2.44	2.76	1.95	0.66
20a03	Copper Pass	6572	2925	587	35889	2.26	454	72518	1263	224	1.11	2166	18489	1096	1.83	0.77	0.56	0.55	1.88	2.60	1.25	1.70	1.28	0.68	0.39	0.45	0.21	*0.09*
20a04	Copper Pass	2552	1493	568	23626	1.21	118	40692	407	64.8	0.56	3706	8384	1952	1.91	0.54	0.79	0.70	1.71	1.60	1.79	2.37	1.88	1.04	0.85	1.10	0.56	*0.34*
20a07	Copper Pass	1265	609	257	7776	2.02	52.2	17370	196	51.1	2.29	1475	2126	6494	32.0	4.47	5.35	4.93	12.1	8.98	8.59	12.2	8.83	4.20	3.36	2.66	2.09	0.92
20a08	Copper Pass	6569	1438	313	33067	2.67	95.7	78101	912	157	0.85	2577	14622	4434	9.15	2.37	3.88	4.24	8.85	11.4	7.34	9.98	9.18	3.80	2.52	2.40	1.58	0.67
20a09	Copper Pass	2391	1351	509	13686	13.2	138	33025	434	105	3153	1541	5757	603	0.68	0.15	0.21	0.26	0.56	0.54	0.28	0.68	0.71	0.42	0.08	0.24	0.08	*0.11*
20a12	Copper Pass	2819	1833	643	22608	*0.90*	166	49258	551	148	0.66	2421	8288	6225	3.90	1.31	2.11	2.36	4.81	3.12	4.38	6.22	5.16	2.20	2.21	1.73	1.19	0.76
20a17	Copper Pass	3374	427	1373	12102	3.03	253	50189	683	67.8	0.43	6744	13986	7067	7.98	0.81	1.45	1.63	3.28	2.14	1.90	2.81	2.20	0.83	0.55	*0.38*	*0.50*	*0.40*
20a19	Copper Pass	5540	1147	1274	25090	1.89	147	71906	956	61.4	0.86	6831	12352	1211	2.42	0.50	0.69	0.70	1.50	1.78	1.65	1.33	0.99	0.83	0.37	0.35	0.46	*0.47*
20a21	Copper Pass	4997	1375	967	22567	4.86	222	70322	745	67.9	0.46	4347	10134	7239	17.6	3.87	5.49	5.13	10.8	10.5	11.2	13.8	9.47	4.84	3.95	3.21	2.66	1.64
20a23	Copper Pass	4907	1579	804	26386	2.09	474	57266	589	81.0	0.62	2906	7211	17403	35.5	8.62	11.9	11.9	26.5	32.6	24.3	31.1	27.1	11.9	10.8	6.69	6.78	3.89
20a24	Copper Pass	2316	856	231	8935	1.04	115	21344	314	41.4	0.28	983	3228	16589	28.4	8.47	13.2	14.3	26.9	24.3	28.3	36.2	30.7	14.4	12.1	8.35	6.45	3.99
20a25	Copper Pass	5841	2024	645	27178	1.09	312	59986	730	114	0.27	2359	10890	2774	8.71	1.80	2.44	2.20	4.93	3.03	4.57	5.30	4.16	2.10	1.82	1.27	0.95	0.43
20a26	Copper Pass	2502	1941	627	25810	1.16	155	41728	657	162	0.46	2838	8968	200	*0.29*	0.05	*0.06*	*0.07*	*0.24*	0.18	*0.42*	0.21	0.10	*0.09*	*0.11*	*0.10*	*0.08*	*0.23*
20a27	Copper Pass	5070	3120	1093	43408	*1.04*	288	95015	1266	289	1.02	5198	14886	1733	0.93	0.42	0.70	0.49	1.36	1.39	1.70	1.69	1.88	1.10	0.42	0.66	*0.39*	0.37
20a28	Copper Pass	5595	2916	823	38727	3.55	56.3	60758	1017	213	0.73	4372	12620	196	0.72	0.16	0.17	0.10	0.66	0.32	0.50	0.52	0.35	0.40	0.12	0.24	*0.11*	*0.17*
20a29	Copper Pass	2645	685	504	16311	0.79	87.1	35591	423	94.5	0.32	2461	5235	593	0.69	0.11	0.09	0.11	0.18	0.36	0.25	0.10	0.20	0.14	0.09	*0.16*	*0.11*	*0.33*
20a30	Copper Pass	3465	1255	567	17577	0.76	115	30165	455	90.3	0.46	2372	6739	4225	8.40	1.85	2.80	2.80	5.57	4.67	5.23	7.46	6.04	2.82	2.18	1.86	1.59	0.83
20a31	Copper Pass	2876	1598	541	20335	0.62	119	33960	448	136	0.62	1835	7575	1277	1.75	0.40	0.45	0.58	1.47	0.84	1.25	1.57	1.17	0.89	0.86	0.28	0.40	*0.35*
20a32	Copper Pass	997	432	172	6034	*0.49*	41.9	12780	149	46.3	0.46	641	2550	243	0.50	0.07	4.12	0.09	0.14	0.25	0.42	0.32	0.28	0.12	0.08	*0.11*	*0.15*	*0.12*
20a37	Copper Pass	2094	1260	502	15503	*1.23*	208	28869	508	80.2	0.63	1693	5229	7897	11.9	3.51	4.71	4.51	11.5	7.90	11.6	14.2	12.4	5.83	4.56	3.64	3.97	1.45
20a38	Copper Pass	1611	858	370	9802	*0.64*	79.1	17665	280	66.8	0.28	917	3353	2677	2.76	0.81	0.70	0.99	2.74	2.28	2.10	3.36	2.68	1.46	0.91	0.61	0.58	0.18
20a39	Copper Pass	1983	823	330	11625	*0.74*	93.8	21608	302	55.5	0.41	1074	3100	8852	10.1	3.48	4.75	5.33	10.7	13.3	10.8	14.0	11.8	5.64	4.41	2.99	2.96	2.10
20a40	Copper Pass	3253	1326	422	18232	*1.13*	146	37224	369	71.6	0.37	2301	5370	1722	5.02	0.80	1.09	1.23	3.01	2.28	2.51	3.43	2.80	1.37	1.14	0.83	0.60	0.31
20a41	Copper Pass	1104	618	247	8163	*0.89*	61.2	17265	231	65.9	0.34	1035	3669	138	*0.27*	0.03	*0.11*	*0.12*	*0.44*	*0.15*	*0.31*	0.15	0.10	*0.16*	*0.19*	*0.20*	*0.13*	*0.21*
20a42	Copper Pass	2033	1212	428	17155	*1.15*	91.4	28514	340	100	0.42	2766	4956	4264	3.72	1.01	1.91	1.58	3.79	4.04	3.89	6.40	5.08	2.38	1.59	2.09	0.96	*0.44*
20a43	Copper Pass	2061	572	166	5979	0.43	85.3	16369	248	36.6	0.27	1036	2681	7908	1830	154	135	103	63.4	24.0	31.3	23.0	15.6	7.55	5.45	4.34	3.00	1.99
20a44	Copper Pass	1853	1022	454	13830	*0.69*	81.9	26249	361	69.1	0.36	1591	4353	3714	2.90	0.81	1.23	1.25	3.11	3.59	3.22	3.85	3.61	1.41	1.54	1.21	1.10	0.48
20a45	Copper Pass	3823	356	1024	11887	2.73	46.0	38763	492	15.3	0.63	3230	7060	1781	9.32	1.68	1.66	1.66	2.29	3.69	3.34	2.79	2.43	1.21	0.84	0.63	0.47	0.24
20a46	Copper Pass	1222	962	389	12666	*0.75*	97.1	18261	461	81.8	0.40	1238	4242	305	0.26	0.10	0.26	0.14	0.42	0.40	0.40	0.34	0.45	0.10	*0.09*	*0.32*	*0.12*	*0.34*
20a47	Copper Pass	2813	684	566	9969	3.90	50.9	29016	250	29.8	0.54	1961	4548	6018	23.0	4.11	5.07	4.53	8.48	8.12	8.55	10.2	9.20	4.08	3.77	2.42	1.96	1.32
20a48	Copper Pass	644	413	196	5101	0.78	60.1	11168	196	41.7	*0.10*	577	2275	3056	2.78	0.93	1.49	1.38	3.82	2.79	3.29	4.83	3.59	1.49	1.58	1.07	0.78	0.48
20a49	Copper Pass	472	345	182	4062	0.77	51.2	10120	135	34.5	*0.06*	490	2019	2037	1.54	0.72	1.12	1.03	1.62	2.16	2.05	3.42	2.81	1.15	1.14	0.66	0.76	0.28
30a16	Union Island	*14.1*	1.09	338	4.85	*2.06*	*6.25*	*0.21*	1.67	*0.50*	0.04	31.3	*0.10*	*0.00*	*0.01*	*0.01*	*0.00*	*0.03*	*0.03*	0.01	*0.03*	*0.00*	*0.02*	*0.02*	*0.05*	*0.02*	*0.11*	*0.00*
30a17	Union Island	*10.1*	1.28	372	16.6	1.79	*4.62*	*0.12*	1.63	*0.42*	0.04	35.0	*0.07*	*0.00*	*0.01*	0.01	*0.00*	*0.02*	*0.02*	*0.02*	*0.08*	*0.01*	*0.01*	*0.02*	*0.01*	*0.00*	*0.05*	*0.01*
30a18	Union Island	*10.2*	0.68	225	5.46	2.85	*4.78*	*0.12*	1.95	*0.38*	0.03	11.5	*0.06*	*0.00*	0.01	0.02	*0.00*	*0.07*	*0.02*	*0.01*	*0.02*	0.00	*0.01*	0.01	*0.01*	*0.00*	*0.02*	*0.00*
30a19	Union Island	*10.1*	0.95	278	14.1	2.26	*4.78*	0.09	1.65	*0.38*	0.03	11.8	*0.07*	*0.02*	*0.02*	0.02	0.01	*0.02*	*0.03*	*0.02*	*0.03*	*0.00*	*0.02*	*0.00*	*0.01*	*0.00*	*0.02*	*0.00*
30a20	Union Island	*10.9*	0.77	220	7.80	1.78	*5.22*	0.06	1.38	*0.44*	*0.02*	41.9	*0.07*	*0.00*	0.00	*0.02*	*0.00*	*0.02*	*0.03*	*0.01*	*0.11*	*0.00*	*0.01*	*0.00*	*0.02*	*0.00*	*0.02*	*0.00*
30a21	Union Island	*10.5*	1.42	184	5.63	2.56	*5.15*	*0.19*	1.70	*0.38*	*0.02*	15.0	*0.06*	*0.00*	*0.01*	*0.00*	*0.00*	*0.02*	*0.03*	*0.01*	*0.08*	*0.01*	*0.02*	*0.00*	*0.01*	*0.00*	*0.02*	*0.01*
30a22	Union Island	*15.7*	0.78	269	12.6	4.83	*7.74*	0.13	2.51	*0.49*	*0.04*	11.3	*0.10*	*0.02*	*0.01*	*0.02*	*0.01*	*0.03*	*0.04*	*0.01*	*0.04*	*0.01*	*0.02*	*0.02*	*0.02*	*0.01*	*0.03*	*0.01*
30a23	Union Island	*16.1*	0.34	194	5.19	3.63	*8.16*	*0.19*	2.29	*0.61*	*0.03*	8.01	*0.08*	*0.02*	*0.01*	*0.01*	*0.01*	*0.04*	*0.04*	*0.01*	*0.04*	*0.01*	*0.03*	*0.02*	*0.02*	*0.01*	*0.03*	*0.01*
30a24	Union Island	*14.6*	0.80	354	9.26	3.24	*7.41*	0.12	2.83	*0.54*	*0.04*	5.89	*0.10*	*0.03*	*0.01*	*0.01*	*0.01*	*0.04*	*0.04*	*0.03*	*0.04*	*0.01*	*0.03*	*0.01*	*0.02*	*0.02*	*0.03*	*0.01*
30a27	Athabasca Basin	819	1.48	13.1	9.80	39.6	17.6	93.3	0.17	12.3	0.02	115	0.04	1701	0.79	3.26	0.80	4.61	2.42	0.51	0.77	0.15	0.93	0.13	0.33	0.04	0.16	0.01
30a28	Athabasca Basin	4117	5.69	35.8	87.2	213	90.3	167	0.63	28.1	0.06	1462	*0.05*	4328	1.82	7.14	1.55	6.95	2.82	0.41	1.10	0.27	1.43	0.19	0.43	0.08	0.43	0.05
30a29	Athabasca Basin	9998	7.79	67.6	126	337	77.6	1104	1.49	158	0.17	1191	0.38	4909	2.93	9.98	1.74	10.4	2.69	0.50	0.85	0.31	1.73	0.12	0.29	*0.07*	0.40	*0.06*
30a30	Athabasca Basin	5104	5.76	37.5	62.3	102	69.7	1009	0.83	81.2	0.13	579	*0.12*	4603	1.09	8.51	1.26	4.76	2.34	0.37	0.62	0.21	1.17	0.12	0.25	0.06	0.20	*0.02*
30a31	Athabasca Basin	6434	7.43	51.7	49.8	177	77.4	740	0.27	50.5	0.05	692	0.29	12224	3.41	22.8	4.56	18.8	8.04	1.26	2.68	0.71	4.17	0.49	1.28	0.13	0.78	0.07
30a32	Athabasca Basin	1304	1.39	17.5	9.60	20.0	15.9	12.4	0.78	3.49	0.04	164	0.07	1937	0.81	4.06	5.27	4.49	1.87	0.34	0.97	0.32	0.72	0.10	0.18	0.03	0.19	0.05
30a33	Athabasca Basin	2129	1.74	15.3	14.8	31.8	44.4	94.2	0.23	15.6	0.02	394	0.04	2465	1.00	6.84	1.46	8.50	3.16	0.48	1.08	0.26	1.33	0.19	0.40	0.05	0.24	0.02
30a34	Athabasca Basin	5566	4.23	38.5	34.6	82.3	194	532	0.57	66.3	0.09	6334	0.11	12449	11.7	60.6	18.5	74.8	41.1	6.44	17.9	4.03	23.4	2.89	7.85	0.66	4.56	0.31
30a35	Athabasca Basin	779	1.69	21.4	5.60	24.6	30.0	97.5	0.20	14.8	0.02	169	*0.03*	1156	1.78	5.52	0.94	3.20	0.75	0.15	0.30	0.07	0.41	0.03	0.08	0.01	0.06	*0.01*
30a36	Athabasca Basin	2561	5.72	47.9	38.1	86.9	27.4	33.7	0.35	32.9	0.04	265	*0.05*	3076	1.26	4.65	1.09	5.52	1.89	0.23	0.56	0.11	0.91	0.07	0.21	0.02	0.19	*0.01*
30a37	Athabasca Basin	7749	13.1	99.2	189	1731	73.2	393	1.23	121	0.22	583	0.19	12125	3.67	26.7	7.97	45.7	20.1	4.73	11.0	2.19	16.1	1.58	3.30	0.33	2.78	0.17
30a38	Athabasca Basin	2206	5.43	68.2	22.2	113	82.5	147	0.65	71.5	0.13	315	*0.15*	10882	3.61	38.2	12.9	77.9	31.9	7.39	21.8	4.13	24.9	3.76	6.75	0.56	4.09	0.47
30a39	Athabasca Basin	5866	9.88	58.1	66.6	172	63.5	64.9	0.77	38.9	0.05	420	0.20	26014	9.82	105	28.0	195	57.9	10.6	28.1	4.94	26.8	3.71	7.24	0.77	4.43	0.40
30a40	Athabasca Basin	4903	17.1	97.8	46.4	133	56.9	123	0.34	84.6	0.02	159	0.52	137344	40.1	314	109	555	243	43.0	75.6	23.4	123	14.0	28.8	3.39	20.7	1.56
30a41	Athabasca Basin	13166	11.8	96.8	65.7	177	86.0	63.1	0.30	62.4	0.03	373	0.19	79649	33.0	209	56.3	268	101	18.4	34.0	9.22	51.3	6.06	12.5	1.64	10.3	0.90
30a42	Athabasca Basin	11721	18.3	116	69.2	236	167	242	0.99	128	0.03	627	0.83	133272	29.6	227	72.8	353	152	27.0	48.4	14.1	77.6	8.88	17.4	2.18	13.7	1.11
30a43	Athabasca Basin	8668	14.8	101	58.8	174	68.8	238	0.67	67.3	0.02	415	0.12	89296	27.7	223	78.6	400	165	33.0	51.3	15.8	87.0	11.3	23.6	2.71	17.1	1.33
30a44	Athabasca Basin	411	0.96	5.62	3.29	10.3	7.63	19.6	0.05	5.86	0.00	33.56	0.02	7694	1.89	15.94	5.69	28.2	12.1	2.35	3.88	1.10	6.48	0.79	1.60	0.19	1.22	0.10
30a45	Athabasca Basin	11401	16.3	108	62.5	231	142	193	0.61	66.1	0.02	1118	0.32	83877	30.6	193	58.2	287	120	20.3	34.5	10.2	56.6	6.88	14.4	1.70	10.8	0.84
30a46	Athabasca Basin	7122	9.55	71.3	39.4	137	73.6	219	0.43	66.4	0.01	167	0.44	53922	17.8	113	33.5	148	66.0	10.9	17.4	5.24	29.7	3.23	6.74	0.86	5.61	0.43
30a47	Athabasca Basin	12401	20.5	130	71.2	258	145	431	0.48	45.9	0.06	407	0.17	75239	16.1	122	39.7	198	76.0	14.8	27.6	7.51	41.9	5.17	10.5	1.25	7.84	0.56
30a48	Athabasca Basin	7599	11.7	82.2	40.2	152	89.1	147	0.62	77.8	0.03	170	0.32	79741	16.8	123	39.5	198	80.5	14.2	25.6	7.29	38.3	4.62	9.59	1.12	8.05	0.58
30a49	Athabasca Basin	7869	12.8	88.7	44.9	151	78.7	300	0.64	74.3	0.02	217	0.27	83742	21.8	152	50.7	234	106	18.5	31.8	8.90	53.4	6.20	12.2	1.54	10.1	0.81
30a50	Athabasca Basin	7567	19.6	86.5	68.8	222	93.7	804	0.35	155	0.06	733	0.58	330234	92.5	1084	375	2134	988	173	348	87.2	458	58.1	122	13.6	76.9	6.38

Note: [a] Concentration listed in µg/g (ppm); [b] Grey italicized values are bdl = below detection limit (varies based on inclusion size and other parameters); Superscript indicates the isotope measured for each analyte but quantified concentrations are for total analyte not isotope

Table 7 - LA-ICPMS analyses of vein carbonates at Copper Pass and Union Island

Location	Sample	Analysis	Species	^{43}Ca	^{95}Mo	^{56}Fe	^{55}Mn	^{7}Li	^{11}B	^{23}Na	^{27}Al	^{29}Si	^{39}K	^{59}Co	^{60}Ni	^{65}Cu	^{66}Zn	^{75}As	^{85}Rb	^{88}Sr	^{89}Y	^{133}Cs	^{137}Ba	^{139}La	^{140}Ce	^{141}Pr	^{146}Nd	^{147}Sm	^{153}Eu	^{157}Gd	^{159}Tb	^{163}Dy	^{165}Ho	^{166}Er	^{169}Tm	^{172}Yb	^{175}Lu	^{208}Pb	^{232}Th	^{238}U
				wt%	wt%	wt%	wt%	ppm	ppm	ppm	ppm	ppm	ppm	ppm	ppm	ppm	ppm	ppm	ppm	ppm	ppm	ppm	ppm	ppm	ppm	ppm	ppm	ppm	ppm	ppm	ppm	ppm	ppm	ppm	ppm	ppm	ppm	ppm	ppm	ppm
Copper Pass	15JB03B-U3	1	Fe- dolomite	19.50	7.67	6.90	0.37	0.16	bdl	44.5	159.6	231.1	4.03	1.32	5.83	0.29	4.02	0.56	0.04	215.82	67.45	bdl	0.57	1.77	14.10	3.67	25.12	14.69	1.10	17.27	2.43	13.74	2.51	6.38	0.86	4.79	0.63	0.119	0.003	bdl
Copper Pass	15JB03B-U3	2	Fe- dolomite	19.50	7.58	6.89	0.36	0.38	bdl	53.2	155.7	248.4	5.96	1.30	5.68	0.21	4.27	0.65	bdl	212.53	69.51	bdl	0.58	1.62	13.24	3.39	23.55	14.26	1.02	17.11	2.41	13.79	2.53	6.83	0.86	5.31	0.69	0.122	bdl	bdl
Copper Pass	15JB03B-U3	3	Fe- dolomite	19.50	7.59	6.85	0.37	bdl	bdl	46.1	158.6	217.9	4.97	1.30	5.54	0.21	3.93	0.33	bdl	210.81	63.14	0.02	0.60	1.30	10.24	2.63	17.90	11.25	1.04	13.94	1.99	11.98	2.26	6.28	0.84	5.08	0.72	0.106	bdl	bdl
Copper Pass	15JB03B-U3	4	Fe- dolomite	19.50	7.44	6.91	0.36	0.22	bdl	64.6	159.2	220.8	4.55	1.29	6.17	0.12	4.21	0.75	0.03	208.85	56.89	bdl	0.63	1.69	12.84	3.25	21.51	12.74	1.18	14.83	2.11	11.47	2.19	5.75	0.70	3.99	0.49	0.129	bdl	bdl
Copper Pass	15JB03B-U3	5	Fe- dolomite	19.50	7.48	7.08	0.38	0.39	1.48	182.5	125.5	195.8	14.78	1.37	5.07	0.25	4.16	1.10	0.08	225.98	52.83	bdl	1.25	1.73	12.74	3.09	20.66	11.97	1.07	13.63	1.92	10.91	1.99	5.14	0.66	4.00	0.49	0.214	bdl	bdl
Copper Pass	15JB03B-U3	6	Fe- dolomite	19.50	7.42	7.14	0.39	0.62	bdl	210.5	86.4	238.1	17.88	1.82	5.55	0.32	4.71	0.70	0.10	206.44	35.64	0.05	2.39	1.17	8.32	2.01	13.03	7.33	0.78	9.02	1.20	7.30	1.40	3.71	0.51	2.98	0.41	0.284	bdl	bdl
Copper Pass	15JB03B-U3	7	Fe- dolomite	19.50	7.44	6.98	0.38	0.42	bdl	176.3	94.5	243.2	16.84	1.25	5.08	0.32	5.24	1.47	0.08	220.83	37.31	0.04	1.94	1.10	8.22	2.00	14.03	7.86	0.77	8.82	1.24	7.62	1.42	3.98	0.54	3.16	0.48	0.339	bdl	bdl
Copper Pass	15JB03B-U3	8	Fe- dolomite	19.50	7.42	7.05	0.38	bdl	bdl	85.9	127.5	255.9	7.31	1.26	5.44	0.20	4.19	0.96	bdl	232.39	47.59	0.02	0.83	1.60	11.61	2.84	18.77	10.49	1.09	12.19	1.68	9.72	1.75	4.77	0.60	3.51	0.45	0.173	0.002	bdl
Copper Pass	15JB03B-U3	9	Fe- dolomite	19.50	7.29	6.98	0.38	bld	bdl	139.4	164.2	bdl	11.73	1.30	11.38	bdl	5.18	bdl	bdl	223.02	67.14	bdl	0.62	1.89	14.27	3.68	24.02	14.42	1.31	17.22	2.49	13.94	2.49	6.12	0.82	4.49	0.60	0.238	bdl	bdl
Copper Pass	15JB03B-U3	10	Fe- dolomite	19.50	7.52	6.85	0.37	0.24	bdl	61.2	164.0	257.3	6.85	1.22	5.57	0.16	4.73	0.42	0.04	210.41	60.10	0.02	0.61	1.16	8.96	2.35	16.20	10.03	1.04	12.45	1.87	11.20	2.17	6.13	0.84	5.13	0.73	0.147	0.002	bdl
Copper Pass	15JB03B-U3	11	Fe- dolomite	19.50	7.58	7.00	0.37	bdl	bdl	35.4	162.6	215.7	4.02	1.38	6.16	0.25	4.22	0.56	0.03	223.23	68.19	0.01	0.31	1.95	14.90	3.86	25.86	15.15	1.25	18.12	2.47	14.18	2.55	6.52	0.83	4.75	0.62	0.132	bdl	bdl
Copper Pass	15JB03B-U3	12	Fe- dolomite	19.50	7.83	6.58	0.36	0.39	bdl	177.9	88.5	377.9	22.52	0.35	3.89	0.36	5.07	1.17	0.09	182.08	71.07	0.06	1.42	1.64	12.21	3.18	21.77	13.87	0.95	18.10	2.47	13.71	2.49	6.49	0.83	5.21	0.74	0.233	bdl	bdl
Copper Pass	15JB03B-U3	13	Fe- dolomite	19.50	7.44	6.95	0.38	0.51	bdl	144.9	101.6	294.1	13.90	0.71	5.73	0.30	4.95	0.97	0.07	194.55	71.16	0.04	1.75	1.68	12.34	3.16	21.69	14.17	1.08	18.35	2.56	14.28	2.54	6.55	0.85	5.18	0.71	0.221	0.002	bdl
Copper Pass	15JB03B-U3	14	Fe- dolomite	19.50	7.45	6.95	0.37	bdl	bdl	9.8	159.3	246.4	1.86	1.28	6.54	0.21	3.88	1.89	bdl	234.00	59.98	bdl	0.15	2.06	14.87	3.72	25.06	13.95	1.43	15.74	2.16	12.53	2.27	5.91	0.72	4.18	0.53	0.106	bdl	bdl
Copper Pass	15JB03B-U3	15	Fe- dolomite	19.50	7.56	6.77	0.36	bd	bd	72.0	158.5	261.4	7.60	1.32	6.02	0.22	4.45	0.60	0.04	218.18	60.46	bdl	0.36	1.24	9.72	2.51	17.14	10.49	1.00	12.82	1.89	11.10	2.16	6.19	0.84	5.10	0.72	0.153	0.003	bdl
Copper Pass	15JB03B-U3	16	Fe- dolomite	19.50	5.79	11.06	0.59	bdl	bdl	8.5	2.5	222.2	3.40	1.76	7.92	0.18	1.85	0.56	bdl	26.20	6.25	bdl	0.05	0.02	0.29	0.11	0.55	0.51	0.15	0.90	0.19	1.01	0.19	0.56	0.06	0.29	0.04	0.026	bdl	bdl
Copper Pass	15JB03B-U3	17	Fe- dolomite	19.50	5.97	10.16	0.54	bdl	bdl	11.2	11.0	246.9	bdl	3.09	7.03	0.18	1.87	0.39	bdl	30.79	9.70	bdl	0.07	0.12	0.93	0.22	1.24	0.75	0.16	1.23	0.23	1.46	0.31	0.84	0.11	0.66	0.09	bdl	bdl	bdl
Copper Pass	15JB03B-U3	18	Fe- dolomite	19.50	6.83	8.58	0.38	0.30	0.62	236.3	36.6	259.9	22.48	4.94	6.95	0.27	2.11	0.56	0.10	24.41	13.08	0.03	0.75	0.16	1.07	0.27	1.58	1.24	0.10	1.96	0.37	2.25	0.41	1.06	0.12	0.50	0.07	0.072	0.001	bdl
Copper Pass	15JB03B-U3	19	Fe- dolomite	19.50	6.49	9.27	0.42	0.23	bdl	120.5	32.9	287.5	21.84	4.32	9.27	0.35	2.09	5.29	0.09	27.89	23.29	0.02	0.62	0.14	0.92	0.23	1.45	1.18	0.12	2.30	0.51	3.67	0.76	2.05	0.26	1.28	0.15	0.054	bdl	bdl
Copper Pass	15JB03B-U3	20	Fe- dolomite	19.50	6.66	9.03	0.38	0.33	0.78	163.9	14.3	262.4	12.25	5.00	6.23	0.19	1.97	0.84	0.06	25.39	18.42	0.04	1.13	0.24	1.66	0.33	2.20	1.33	0.17	2.16	0.45	3.06	0.60	1.56	0.17	0.91	0.08	0.098	bdl	bdl
Union Island	UI1	1	dolomite	22.02	11.00	2.12	0.34	0.24	bdl	bdl	78.5	bdl	bdl	0.10	bdl	0.36	24.15	17.10	0.02	146.05	-	bdl	1.20	3.93	14.81	2.33	11.38	3.41	1.57	3.98	0.60	3.64	0.67	1.70	0.18	0.94	0.10	0.31	-	-
Union Island	UI2	2	dolomite	22.11	10.82	2.28	0.32	0.16	bdl	bdl	84.5	bdl	bdl	0.08	bdl	0.38	24.02	17.19	0.01	146.62	-	bdl	0.81	4.58	16.02	2.32	11.09	2.82	1.74	2.85	0.35	1.87	0.30	0.66	0.07	0.32	0.03	0.30	bdl	bdl
Union Island	UI3	3	dolomite	22.05	10.99	2.10	0.34	0.60	bdl	27.4	73.7	bdl	3.05	0.10	0.46	0.38	22.21	17.12	0.05	138.65	-	0.02	3.15	3.30	12.53	1.94	9.45	2.84	1.29	3.25	0.51	3.00	0.57	1.51	0.17	0.90	0.11	0.44	-	-
Union Island	UI4	4	dolomite	22.04	11.07	2.04	0.32	0.47	0.97	23.5	72.7	bdl	1.82	0.09	bdl	0.35	23.28	18.24	0.04	132.24	-	0.03	2.30	3.09	11.54	1.79	8.89	2.48	1.25	3.05	0.44	2.73	0.53	1.30	0.15	0.77	0.08	0.33	-	bdl
Union Island	UI5	5	dolomite	21.85	10.68	2.79	0.29	0.16	bdl	7.9	5.7	bdl	bdl	0.10	bdl	0.37	13.39	17.79	0.03	85.45	-	0.02	2.69	0.26	1.39	0.26	1.31	0.36	0.11	0.36	0.04	0.26	0.05	0.13	0.02	0.06	0.01	0.19	-	bdl
Union Island	UI6	6	dolomite	22.03	11.05	2.07	0.32	0.68	1.39	44.6	71.2	bdl	5.95	0.08	bdl	0.34	21.07	17.59	0.08	137.33	-	0.06	3.14	2.97	10.97	1.69	7.96	2.10	1.11	2.36	0.33	1.96	0.38	0.96	0.11	0.52	0.06	0.37	bdl	bdl
Union Island	UI7	7	dolomite	22.12	10.94	2.11	0.33	0.41	bdl	13.7	80.3	bdl	14.24	0.09	bdl	0.42	21.71	17.35	0.12	154.46	-	0.01	2.02	3.83	14.01	2.05	9.78	2.45	1.32	2.48	0.33	2.04	0.36	0.84	0.10	0.48	0.05	0.34	bdl	-
Union Island	UI8	8	dolomite	21.93	11.20	2.06	0.27	0.49	bdl	7.3	6.0	bdl	bdl	0.08	bdl	0.45	22.82	17.90	0.03	101.82	-	0.02	1.69	0.58	2.03	0.29	1.38	0.35	0.18	0.38	0.05	0.27	0.05	0.11	0.01	0.06	0.01	0.25	bdl	bdl
Union Island	UI9	9	dolomite	22.03	10.91	2.23	0.33	0.73	0.97	49.5	77.1	bdl	6.45	0.08	bdl	0.54	18.82	17.41	0.09	151.43	-	0.04	4.82	3.62	11.52	1.66	7.67	1.85	1.12	1.82	0.26	1.40	0.27	0.63	0.07	0.33	0.04	0.38	bdl	bdl

Note: dash = not quantifiable. Superscript indicates the isotope measured for each analyte but quantified concentrations are for total analyte not isotope

Table 8. Stable (O-C) and radiogenic (Sr) isotope, and ICP-OES/ICP-MS analyses of vein carbonates at Blanchet Island, Copper Pass, Labelle Penninsula and Rabbit Lake

Sample no.	Location	$^{87}Rb/^{86}Sr$	$^{87}Sr/^{86}Sr_0$	StdErr (Abs)	$^{1}\delta^{13}C_{VPDB}$	$^{2}\delta^{18}O_{VSMOW}$	Al	Ba	Ca	Fe	K	Mg	Mn	Na	Rb	Sr	1/Sr
					‰	‰	ppm	ppm	ppm	ppm	ppm	ppm	ppm	ppm	ppm	ppm	ppm^{-1}
01A-carbvein	Blanchet Island	0.001	0.709655	0.000009	-2.73	12.1	0.00	4.03	372544	2600	bdl	2875	1157	94.6	0.06	144	0.007
01A-Host	Blanchet Island	0.034	0.709791	0.000030	-2.49	13.5	695	3.29	147508	17629	29.5	51178	1448	224	0.37	31.0	0.032
01C-M	Blanchet Island	0.006	0.710387	0.000178	-2.02	13.0	5.42	4.00	137339	19052	4.85	63851	1747	96.9	0.08	35.4	0.028
01-ore pile	Blanchet Island	0.005	0.710065	0.000037	-2.73	13.4	13.8	4.66	136250	22878	0.000	64107	1617	106	0.06	37.7	0.027
SL-M-1-2	Copper Pass	0.004	0.710704	0.000016	-4.06	11.3	113	7.67	116062	46057	6.74	51569	2329	63.3	0.14	113	0.009
SL-M-2-1	Copper Pass	0.015	0.710555	0.000049	-1.32	14.1	56.6	7.60	140703	76225	bdl	50268	3596	91.3	0.11	20.1	0.050
SL-W-2-1	Copper Pass	0.016	0.708093	0.000085	-3.04	16.2	38.9	3.04	129059	28786	bdl	67120	2469	73.9	0.08	14.0	0.072
SL-M-2-3	Copper Pass	0.006	0.719578	0.006177	-1.13	15.4	37.8	4.18	124656	84205	bdl	37165	4675	76.2	0.04	17.7	0.057
SL-W-2-3	Copper Pass	0.001	0.712067	0.000019	-3.15	11.7	26.7	2.66	118664	47030	bdl	52448	3511	63.0	0.05	104	0.010
03B-U	Copper Pass	0.008	0.709432	0.000149	-2.56	10.8	33.5	3.83	132900	53447	bdl	57864	2604	96.7	0.08	29.2	0.034
LB-2B-1	Labelle Penninsula	0.029	0.711159	0.000046	0.19	18.7	74.0	9.43	148772	81935	bdl	50966	5718	89.2	0.24	23.1	0.043
JH-1	Rabbit Lake	0.031	0.708198	0.000078	-5.08	24.4	43.5	3.11	52162	334.98	bdl	32913	319	41.8	0.09	8.33	0.120
JH-2	Rabbit Lake	0.026	0.708191	0.000067	-4.22	23.4	21.5	2.67	46293	449.64	bdl	29036	421	44.3	0.03	3.74	0.268
JH-3	Rabbit Lake	0.004	0.709081	0.000015	-4.16	21.1	25.3	3.08	67905	1439.08	6.99	29234	2266	59.4	0.03	20.0	0.050
JH-4	Rabbit Lake	0.021	0.708156	0.000024	-4.53	22.2	29.5	2.70	71624	738.70	bdl	44347	563	54.8	0.06	7.44	0.134

Notes: bdl= below detection limits

Table 9. Secondary ion mass spectrometry oxygen isotope data in early zoned quartz, Copper Pass

analysis	[1]$\delta^{18}O$ (‰)	[2]zone	analysis	$\delta^{18}O$ (‰)	zone	analysis	$\delta^{18}O$ (‰)	zone
CT-2-20	3.9	A	CT-4-08	7.0	C	P05	16.7	D3
CT-3-04	4.6	A	CT-5-04	7.3	C	JB-13	13.7	D3
CT-2-24	4.7	A	CT-3-15	8.2	C	JB-14	13.0	D3
CT-3-06	5.0	A	CT-5-10	10.6	C	JB-15	13.5	D3
CT-3-10	7.4	A	CT-4-09	5.2	D1	JB-16	15.6	D3
CT-3-07	4.0	B	CT-6-01	10.8	D1	JB-17	15.6	D3
CT-2-26	4.7	B	CT-6-03	11.0	D1	P07	15.5	E
CT-3-09	7.6	B	CT-3-01	11.7	D1	P08	15.1	E
CT-3-08	5.8	B	CT-5-09	12.3	D1	P11	12.6	E
CT-2-30	6.0	B	P18	11.1	D1	P01	16.8	E
CT-2-32	4.0	B	P14	10.1	D1	P02	15.5	E
CT-3-11	8.4	B	P09	9.3	D1	P16	21.0	E
CT-2-35	5.6	B	P06	6.2	D1	P17	16.6	E
CT-2-28	7.3	B	JB-22	11.9	D1	P20	20.1	E
CT-3-13	8.5	B	JB-23	9.8	D1	P21	17.6	E
CT-2-25	7.1	B	JB-24	10.7	D1	CT-3-29	9.2	E
CT-3-17	8.6	B	JB-25	10.4	D1	CT-3-27	10.3	E
CT-2-31	5.2	B	JB-26	10.0	D1	CT-5-02	15.1	E
CT-3-18	7.4	B	JB-27	9.0	D1	CT-3-36	15.9	E
CT-2-33	5.6	B	JB-28	8.0	D1	CT-3-38	16.4	E
CT-3-19	10.4	B	JB-29	8.3	D1	CT-4-01	16.9	E
CT-2-34	5.7	B	JB-31	11.3	D1	CT-2-41	16.9	E
CT-2-37	6.8	C	JB-33	12.0	D1	CT-2-40	6.7	E
CT-3-02	8.4	C	JB-34	9.4	D1	CT-2-42	7.5	E
CT-4-05	9.0	C	CT-4-04	9.2	D2	CT-3-23	11.2	E
CT-6-07	11.6	C	CT-6-08	9.4	D2	CT-3-39	13.9	E
CT-5-05	6.3	C	CT-5-13	11.8	D2	CT-5-01	15.1	E
CT-5-12	8.5	C	CT-3-21	14.2	D2	CT-6-04	16.1	E
CT-5-06	9.2	C	P04	6.9	D2	JB-4	18.4	E
CT-5-14	9.6	C	P10	6.8	D2	JB-5	19.2	E
CT-4-06	6.1	C	P13	8.2	D2	JB-6	22.6	E
CT-3-03	7.2	C	CT-6-02	9.8	D3	JB-7	22.4	E
CT-2-16	8.5	C	CT-4-10	15.3	D3	JB-10	19.7	E
CT-5-11	8.7	C	CT-5-03	16.8	D3	JB-11	20.7	E
CT-2-14	9.7	C	CT-6-06	19.8	D3	JB-12	21.6	E
CT-6-05	10.2	C	P03	15.3	D3	JB-18	17.3	E
CT-5-08	10.3	C	P19	19.9	D3	JB-19	19.7	E
CT-3-22	11.7	C	P15	20.2	D3	JB-20	19.5	E
CT-4-07	6.8	C	P12	11.7	D3	JB-21	19.1	E

Notes: [1]uncertainty on analysis = 1.2‰ (1σ) ; spot-to-spot reproducibility on quartz standard = 0.5‰. [2] zones classification based on hot cathode CL fluorescence colouration; A=core, dark (black-blue); B=core, mid (pink-orange); C=bright (pink-orange); D1=transitional (very bright yellow-pink); D2=transitional (very bright pink); D3=(very bright blue); E=rim (dark black-blue); coeval bitumen and fluid inclusions hosted in D3, at or near the D2-D3 interface

Table 10. K-U-Th scintillometry (concentrations equivalency derived from activity) on mineralized veins at Copper Pass

Sample	K	U	Th	Sample	K	U	Th
	%	ppm	ppm		%	ppm	ppm
15JB03A1	1.2	14	7.9	15JB03-R	1.5	9.7	8.7
15JB03A1	1.3	19.2	6	15JB04A	1	55.7	6.2
15JB03A2	1.3	116.7	9.9	15JB04B	1.6	9.7	5.7
15JB03A2	1.5	14.9	7.1	15JB05A	1.5	12.9	6.5
15JB03B	1.8	115.6	5	15JB05A	1.5	10.3	7.2
15JB03B	1.1	12.5	7.9	15JB05B-V	1.4	19.9	4.7
15JB03B	1.7	29	3.3	15JB05B	1.4	8.9	7.8
15JB03B	1.5	66.9	4.1	15JB05B	1.3	70.8	5.5
15JB03B	1.9	68.5	9.9	15JB05C	1.5	9.7	7.2
15JB03C	1.6	6.7	4.7	15JB05C	1.4	9.6	7.6
15JB03C	1.2	6.4	8.1				